NASA TECHNICAL MEMORANDUM

NASA TM X-2632

NASA TM X-2632

EFFECT OF NOZZLE LATERAL SPACING ON AFTERBODY DRAG AND PERFORMANCE OF TWIN-JET AFTERBODY MODELS WITH CONE PLUG NOZZLES AT MACH NUMBERS UP TO 2.20

by Bobby L. Berrier

Langley Research Center
Hampton, Va. 23365

NATIONAL AERONAUTICS AND SPACE ADMINISTRATION • WASHINGTON, D. C. • DECEMBER 1972

1. Report No.	2. Government Accession No.	3. Recipient's Catalog No.
NASA TM X-2632		

4. Title and Subtitle	5. Report Date
EFFECT OF NOZZLE LATERAL SPACING ON AFTERBODY DRAG AND PERFORMANCE OF TWIN-JET AFTERBODY MODELS WITH CONE PLUG NOZZLES AT MACH NUMBERS UP TO 2.20	December 1972
	6. Performing Organization Code
7. Author(s)	8. Performing Organization Report No.
Bobby L. Berrier	L-8481
	10. Work Unit No.
9. Performing Organization Name and Address	501-24-06-01
NASA Langley Research Center Hampton, Va. 23365	11. Contract or Grant No.
	13. Type of Report and Period Covered
12. Sponsoring Agency Name and Address	Technical Memorandum
National Aeronautics and Space Administration Washington, D.C. 20546	14. Sponsoring Agency Code

15. Supplementary Notes

16. Abstract

Twin-jet afterbody models were investigated by using two balances to measure separately the thrust minus total drag and the afterbody drag at Mach numbers of 0.0 and 0.50 to 2.20 for a constant angle of attack of 0°. Translating shroud cone plug nozzles were tested at dry and maximum afterburning power settings with a high-pressure air system used to provide jet total-pressure ratios up to 20.0. Two nozzle lateral spacings were studied by using afterbodies with several interfairing shapes. The close- and wide-spaced afterbodies had identical cross-sectional area distributions when similar interfairings were installed on each. Nozzle cant angles of -5°, 0°, and 5° were investigated. The results show that the highest overall performance was generally obtained with the close-spaced afterbody, basic interfairings (no base), and uncanted nozzles.

17. Key Words (Suggested by Author(s))	18. Distribution Statement
Twin-engine installation Cone plug nozzles Nozzle lateral spacing Nozzle cant angle	Unclassified – Unlimited

19. Security Classif. (of this report)	20. Security Classif. (of this page)	21. No. of Pages	22. Price*
Unclassified	Unclassified	131	$3.00

*For sale by the National Technical Information Service, Springfield, Virginia 22151

EFFECT OF NOZZLE LATERAL SPACING ON AFTERBODY DRAG AND PERFORMANCE OF TWIN-JET AFTERBODY MODELS WITH CONE PLUG NOZZLES AT MACH NUMBERS UP TO 2.20

By Bobby L. Berrier
Langley Research Center

SUMMARY

An investigation has been conducted to determine the effect of nozzle lateral spacing on the drag and performance of twin-engine afterbody configurations with translating shroud cone plug nozzles at Mach numbers of 0.0 and 0.50 to 2.20. Angle of attack was held at a constant value of 0^{o}. Two nozzle power settings were investigated, namely, dry and maximum afterburning. A high-pressure air system was used to provide jet total-pressure ratios up to 20.0. Two nozzle lateral spacings (ratio of distance between nozzle center lines to maximum nozzle diameter equal to 1.12 and 1.61) were studied by using afterbodies with several interfairing shapes. The close- and wide-spaced afterbodies had identical cross-sectional area distributions when similar interfairings were installed on each. The nozzles were tested at -5^{o}, 0^{o}, and 5^{o} cant angles.

The results of the investigation indicate that the overall performance term, thrust-minus-total-drag ratio, was generally highest for the close-spaced afterbody, basic interfairings (no base), and uncanted nozzles.

INTRODUCTION

Multiengine airplanes require careful integration of the airframe with the engines in order to assure good performance over a wide speed range. Although twin-engine airplanes with engines buried in the aft fuselage offer the advantage of compactness and alleviation of the one-engine-out stability problem, this afterbody-nozzle arrangement can also be extremely sensitive to nozzle-airframe interactions (refs. 1 to 6). Therefore, attention has been directed toward the twin-engine aircraft back-end problem in order to examine the effects on performance of axial location of the jet exits (ref. 7), engine lateral spacing (refs. 8, 9, and 10), engine interfairing shape (refs. 3, 9, 10, and 11), and the effects of tail-actuator fairings and tail-mounting booms (refs. 6, 8, and 11).

As part of a program on engine-airframe integration, the Langley Research Center is evaluating the performance of various twin-jet nozzles installed near the rear of model

fuselages. References 9 and 10 report the results of investigations on the effects of engine-nozzle lateral spacing for shrouded and unshrouded hinged-flap convergent nozzles and hinged-flap convergent-divergent nozzles, respectively. The present investigation shows the effects on performance of engine-nozzle lateral spacing, engine interfairing shape (varying base area), and nozzle cant angle for translating shroud cone plug nozzles. Close- and wide-spaced afterbodies were tested with several alternate engine-interfairing shapes. Each afterbody, with corresponding engine interfairings, had identical cross-sectional area distributions. Nozzle cant angles of 5°, 0°, and -5° were investigated since engine-airframe compatibility (fuel tanks, electronics, accessories, etc.) or one-engine-out stability problems may impose some angle other than 0°.

The investigation was conducted in the Langley 16-foot transonic tunnel at Mach numbers from 0.5 to 1.3 with nozzle throat areas corresponding to dry power (minimum throat area) and maximum afterburning power (maximum throat area) and in the Langley 4- by 4-foot supersonic pressure tunnel at a Mach number of 2.20 with the nozzles at maximum-afterburner-power setting (max A/B). Jet total-pressure ratio was varied from approximately 1.0 (jet-off) to 9 in the transonic facility and to approximately 20 in the supersonic tunnel. All configurations were tested without tails and at 0° angle of attack.

SYMBOLS

A cross-sectional area, meters^2

$A_{e,ext}$ external nozzle exit area for fully expanded flow (fig. 6) of one nozzle, meters^2

$A_{e,int}$ internal nozzle exit area at shroud exit (fig. 6) of one nozzle, meters^2

A_{eng} engine-tailpipe maximum cross-sectional area, meters^2

A_{max} maximum cross-sectional area of afterbody, meters^2

A_{seal} cross-sectional area enclosed by seal strip, meters^2

A_t throat area of one nozzle, meters^2

$C_{D,a}$ drag coefficient of afterbody including force on nozzle-clearance annuli, $\dfrac{D_a}{q_\infty A_{max}}$

$C_{D,f}$ friction drag coefficient of afterbody

$C_{D,w}$ supersonic wave-drag coefficient of afterbody

$C_{p,a}$ afterbody-pressure coefficient, $\frac{p_a - p_\infty}{q_\infty}$

d_{eng} diameter of engine tailpipe at maximum cross section, meters

d_{plug} maximum diameter of plug, meters

D afterbody drag plus nozzle-shroud drag, $D_a + D_{noz}$, newtons

D_a afterbody drag including drag on nozzle-clearance annuli, newtons

D_{bal} drag measured by afterbody drag balance, positive downstream, newtons

D_{noz} nozzle-shroud drag, newtons

F nozzle thrust, positive upstream, newtons

F_i ideal thrust for complete isentropic expansion of jet flow,

$$\dot{m}_j\sqrt{\frac{2\gamma}{\gamma - 1}RT_{t,j}\left[1 - \left(\frac{p_\infty}{p_{t,j}}\right)^{\frac{\gamma-1}{\gamma}}\right]}, \text{ newtons}$$

$(F - D)_{bal}$ jet thrust minus drag measured by thrust-minus-drag balance, positive upstream, newtons

h_1, h_2, h_3 height of afterbody interfairings, meters (see fig. 3)

H afterbody height at maximum cross section, meters (see fig. 3)

l length of model measured from model nose to dry-power shroud exit, meters

l_a afterbody length measured from seal station, meters (see fig. 1)

l_p plug length measured from nozzle throat, meters (see fig. 5)

$\dot{m}_j$	measured mass-flow rate, kilograms/second
M	free-stream Mach number
p_a	afterbody static pressure, newtons/meter^2
p_{ex}	external static pressure at seal station, newtons/meter^2
p_i	internal static pressure, newtons/meter^2
p_{plug}	plug static pressure, newtons/meter^2
$p_{t,j}$	jet total pressure, newtons/meter^2
p_∞	free-stream static pressure, newtons/meter^2
q_∞	free-stream dynamic pressure, newtons/meter^2
r	radius of engine nacelle, meters (see fig. 3)
R	gas constant (γ = 1.4), 287.3 newton-meters/kilogram-kelvin
s	spacing distance between engine-nozzle center lines, meters (see fig. 3)
$T_{t,j}$	jet stagnation temperature, kelvins
x	axial distance from model nose, positive downstream, meters
x_p	axial distance from nozzle throat location on plug surface, positive downstream, meters
β	nozzle cant angle, positive with tip toward model center line, degrees
Δ	indicates an increment
γ	ratio of specific heats

A bar over a symbol denotes an average condition.

APPARATUS AND METHODS

Wind Tunnels

The experimental investigation was conducted in the Langley 16-foot transonic tunnel and in the Langley 4- by 4-foot supersonic pressure tunnel. The Langley 16-foot transonic tunnel is a single-return, atmospheric tunnel with a slotted, octagonal test section and continuous air exchange. The tunnel has a continuously variable speed range from $M = 0.20$ to $M = 1.30$. The Langley 4- by 4-foot supersonic pressure tunnel is a single-return, continuous-flow wind tunnel with a stagnation-pressure range from 0.2758×10^5 N/m^2 to 2.0684×10^5 N/m^2 and a stagnation-temperature range from 310.9 K to 322.2 K. By mechanically deflecting the tunnel floor and ceiling between fixed sidewalls, to form a divergent nozzle, the Mach number can be varied from 1.25 to 2.20.

Model and Support System

A sketch of the strut-supported model with dry power nozzles installed is presented in figure 1, and photographs of the model installed in the Langley 16-foot transonic tunnel and 4- by 4-foot supersonic pressure tunnel are shown in figure 2. The model is supported from the tunnel wall by a thin sweptback strut which attaches to the model forebody and starts at the model nose. (See figs. 1 and 2.)

The term "afterbody," as used in this paper, is the metric portion of the model (that portion of the model on which forces and moments are measured), not including the nozzles, and starts at the model metric break or seal station (station 83.82). The seal station is indicated in the sketch of figure 1 and can be seen in the photographs shown in figure 2. A teflon strip inserted into grooves machined into the metric afterbody and nonmetric forebody was used as a seal to prevent internal flow in the model. The afterbody was attached to a drag balance which was attached in tandem to a thrust-minus-nozzle-drag balance. An annular clearance gap between the afterbody and nozzles was required to prevent fouling of the afterbody drag balance. This balance arrangement was discussed in references 7 and 10. To insure a turbulent boundary layer over the afterbody, a 0.38-cm-wide transition strip of No. 100 carborundum grit was fixed 5.08 cm from the model nose.

The twin-engine simulator utilized a high-pressure air system, described in reference 10, to simulate the exhaust flow of a twin-jet configuration.

Two basic afterbody configurations, one close spaced and one wide spaced, in conjunction with several alternate engine interfairings were used in this investigation. Figure 3 presents sketches and geometry details of the afterbody and interfairing configurations. Two lateral spacings between engine-nozzle center lines ($s/d_{eng} = 1.12$ for close-spaced afterbody and $s/d_{eng} = 1.61$ for wide-spaced afterbody) were selected for

the basic afterbodies. The close spacing was determined by the minimum practical clearance between parallel tailpipes, and the wide spacing was limited to the confines of the maximum model width. The basic afterbodies had engine interfairings which ended ahead of the nozzle at $x/l = 0.962$ and had no base. The alternate interfairings, which attached directly to the afterbodies, had reduced closure angles but ended with a base at the dry-power-nozzle exit plane. The basic afterbody configurations had identical longitudinal distributions of cross-sectional area as shown in figure 4. Addition of the large base alternate interfairings to the basic afterbodies also results in identical cross-sectional area distributions. The area distribution of the basic afterbodies shown in figure 4, between $x/l = 0.62$ and $x/l = 0.97$, was calculated by a computer program for axisymmetric bodies adapted from reference 12 and is representative of a minimum wave-drag body at $M = 1.000001$ with the restraint of a given forebody geometry, afterbody length, base area, and an infinite cylindrical-base streamtube. Afterbody configurations with alternate interfairings represent a deviation from the theoretically obtained area distribution.

Sketches presenting the geometry of the cone plug nozzles are given in figure 5, and important geometric parameters are given in figure 6. Two power settings were investigated at nozzle cant angles of 5° (in), 0°, and -5° (out) and represent dry power setting (see fig. 5(a)) and maximum-afterburner-power setting (herein referred to as max A/B) (see fig. 5(b)). The nozzles were designed for use with air as a fluid medium ($\gamma = 1.4$). The ratio of max A/B power throat area to dry-power throat area was 2.5. Photographs of several afterbody-interfairing-nozzle configurations are shown in figure 7.

Instrumentation

External static-pressure orifices were located on the afterbodies and interfairings at the locations indicated in figure 3. External static-pressure orifice locations on the nozzle plugs are shown in figure 5. Internal pressures were measured in the afterbody cavity at six internal orifice locations. The average external-seal static pressure was obtained from eight external orifices located on both sides of the seal gap between the forebody and afterbody. Four equal area-weighted total pressures and the stagnation temperature of the jet flow were measured in each tailpipe at locations indicated in figure 1.

Forces and moments on the metric portions of the model were measured by strain-gage balances. Nozzle thrust minus afterbody and nozzle drag was measured by a three-component main balance in the Langley 16-foot transonic tunnel and by a five-component balance in the 4- by 4-foot supersonic pressure tunnel. Forces and moments on the afterbody shell were measured with a tandem-mounted five-component balance in both facilities. An electronic turbine flow meter was used to obtain the air mass-flow rate to the nozzles.

All data for both the model and wind-tunnel facilities were recorded simultaneously on magnetic tape. Approximately seven frames of data were taken over a time period of about 2 seconds for each data point in the 16-foot transonic tunnel, and 10 frames of data were taken over a time period of about 10 seconds for each data point in the 4- by 4-foot supersonic pressure tunnel; average values were used in computations.

Tests

Data were obtained in the Langley 16-foot transonic tunnel at Mach numbers from 0 to 1.3 and in the Langley 4- by 4-foot supersonic pressure tunnel at a Mach number of 2.20 at a stagnation pressure of 1.25×10^5 N/m^2 and at a stagnation temperature of 318 K. The angle of attack was held at a constant value of 0^o during the entire investigation. Reynolds number based on model length (134.71 cm) varied from approximately 1.30×10^7 at $M = 0.50$ to 1.64×10^7 at $M = 1.30$ in the Langley 16-foot tunnel and was 1.72×10^7 at $M = 2.20$ in the Langley 4- by 4-foot supersonic pressure tunnel. The ratio of jet total pressure to free-stream static pressure was varied from approximately 1.0 (jet off) to about 20.0 depending on Mach number.

Data Reduction

The recorded data were used to compute standard force and pressure coefficients. The external-seal and internal pressure forces on the afterbodies were obtained by multiplying the difference between the average pressure (external-seal or internal) and free-stream static pressure by the affected projected area normal to the model axis.

Nozzle thrust minus the afterbody and nozzle drag was obtained directly by the thrust-minus-drag balance. (See fig. 1.) This performance term was computed as follows:

$$F - D = (F - D)_{bal} + (\bar{p}_{ex} - p_\infty)(A_{max} - A_{seal}) + (\bar{p}_i - p_\infty)A_{seal} \quad (1)$$

The forces sensed by the balance and included in the term $(F - D)_{bal}$ are nozzle thrust, external and internal axial forces on the nozzle shroud and plug, and afterbody external and internal axial forces transferred to the thrust-minus-drag balance through the tandem-mounted drag balance.

Afterbody drag was obtained directly from the tandem-mounted drag balance (see fig. 1) and computed from the equation

$$D_a = D_{bal} - (\bar{p}_{ex} - p_\infty)(A_{max} - A_{seal}) - (\bar{p}_i - p_\infty)(A_{seal} - 2A_{eng}) \quad (2)$$

Included in the afterbody-drag balance term D_{bal} are external and internal axial forces on the afterbody shell (including base areas of afterbody and alternate interfairings). Included in the afterbody drag D_a but not felt by the balance term D_{bal} is a pressure-area term to account for the annuli between the afterbody and nozzles.

The internal-pressure correction terms used in force equations (1) and (2) can be large, as was reported in reference 7. The magnitude of this correction can be equal to the drag-balance readings.

Thrust-minus-nozzle-drag performance is obtained by combining the two balance measurements as follows:

$$F - D_{noz} = F - D + D_a = (F - D)_{bal} + D_{bal} + \left(\bar{p}_i - p_\infty\right)\left(2A_{eng}\right) \tag{3}$$

At static conditions (M = 0), this equation yields nozzle internal performance since nozzle boattail (shroud) drag is approximately zero with no external flow. However, at Mach numbers other than zero, equation (3) includes nozzle boattail drag and external-flow effects on nozzle internal performance (effect of external flow on plug pressures).

Afterbody external skin-friction drag (used for theoretical wave-drag comparisons) was calculated by using the Sommer and Short reference temperature method as outlined in reference 13.

DISCUSSION

Pressure Distributions

Afterbody pressures.- Figures 8 and 9 present typical pressure distributions on the engine interfairing (model center line) for various Mach numbers and jet total-pressure ratios. Data are shown for the dry power nozzles at subsonic and low supersonic speeds and for the max A/B power nozzles at $M = 2.20$. Jet operation generally increased the interfairing pressure coefficients near the end of the afterbody for $M \leq 1.3$. At subsonic speeds, jet-interference effects carried forward to station $x/l = 0.84$; whereas at the low supersonic speeds, jet-interference effects were limited to areas aft of station $x/l = 0.91$. At $M = 2.20$, jet-interference effects were limited to the close-spaced, basic-interfairing configuration.

Figures 10, 11, and 12 present the effects of nozzle lateral spacing, interfairing shape and nozzle power setting, and nozzle cant angle, respectively, on engine-interfairing pressure distributions. These data are shown at jet total-pressure ratios which are representative of a typical turbofan engine.

The interfairing pressures on the wide-spaced afterbodies recovered to higher pressures aft of station $x/l = 0.88$ than on the close-spaced afterbodies (see fig. 10), regard-

less of interfairing shape, nozzle power setting, nozzle cant angle, or Mach number. However, with the large base interfairing (alternate 2) installed, the pressures on the interfairing forward of station $x/l = 0.88$ were generally lower on the wide-spaced afterbody than those obtained on the close-spaced afterbody. It should be noted that some positive pressure coefficients were obtained near the end of the afterbody, especially for the configurations having a wide-spaced afterbody and max A/B power nozzle.

The effect of interfairing shape on interfairing pressures, shown in figure 11, was found to be highly dependent on Mach number, nozzle lateral spacing, and nozzle power setting, but relatively independent of nozzle cant angle. The most consistent trend was observed for the close-spaced afterbody, which generally had higher interfairing pressures when the large base interfairing (alternate 2) was installed. One exception to this trend may be noted for the max A/B power nozzle, $M = 0.9$ case.

The effect of nozzle power setting on interfairing pressure distributions can be determined by comparing the left- and right-hand sides of figure 11. Changing the nozzle power setting from dry to max A/B increased the pressures near the rear of the afterbody for all the configurations shown at $M = 0.9$ and for the basic-interfairing configurations at $M = 1.3$. The effect of nozzle power setting on interfairing pressures was small at $M = 1.3$ for the alternate-interfairing configurations.

The results of canting the nozzles 5° inward and 5° outward are shown in figure 12. The wide-spaced afterbody was tested with nozzle cant angles of 0° and 5° inward only. With the basic-interfairing configurations, canting the nozzles inward increased the pressures near the rear of the interfairing, and canting the nozzles outward generally decreased the pressures. The effects from canting the nozzles were more pronounced for the close-spaced afterbody, as would be expected, since the wide-spaced afterbody nozzles are further removed from the model center line. With the large base interfairing (alternate 2) installed, canting the nozzles had little effect on the interfairing pressure distribution, probably because the pressure-orifice locations were moved upward and away from the nozzles with the alternate-interfairing configurations.

It should be pointed out that although the previous results and discussion are indicative of various effects on the interfairing pressures, they do not necessarily indicate what happens to the pressures on each nozzle nacelle or to the base pressures on the alternate interfairings. Thus, afterbody drag may or may not have the trends expected based on interfairing pressures.

Plug pressures.- Typical plug static-pressure distributions at several Mach numbers and jet total-pressure ratios for the close-spaced, basic-interfairing configuration and for the wide-spaced, basic-interfairing configuration are presented in figures 13 and 14. The left half of each figure shows the left-plug static-pressure distributions and the right half shows the right-plug static-pressure distributions; similarly, the upper half

presents results for the dry power nozzles and the lower half presents results for the max A/B power nozzles. The geometric nozzle throat (minimum area) is located at plug station $x_p/l_p = 0$. The pressure distributions are given in the form of a ratio of plug static pressure to jet total pressure, $p_{plug}/p_{t,j}$; for convenience, values of $p_\infty/p_{t,j}$, which indicate whether the plug static pressures are greater or less than free-stream static pressure (i.e., $p_{plug}/p_{t,j} > p_\infty/p_{t,j}$ indicates $p_{plug} > p_\infty$, and vice versa), are shown as solid symbols.

The plug static-pressure distributions shown in figures 13 and 14 are typical of cone plug nozzles. (See refs. 14 and 15.) At $p_{t,j}/p_\infty < 5.0$ for the dry power nozzles and $p_{t,j}/p_\infty < 2.0$ for the max A/B power nozzles, the pressure distributions at $M = 0$ are characterized by a region of relatively constant plug pressure which indicates possible exhaust flow separation from the plug. The flow separation exists over a wider range of $p_{t,j}/p_\infty$ for the dry power nozzles than for the max A/B power nozzles because of the greater dry-power cone-plug angle. As $p_{t,j}/p_\infty$ is increased, the initial expansion, starting at the nozzle throat, extends further down the plug surface; and, thus, the minimum plug static pressure has a lower value and its location tends to move downstream such that lower static pressures occur over more of the plug surface. At $p_{t,j}/p_\infty > 5.0$ for the dry power nozzles and $p_{t,j}/p_\infty > 2.0$ for the max A/B power nozzles, the plug static-pressure distributions are made up of a series of minimums and maximums caused by a series of flow expansions and compressions. As Mach number increases from the $M = 0$ case, the number of expansions and compressions occurring on the plug surface decreases such that, at transonic speeds, the exhaust flow is characterized by a large initial flow expansion followed by a slow compression of the plug static pressures to values approaching free-stream static pressure, especially for the dry power nozzles.

Figure 15 presents the effect of afterbody geometry and nozzle cant angle on the plug static-pressure distributions for the dry-power-nozzle setting. The solid line was faired through the data points for the configuration with a wide-spaced afterbody, basic interfairing, and uncanted nozzle since it is believed that this configuration should have the least interference effects on the plug surfaces. Interference effects on plug pressures of all other configurations are discussed relative to this configuration. Also shown, as a dashed line, is the theoretical plug static-pressure distribution at $M = 0$ obtained from a method of characteristics program adapted from reference 14. Reference 14 also lists the assumptions for this program but it should be noted that it was written for isentropic flow (no shock waves or strong compressions). At $M = 0.5$, the interference effects, although generally small, appear to be detrimental (i.e., plug static pressure was reduced); at higher Mach numbers, the interference effects were generally detrimental over the first half of the plug length but were sometimes beneficial over the last half.

The largest interference effects occurred with the close-spaced afterbody and particularly with the large base interfairing (alternate 2). The probable cause is that for these configurations a large wake of separated flow from the interfairing base exists between the nozzles.

Performance Characteristics

Comparison of theoretical and measured afterbody drag.- The afterbody cross-sectional area progression shown in figure 4 for basic-interfairing configurations was calculated by a computer program for axisymmetric bodies as discussed previously in the model and support-system section. The theoretical afterbody drag values, however, were obtained by using three-dimensional mathematical models. Figure 16 presents the machine-plotted mathematical models used for this purpose. Supersonic wave drag was determined by the methods outlined in reference 12 for nonaxisymmetric body wave-drag calculations. Skin friction was obtained from surface-area calculations and the Sommer and Short reference temperature method discussed in reference 13.

Figure 17 presents the comparison of the measured (jet off) and calculated afterbody drags for the wide- and close-spaced afterbodies with basic interfairings. Theoretical values were obtained only for the basic-interfairing configurations since the wave-drag program could not handle the base areas of the alternate interfairings. Since nozzle drag was not included in the theoretical values, the calculated afterbody-drag values were independent of nozzle power setting. It should also be noted that although the wide- and close-spaced afterbodies had identical normal cross-sectional area distributions, different theoretical drag values were obtained because of skin-friction differences and the nonaxisymmetric aspects of the two afterbodies. Good agreement was obtained for the max A/B power-nozzle configurations, particularly at $M = 2.2$; poor agreement was obtained for the dry-power-nozzle configurations. The better agreement for the max A/B power-nozzle configurations might be expected since the nozzle surface more nearly simulates the cylindrical base streamtubes assumed by the wave-drag program.

Measured afterbody drag coefficients.- Figures 18 to 27 present the variation of afterbody drag coefficient with jet total-pressure ratio for all test configurations and Mach numbers. Initial operation of the jet below choked conditions $\left(p_{t,j}/p_\infty < 1.89\right)$ generally reduced afterbody drag, particularly with the max A/B nozzles installed. One noticeable exception to this trend was the large base (alternate 2) interfairing configurations with dry power nozzles installed (see fig. 18(a), for example); this was particularly noticeable for the close-spaced afterbody, where initial jet operation caused an increase in afterbody drag, probably as a result of the jet-exhaust-flow pumping action on the large interfairing base. After the initial effect of turning on the jet flow, afterbody drag generally tended to level out or slightly increase until some value of $p_{t,j}/p_\infty$ between 2.0

and 5.0 (depending on configuration) was reached; increasing $p_{t,j}/p_\infty$ above this value generally reduced afterbody drag.

Static (M = 0) nozzle performance.- The variation of gross thrust-minus-nozzle-drag ratio with jet total-pressure ratio at M = 0 is shown in figures 28(a) and 28(b) for the dry power nozzles and max A/B power nozzles, respectively. A comparison of measured thrust loss as a result of canting the nozzles inward or outward with the calculated theoretical loss (1 - cos β) is also given for each nozzle power setting. Since these data were obtained at M = 0, nozzle drag should be essentially zero except for any jet pumping effects which should be negligible. Hence, these data are a close approximation of static nozzle internal performance or gross thrust ratio F/F_i. The nozzle static-performance curves have two maximums: for the dry power nozzles, these maximums occur at approximate jet total-pressure ratios of 2.5 and 6.0; and for the max A/B power nozzles, the maximums occur at $p_{t,j}/p_\infty \approx 1.25$ and at some of $p_{t,j}/p_\infty$ greater than 3.5 which was not obtained. The unusual shape of these curves is probably a result of the flow-separation characteristics on the cone plugs as discussed in the section entitled "Pressure Distributions."

For jet total-pressure ratios greater than the choked value, thrust-minus-nozzle-drag performance for both nozzle power settings was generally independent of configuration which indicates that mutual interference effects between the adjacent nozzle exhaust flows are negligible. Canting the nozzles reduced the thrust-minus-drag performance in all instances, as might be expected since the thrust axis is not parallel to the flight direction for the canted nozzles. The performance loss, as a result of canting the nozzles, is shown in the form of an increment of $(F - D_{noz})/F_i$ or as a percentage of ideal isentropic thrust. The calculated performance loss is shown as a dashed line and was 0.38 percent of the ideal isentropic thrust for both nozzle power settings. The maximum and minimum measured losses were 0.58 and 0.08 percent, respectively.

Thrust-minus-nozzle-drag performance.- Figures 29 and 30 present the variation of thrust-minus-nozzle-drag ratio with jet total-pressure ratio for each configuration and Mach number investigated. Thrust-minus-nozzle drag includes the gross nozzle thrust, the effect of an external stream, and any interference effects on nozzle internal performance and external nozzle drag. Although the effect of an external stream on nozzle internal performance is negligible (for unseparated nozzle flow) for convergent and convergent-divergent nozzles like those presented in references 9 and 10, reference 14 indicates that this effect can be significant for cone plug nozzles.

For the dry-power-nozzle configurations, large variations in thrust-minus-nozzle drag were obtained with varying Mach number. These variations are attributable to varying nozzle drag and changes in nozzle internal performance. It should be noted that several configurations, particularly the basic and small base (alternate 1) interfairing con-

figurations, had higher thrust-minus-nozzle-drag performance at subsonic speeds than was obtained statically (M = 0). (See fig. 29(a), for example.) At low jet total-pressure ratios and at Mach numbers from 0.80 to 0.95, values greater than 1.0 were obtained. Values of thrust-minus-drag ratio greater than 1.0 indicate negative nozzle drag (thrust) and/or favorable external stream effect on nozzle internal performance. Negative nozzle drag (thrust) was obtained on the twin-engine configurations reported in references 8 and 10. At M = 1.20 and 1.30, the thrust-minus-nozzle drag was significantly lower than that obtained at subsonic speeds because of increased nozzle drag and/or detrimental effects of the external stream on nozzle internal performance.

The thrust-minus-nozzle-drag performance of the max A/B power-nozzle configurations was relatively insensitive to changes in Mach number. Max A/B nozzle drag should be very small and vary little with Mach number since the translating shroud was cylindrical in shape. Similarly, since the max A/B cone plug was collapsed and had little projected area when compared to the dry-power cone plug, the effect of Mach number on internal performance should be small.

Thrust-minus-total-drag performance.- The variation of thrust-minus-total-drag ratio with jet total-pressure ratio is presented in figures 31 and 32 for each configuration and Mach number investigated. Thrust-minus-total-drag ratio is the overall performance term of the configuration and includes installed nozzle thrust, nozzle external drag, and afterbody external drag.

Thrust-minus-total-drag ratio generally decreased with increasing Mach number, primarily because afterbody drag increased with increasing Mach number. The small dip in the curves for the thrust-minus-total-drag ratio for the max A/B power nozzles at subsonic speeds was faired after consideration of the static (M = 0) thrust-minus-nozzle-drag performance and of the data obtained at M = 0.80 for the configuration having the wide-spaced afterbody, small base (alternate 1) interfairing, and uncanted nozzles. (See fig. 31(h).)

Performance Characteristics at Jet Total-Pressure Ratios Typical of a Turbofan Engine

Turbofan-jet total-pressure-ratio schedule.- In order to simplify data analysis, data have been cross-plotted at selected jet total-pressure ratios. Figure 33 presents the variation of a typical (maximum dry power) schedule of turbofan-engine total-pressure ratio with Mach number, which was used for comparison purposes in this investigation. Although discussion for this particular schedule of $p_{t,j}/p_{\infty}$ as a function of M would generally be true for other schedules not too greatly different, the relative differences between comparisons may vary.

Effect of nozzle power setting and alternate interfairings.- The variation of afterbody drag coefficient, thrust-minus-nozzle-drag ratio, and thrust-minus-total-drag ratio with Mach number is shown in figure 34 at the scheduled values of $p_{t,j}/p_\infty$ from figure 33. Data are shown for each afterbody and nozzle cant-angle combination at both nozzle power settings. The effects of the alternate interfairings are shown directly, whereas an examination of the left and right sides of each plot gives a comparison of the dry power and max A/B power nozzles.

At subsonic and low-supersonic speeds, installation of the small base and large base interfairings (alternates 1 and 2, respectively) generally increased $C_{D,a}$, decreased $(F - D_{noz})/F_i$, and decreased $(F - D)/F_i$. The effect of alternate interfairings on the performance of the dry-power-nozzle configurations was significant but was generally small for the max A/B power-nozzle configurations. The detrimental effects of the large base interfairing (alternate 2) were always larger than the small base interfairing (alternate 1). At $M = 2.20$ and with the max A/B power nozzles installed, the large base interfairing provided lower $C_{D,a}$ and higher $(F - D)/F_i$ than the basic interfairing.

Comparing the left and right side of each figure indicates that changing the nozzle power setting from dry power to max A/B power generally decreases $C_{D,a}$, decreases $(F - D_{noz})/F_i$, and increases $(F - D)/F_i$, particularly for $M > 0.80$. Several reasons for this performance gain can be given. First, the max A/B power nozzles are designed for operation at higher $p_{t,j}/p_\infty$ than the dry power nozzles such that nozzle internal performance increases with increasing Mach number. Second, since the max A/B power nozzles are cylindrical in shape, nozzle pressure drag is essentially zero; also, a strong compression at the juncture of the afterbody nozzle tends to increase the afterbody pressures (see fig. 11) and thus decrease afterbody drag.

Comparison of the parts of figure 34 (i.e., figs. 34(a), 34(b), etc.) shows that the highest overall performance was generally obtained with the close-spaced afterbody, basic interfairings, and uncanted nozzles.

Effect of nozzle lateral spacing.- Figure 35 presents the variation of $C_{D,a}$, $(F - D_{noz})/F_i$, and $(F - D)/F_i$ with nozzle lateral spacing for each Mach number investigated. This figure is a cross plot of data at the scheduled jet total-pressure ratio for each Mach number.

Although the effect of increasing nozzle spacing on $(F - D_{noz})/F_i$ was generally small, a decreasing trend was established regardless of configuration. For the basic-interfairing configurations, increased nozzle lateral spacing generally increased $C_{D,a}$ and decreased $(F - D)/F_i$.

With the large base interfairing (alternate 2) and dry power nozzles installed, afterbody drag decreased, especially when the nozzles were canted inward 5°, and $(F - D)/F_i$

increased with increasing nozzle lateral spacing. However, with the max A/B power nozzles installed with the large base interfairing (alternate 2), increased nozzle spacing had little effect on $C_{D,a}$, except at $M = 2.20$ where $C_{D,a}$ increased and overall performance $(F - D)/F_i$ decreased.

Effect of nozzle cant angle.- The variation of $C_{D,a}$, $(F - D_{noz})/F_i$, and $(F - D)/F_i$ with nozzle cant angle is shown cross-plotted at the scheduled $p_{t,j}/p_\infty$ in figure 36 at several Mach numbers for both nozzle power settings. The canted nozzle configurations were not investigated at $M = 2.20$.

For the basic- and small-base-interfairing (alternate 1) configurations, canting the nozzles inward 5^o generally decreased $C_{D,a}$ but canting the nozzles outward 5^o generally increased $C_{D,a}$. Canting the nozzles produced mixed results on $C_{D,a}$ for the large-base-interfairing (alternate 2) configurations. Mixed results on $(F - D_{noz})/F_i$ were obtained by canting the nozzles inward, but canting the nozzles outward generally reduced $(F - D_{noz})/F_i$.

Canting the nozzles inward had little or no effect on overall performance $(F - D)/F_i$. Overall performance for the $\beta = 5^o$ configurations was generally within 1 percent of the $\beta = 0^o$ configurations. Canting the nozzles outward significantly reduced $(F - D)/F_i$. The losses associated with the $\beta = -5^o$ configurations were as high as 5 percent of the ideal isentropic thrust at $M = 1.2$.

CONCLUSIONS

An investigation of the effect of nozzle lateral spacing, interfairing shape, and nozzle cant angle on the drag and performance of twin-jet afterbodies utilizing two nozzle power settings of translating-shroud cone plug nozzles was conducted at Mach numbers of 0.0 and 0.50 to 2.20. The jet total-pressure ratio was varied from jet-off to approximately 20, depending on Mach number and nozzle power setting. Two lateral spacings of the nozzle exits were tested with two afterbodies having identical normal cross-sectional area distributions when either the basic or alternate interfairings were installed.

At scheduled jet total-pressure ratios assumed for a turbofan engine, the following conclusions are indicated:

1. Increased nozzle lateral spacing generally increased afterbody drag $C_{D,a}$ and decreased thrust-minus-total-drag ratio $(F - D)/F_i$ for the basic-interfairing configurations. With the large base alternate interfairing and dry power nozzles installed, increased nozzle spacing reduced $C_{D,a}$, especially when the nozzles were canted inward, and increased $(F - D)/F_i$. However, with the maximum afterburning power nozzles installed on the large-base alternate-interfairing configurations, increased nozzle spacing reduced $(F - D)/F_i$.

2. At subsonic and low supersonic speeds, installation of the small base and large base alternate interfairings increased $C_{D,a}$ and decreased $(F - D)/F_i$, especially for the dry-power-nozzle configurations. However, at a Mach number of 2.20 and with the maximum afterburning power nozzles, the large base alternate interfairing produced lower afterbody drag and higher thrust-minus-total-drag ratio than the basic interfairing.

3. Canting the nozzles inward generally reduced $C_{D,a}$ for the basic- and small-base alternate-interfairing configurations, whereas canting the nozzles outward generally increased $C_{D,a}$. Canting the nozzles produced mixed results on $C_{D,a}$ for the large-base alternate-interfairing configurations. Canting the nozzles inward had little or no effect on $(F - D)/F_i$; canting the nozzles outward decreased $(F - D)/F_i$.

4. The highest overall performance was generally obtained with the close-spaced afterbody, basic interfairings (no base), and uncanted nozzles.

Langley Research Center,
National Aeronautics and Space Administration,
Hampton, Va., October 16, 1972.

REFERENCES

1. Runckel, Jack F.: Jet-Exit and Airframe Interference Studies on Twin-Engine-Fuselage Aircraft Installations. NASA TM X-1274, 1966. (Also available as NASA SP-124, pp. 229-244.)

2. Schmeer, James W.; Lauer, Rodney F., Jr.; and Berrier, Bobby L.: Performance of Blow-In-Door Ejector Nozzles Installed on a Twin-Jet Variable-Wing-Sweep Fighter Airplane Model. NASA TM X-1383, 1967.

3. Wilmoth, Richard G.; Norton, Harry T., Jr.; and Corson, Blake W., Jr.: Effect of Engine-Interfairing Modifications on the Performance of a Powered Twin-Jet Fighter-Airplane Model at Mach 1.20. NASA TM X-1534, 1968.

4. Corson, Blake W., Jr.; and Runckel, Jack F.: Exploratory Studies of Aircraft Afterbody and Exhaust-Nozzle Interaction. NASA TM X-1925, 1969.

5. Berrier, Bobby L.; and Maiden, Donald L.: Effect of Nozzle-Exhaust Flow on the Longitudinal Aerodynamic Characteristics of a Fixed-Wing, Twin-Jet Fighter Airplane Model. NASA TM X-2389, 1971.

6. Maiden, Donald L.; and Berrier, Bobby L.: Effect of Airframe Modifications on Longitudinal Aerodynamic Characteristics of a Fixed-Wing, Twin-Jet Fighter Airplane Model. NASA TM X-2523, 1972.

7. Berrier, Bobby Lee; and Wood, Frederick H., Jr.: Effect of Jet Velocity and Axial Location of Nozzle Exit on the Performance of a Twin-Jet Afterbody Model at Mach Numbers up to 2.2. NASA TN D-5393, 1969.

8. Mercer, Charles E.; and Berrier, Bobby L.: Effect of Afterbody Shape, Nozzle Type, and Engine Lateral Spacing on the Installed Performance of a Twin-Jet Afterbody Model. NASA TM X-1855, 1969.

9. Maiden, Donald L.; and Runckel, Jack F.: Effect of Nozzle Lateral Spacing on Afterbody Drag and Performance of Twin-Jet Afterbody Models With Convergent Nozzles at Mach Numbers up to 2.2. NASA TM X-2099, 1970.

10. Pendergraft, Odis C., Jr.; and Schmeer, James W.: Effect of Nozzle Lateral Spacing on Afterbody Drag and Performance of Twin-Jet Afterbody Models With Convergent-Divergent Nozzles at Mach Numbers up to 2.2. NASA TM X-2601, 1972.

11. Lee, Edwin E., Jr.; and Runckel, Jack F.: Performance of Closely Spaced Twin-Jet Afterbodies With Different Inboard-Outboard Fairing and Nozzle Shapes. NASA TM X-2329, 1971.

12. Harris, Roy V., Jr.: An Analysis and Correlation of Aircraft Wave Drag. NASA TM X-947, 1964.

13. Peterson, John B., Jr.: A Comparison of Experimental and Theoretical Results for the Compressible Turbulent-Boundary-Layer Skin Friction With Zero Pressure Gradient. NASA TN D-1795, 1963.

14. Berrier, Bobby L.: Effect of Plug and Shroud Geometry Variables on Plug-Nozzle Performance at Transonic Speeds. NASA TN D-5098, 1969.

15. Schmeer, James W.; Kirkham, Frank S.; and Salters, Leland B., Jr.: Performance Characteristics of a 10^{o} Conical Plug Nozzle at Mach Numbers up to 1.29. NASA TM X-913, 1964.

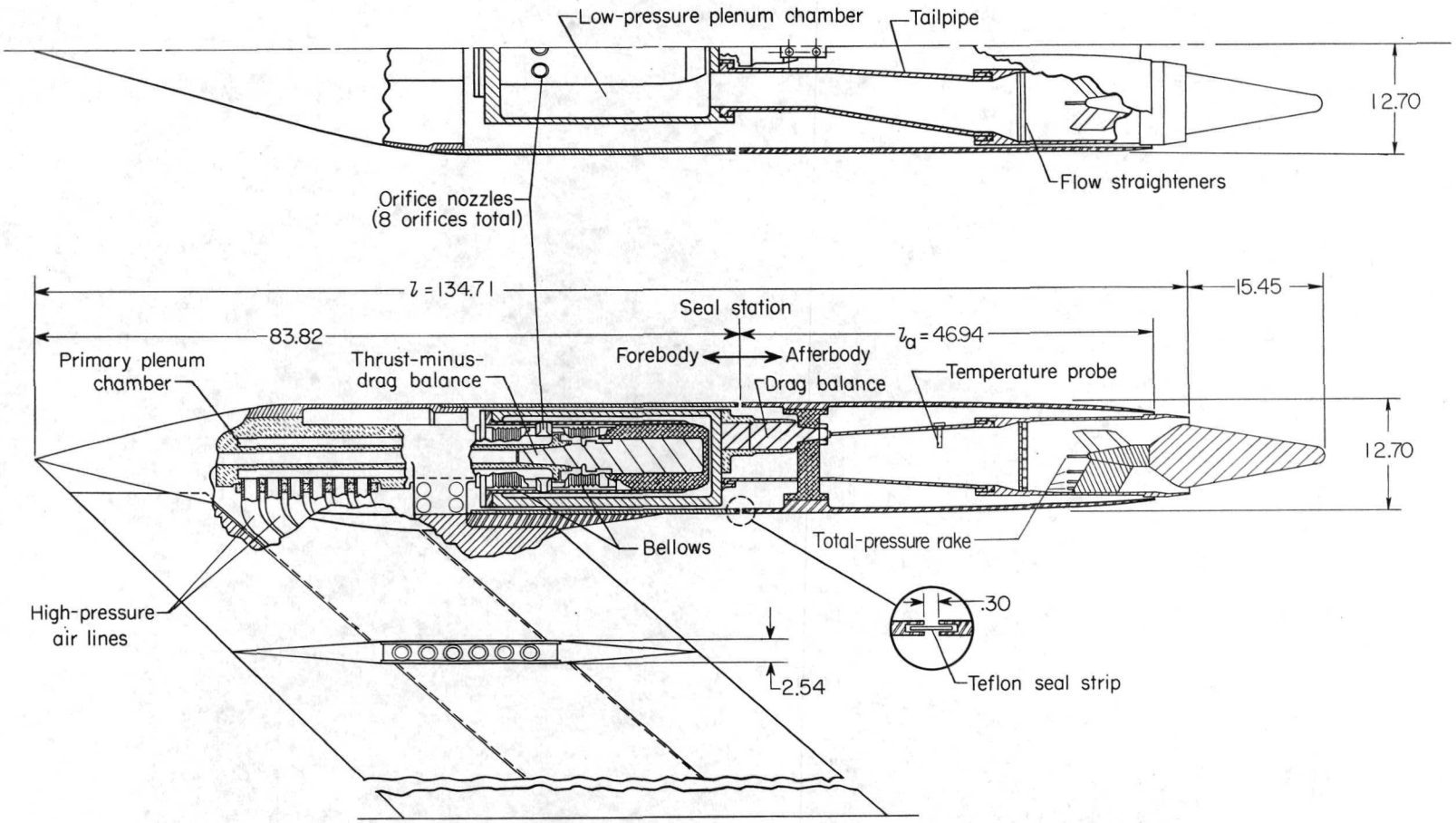

Figure 1.- Sketch of air-powered twin-jet model with dry power plug nozzles installed. All dimensions are in centimeters.

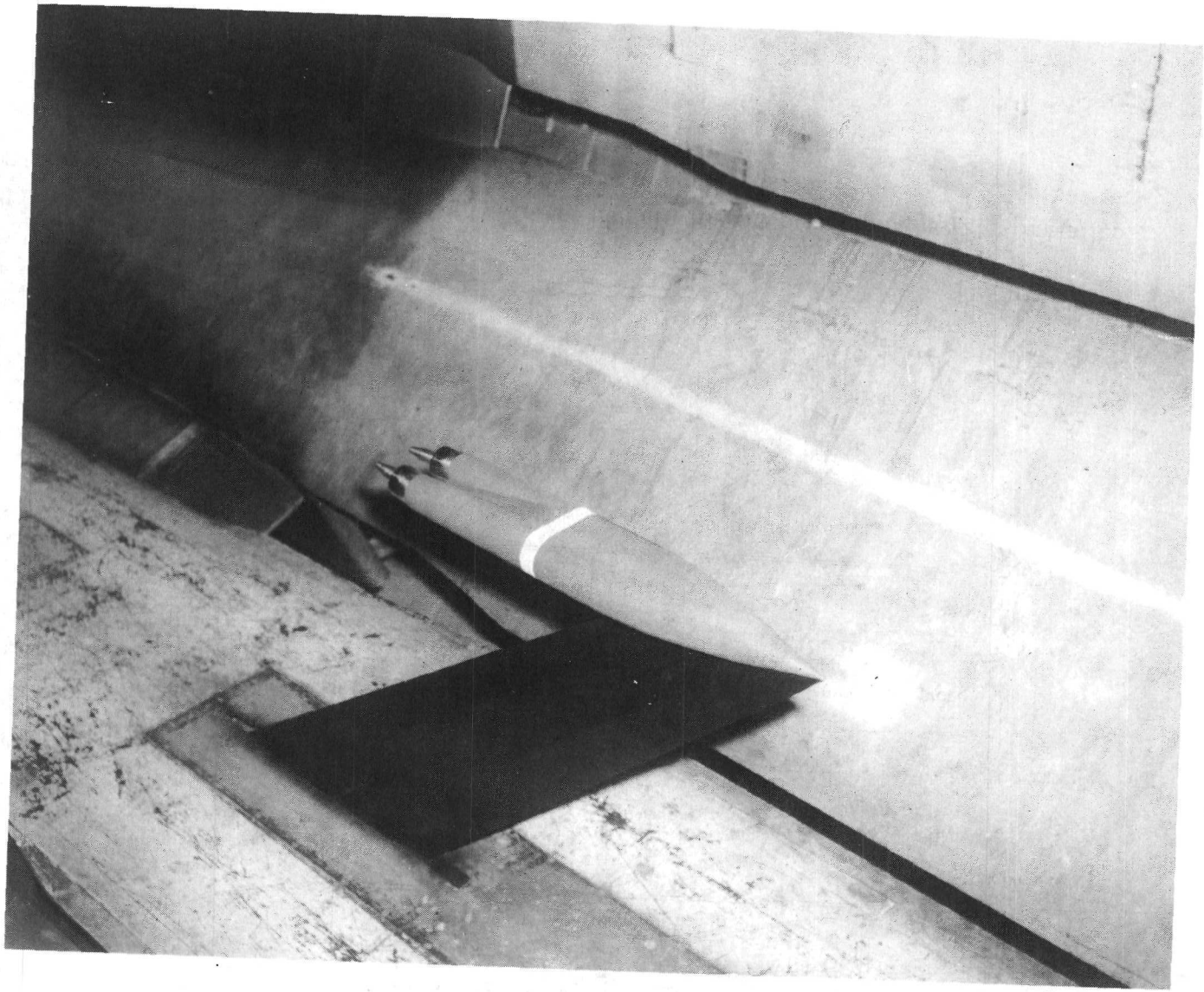

L-71-4816

(a) Langley 16-foot transonic tunnel installation.

Figure 2.- Photographs of twin-jet model mounted in wind tunnels.

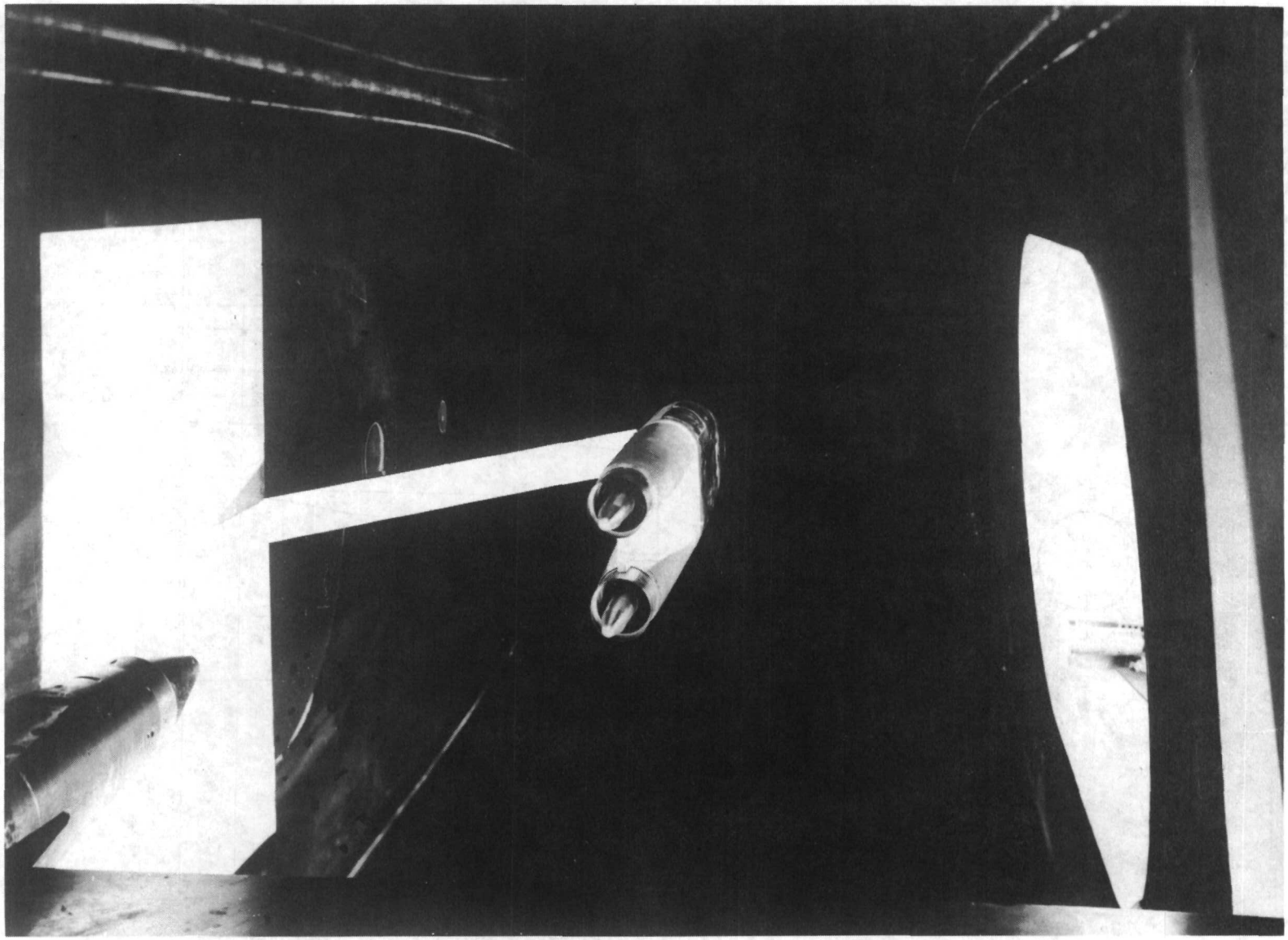

L-72-2054

(b) Langley 4- by 4-foot supersonic pressure tunnel installations.

Figure 2.- Concluded.

Afterbody geometry					Orifice location	
x/ℓ	s/2H	r/H	h_1/H	h_3/H	Top	Bottom
0.623	1.000	1.000	1.000	1.000		
.679	0.988	0.988	0.976	0.988		
.717	.972	.972	.944	.972	X	X
.754	.960	.952	.884	.952		
.792	.948	.926	.830	.926	X	
.849	.930	.880	.720	.880	X	X
.877					X	
.886	.896	.852	.630	.852		
.896					X	
.915					X	
.924	.860	.820	.460	.820		
.933					X	
.952					X	
.962	.822	.778	0	.778		
.971	.820	.760	-----	.760		
.999	-----	-----	-----	.684		

Note: Alternate interfairings have orifices on top only.

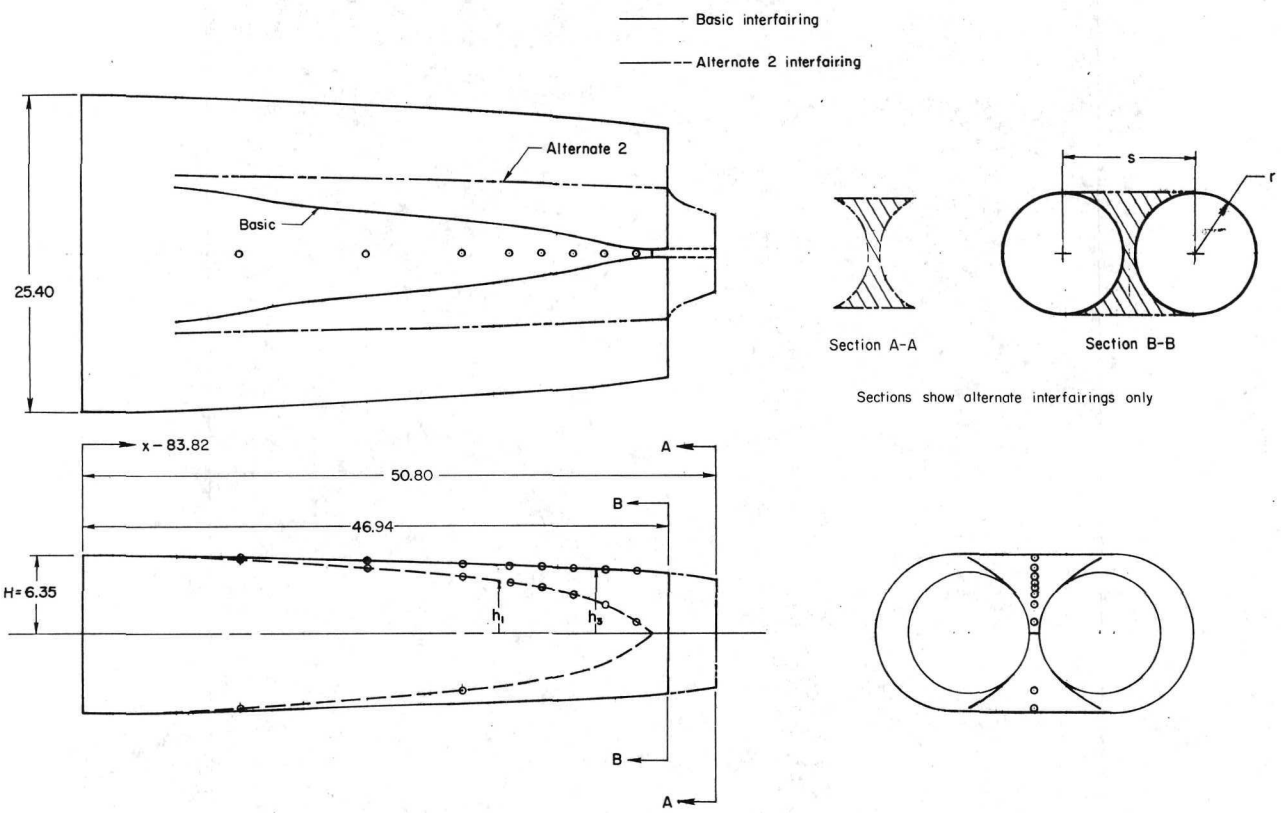

(a) Close-spaced afterbody.

Figure 3.- Sketches of afterbodies and alternate interfairings showing important dimensions and orifice locations. All dimensions are in centimeters.

Afterbody geometry						Orifice location	
x/l	s/2H	r/H	h_1/H	h_2/H	h_3/H	Top	Bottom
0.623	1.000	1.000	1.000	1.000	1.000		
.679	1.012	0.988	0.944	0.960	0.960		
.717	1.028	.972	.860	.908	.908	X	X
.754	1.048	.952	.740	.834	.834		
.792	1.074	.926	.634	.750	.768	X	
.849	1.120	.880	.416	.572	.646	X	X
.877						X	
.886	1.148	.852	.256	.424	.544		
.896						X	
.915						X	
.924	1.180	.820	.106	.250	.444		
.933						X	
.952						X	
.962	1.182	.778	0	.140	.380		
.971	1.180	.760	-----	.124	.380		
.999	-----	-----	-----	.080	.362		

Basic interfairing
Alternate 1 interfairing
Alternate 2 interfairing

Note: Alternate interfairings have orifices on top only.

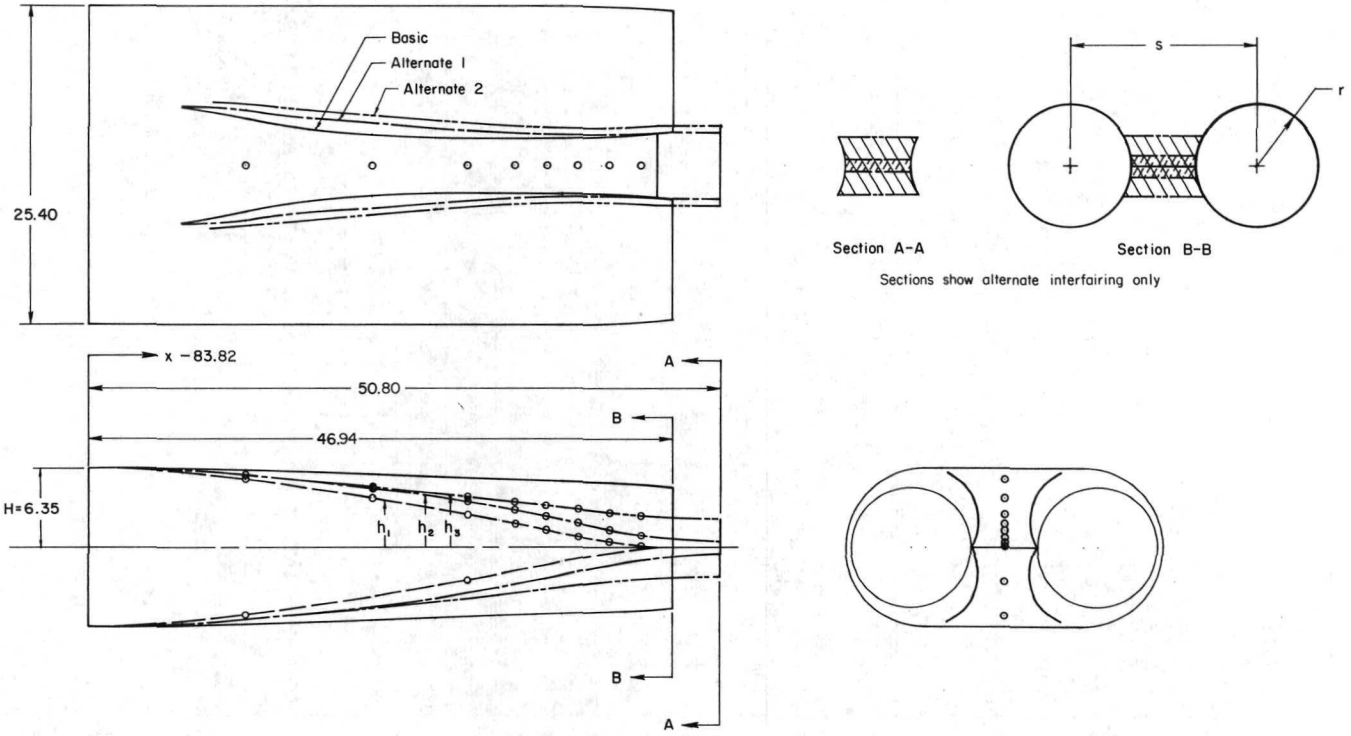

(b) Wide-spaced afterbody.

Figure 3.- Concluded.

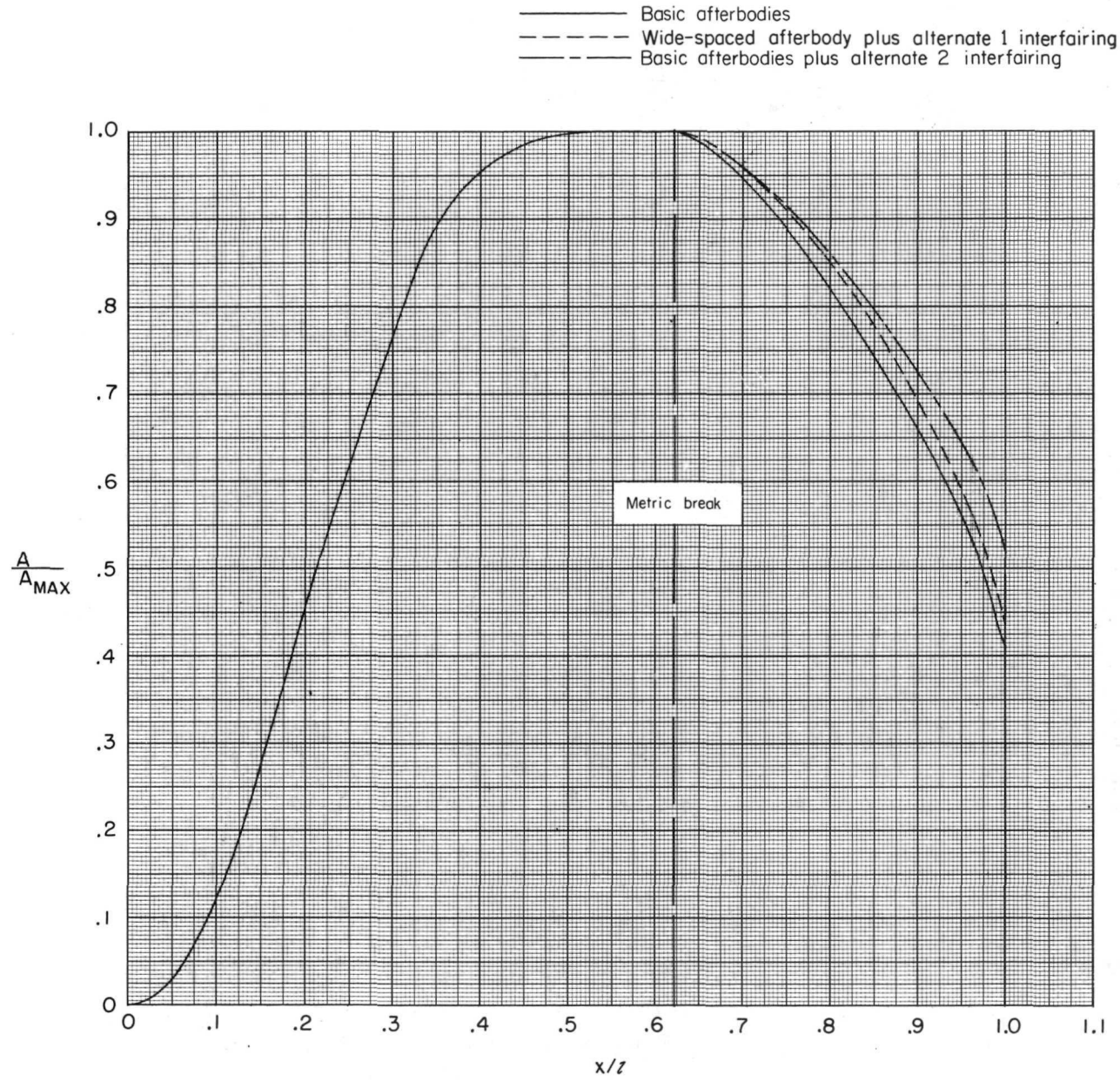

Figure 4.- Area distributions of twin-jet afterbody configurations with dry power nozzles. A_{max} = 287.90 cm^2.

Orifice locations			
x_p/l_p	Row 1	Row 2	Row 3
-0.025		X	
.0	X	X	X
.082	X	X	
.164	X	X	
.327	X	X	X
.409		X	
.491	X	X	
.572		X	
.654	X		X
.736		X	
.818	X		
.899		X	
.970		X	
1.000	X	X	X

Note: Rows 1 and 3 are on left-hand plug looking upstream.
Row 2 is on right-hand plug looking upstream.

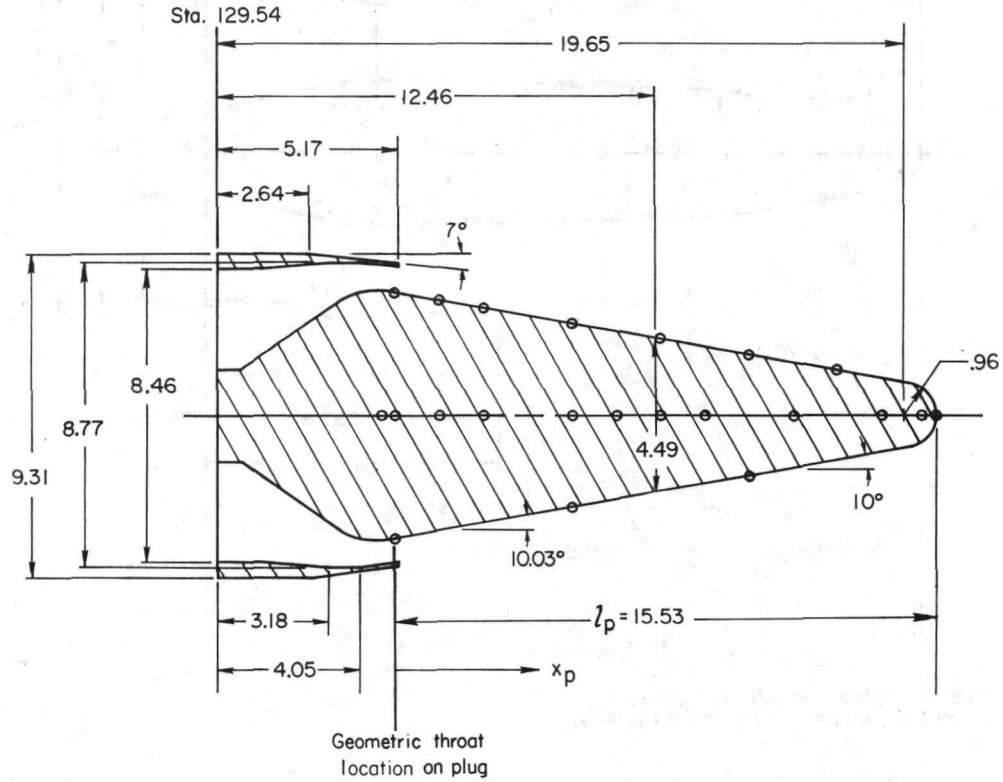

Section A-A

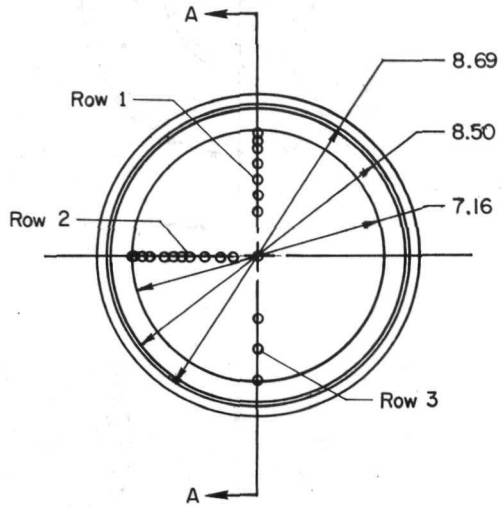

(a) Dry power nozzles.

Figure 5.- Sketches of nozzle configurations showing important dimensions and orifice locations. All dimensions are in centimeters.

Crifice locations			
x_p/l_p	Row 1	Row 2	Row 3
-0.040		X	
.0	X	X	X
.089	X	X	
.170	X	X	
.332	X	X	X
.413		X	
.495	X	X	
.576		X	
.657	X		X
.738		X	
.819	X		
.901		X	
.966		X	
1.000	X	X	X

Note: Rows 1 and 3 are on left-hand plug looking upstream.
Row 2 is on right-hand plug looking upstream.

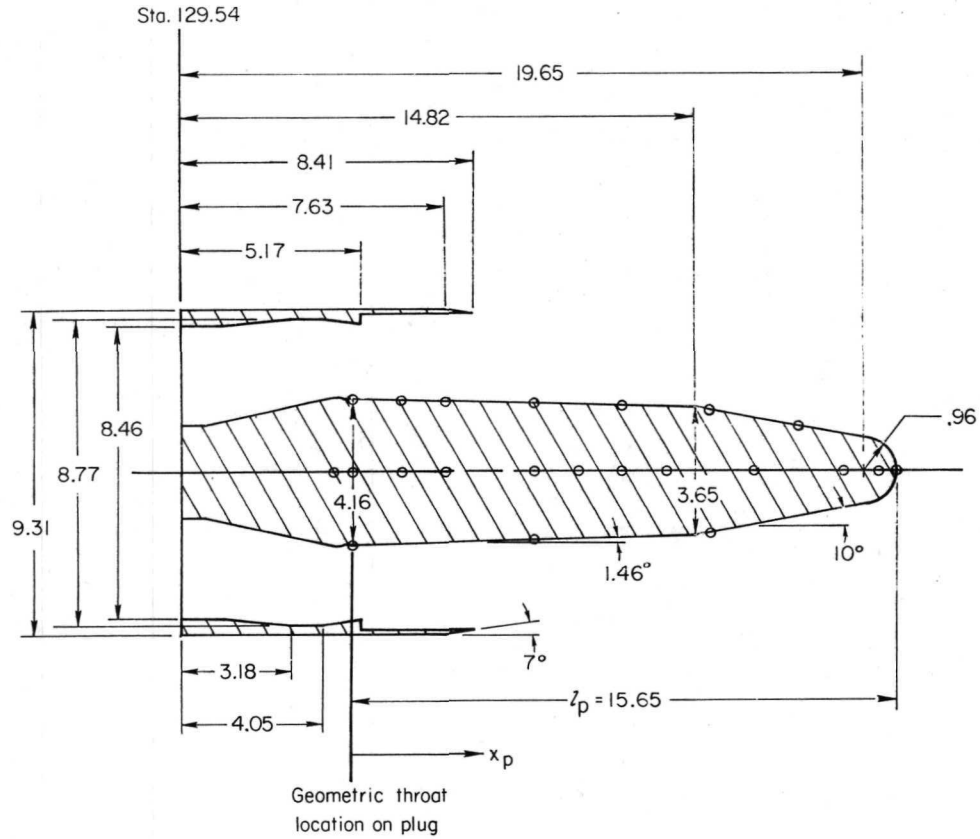

Section A-A

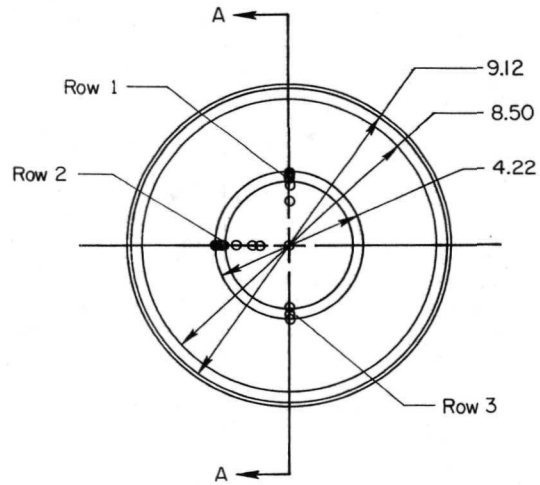

(b) Max A/B power nozzles.

Figure 5.- Concluded.

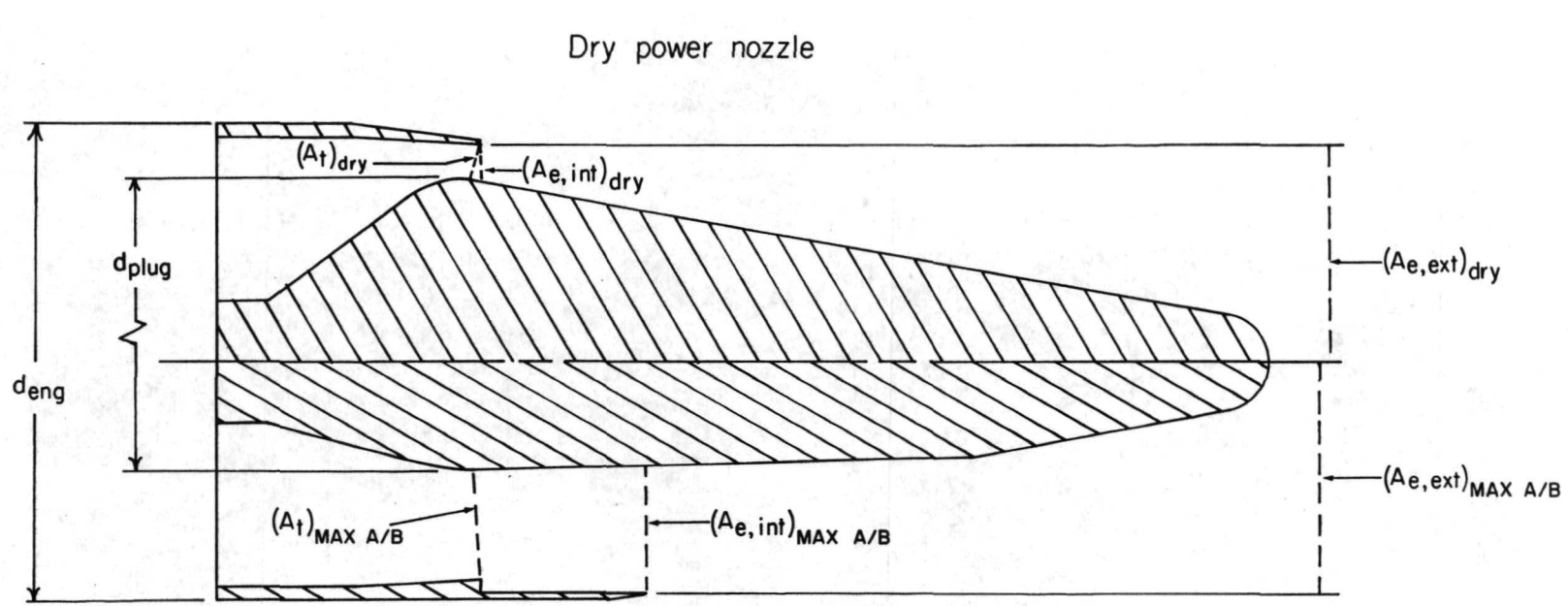

Geometric parameters					
Nozzle power setting	A_t, cm^2	d_{plug}/d_{eng}	A_t/A_{eng}	$A_{e,int}/A_t$	$A_{e,ext}/A_t$
Dry	17.277	0.769	0.254	1.016	3.283
Max A/B	43.200	0.453	0.635	1.217	1.511

Figure 6.- Important geometric parameters of nozzle configurations.

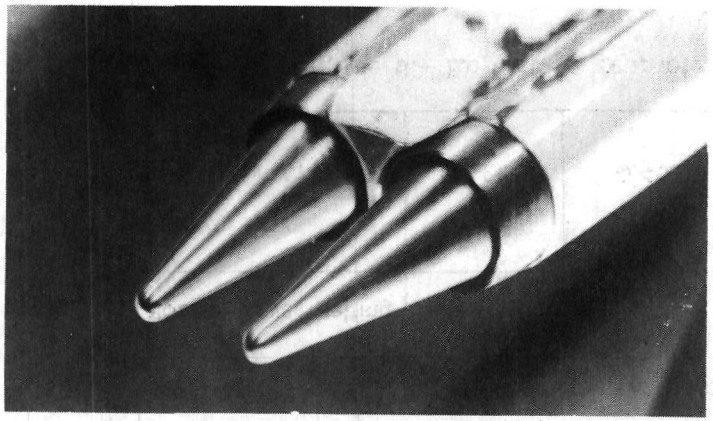

Dry nozzles; alternate 2 interfairing; $\beta = 0°$

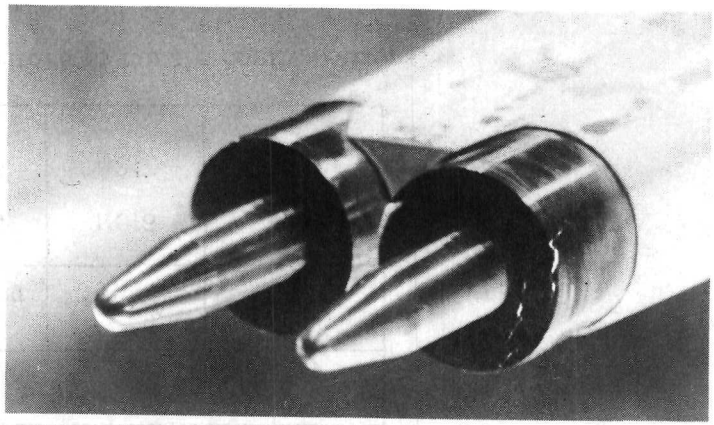

Max A/B nozzles; alternate 2 interfairing; $\beta = 0°$

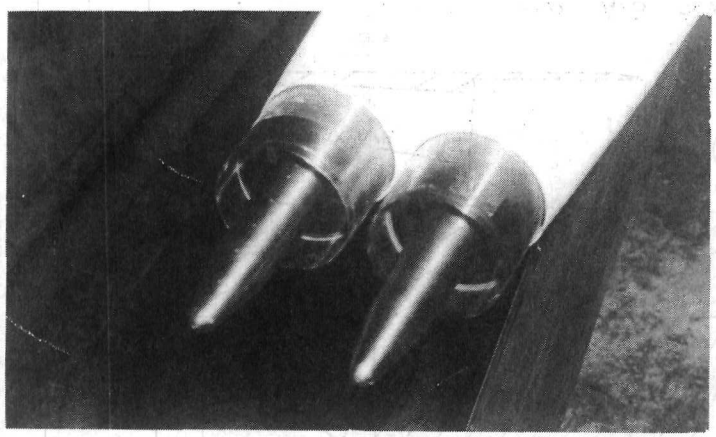

Max A/B nozzles; basic interfairing; $\beta = 0°$

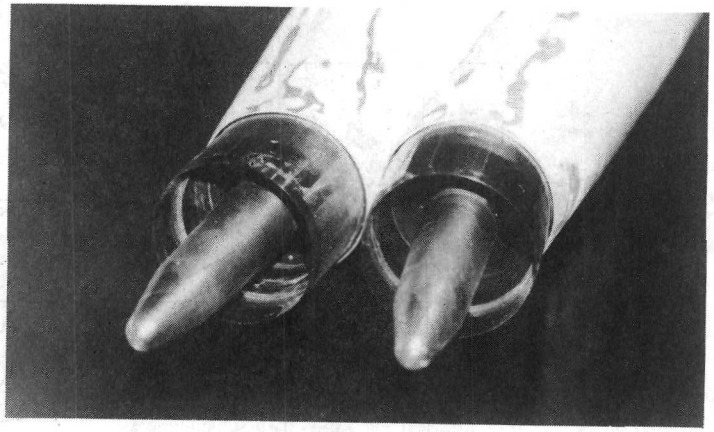

Max A/B nozzles; basic interfairing; $\beta = -5°$

L-72-6556

(a) Close-spaced afterbody.

Figure 7.- Photographs of several twin-jet afterbody configurations.

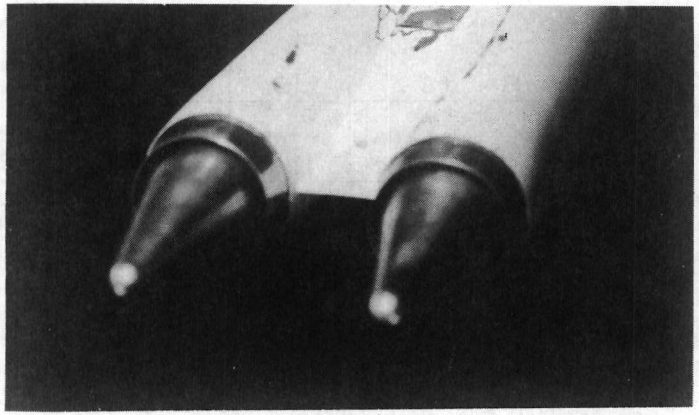

Dry nozzles; basic interfairing; β = 0°

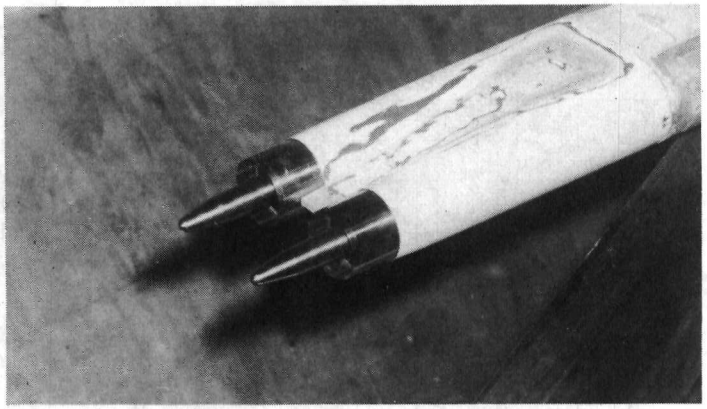

Max A/B nozzles; alternate 1 interfairing; β = 0°

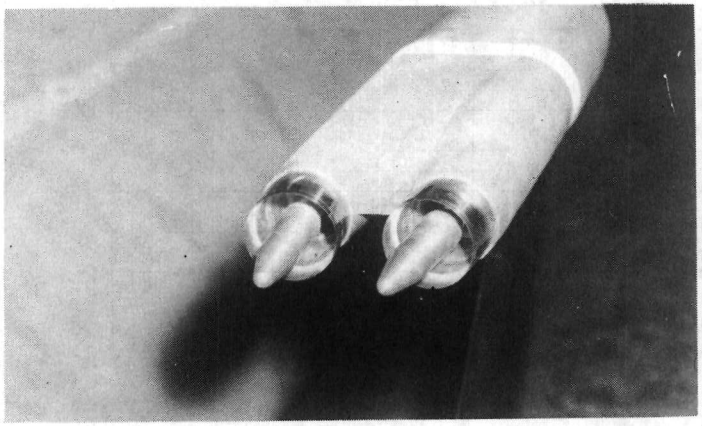

Max A/B nozzles; basic interfairing; β = 5°

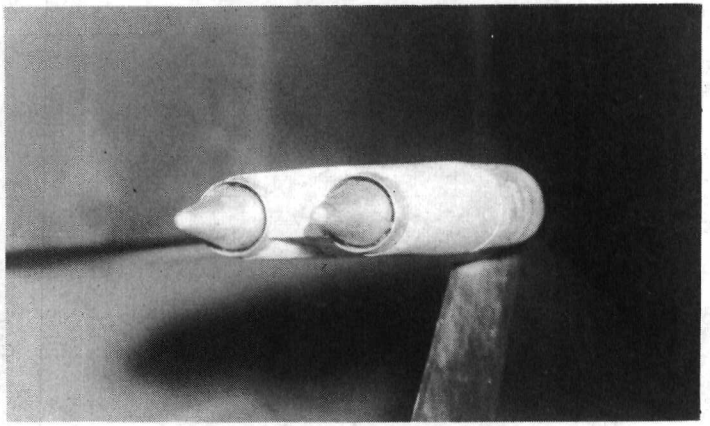

Dry nozzles; alternate 2 interfairing; β = 0°

L-72-6557

(b) Wide-spaced afterbody.

Figure 7.- Concluded.

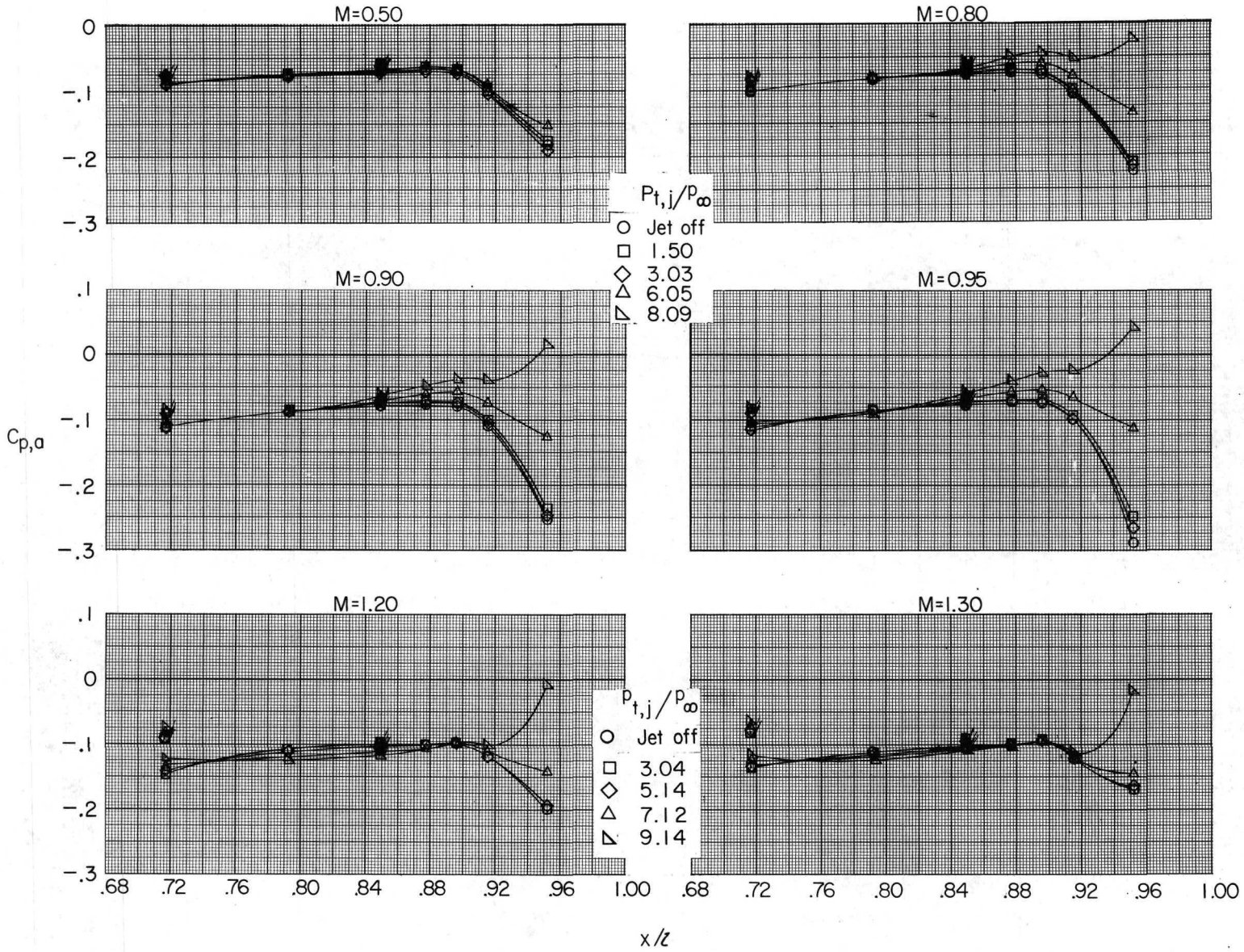

Figure 8.- Typical longitudinal pressure distributions at several jet total-pressure ratios and Mach numbers. Close-spaced afterbody; dry nozzles; basic interfairing; $\beta = 0^o$. Flagged symbols indicate bottom row.

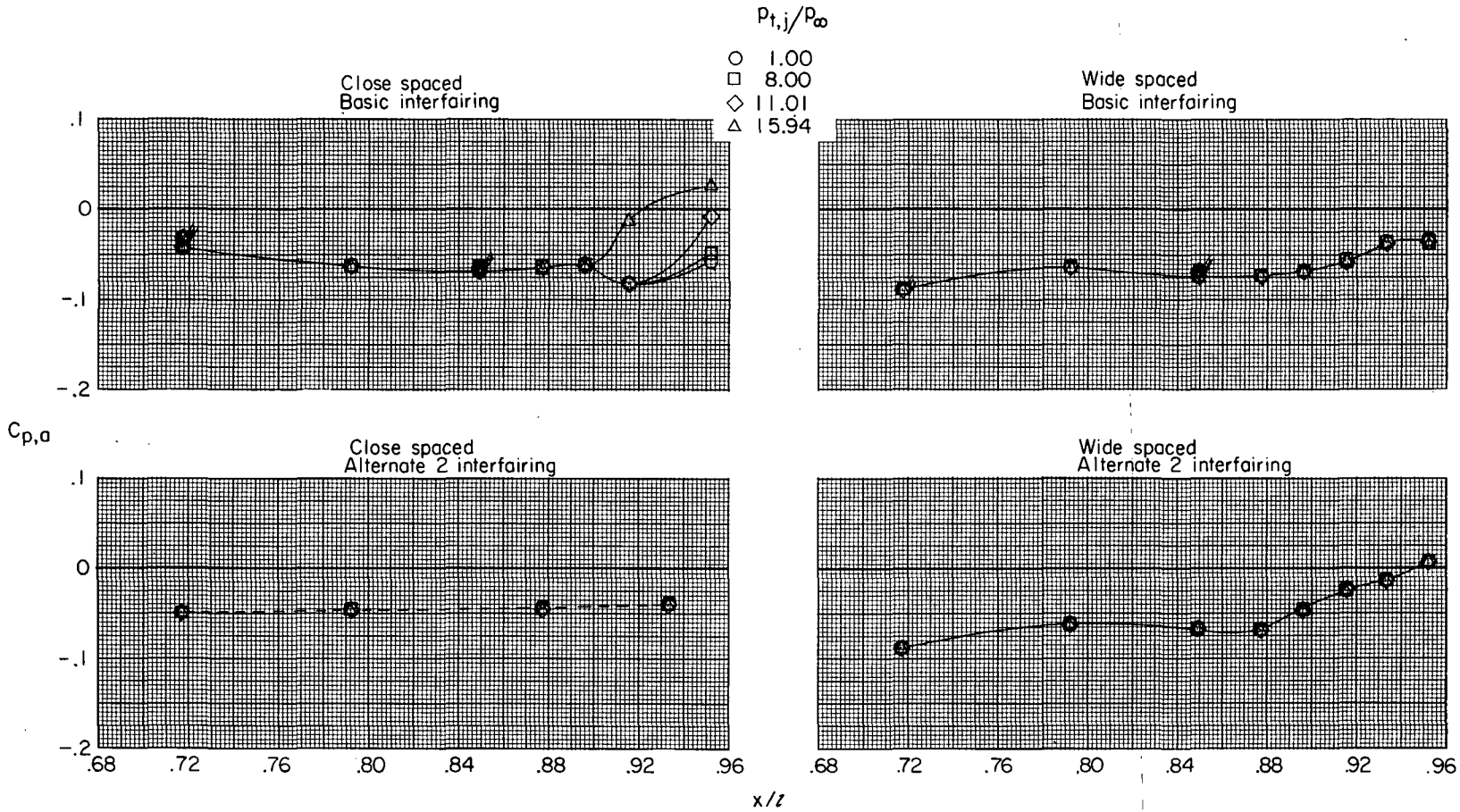

Figure 9.- Typical longitudinal pressure distributions at M = 2.2 and several jet total-pressure ratios. Max A/B nozzles; $\beta = 0^{o}$. Flagged symbols indicate bottom row.

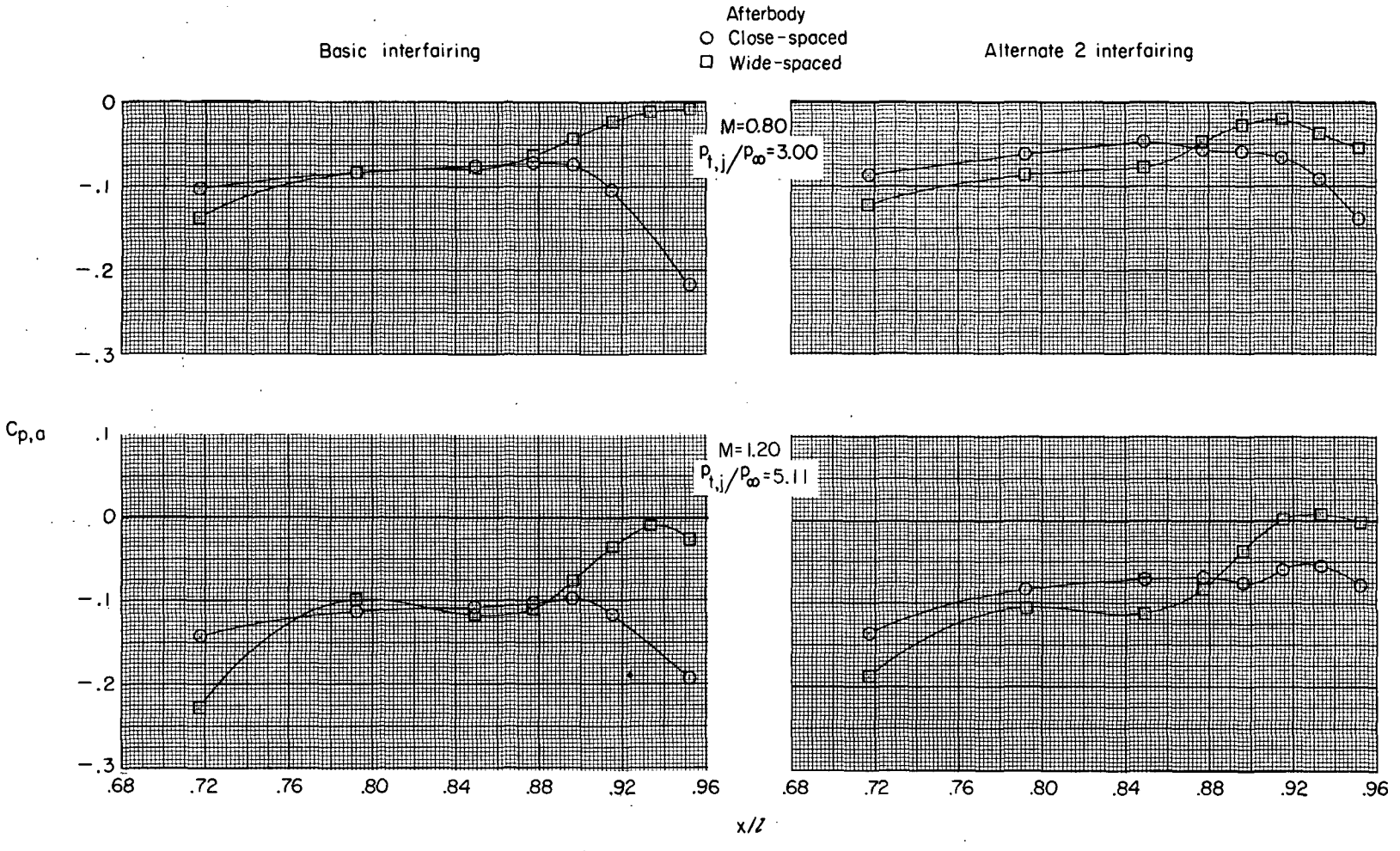

(a) Dry nozzles; $\beta = 0^o$.

Figure 10.- Effect of nozzle lateral spacing on afterbody interfairing pressure distributions.

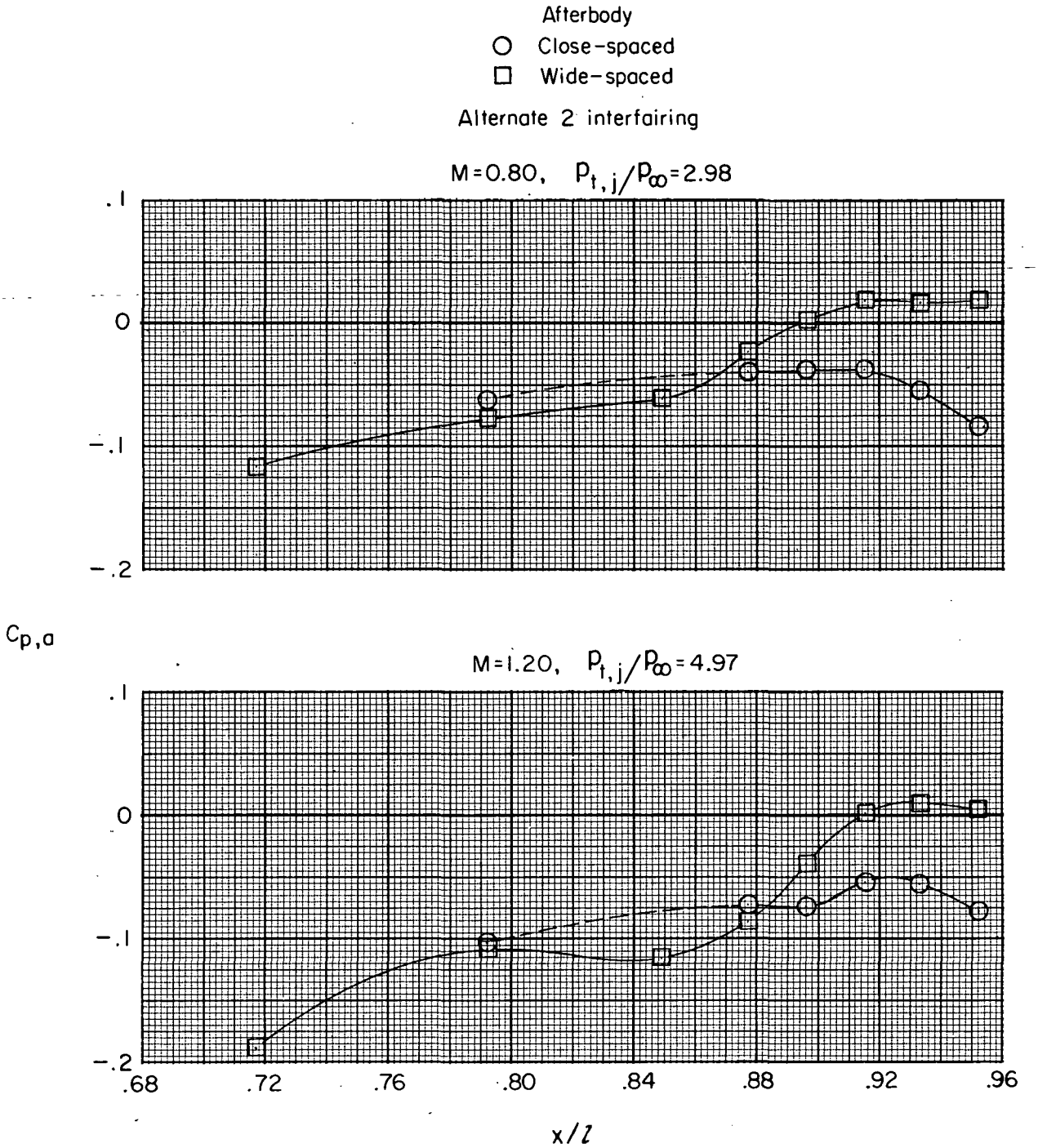

(b) Max A/B nozzles; $\beta = 0^o$.

Figure 10.- Continued.

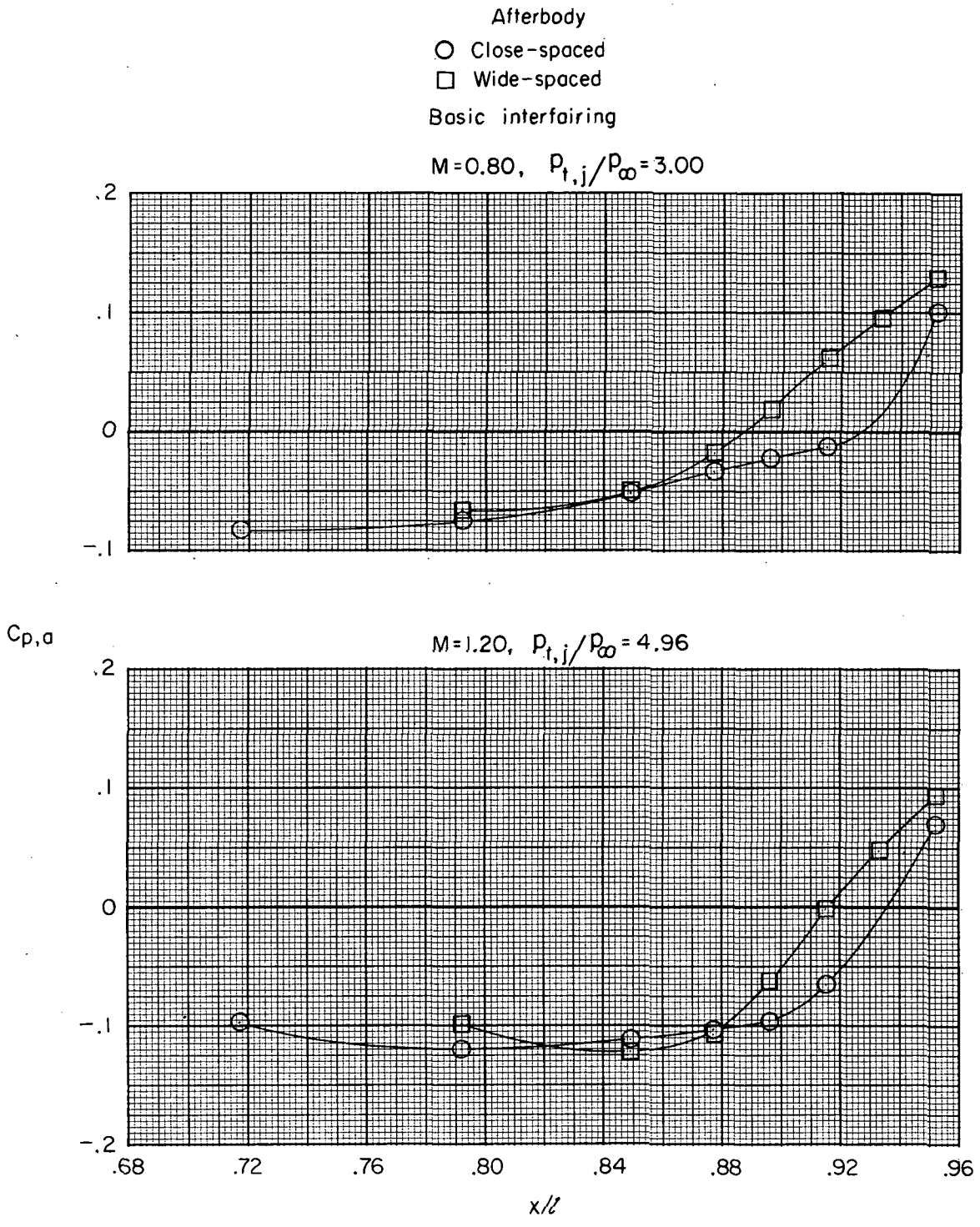

(c) Max A/B nozzles; $\beta = 5^{o}$.

Figure 10.- Concluded.

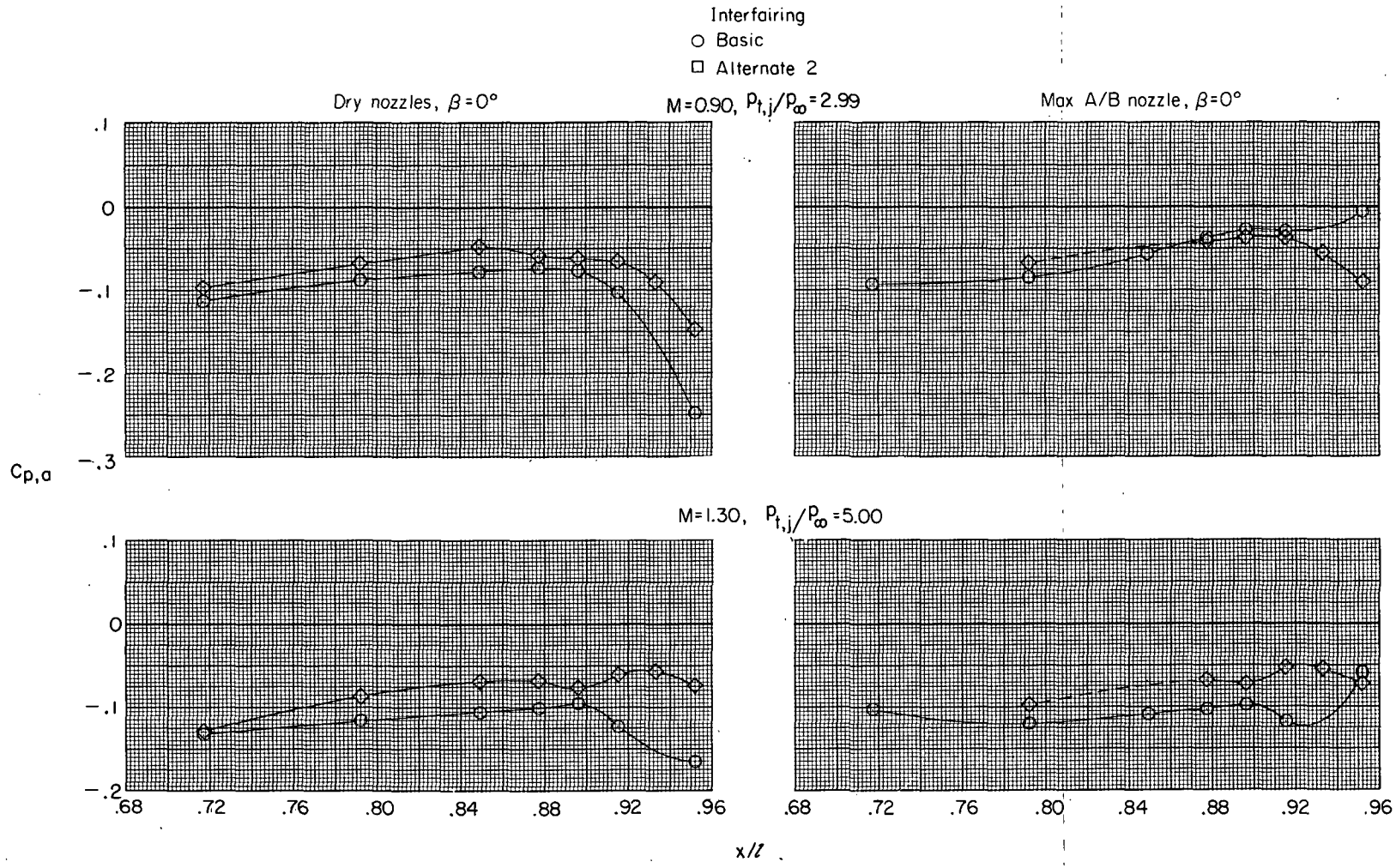

(a) Close-spaced afterbody.

Figure 11.- Effect of engine interfairing and nozzle power setting on interfairing pressure distributions.

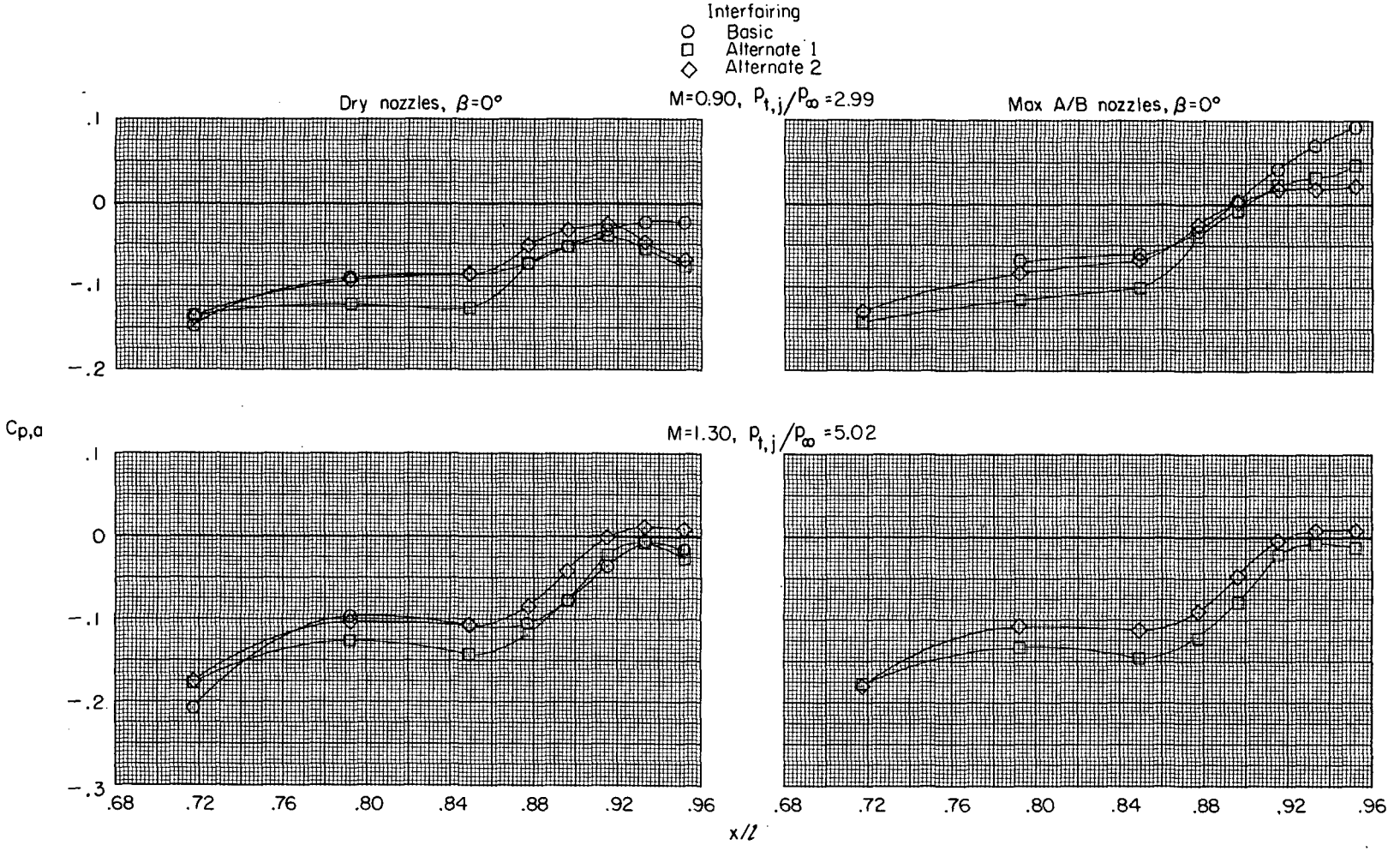

(b) Wide-spaced afterbody.

Figure 11.- Continued.

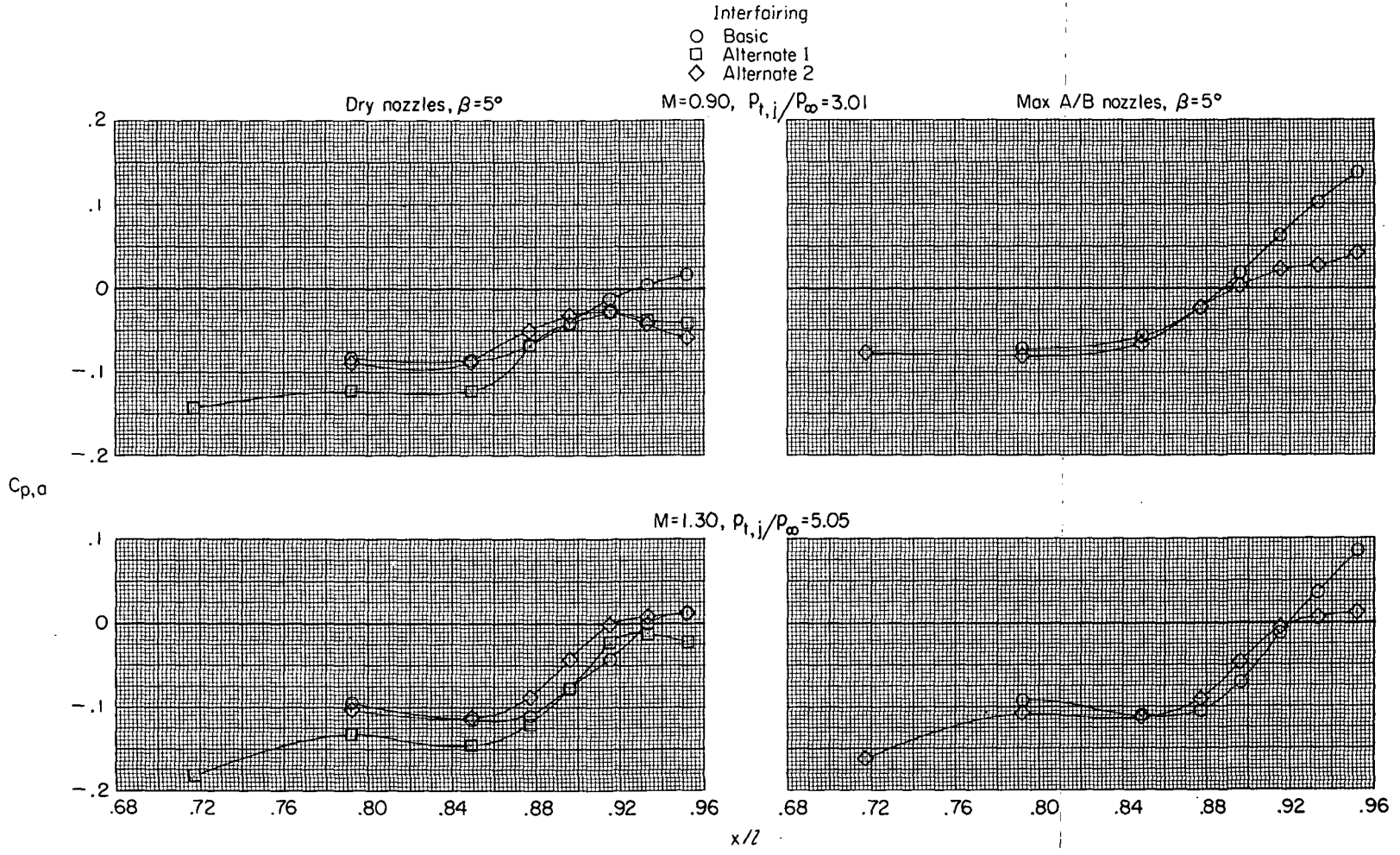

(b) Concluded.

Figure 11.- Concluded.

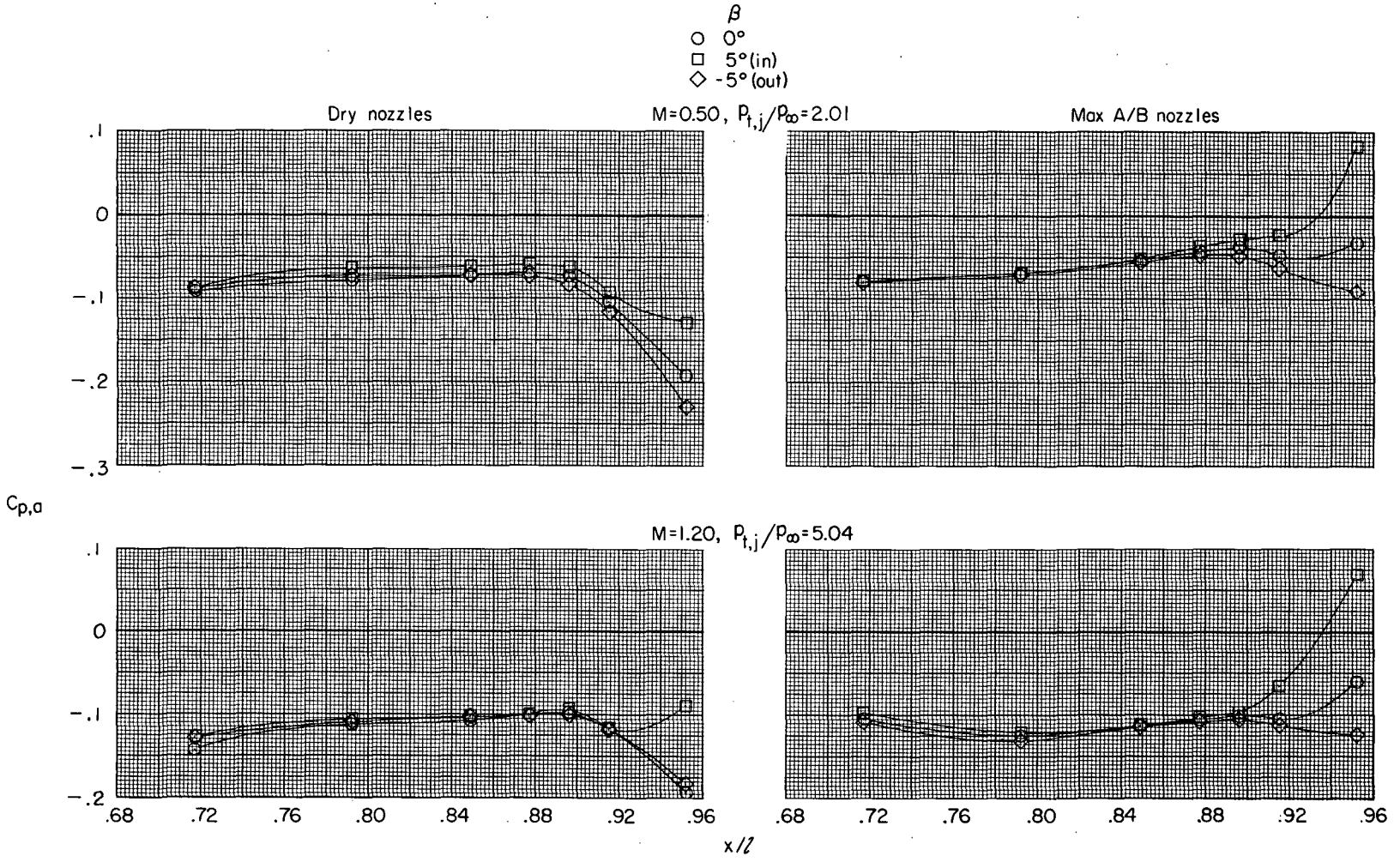

(a) Close-spaced afterbody; basic interfairing.

Figure 12.- Effect of nozzle cant angle on interfairing pressure distribution.

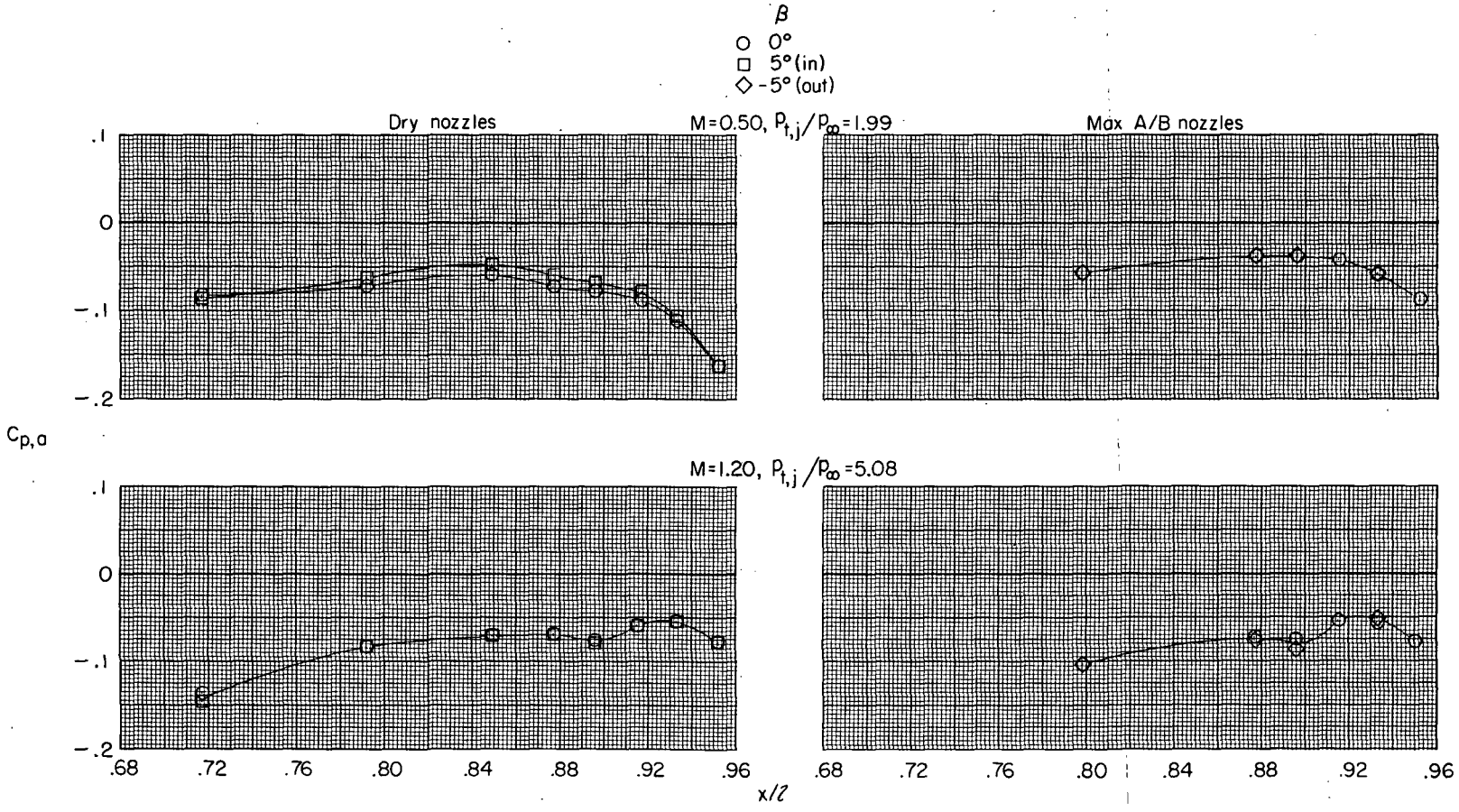

(b) Close-spaced afterbody; alternate 2 interfairing.

Figure 12.- Continued.

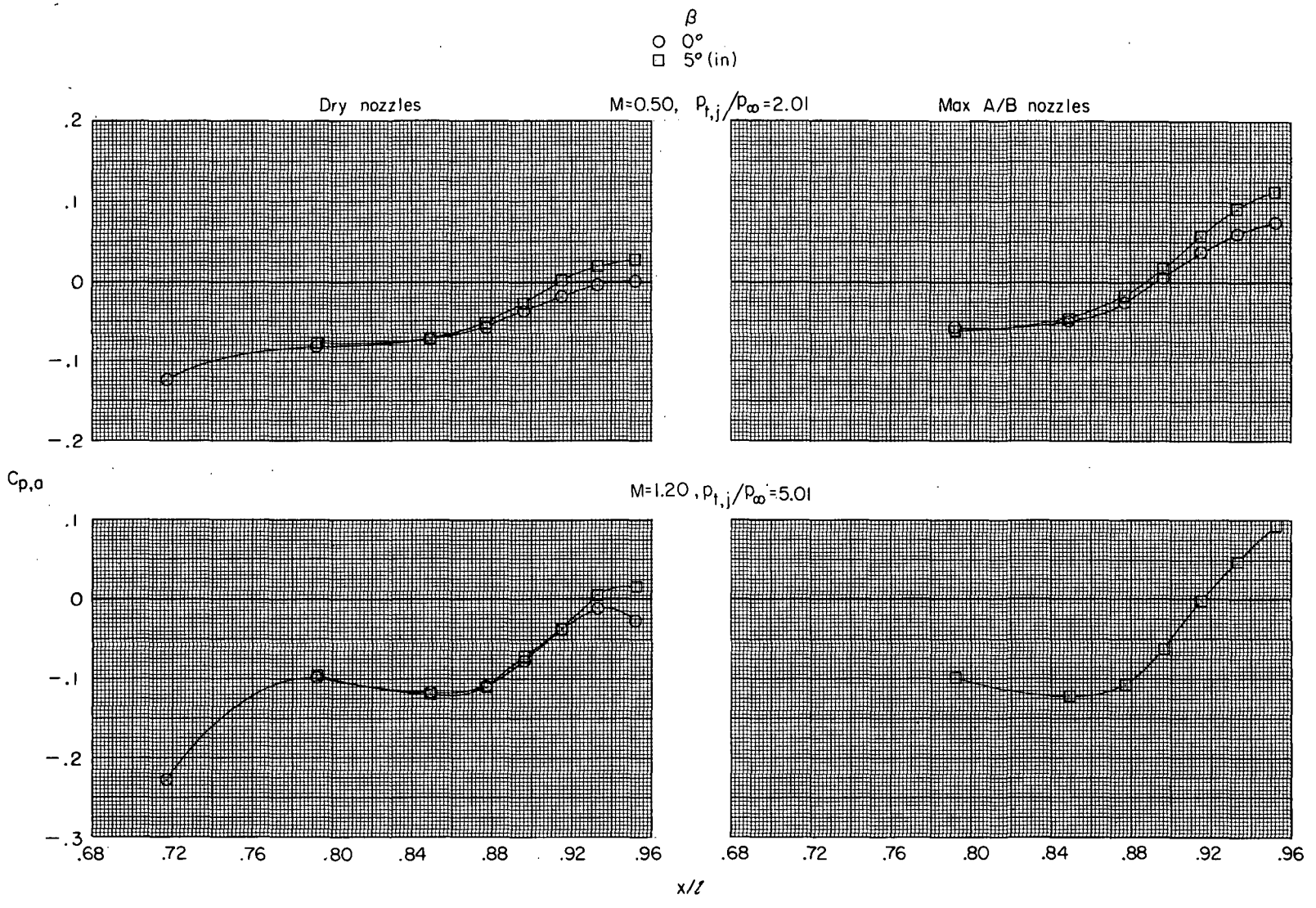

(c) Wide-spaced afterbody; basic interfairing.

Figure 12.- Concluded.

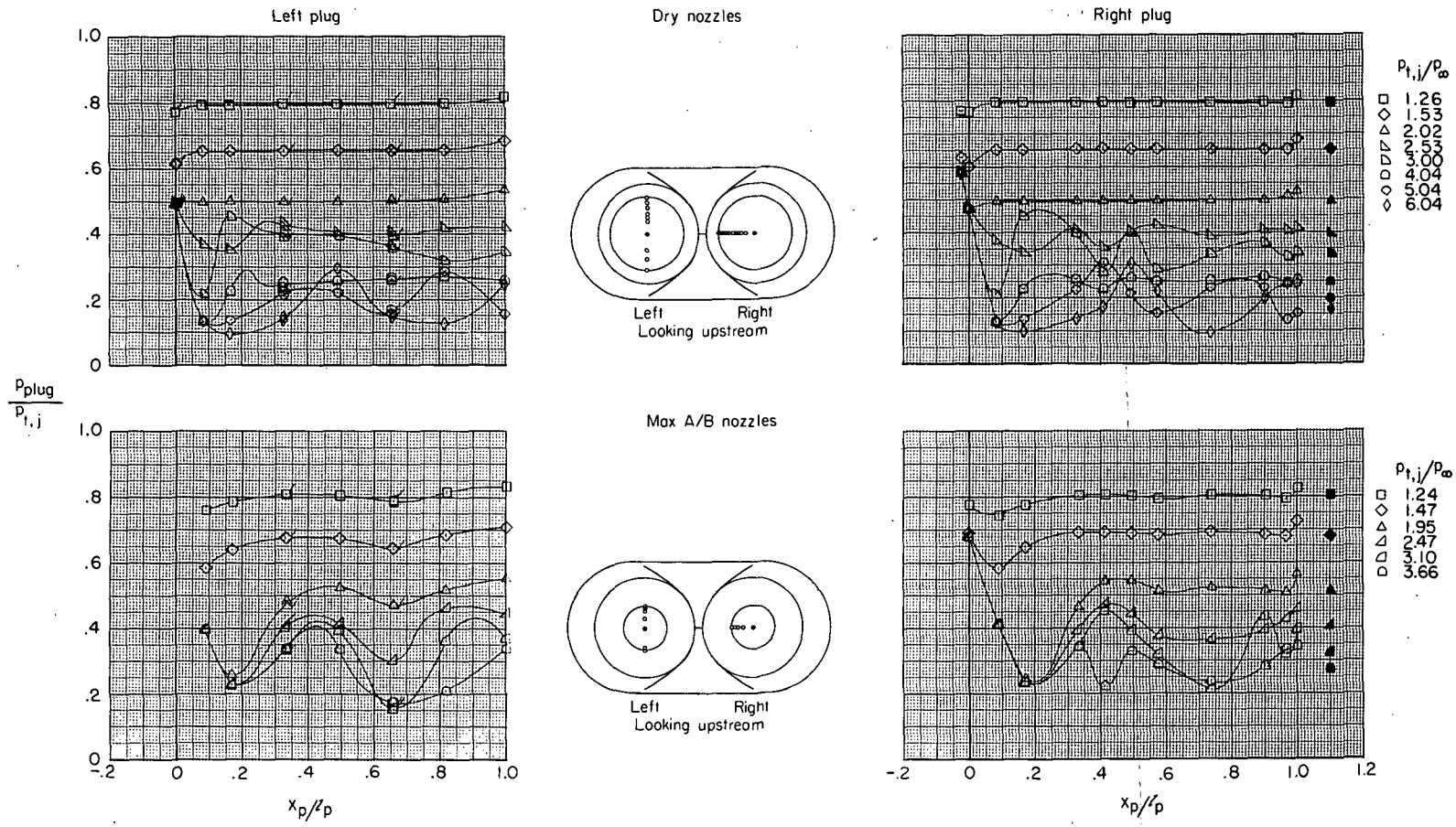

(a) M = 0.

Figure 13.- Plug static-pressure distributions at several Mach numbers. Close-spaced afterbody with basic interfairing. Flagged symbols indicate bottom-row orifices; solid symbols indicate values of $p_\infty/p_{t,j}$.

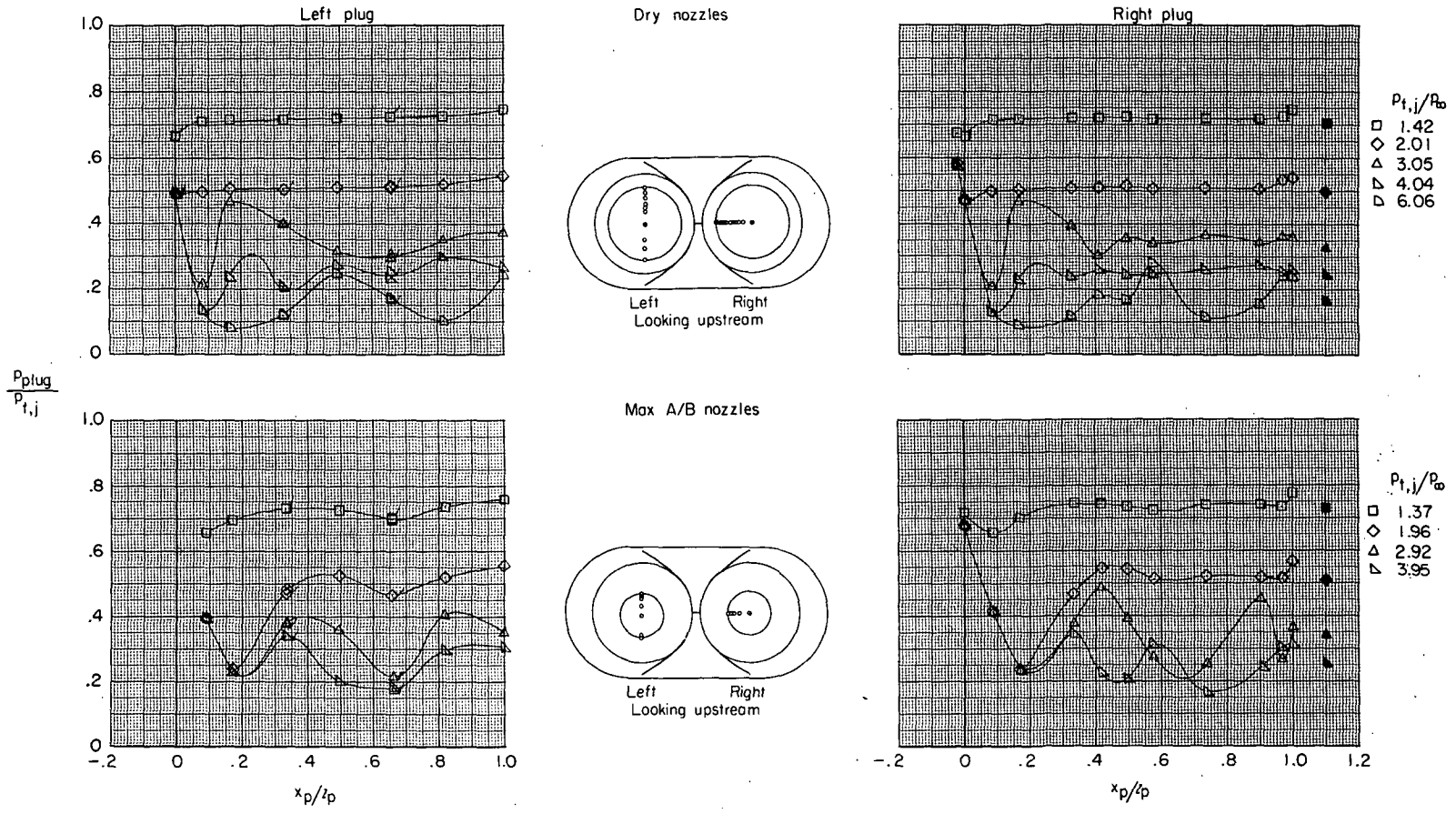

(b) M = 0.50.

Figure 13.- Continued.

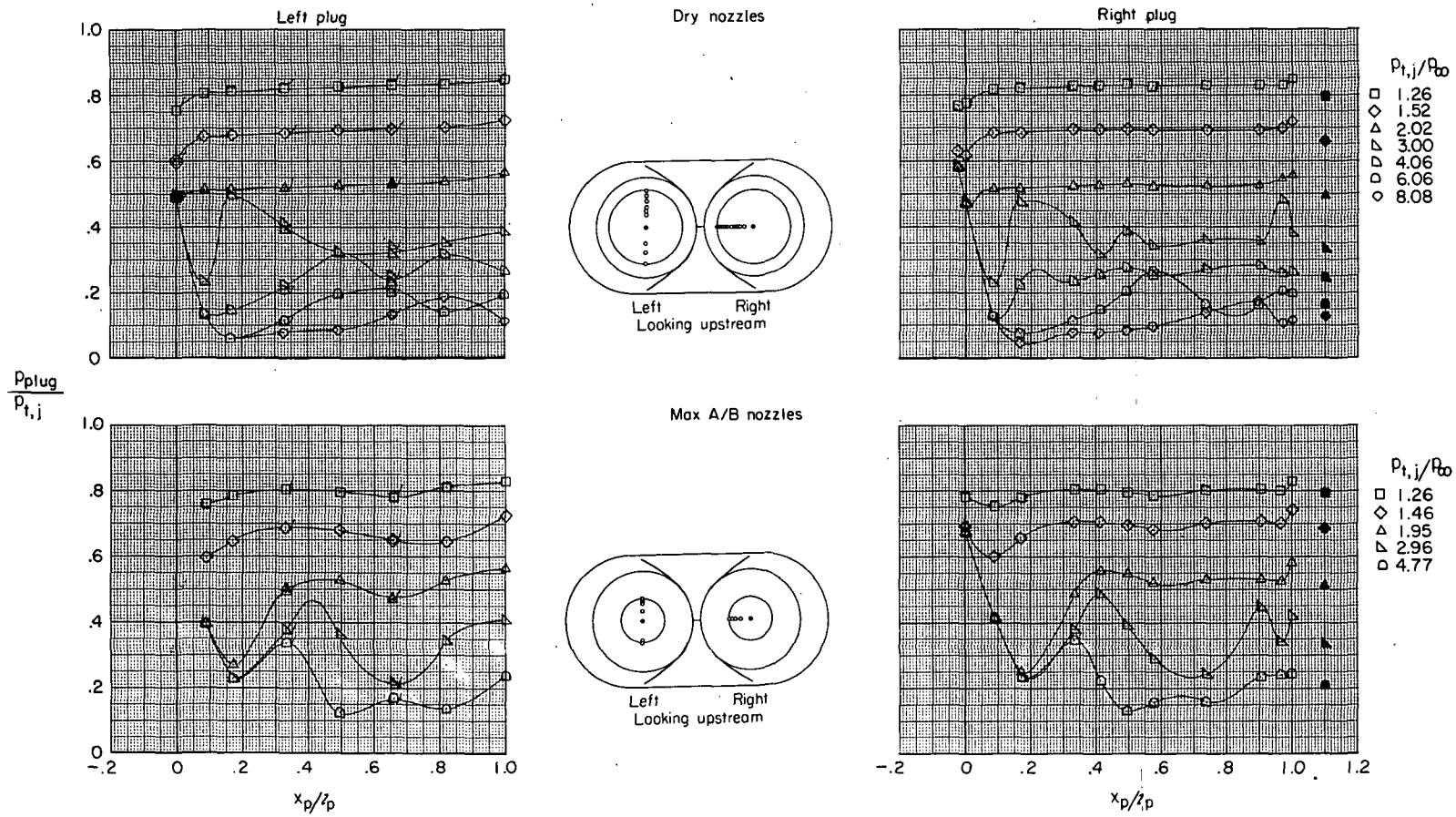

(c) M = 0.80.

Figure 13.- Continued.

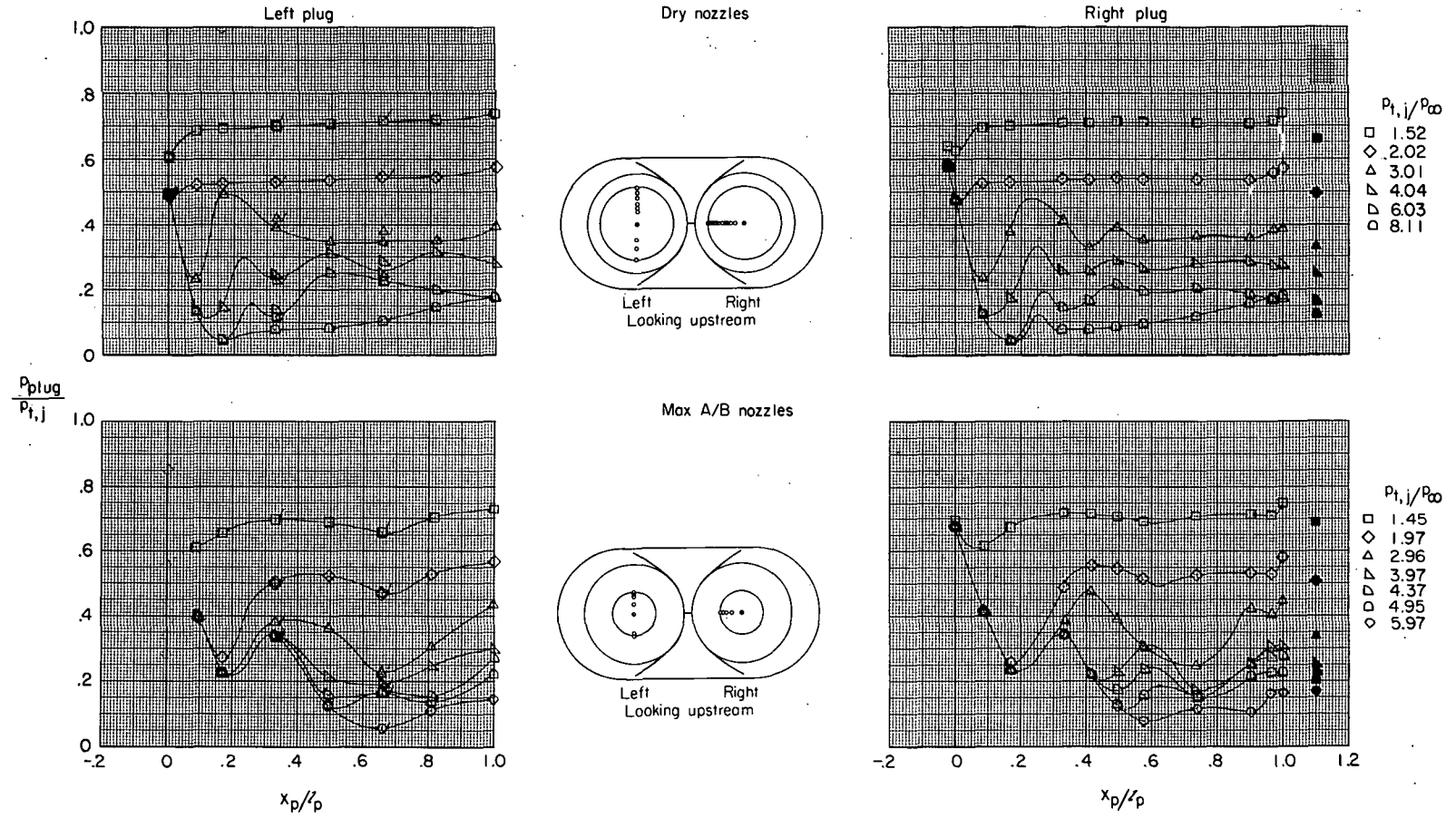

(d) M = 0.90.

Figure 13.- Continued.

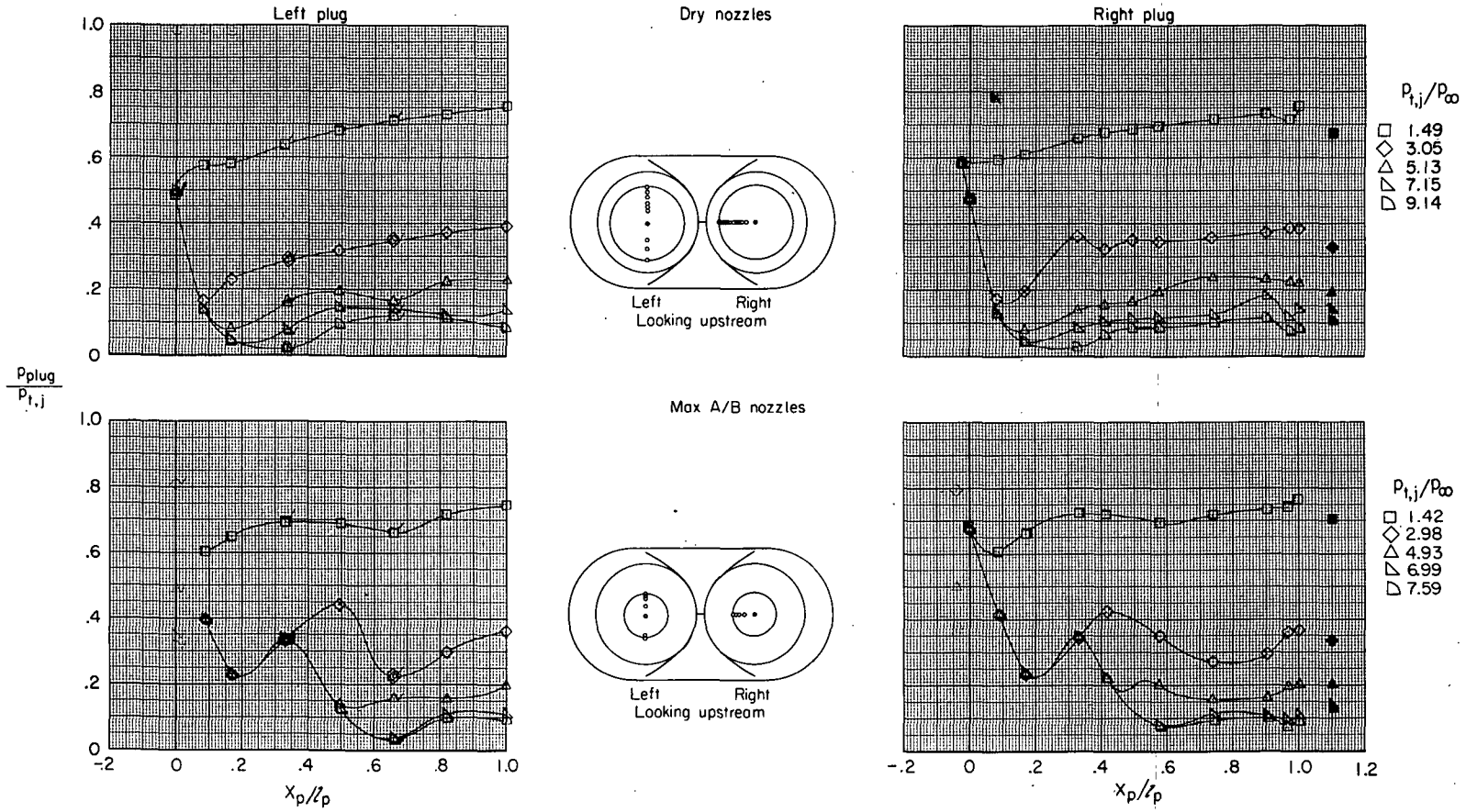

(e) M = 1.20.

Figure 13.- Continued.

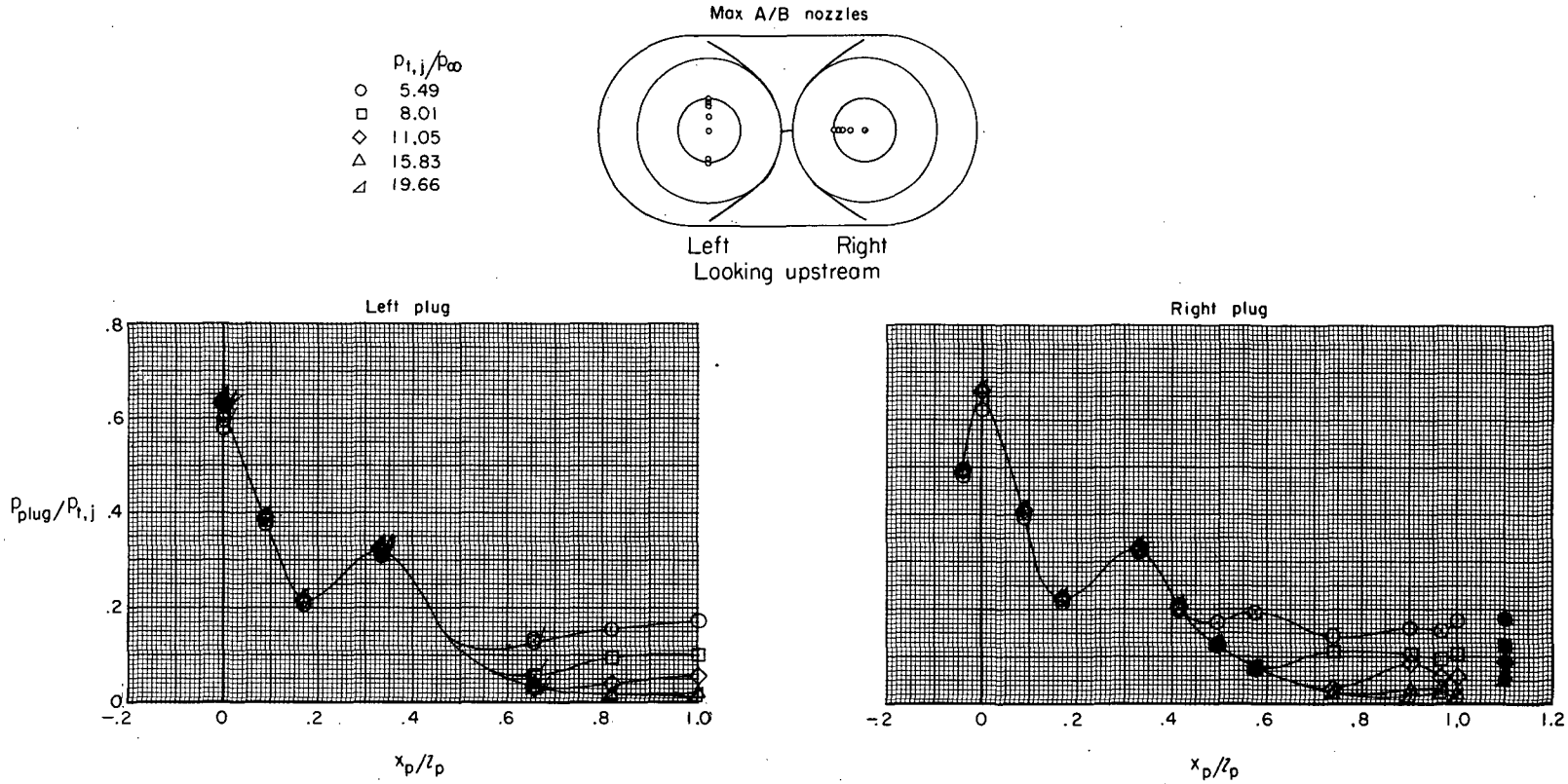

(f) M = 2.20.

Figure 13.- Concluded.

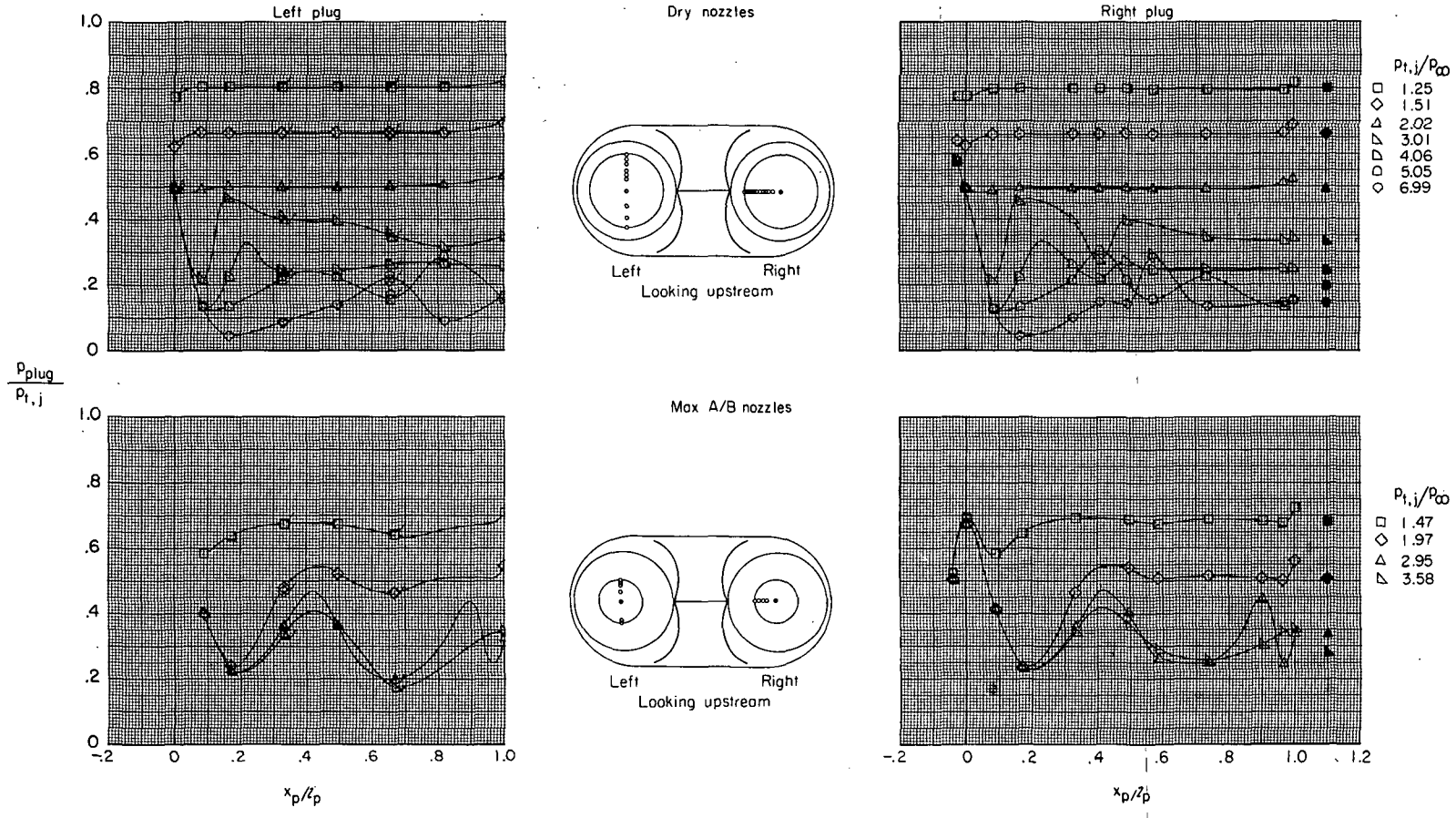

(a) M = 0.

Figure 14.- Plug static-pressure distributions at several Mach numbers. Wide-spaced afterbody with basic interfairing. Flagged symbols indicate bottom-row orifices; solid symbols indicate values of $p_\infty/p_{t,j}$.

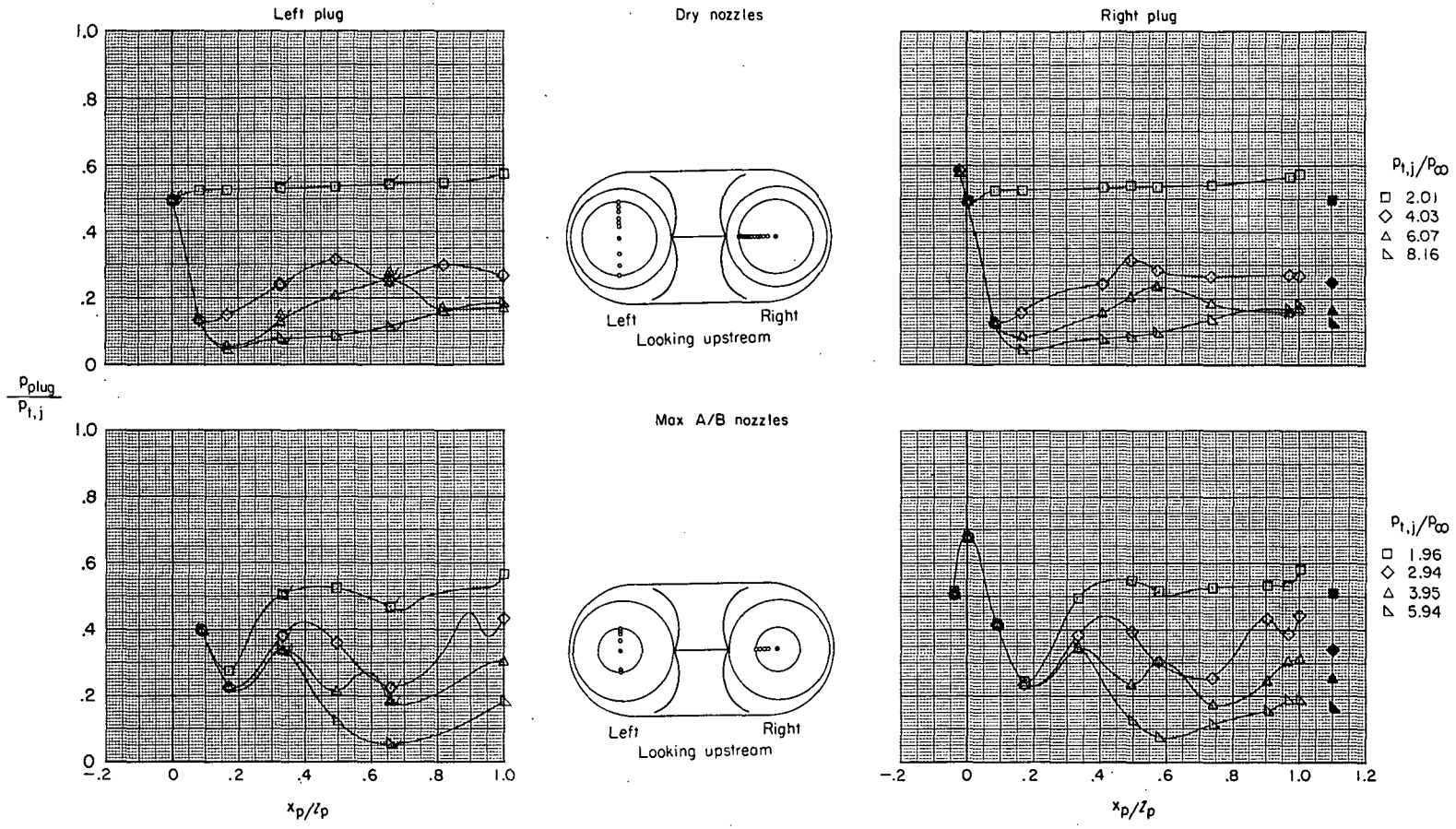

(b) M = 0.90.

Figure 14.- Continued.

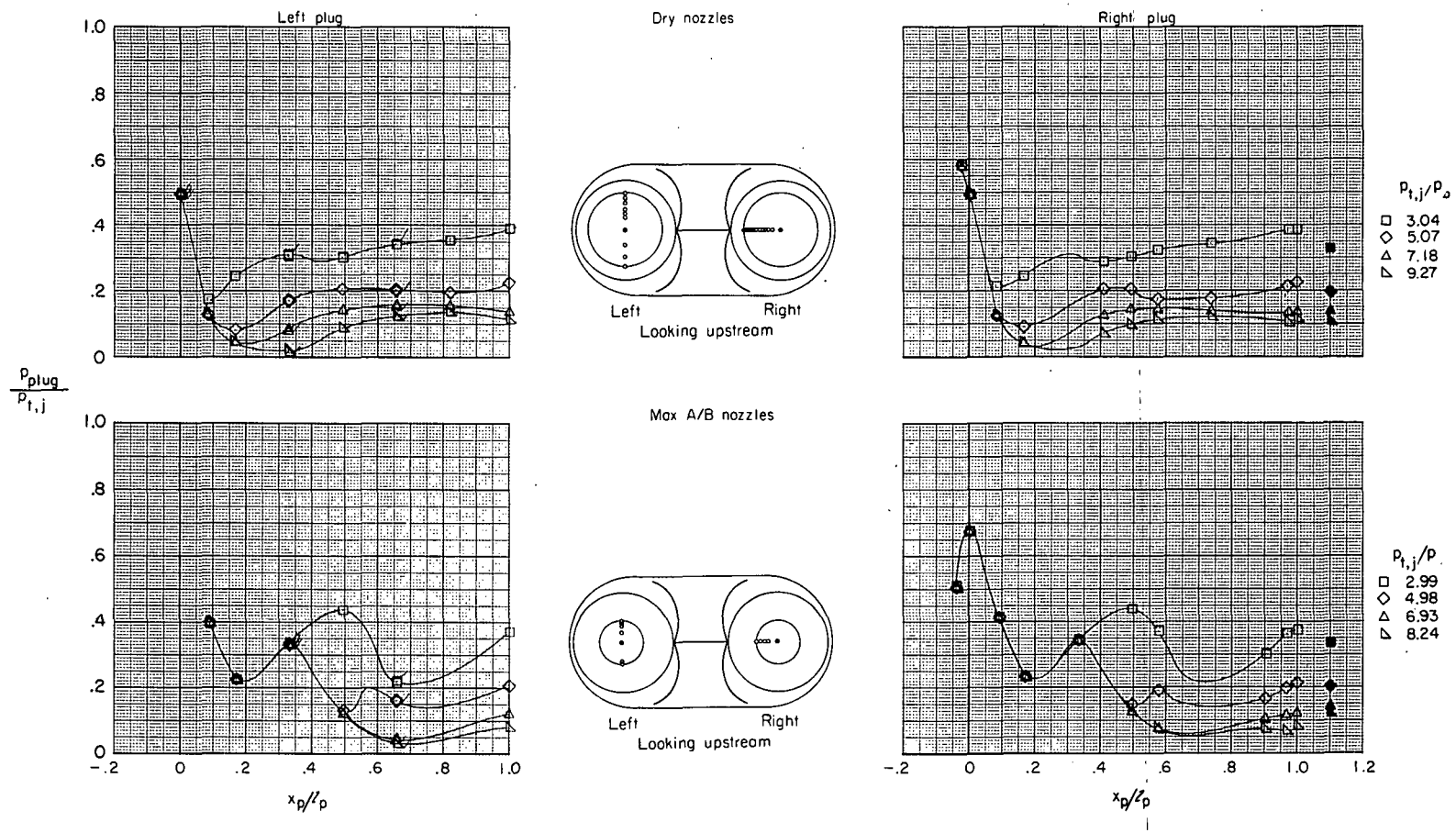

(c) M = 1.20.

Figure 14.- Continued.

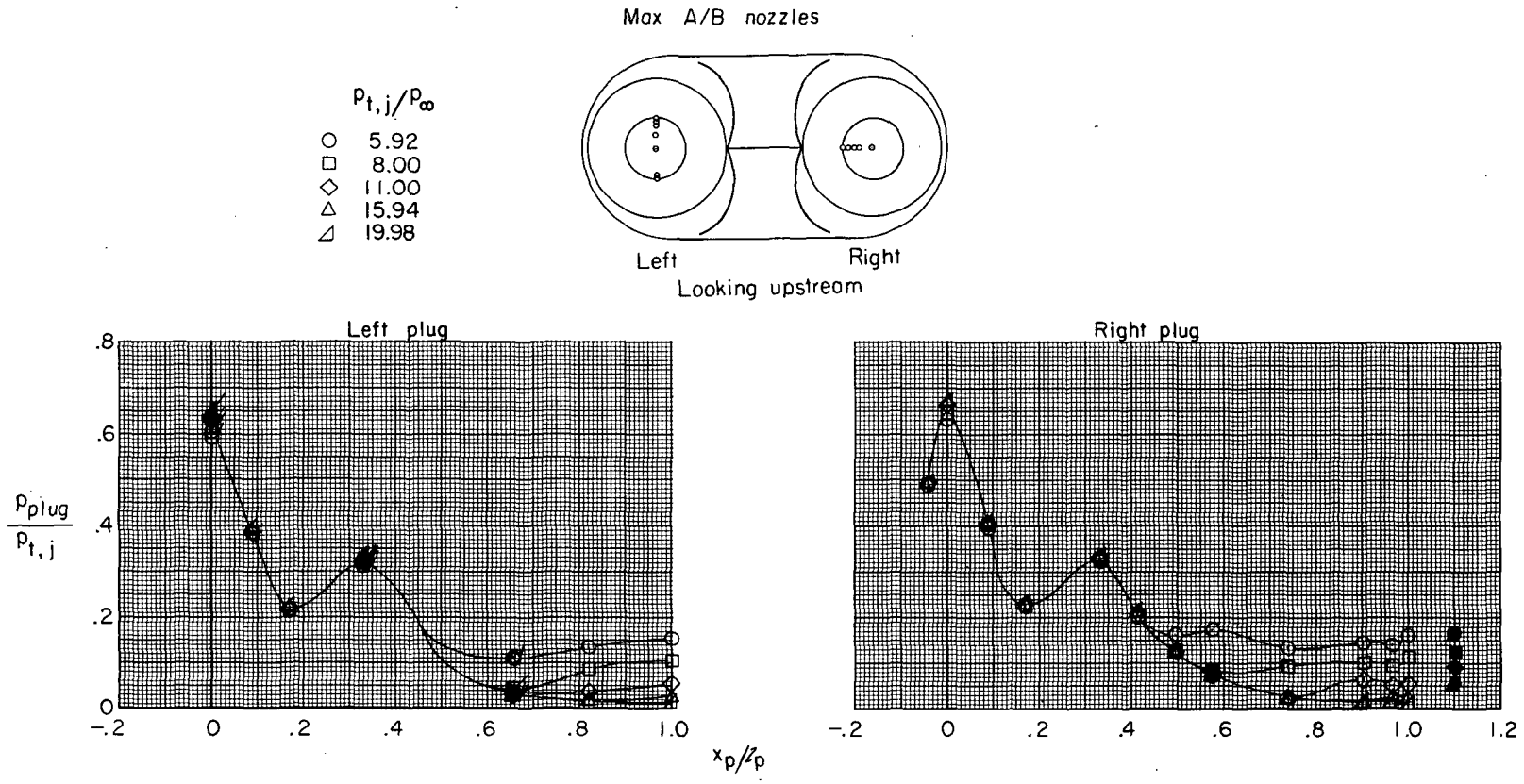

(d) M = 2.20.

Figure 14.- Concluded.

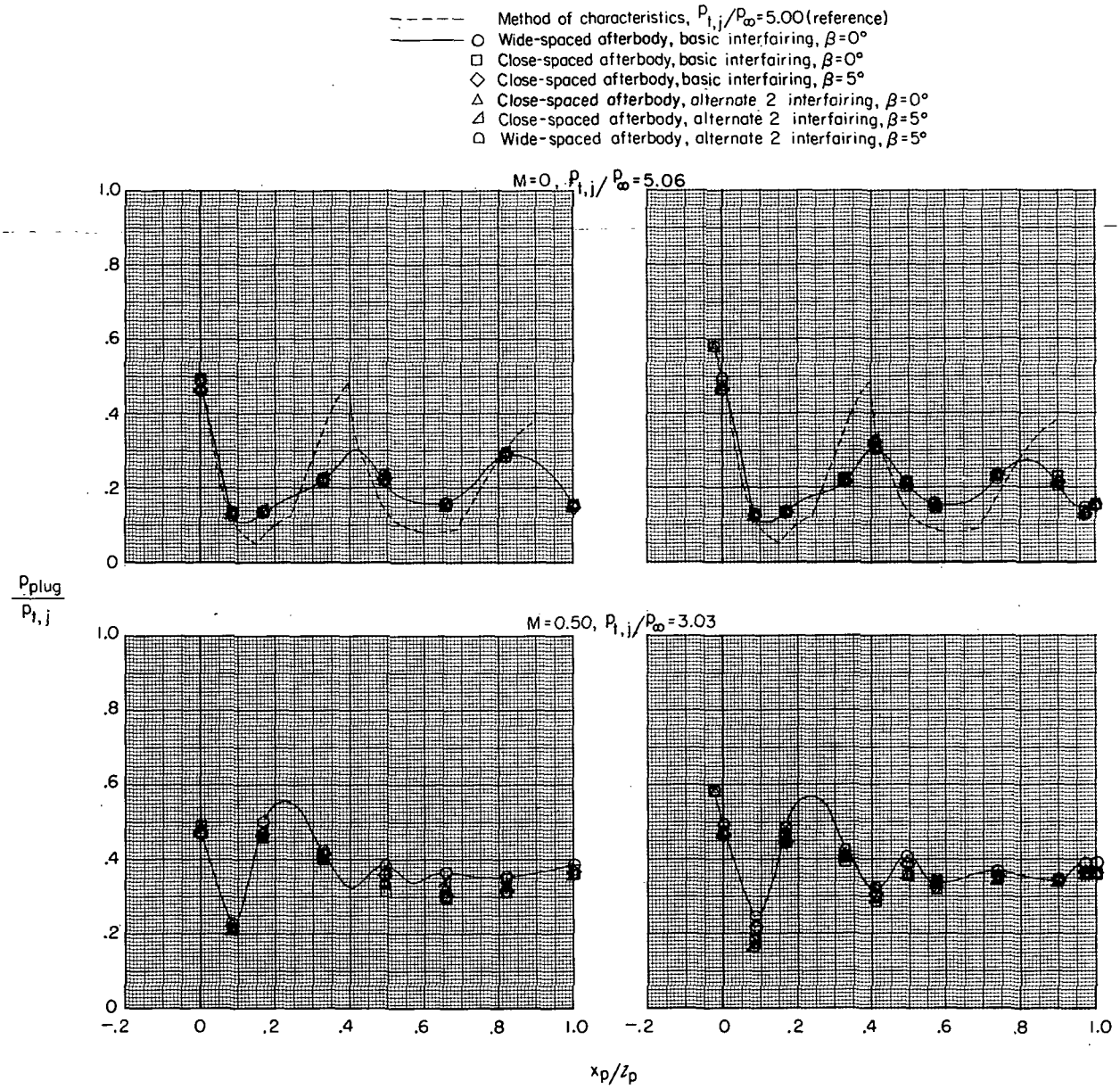

(a) M = 0 and 0.50.

Figure 15.- Effect of afterbody geometry and nozzle cant angle on plug static-pressure distributions. Dry nozzles installed.

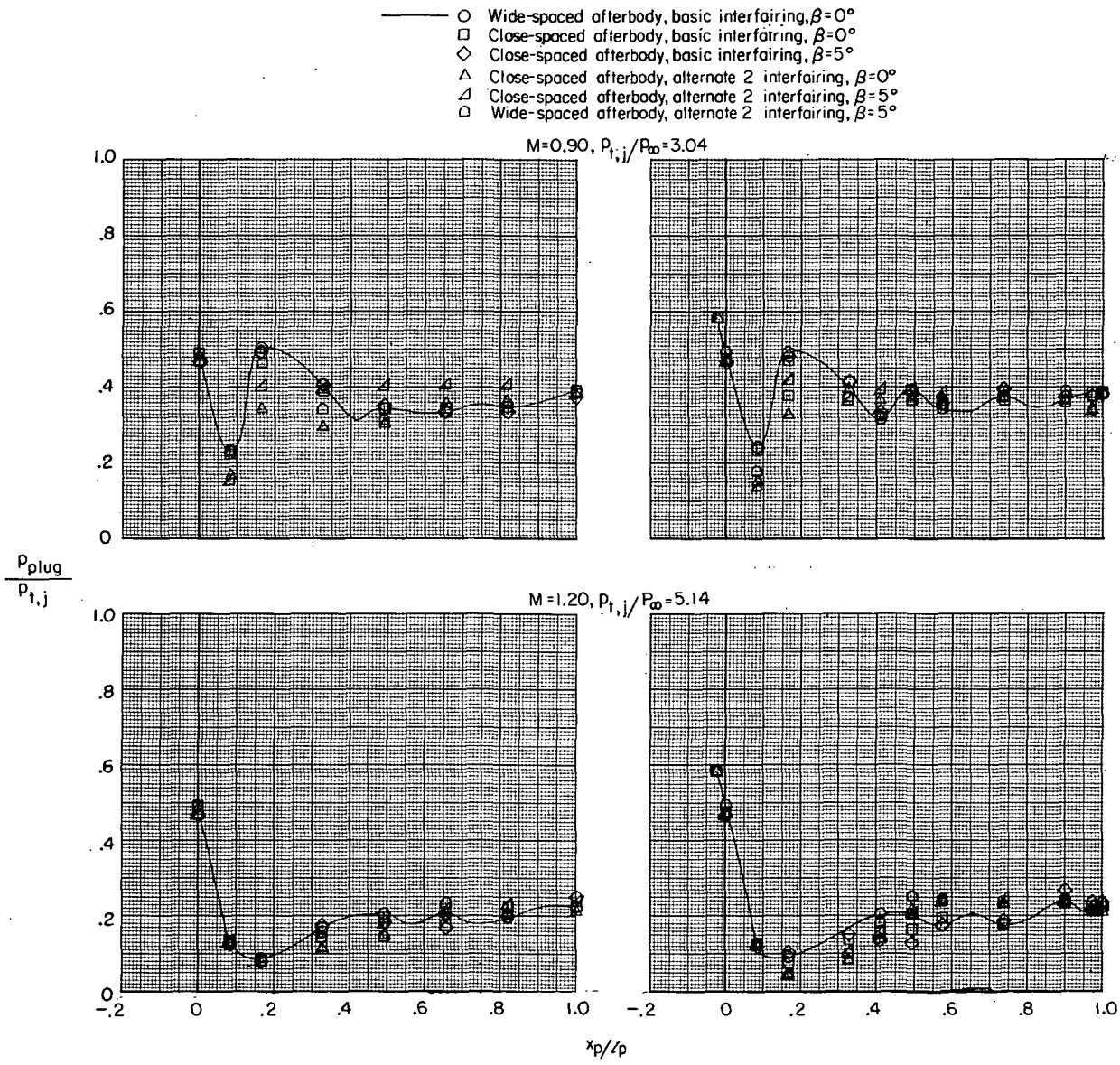

(b) M = 0.90 and 1.20.

Figure 15.- Concluded.

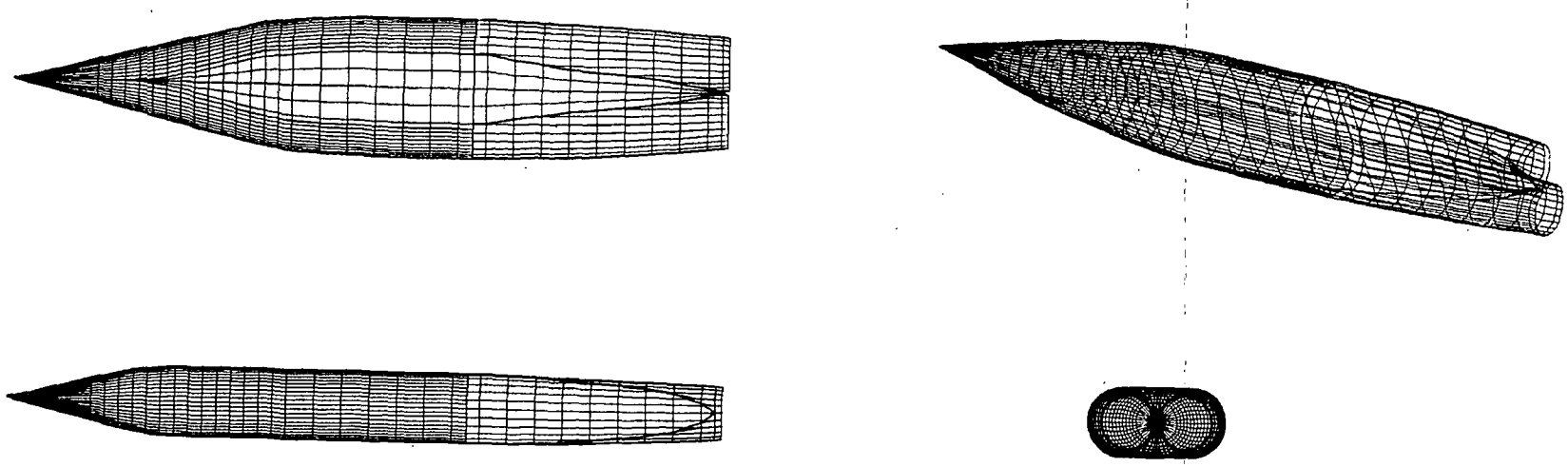

(a) Close-spaced; basic interfairing.

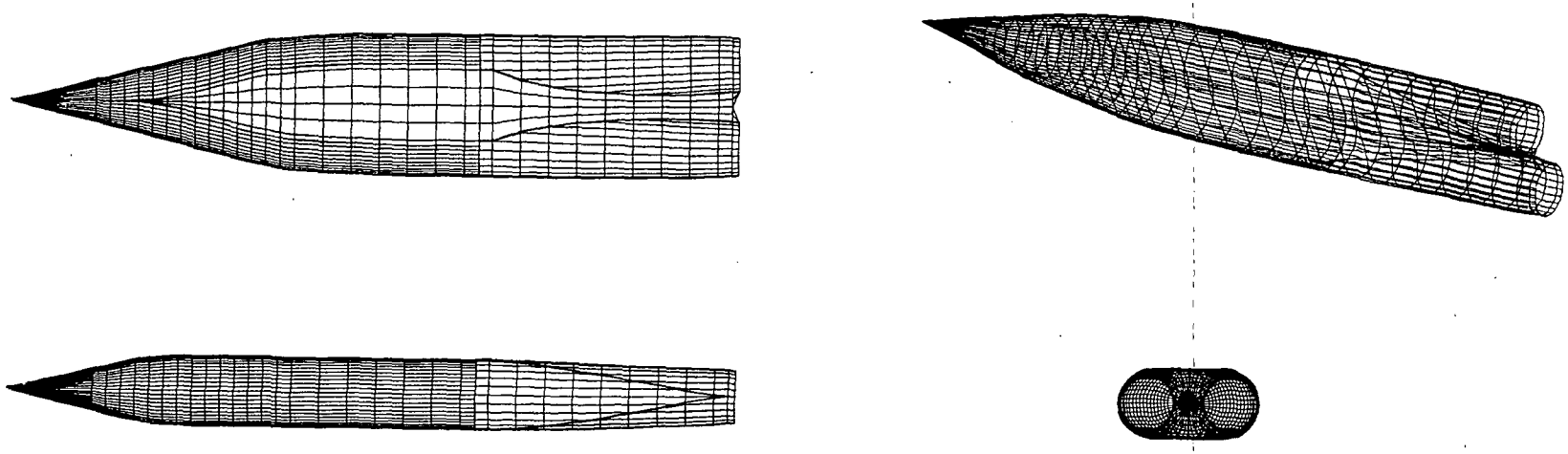

(b) Wide-spaced; basic interfairing.

Figure 16.- Machine-plotted illustrations of mathamatical models used in skin-friction and wave-drag calculations. Nozzle not represented.

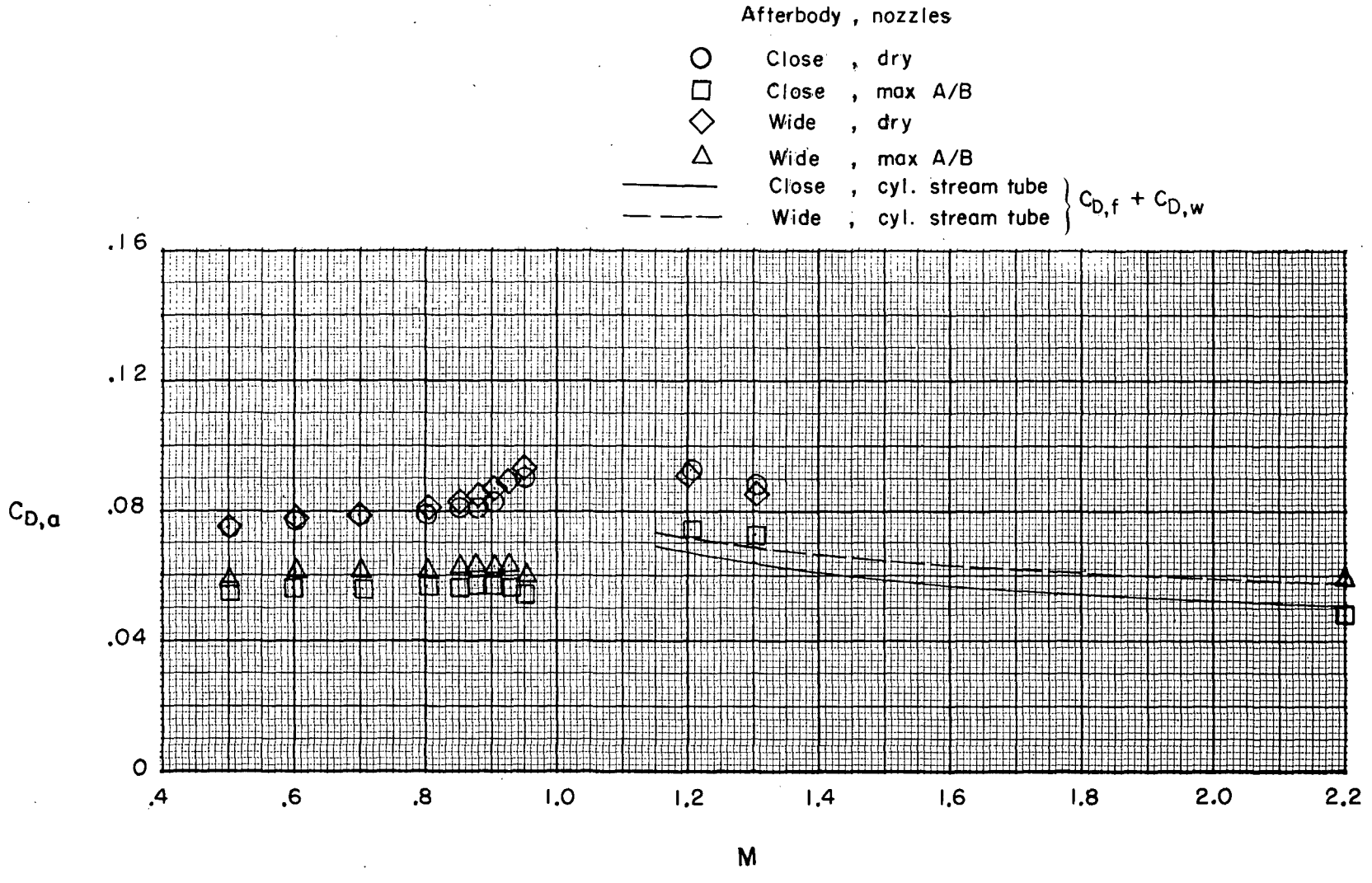

Figure 17.- Comparison of afterbody-drag data with theoretical values of afterbody drag. Basic interfairing; $\beta = 0^{o}$; jet off.

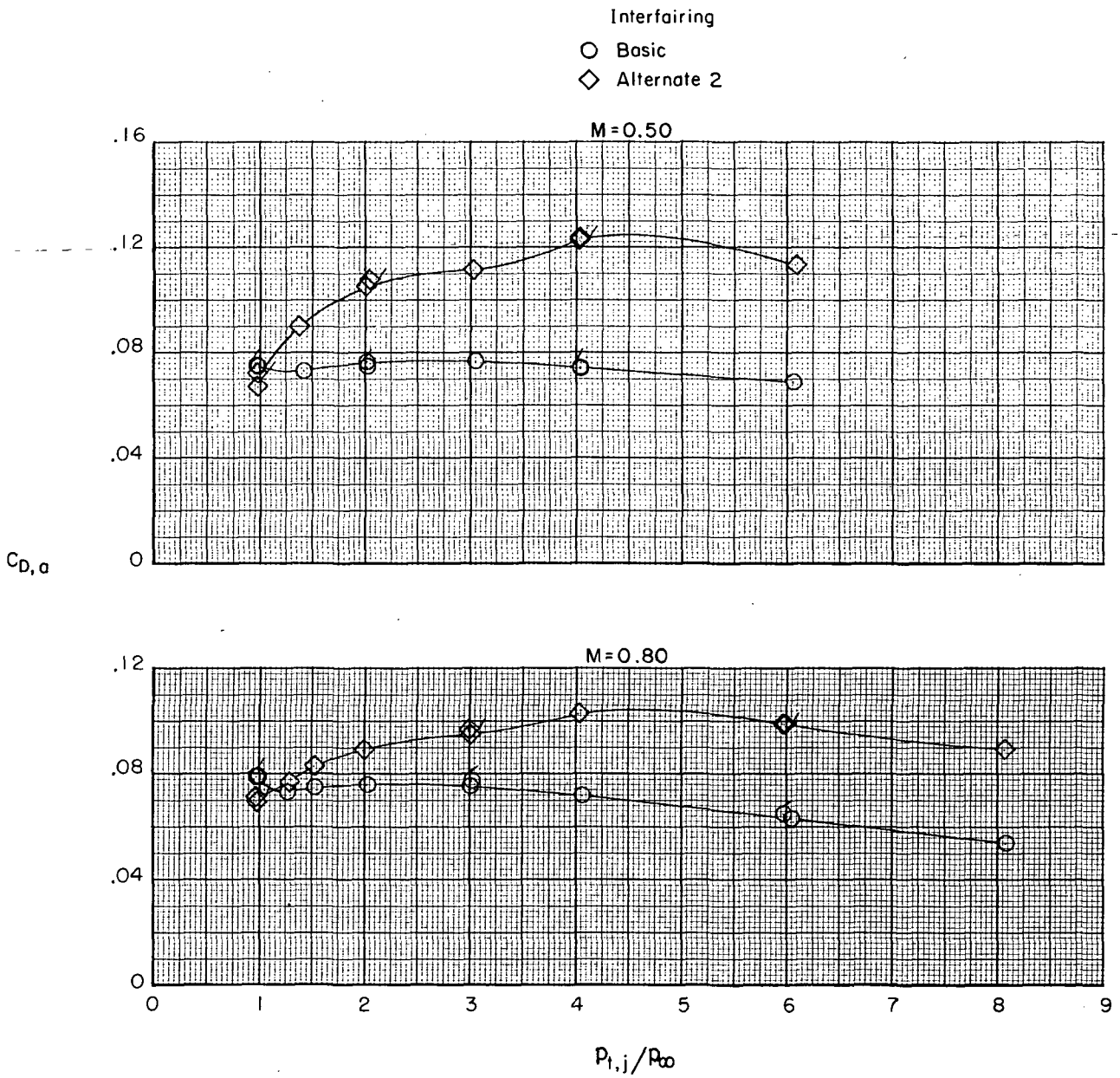

(a) M = 0.50 and 0.80.

Figure 18.- Variation of afterbody drag coefficient with jet total-pressure ratio. Close-spaced afterbody; dry nozzle; $\beta = 0^{o}$. Flagged symbols indicate decreasing jet total-pressure ratio.

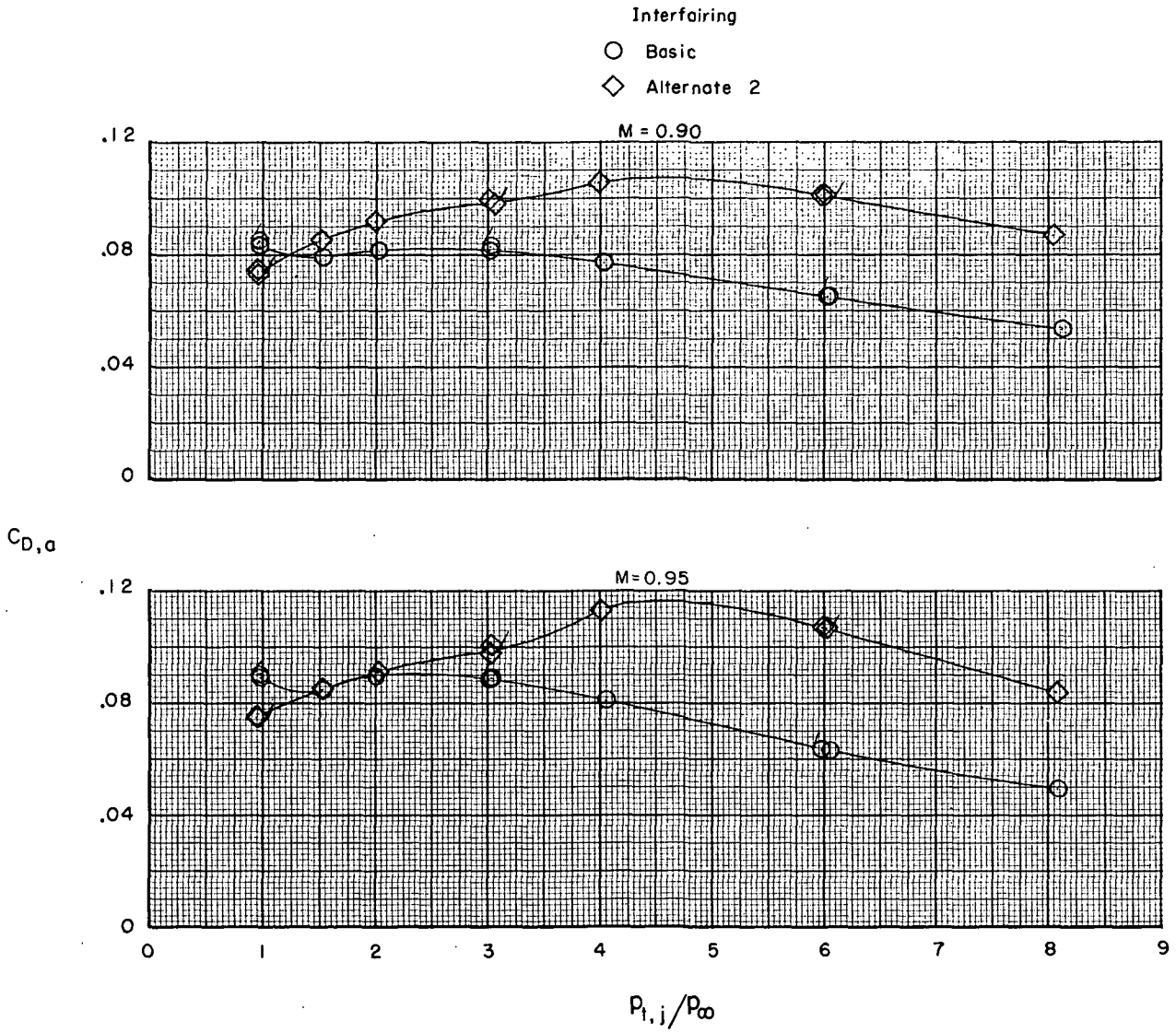

(b) M = 0.90 and 0.95.

Figure 18.- Continued.

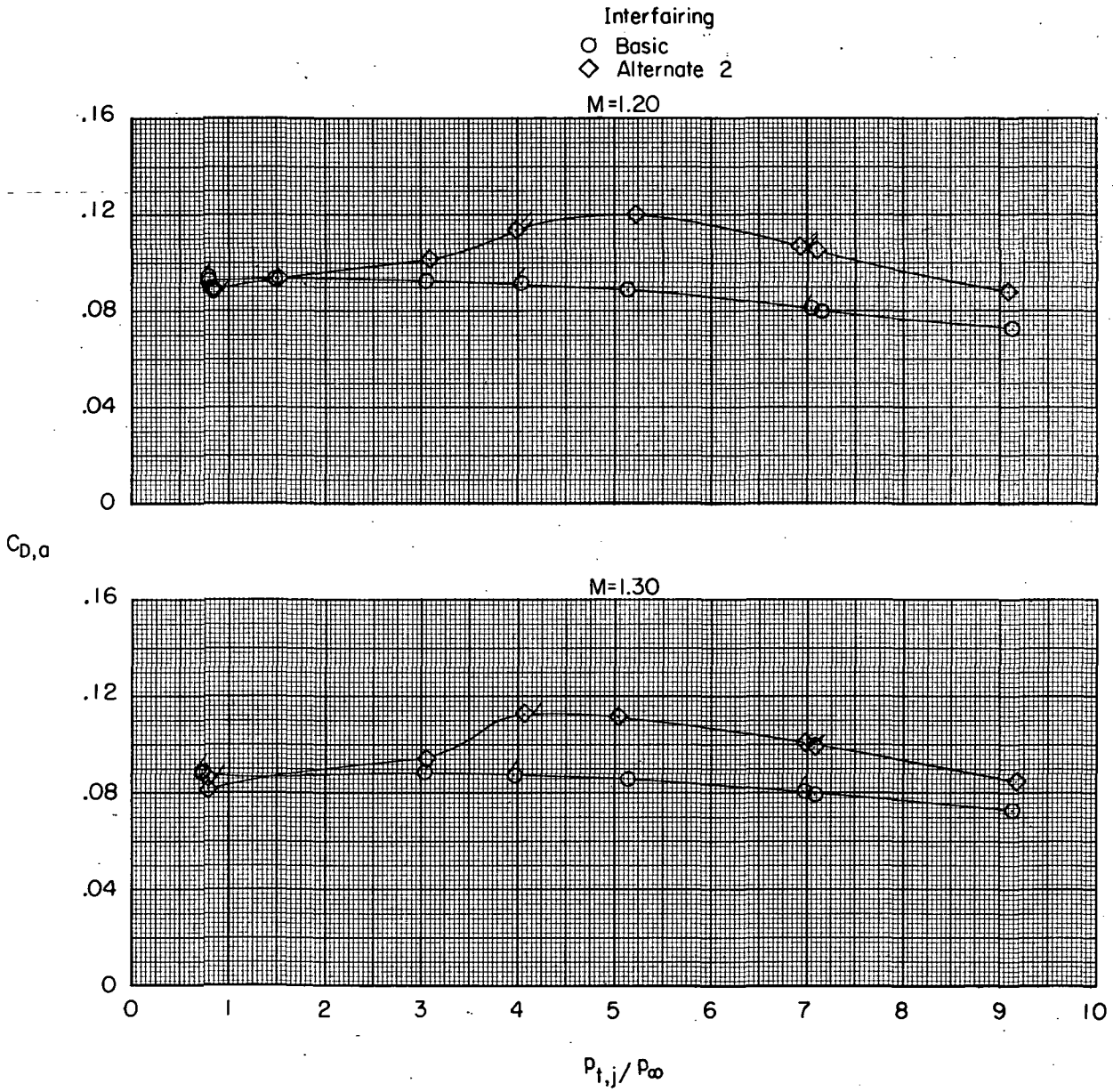

(c) M = 1.20 and 1.30.

Figure 18.- Concluded.

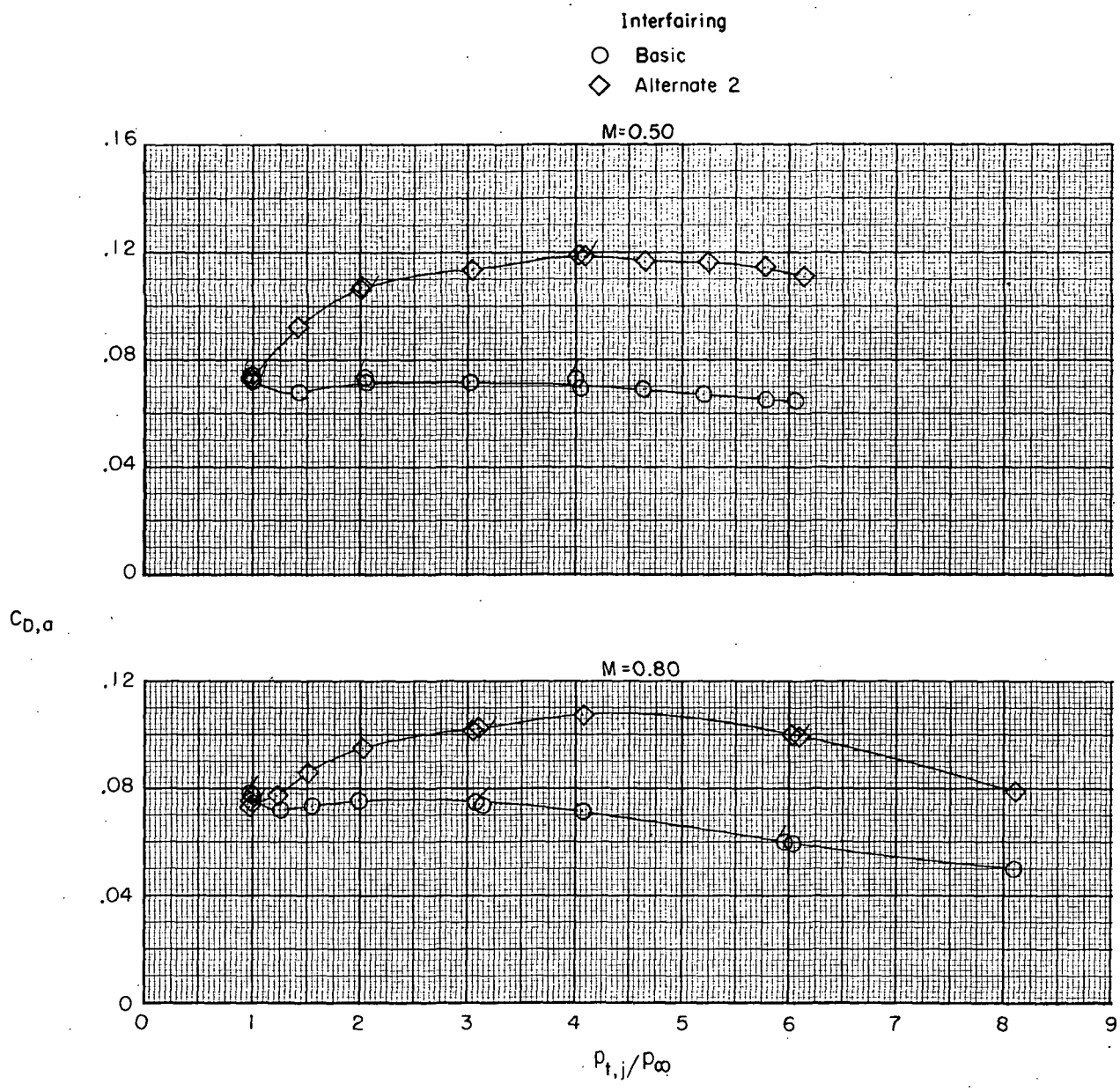

(a) M = 0.50 and 0.80.

Figure 19.- Variation of afterbody drag coefficient with jet total-pressure ratio. Close-spaced afterbody; dry nozzle; $\beta = 5^o$. Flagged symbols indicate decreasing jet total-pressure ratio.

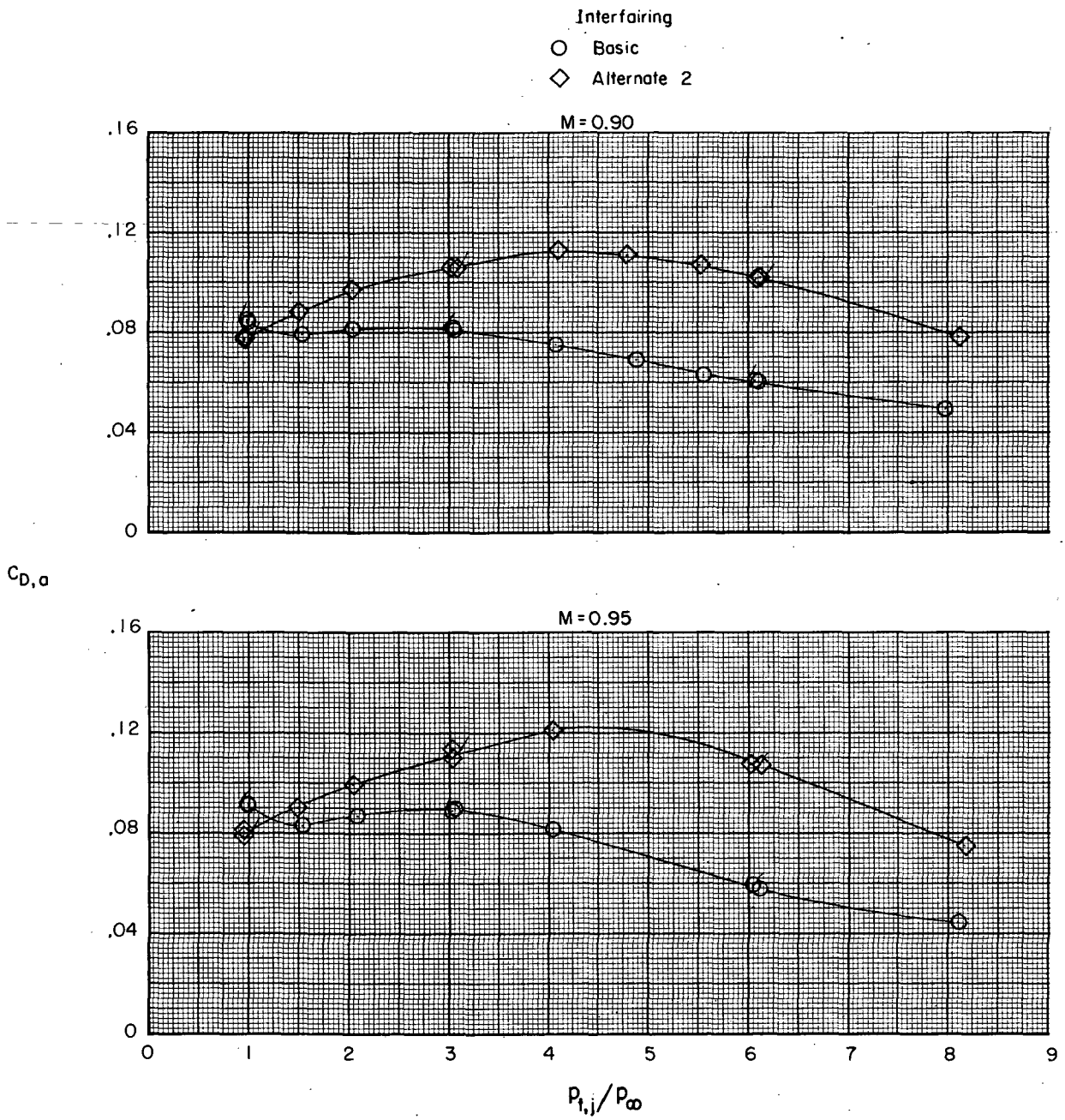

(b) M = 0.90 and 0.95.

Figure 19.- Continued.

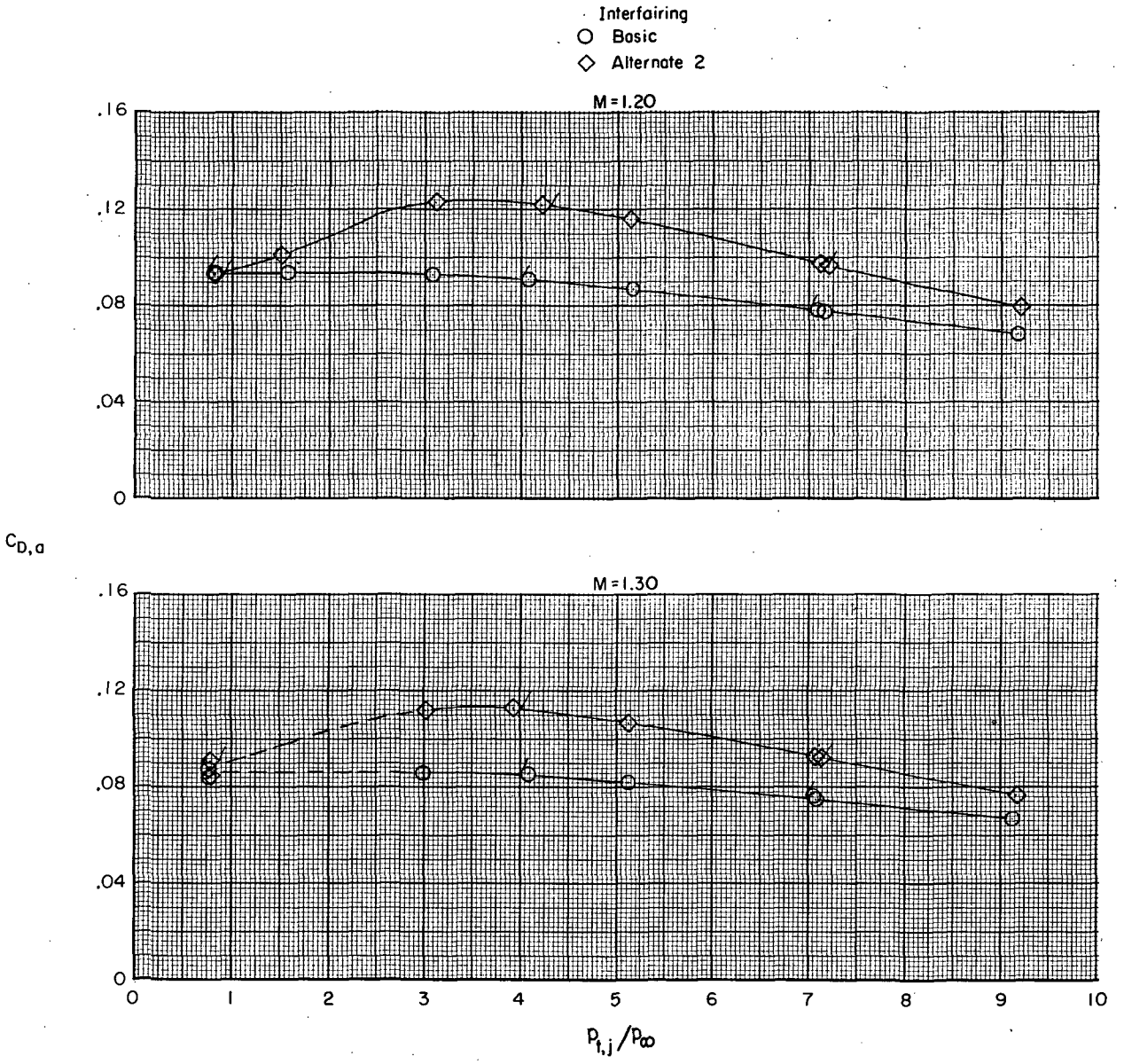

(c) M = 1.20 and 1.30.

Figure 19.- Concluded.

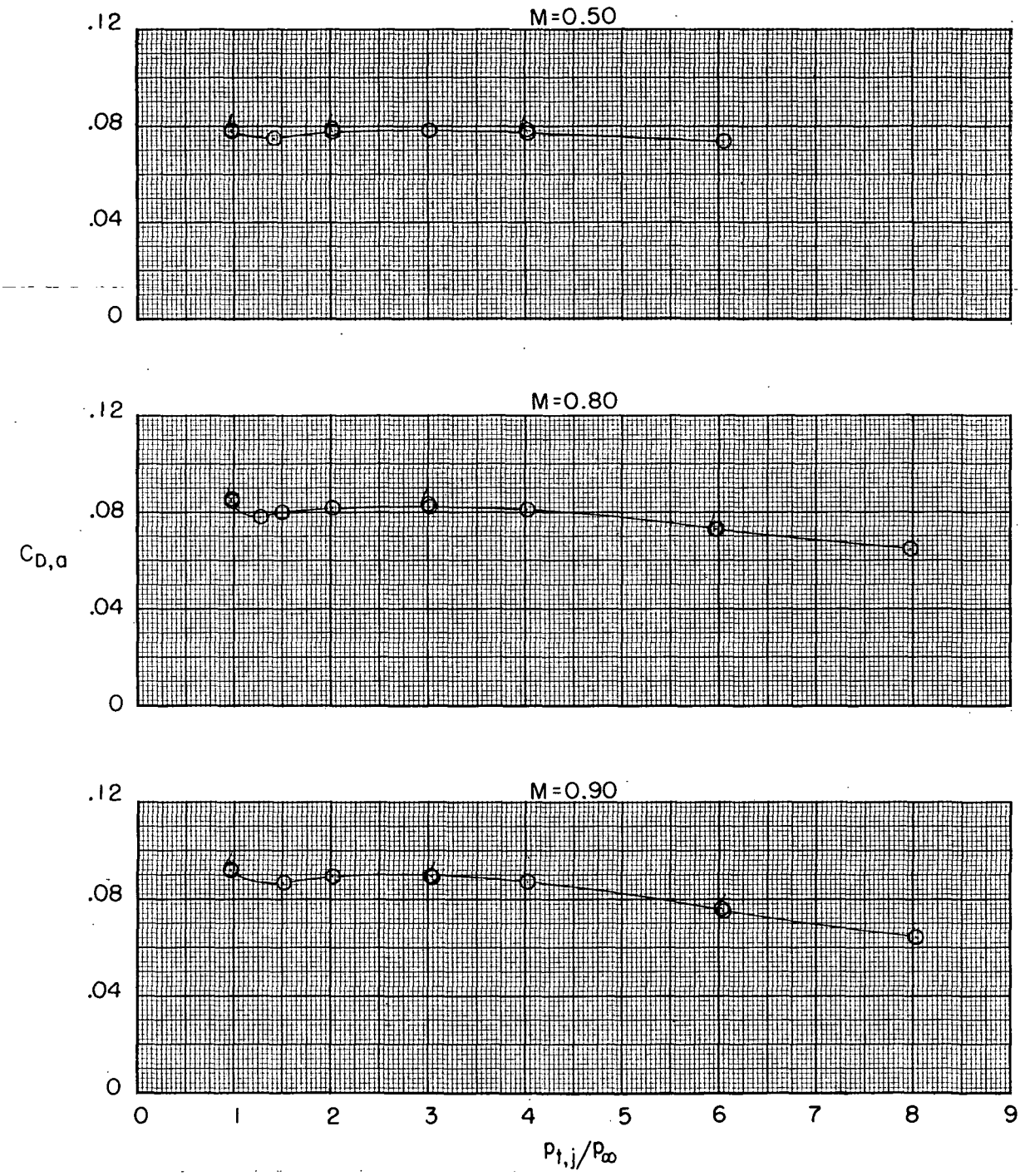

(a) M = 0.50 to 0.90.

Figure 20.- Variation of afterbody drag coefficient with jet total-pressure ratio. Close-spaced afterbody; dry nozzle; $\beta = -5^{o}$; basic interfairing. Flagged symbols indicate decreasing jet total-pressure ratio.

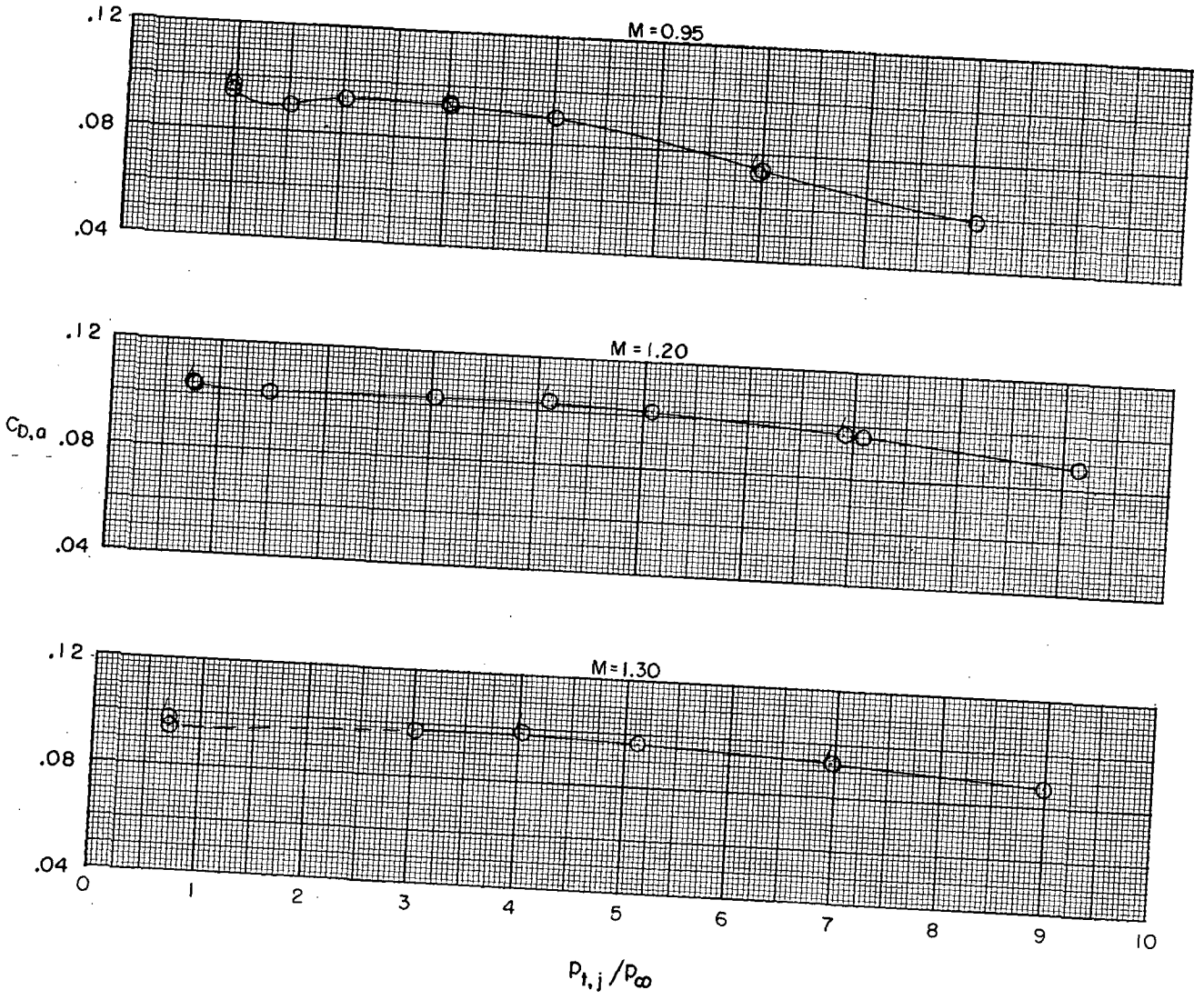

(b) M = 0.95 to 1.30.

Figure 20.- Concluded.

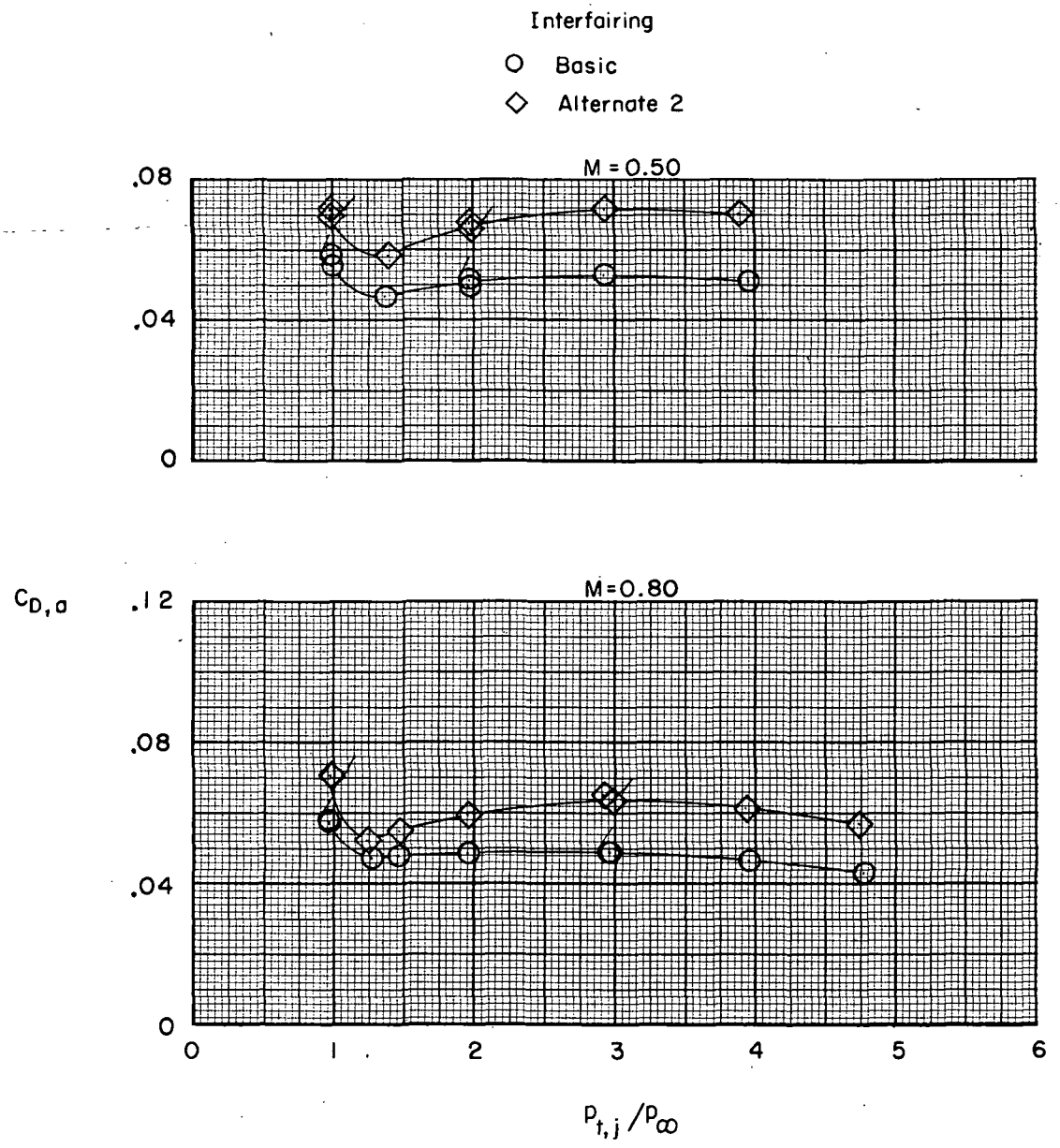

(a) M = 0.50 and 0.80.

Figure 21.- Variation of afterbody drag coefficient with jet total-pressure ratio. Close-spaced afterbody; max A/B nozzle; $\beta = 0^o$. Flagged symbols indicate decreasing jet total-pressure ratio.

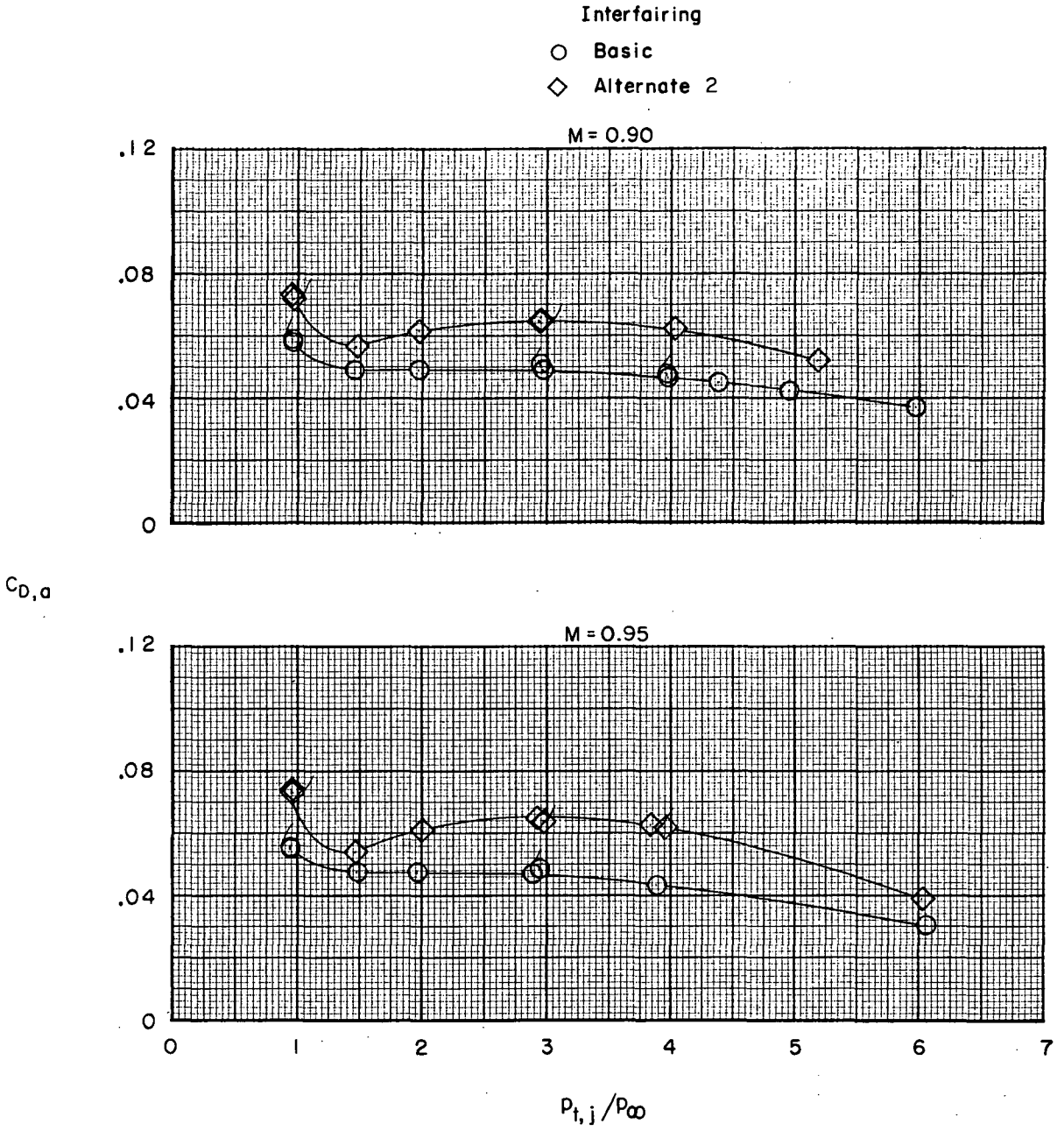

(b) M = 0.90 and 0.95.

Figure 21.- Continued.

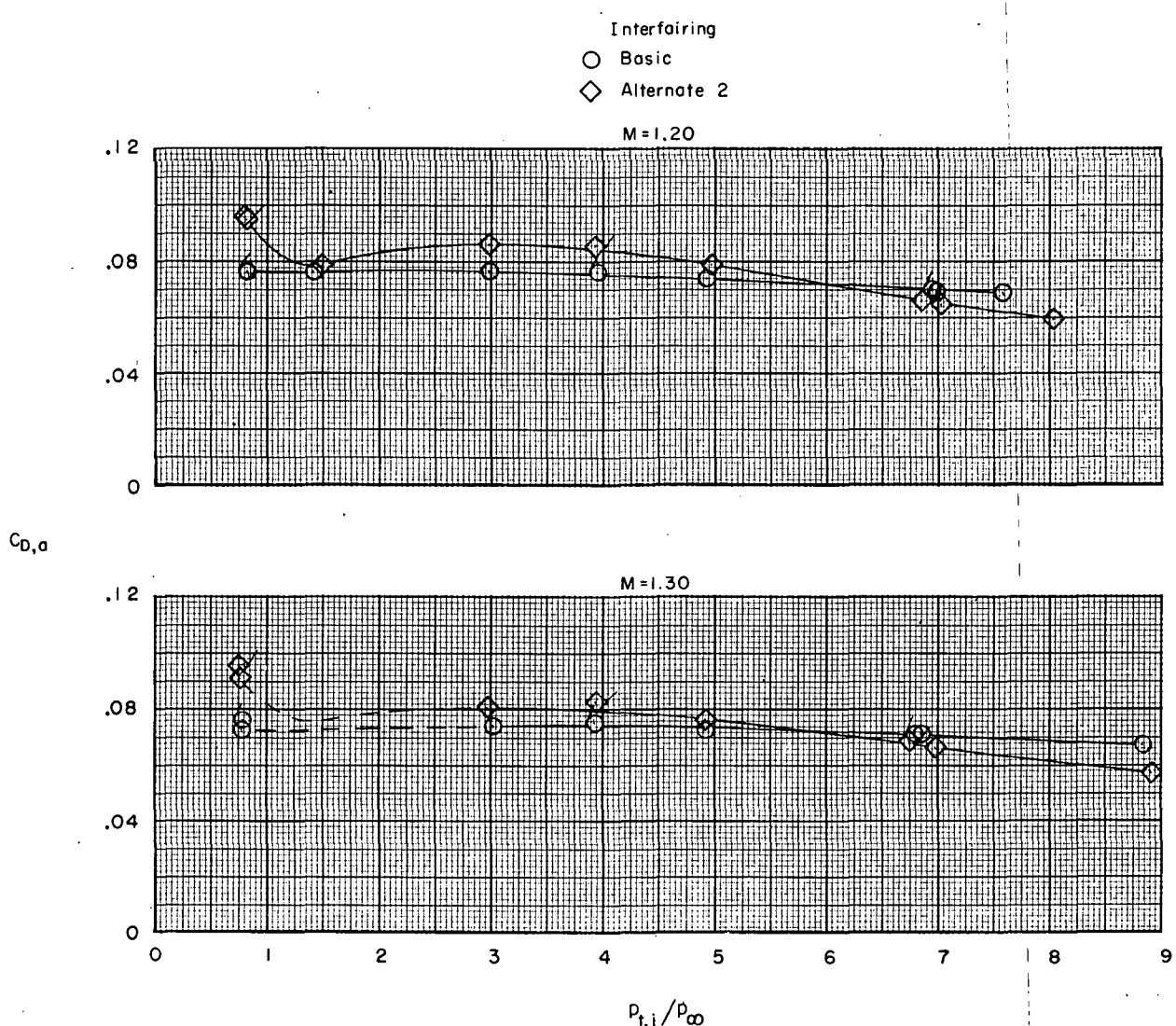

(c) M = 1.20 and 1.30.

Figure 21.- Continued.

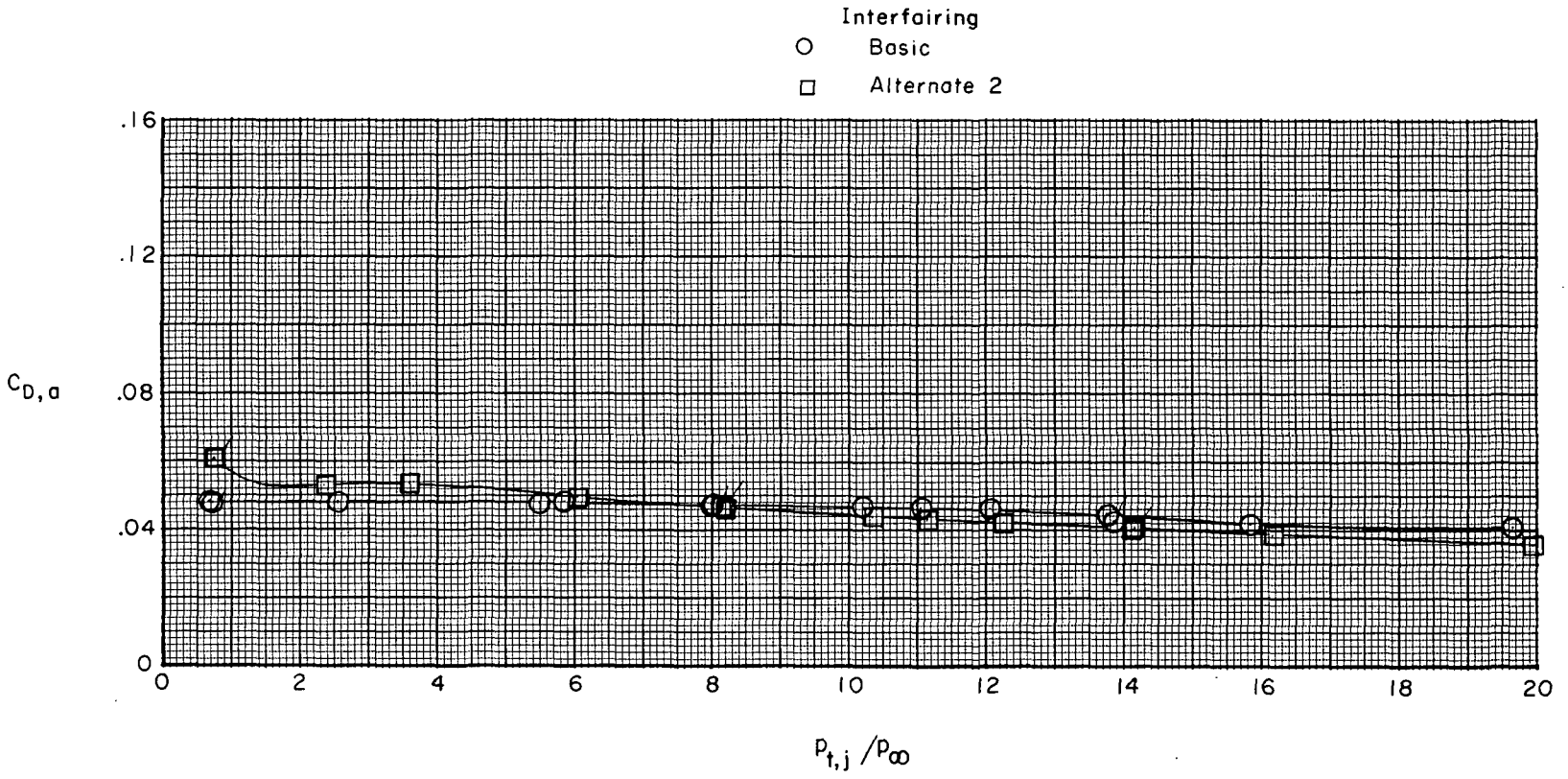

(d) M = 2.20.

Figure 21.- Concluded.

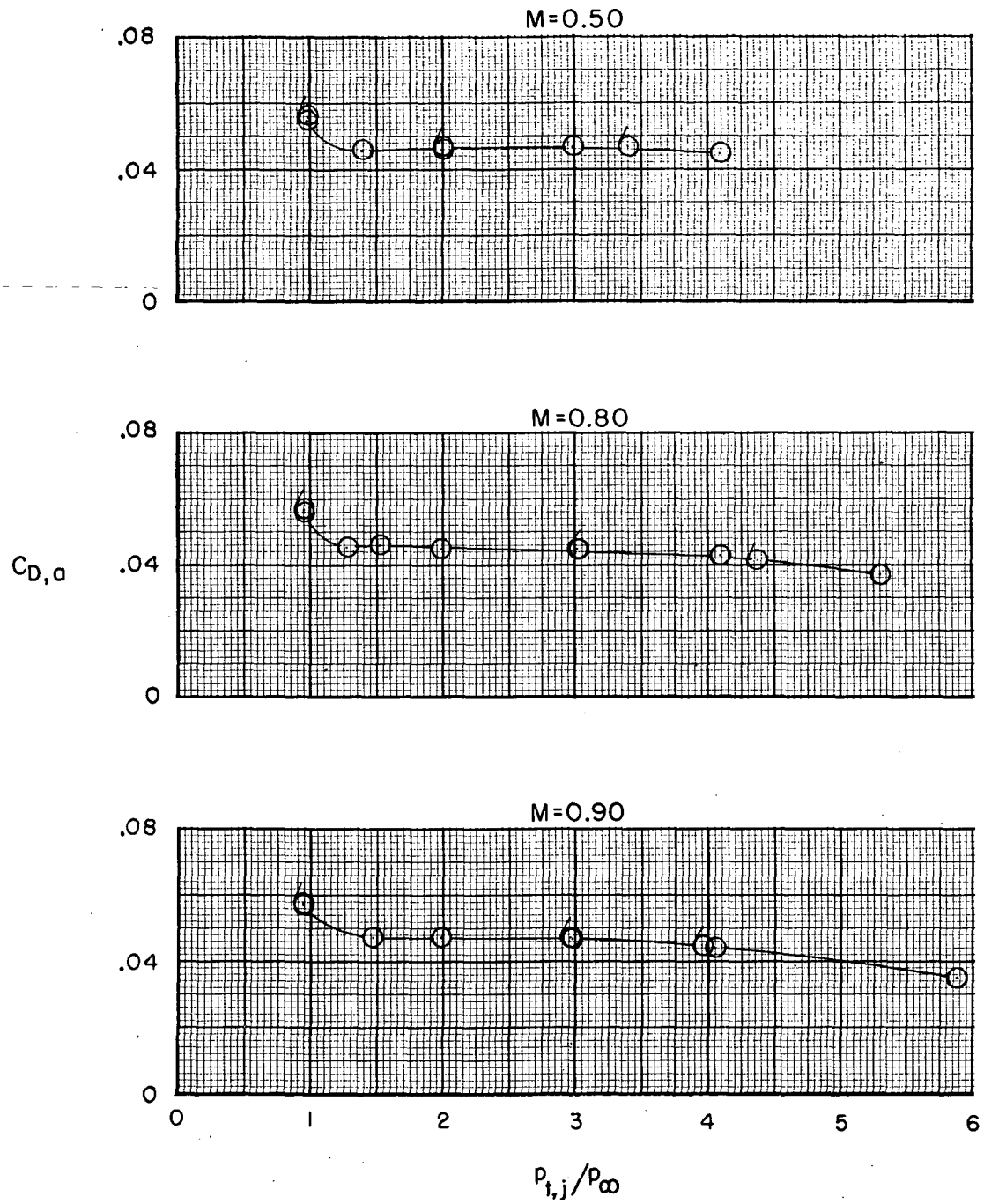

(a) M = 0.50 to 0.90.

Figure 22.- Variation of afterbody drag coefficient with jet total-pressure ratio. Close-spaced afterbody; max A/B nozzle; $\beta = 5^o$; basic interfairing. Flagged symbols indicate decreasing jet total-pressure ratio.

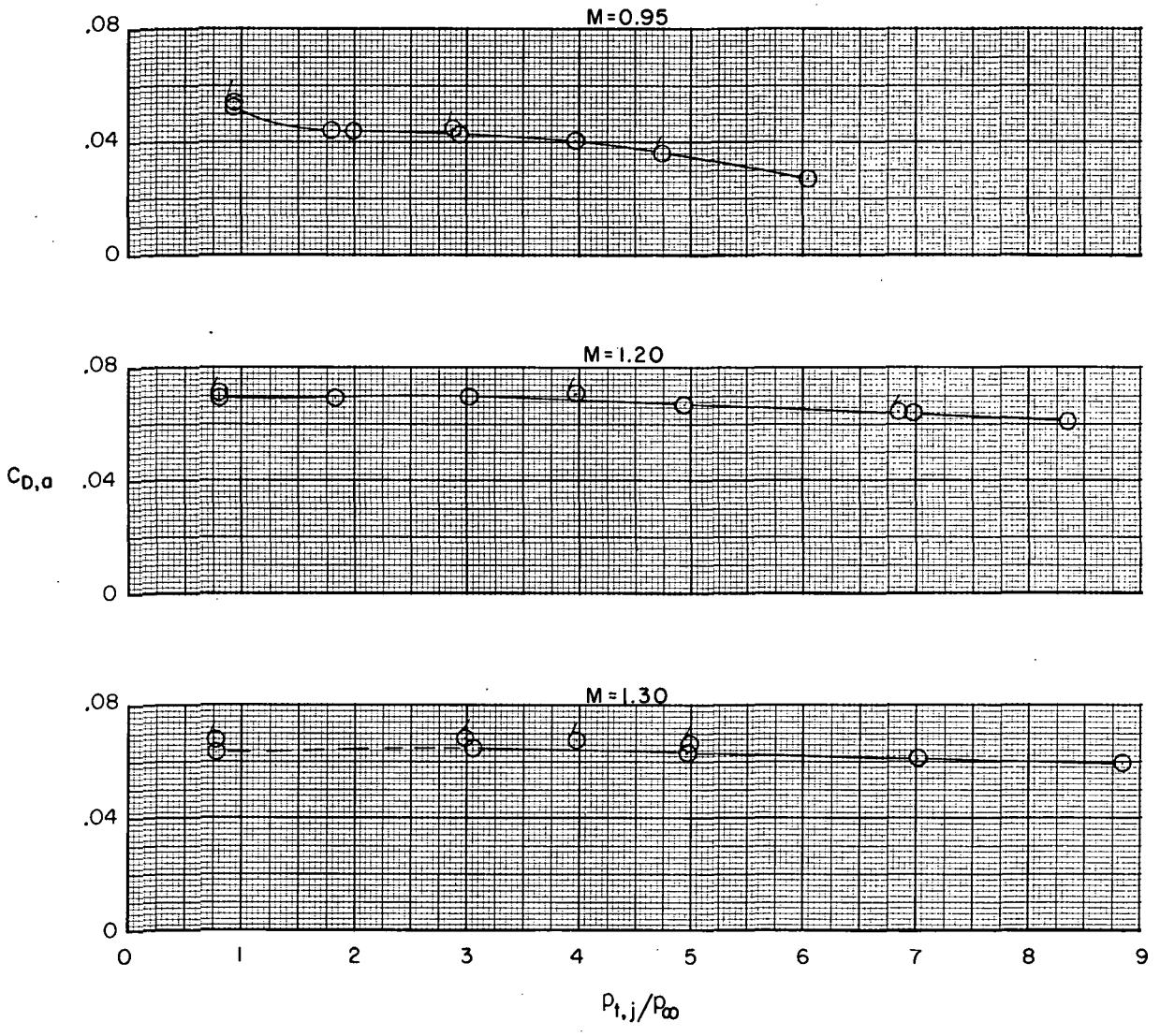

(b) M = 0.95 to 1.30.

Figure 22.- Concluded.

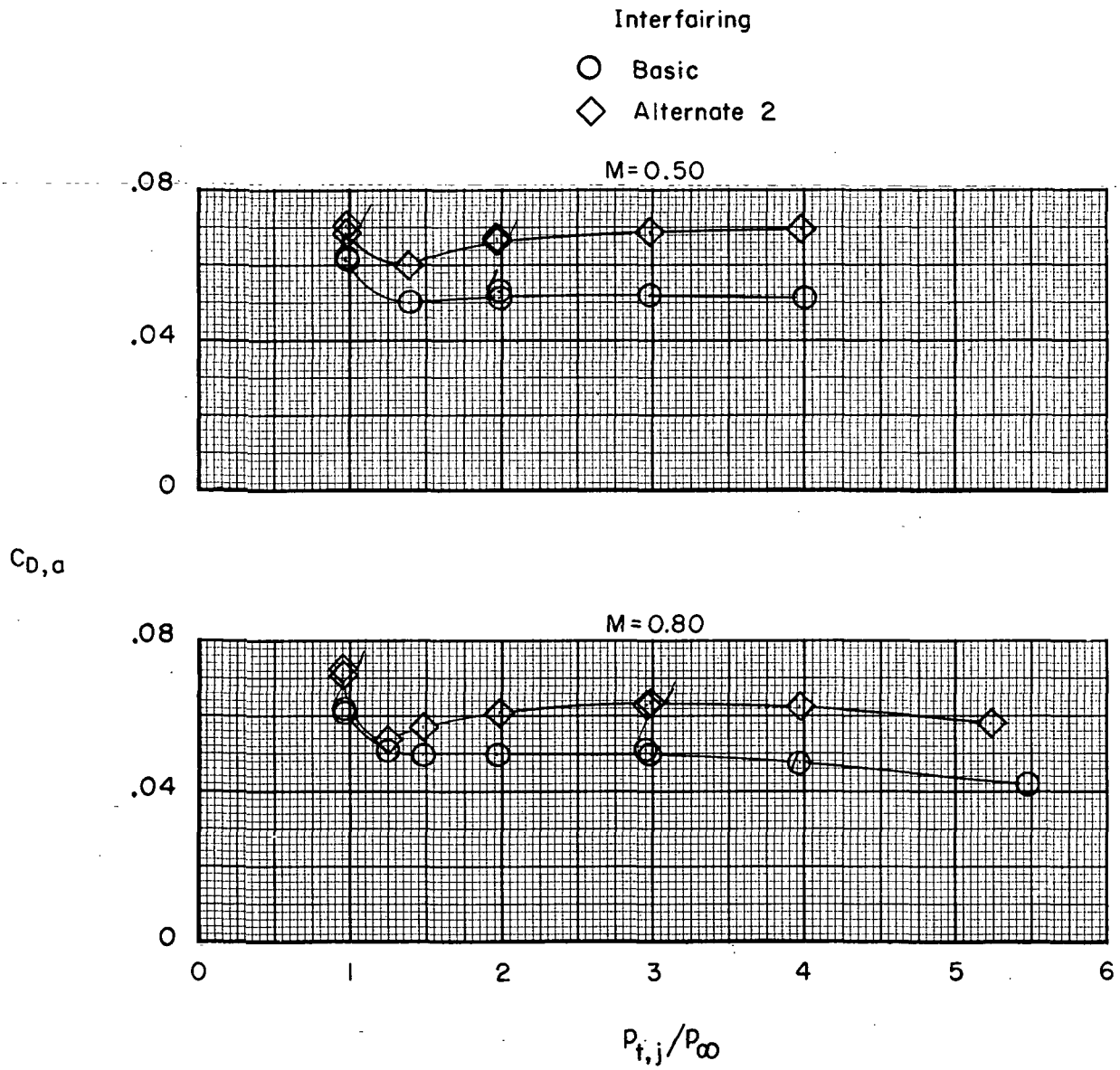

(a) M = 0.50 and 0.80.

Figure 23.- Variation of afterbody drag coefficient with jet total-pressure ratio. Close-spaced afterbody; max A/B nozzle; $\beta = -5^o$. Flagged symbols indicate decreasing jet total-pressure ratio.

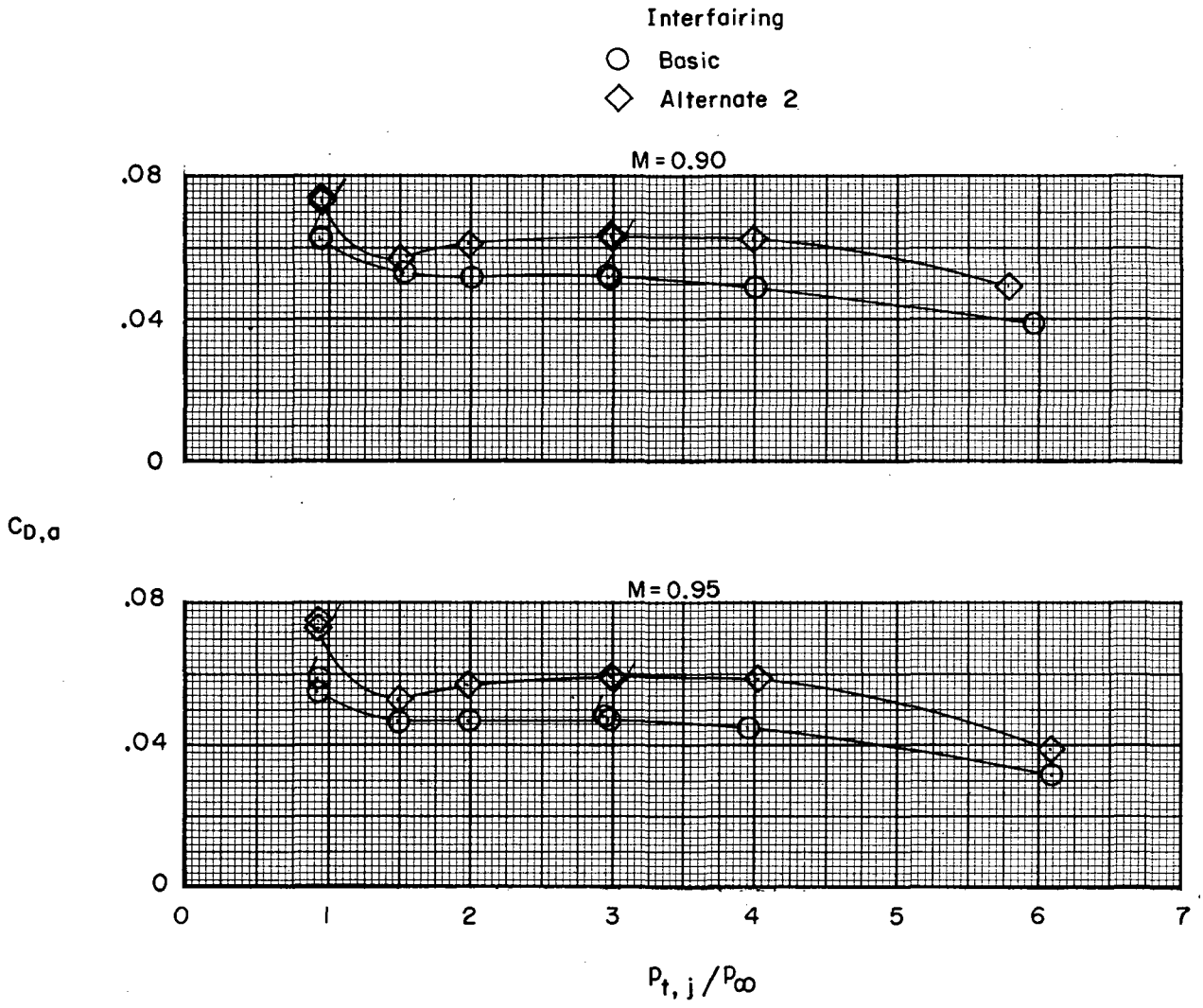

(b) M = 0.90 and 0.95.

Figure 23.- Continued.

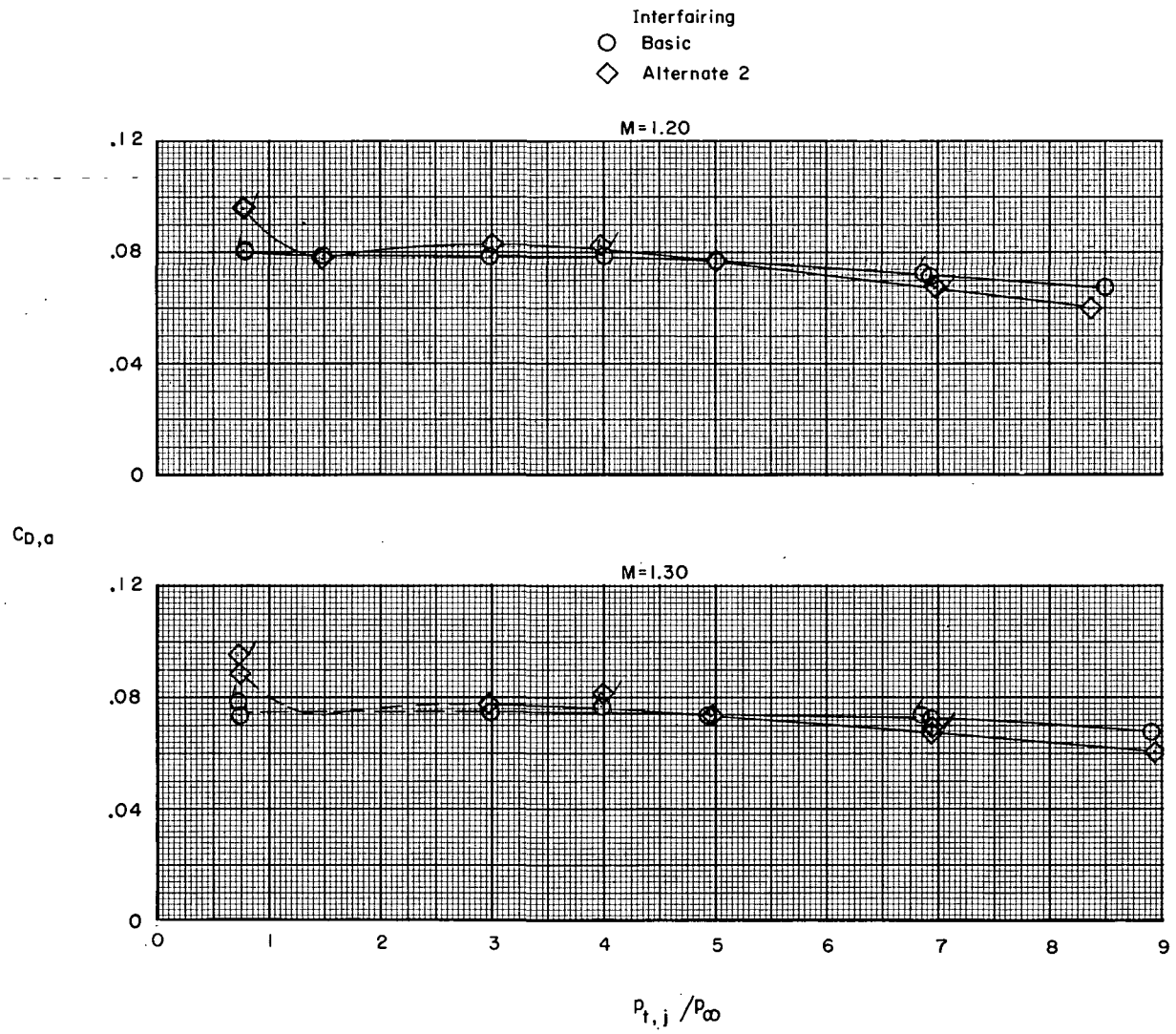

(c) M = 1.20 and 1.30.

Figure 23.- Concluded.

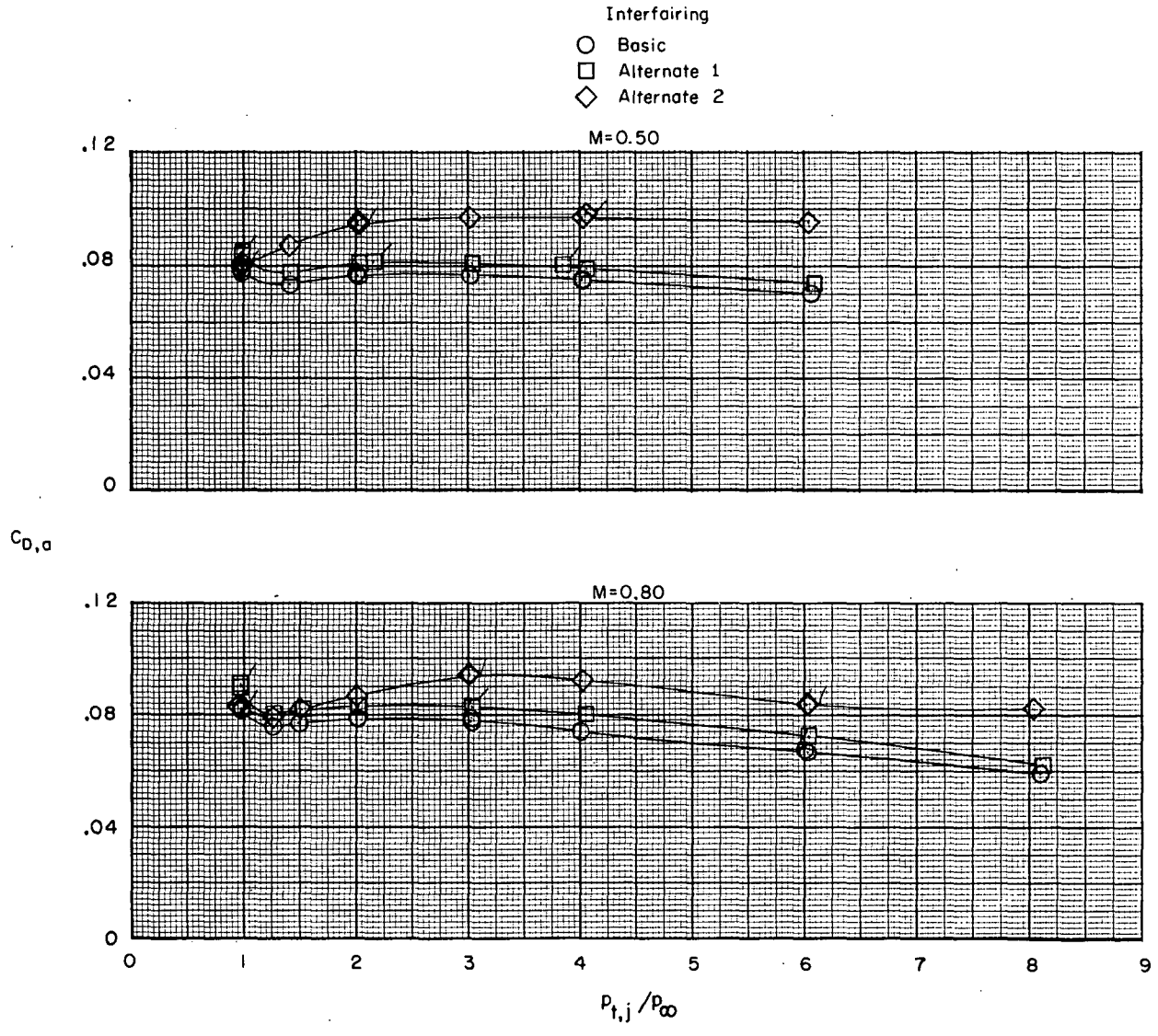

(a) M = 0.50 and 0.80.

Figure 24.- Variation of afterbody drag coefficient with jet total-pressure ratio. Wide-spaced afterbody; dry power; $\beta = 0^o$. Flagged symbols indicate decreasing jet total-pressure ratio.

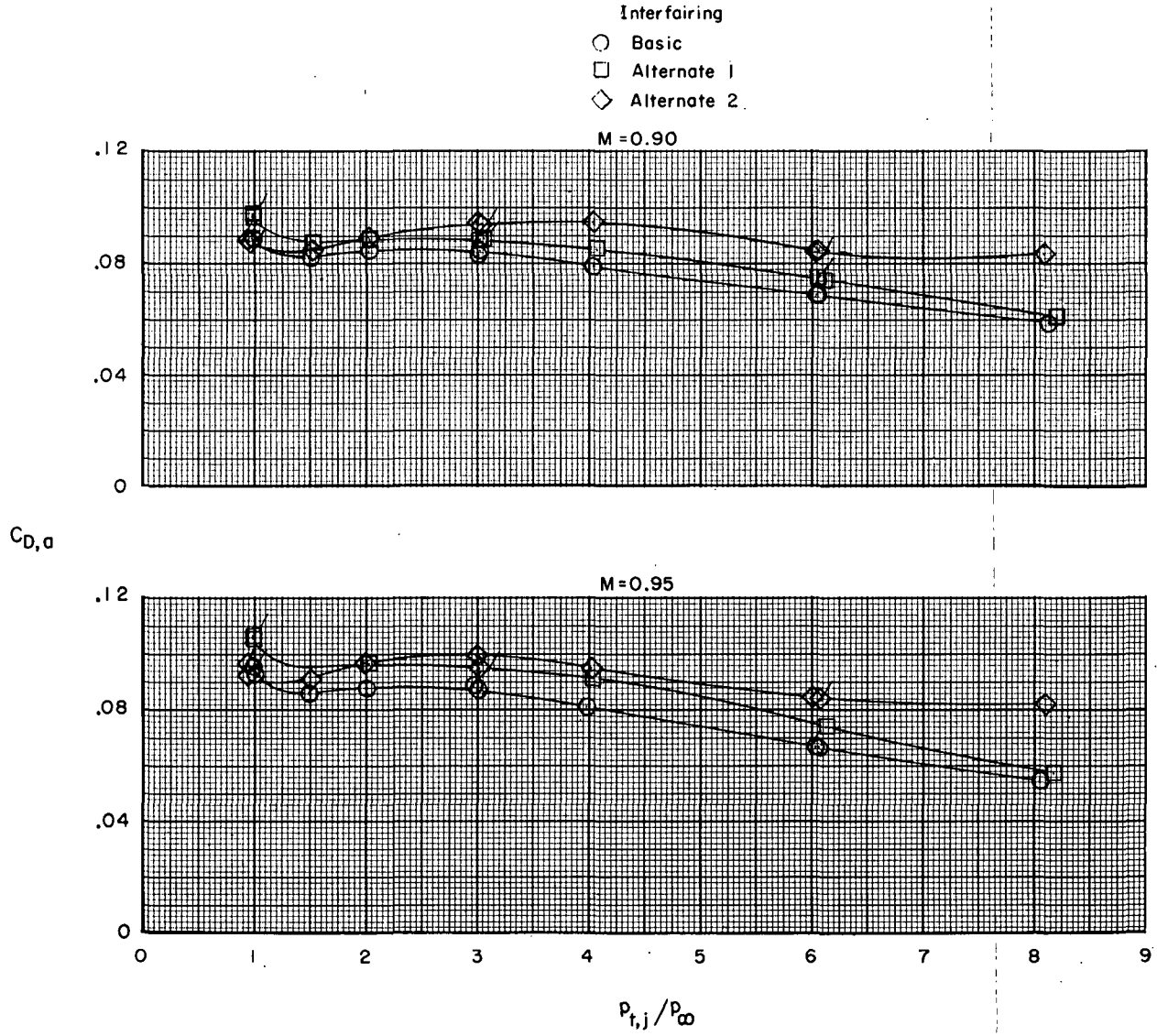

(b) M = 0.90 and 0.95.

Figure 24.- Continued.

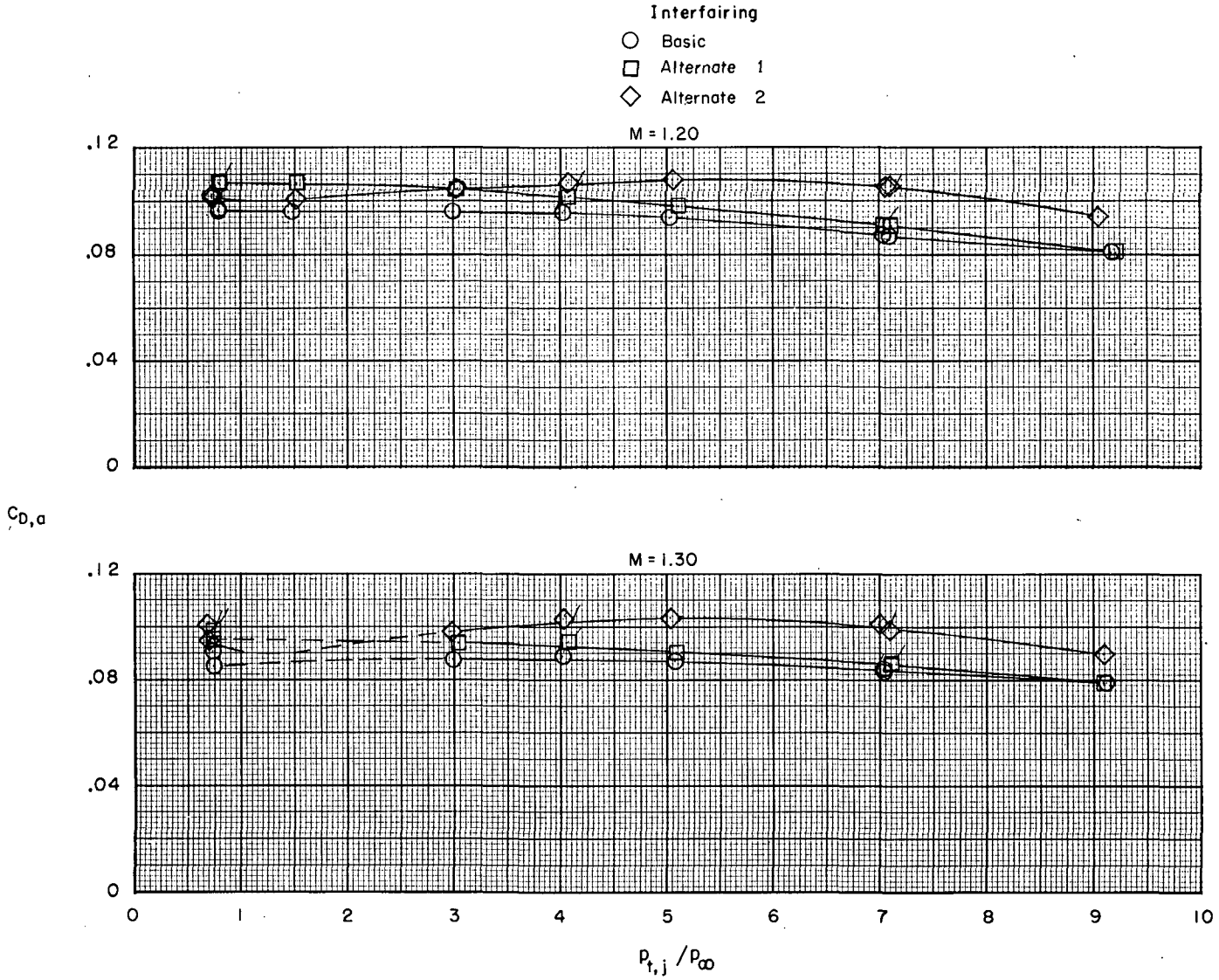

(c) M = 1.20 and 1.30.

Figure 24.- Concluded.

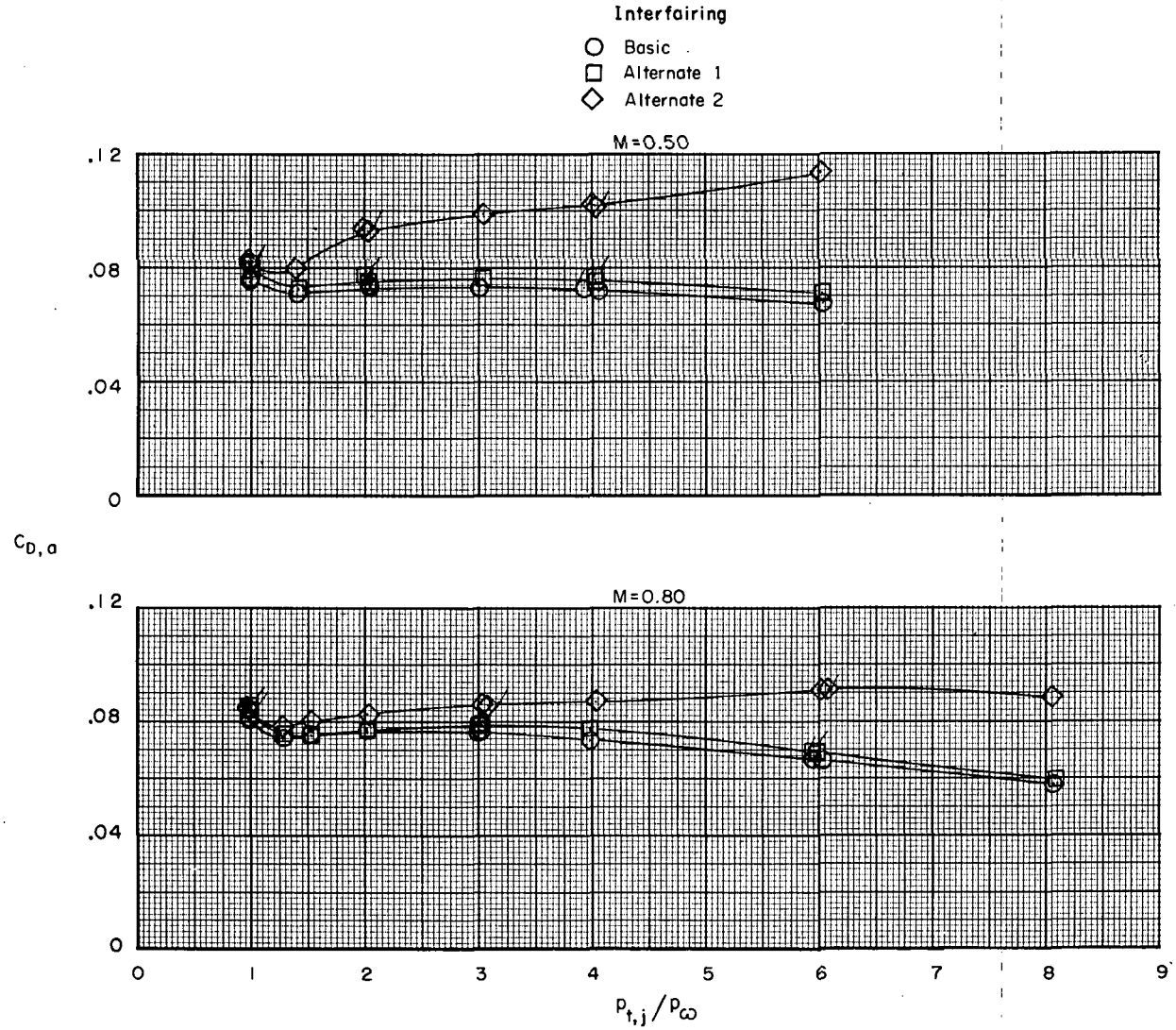

(a) M = 0.50 and 0.80.

Figure 25.- Variation of afterbody drag coefficient with jet total-pressure ratio. Wide-spaced afterbody; dry nozzle; $\beta = 5^{o}$. Flagged symbols indicate decreasing jet total-pressure ratio.

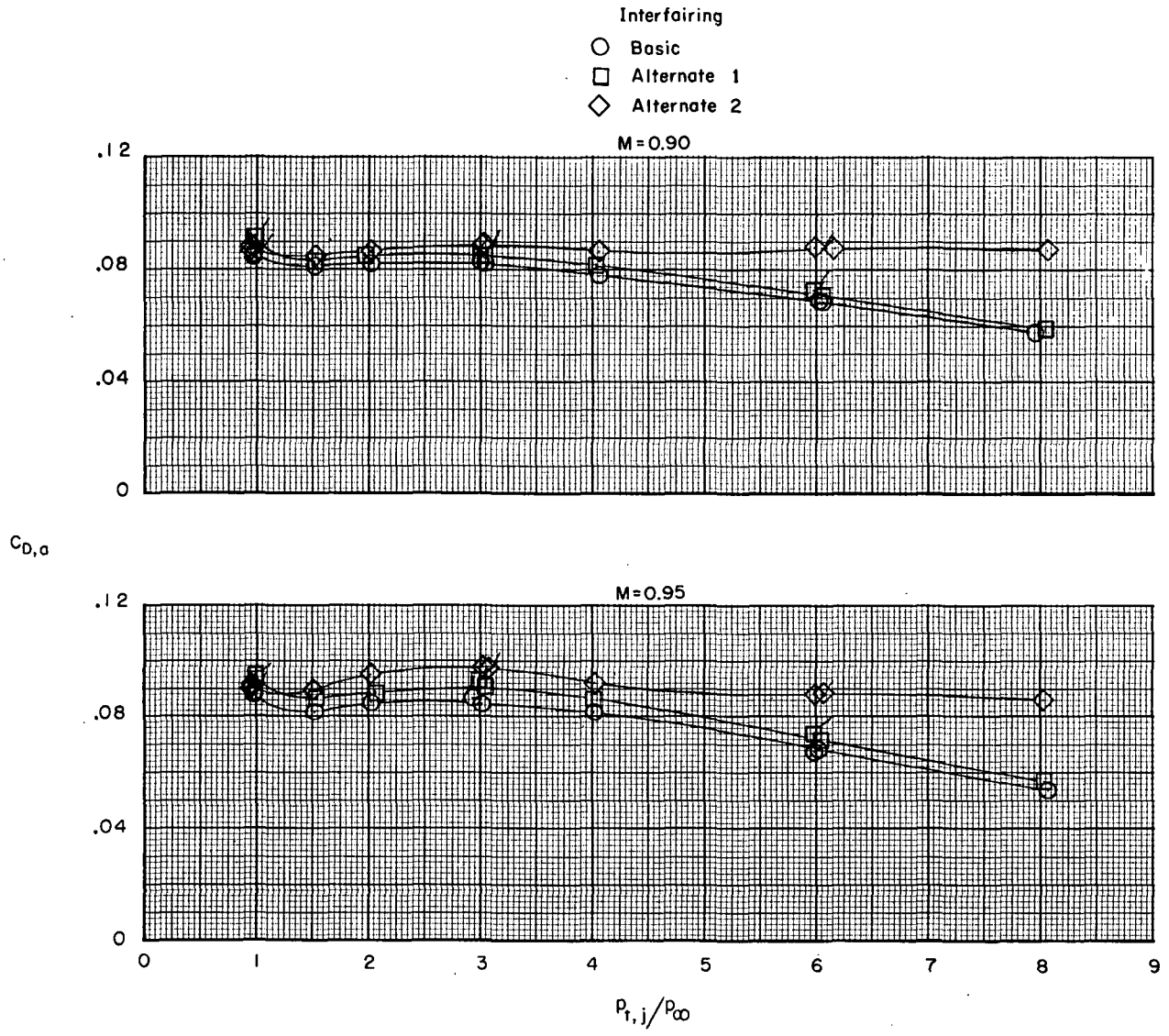

(b) M = 0.90 and 0.95.

Figure 25.- Continued.

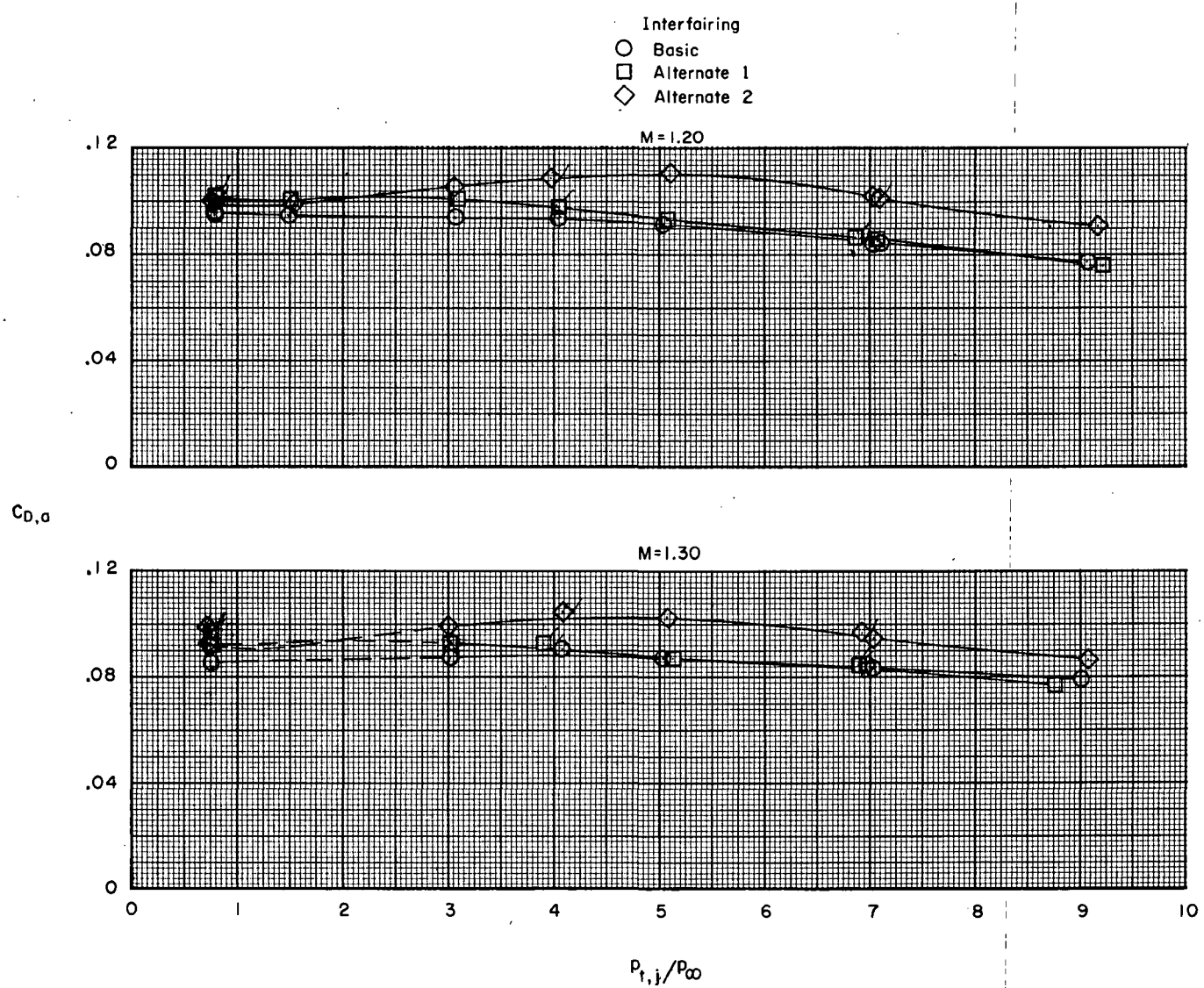

(c) M = 1.20 and 1.30.

Figure 25.- Concluded.

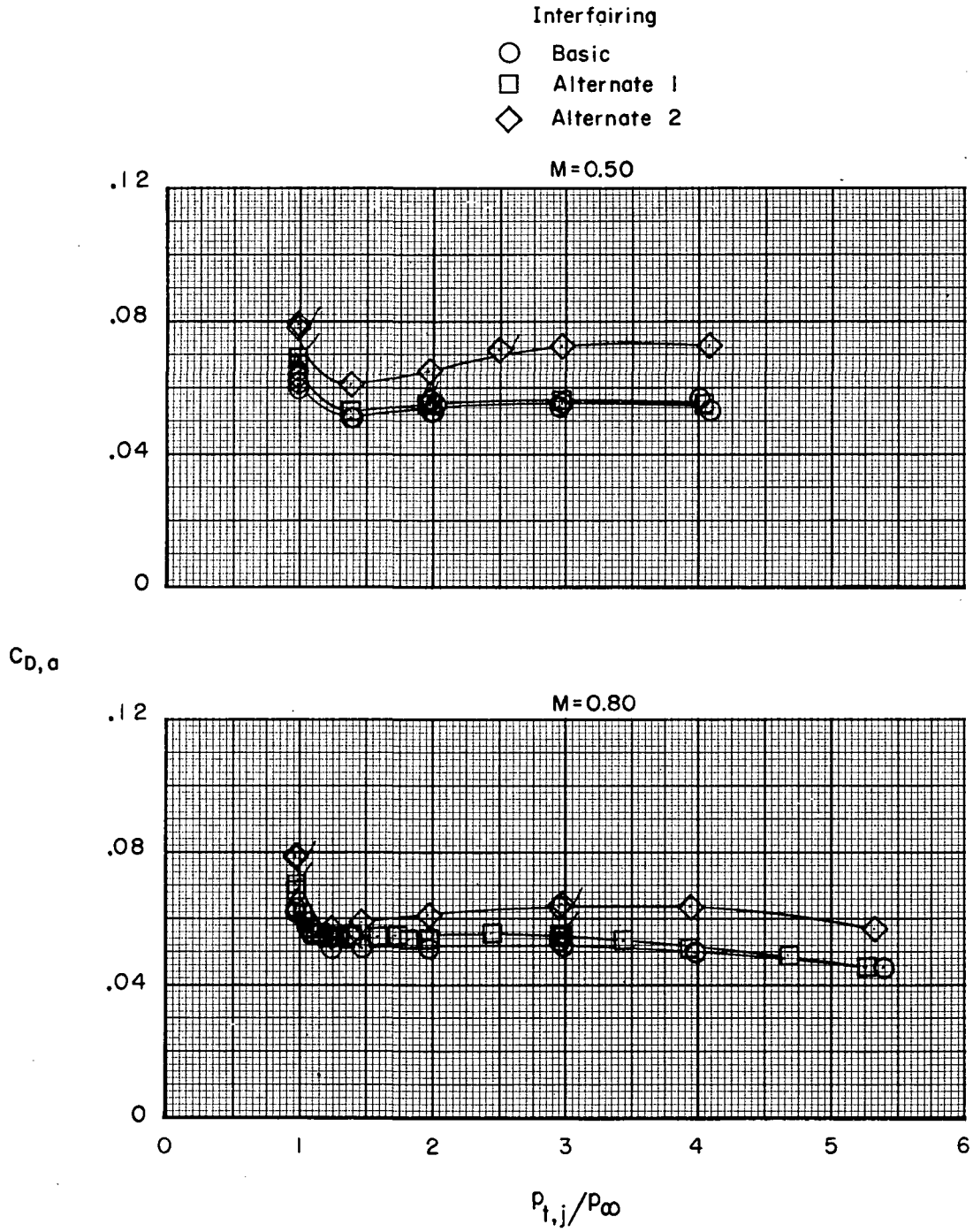

(a) M = 0.50 and 0.80.

Figure 26.- Variation of afterbody drag coefficient with jet total-pressure ratio. Wide-spaced afterbody; max A/B nozzle; $\beta = 0^o$. Flagged symbols indicate decreasing jet total-pressure ratio.

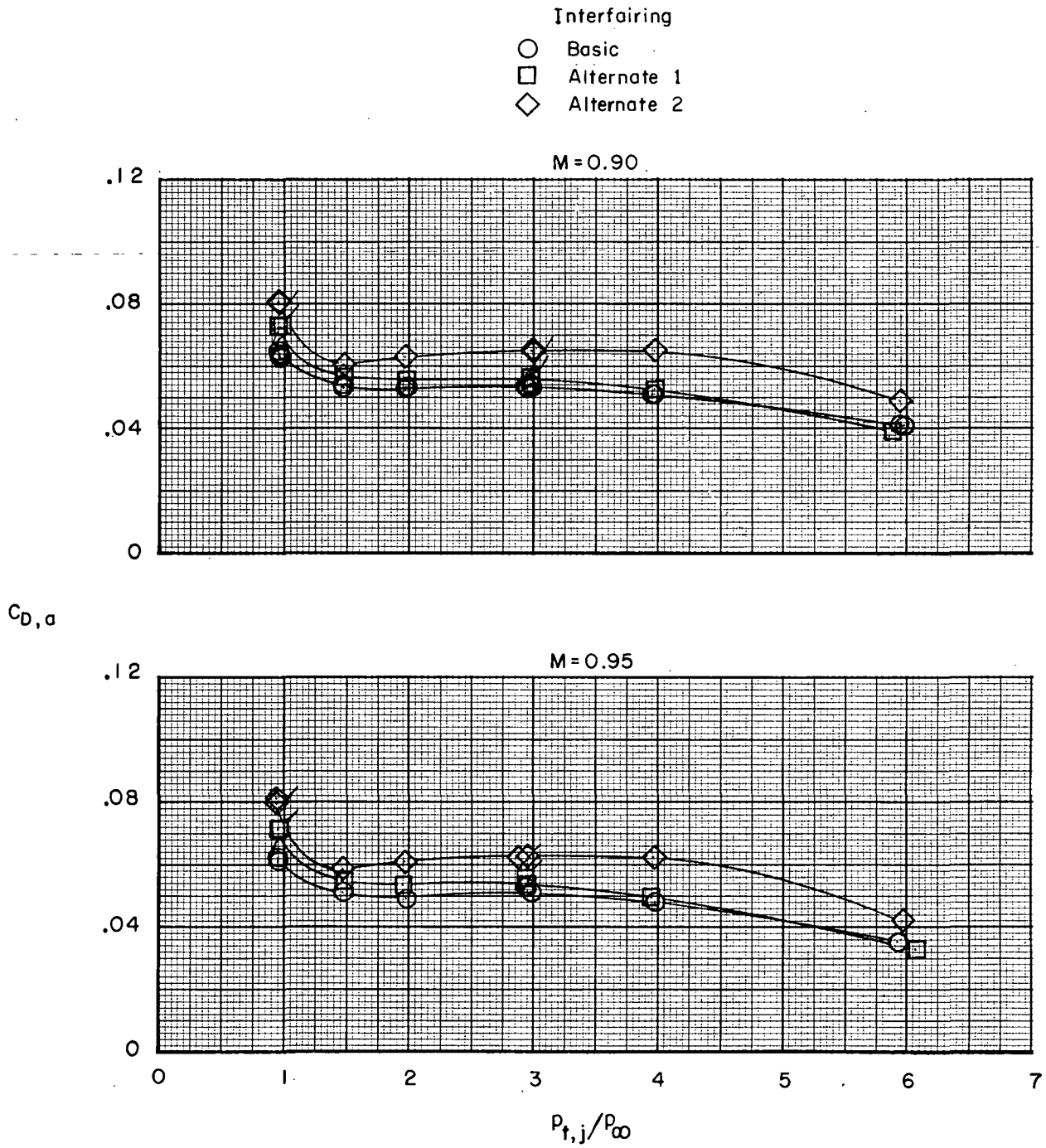

(b) M = 0.90 and 0.95.

Figure 26.- Continued.

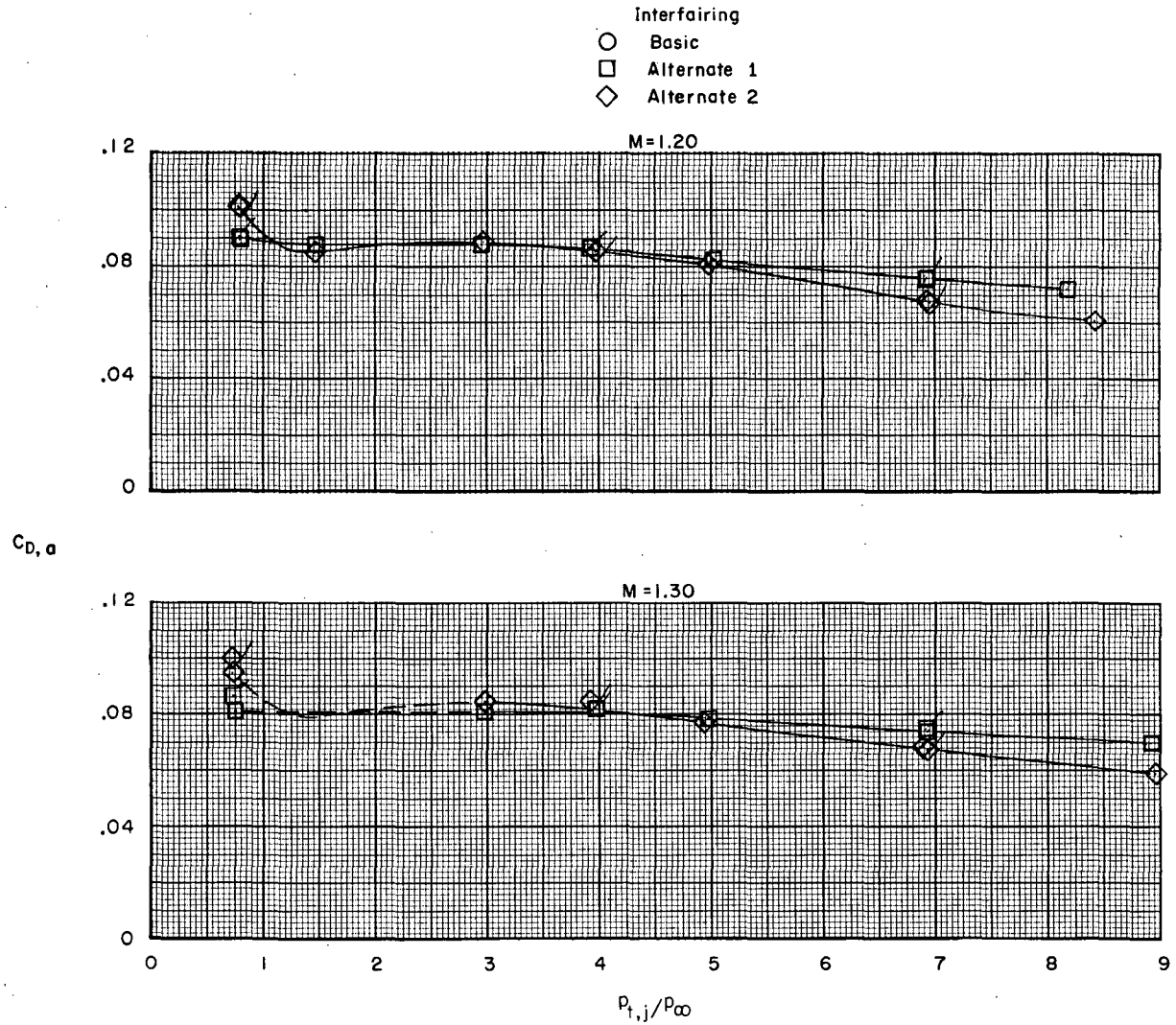

(c) M = 1.20 and 1.30.

Figure 26.- Continued.

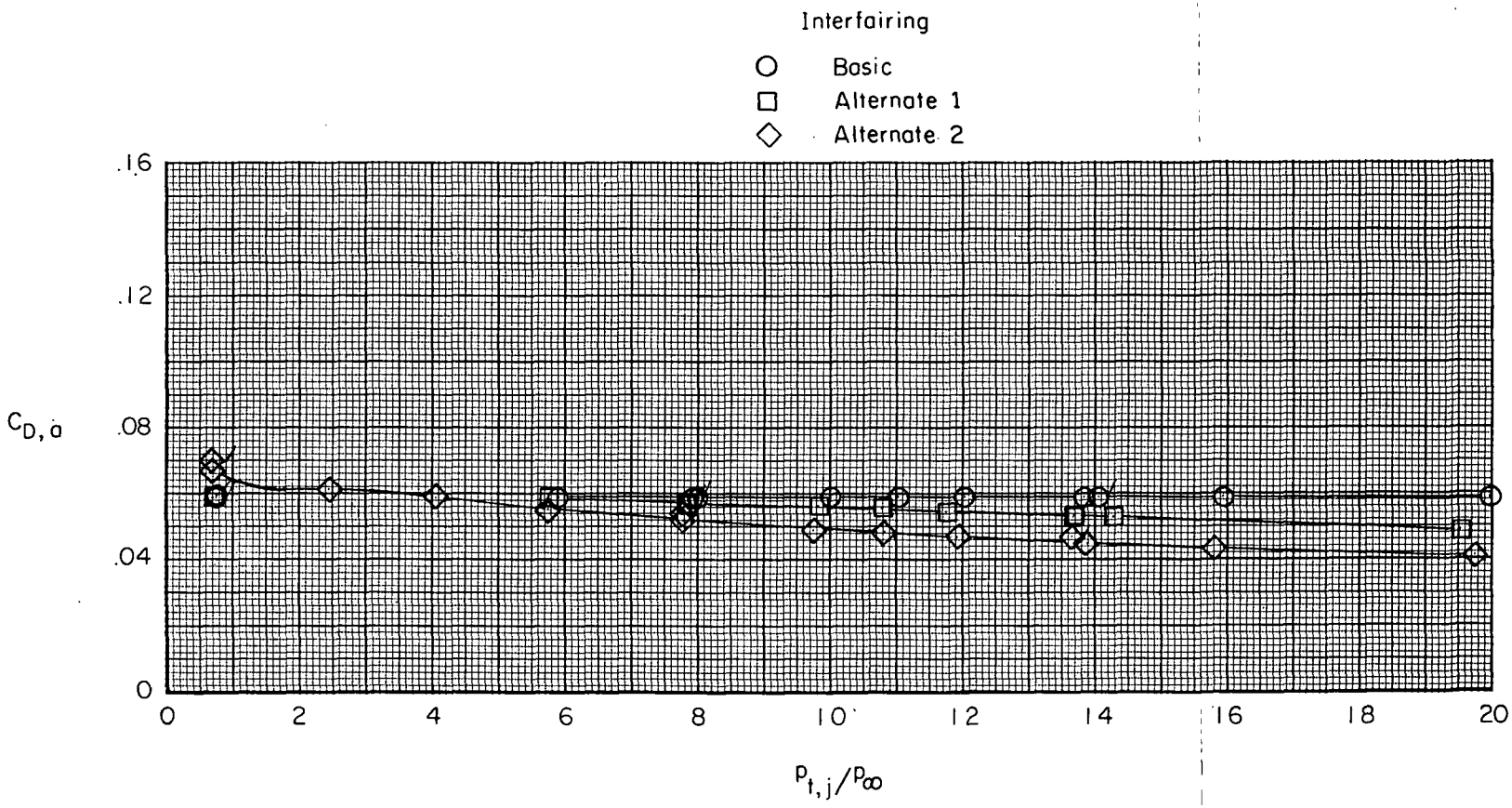

(d) M = 2.20.

Figure 26.- Concluded.

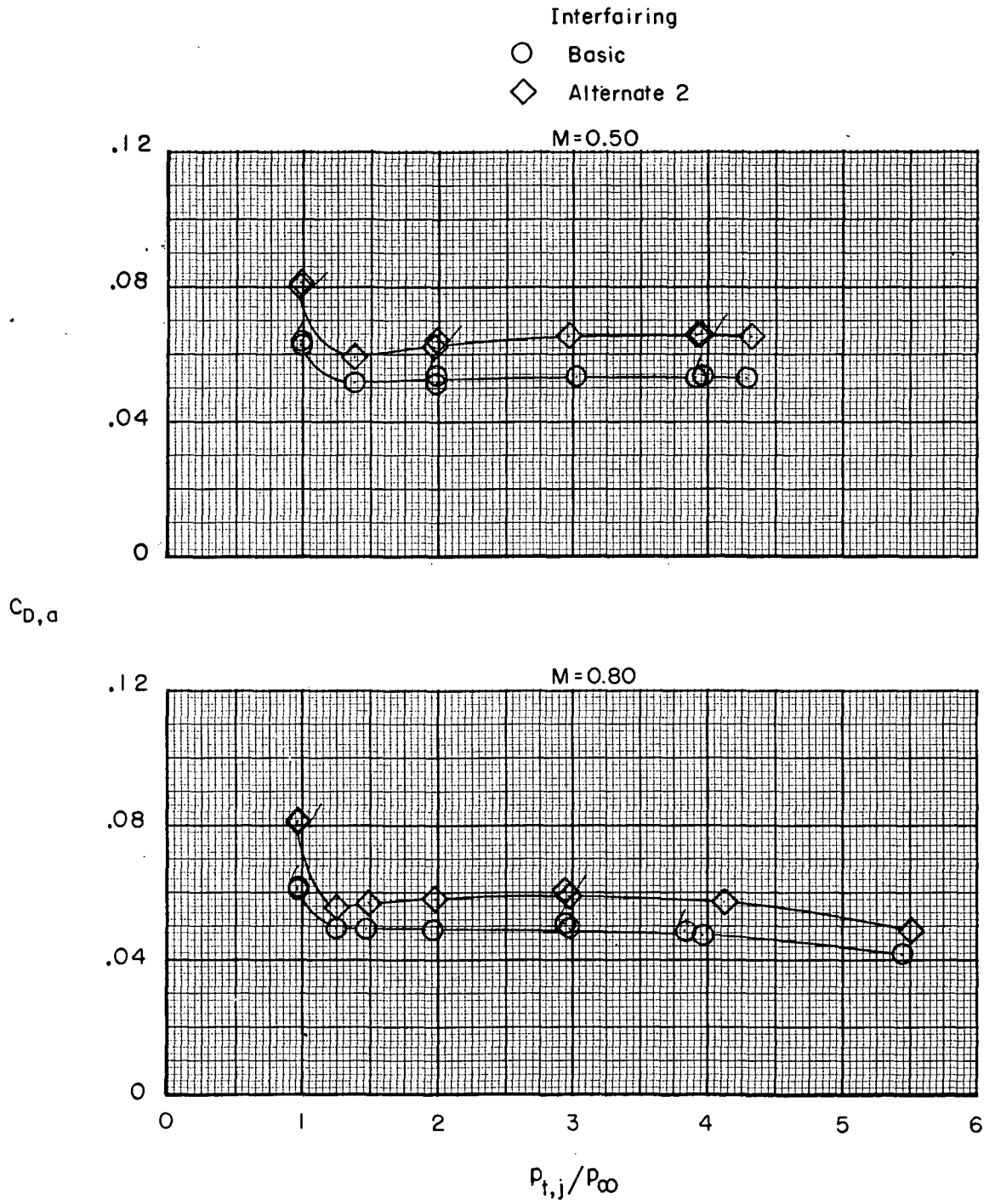

(a) M = 0.50 and 0.80.

Figure 27.- Variation of afterbody drag coefficient with jet total-pressure ratio. Wide-spaced afterbody; max A/B nozzles; $\beta = 5^o$. Flagged symbols indicate decreasing jet total-pressure ratio.

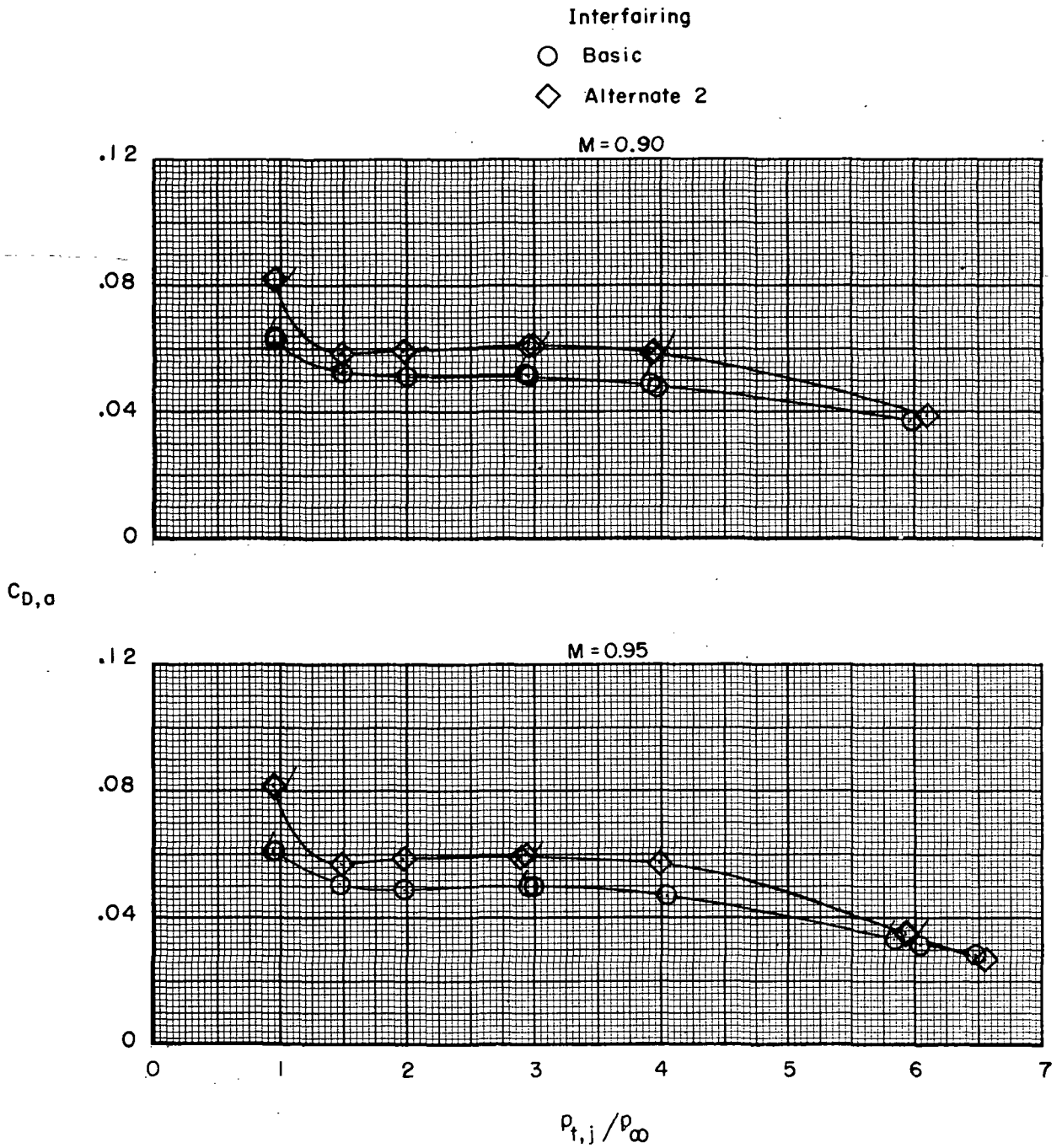

(b) M = 0.90 and 0.95.

Figure 27.- Continued.

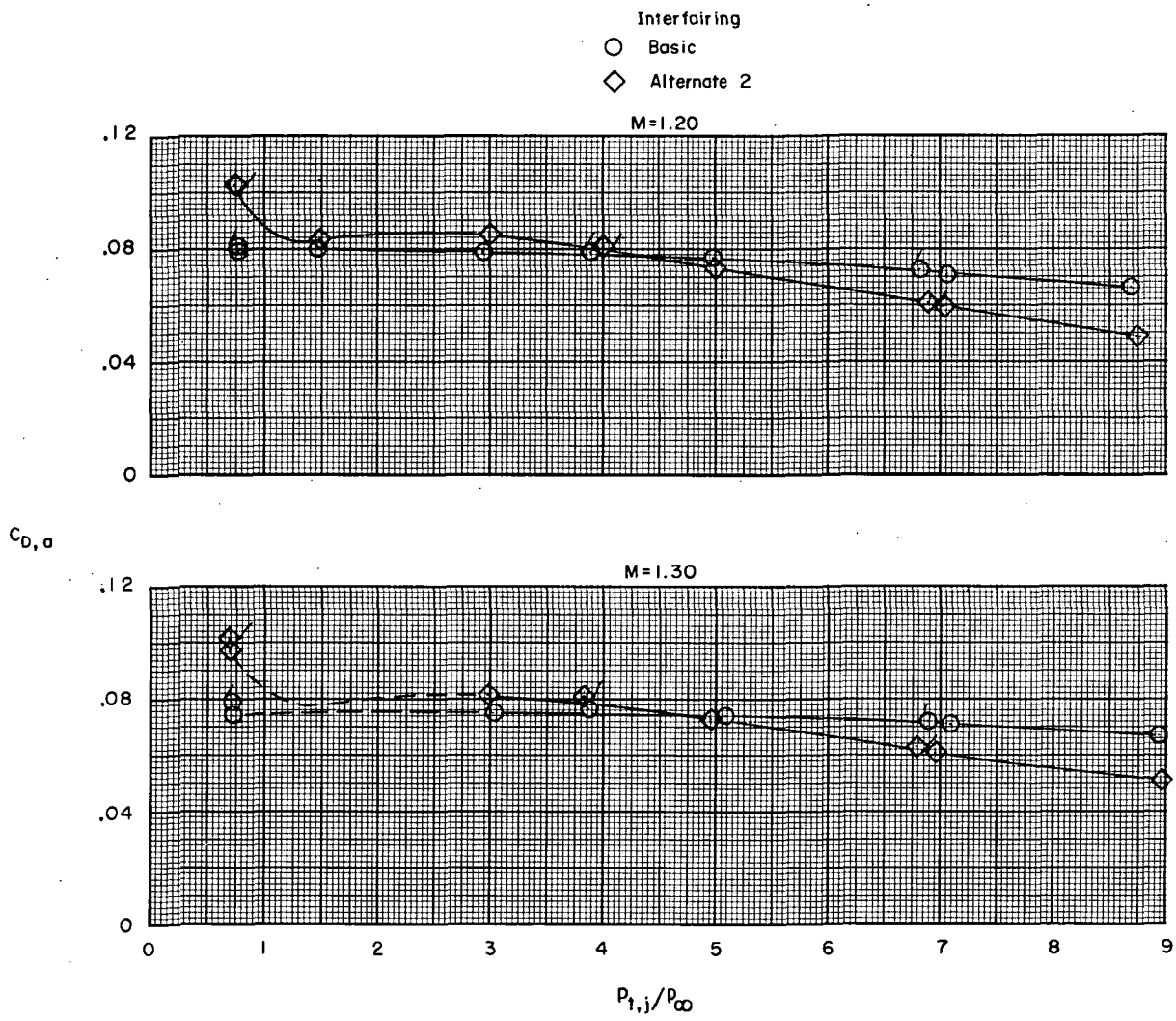

(c) M = 1.20 and 1.30.

Figure 27.- Concluded.

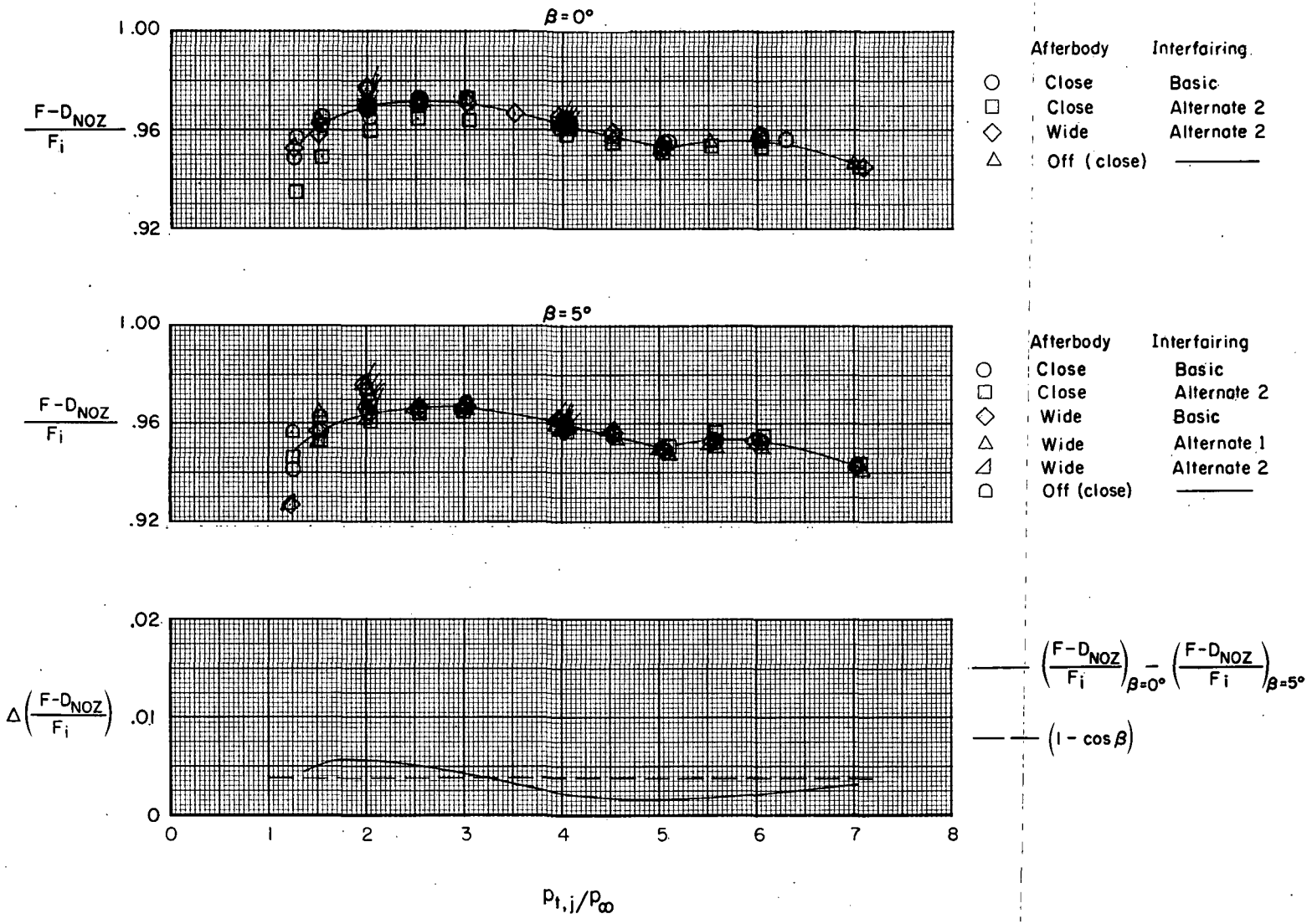

(a) Dry power nozzles.

Figure 28.- Variation of thrust-minus-nozzle-drag ratio at M = 0. Effect of nozzle cant angle. Flagged symbols indicate decreasing jet total-pressure ratio.

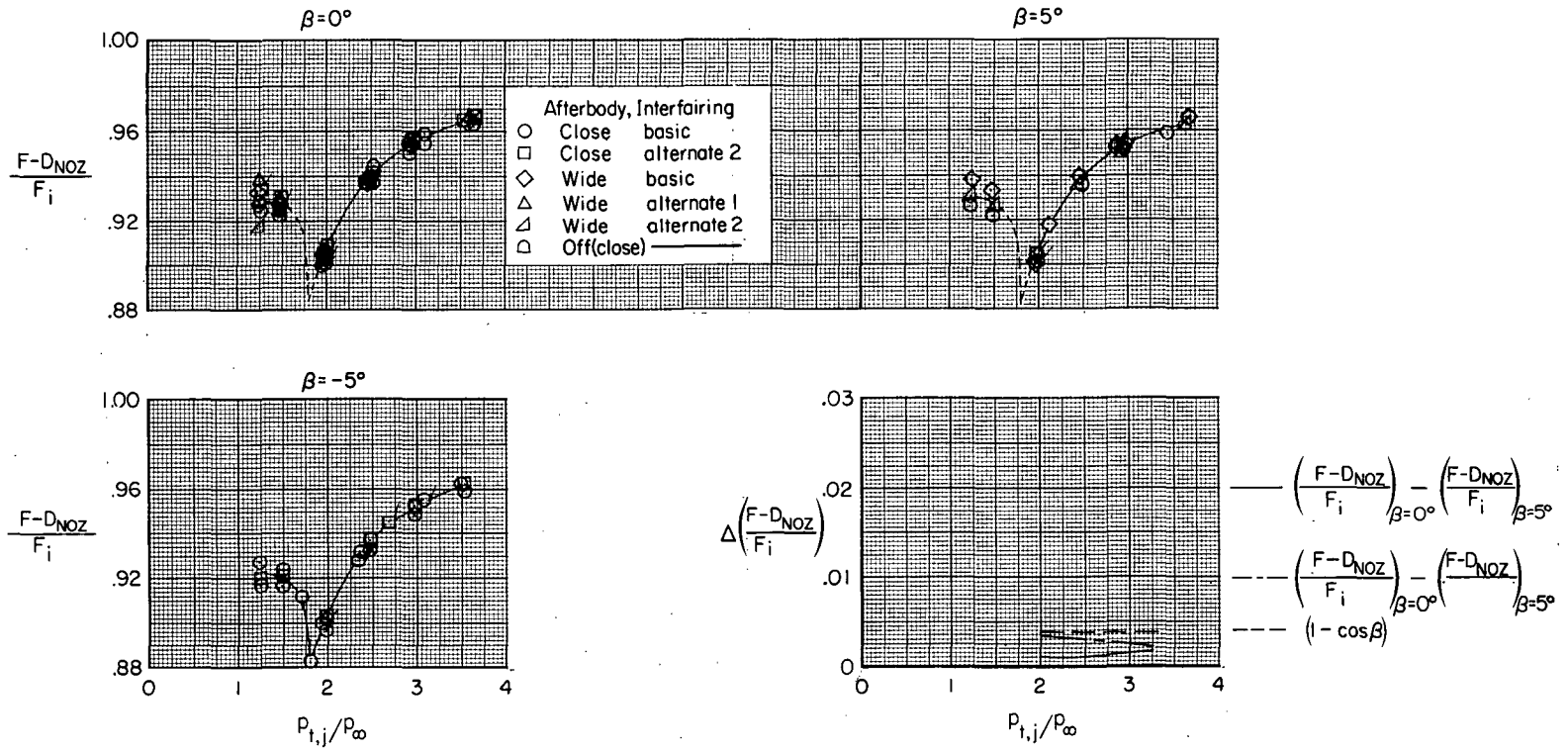

(b) Max A/B power nozzles.

Figure 28.- Concluded.

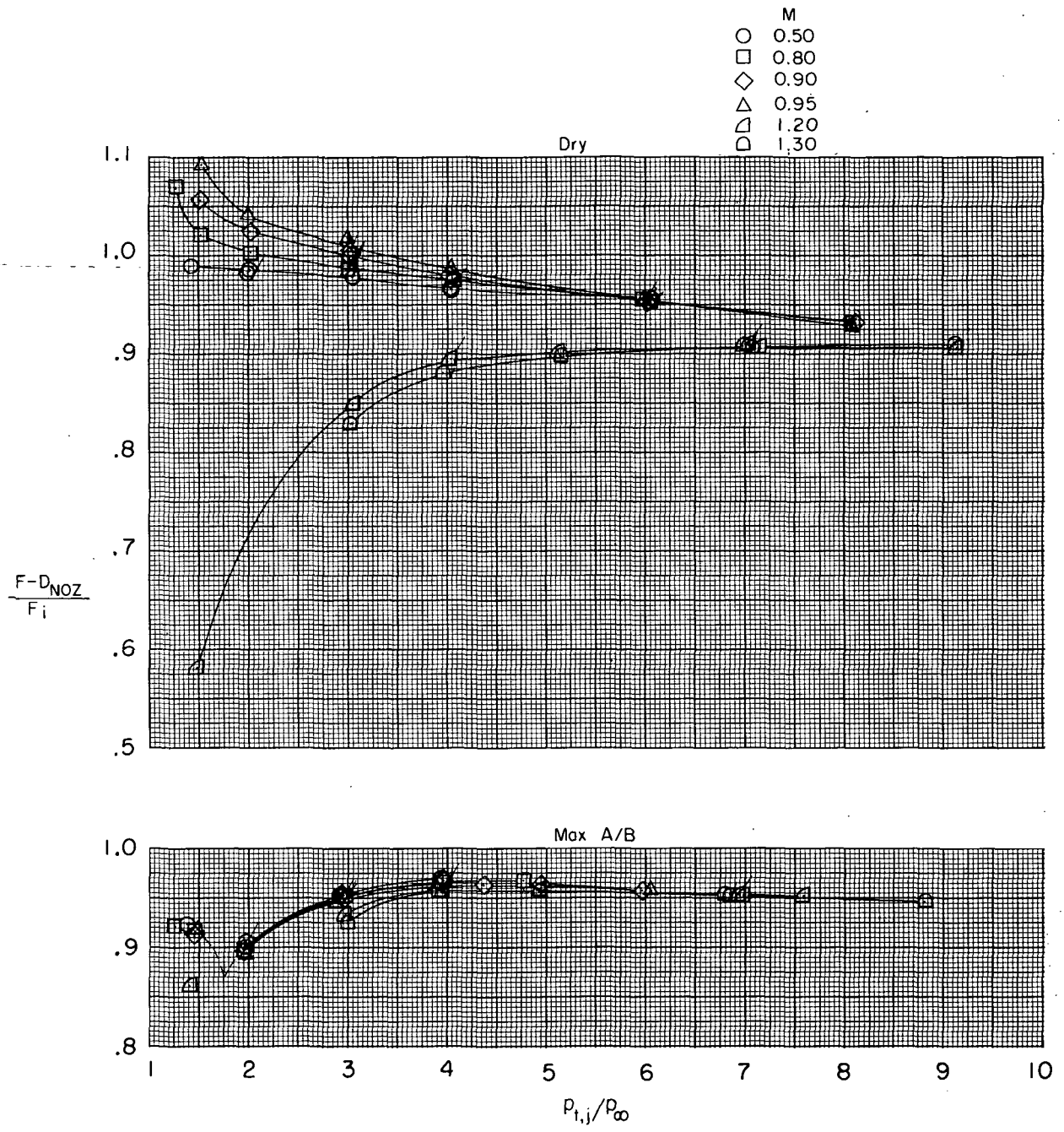

(a) Close-spaced afterbody; basic interfairing; $\beta = 0^o$.

Figure 29.- Variation of thrust-minus-nozzle-drag ratio with jet total-pressure ratio for two nozzle power settings. Flagged symbols indicate decreasing jet total-pressure ratio.

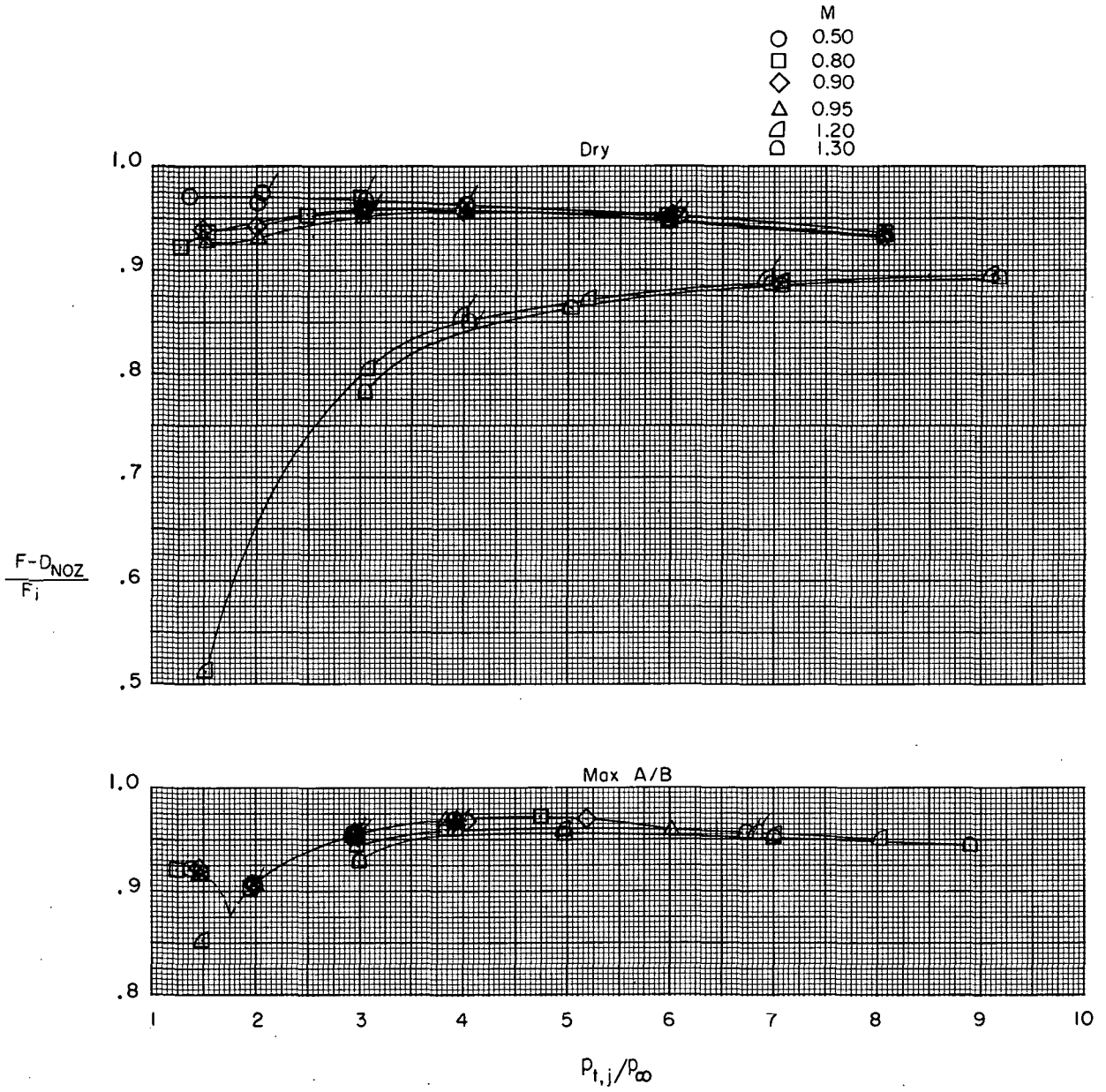

(b) Close-spaced afterbody; alternate 2 interfairing; $\beta = 0^{o}$.

Figure 29.- Continued.

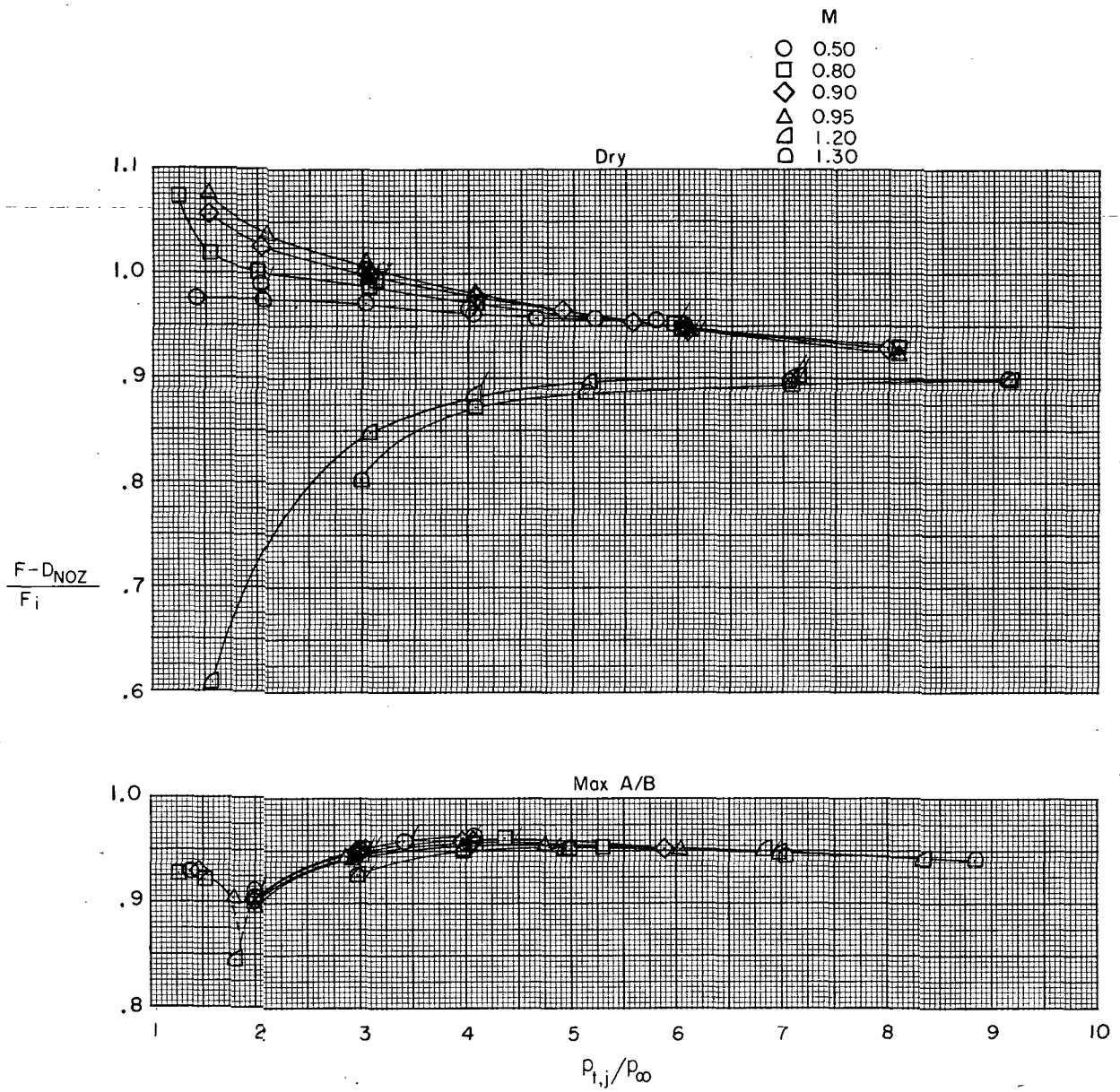

(c) Close-spaced afterbody; basic interfairing; $\beta = 5^o$.

Figure 29.- Continued.

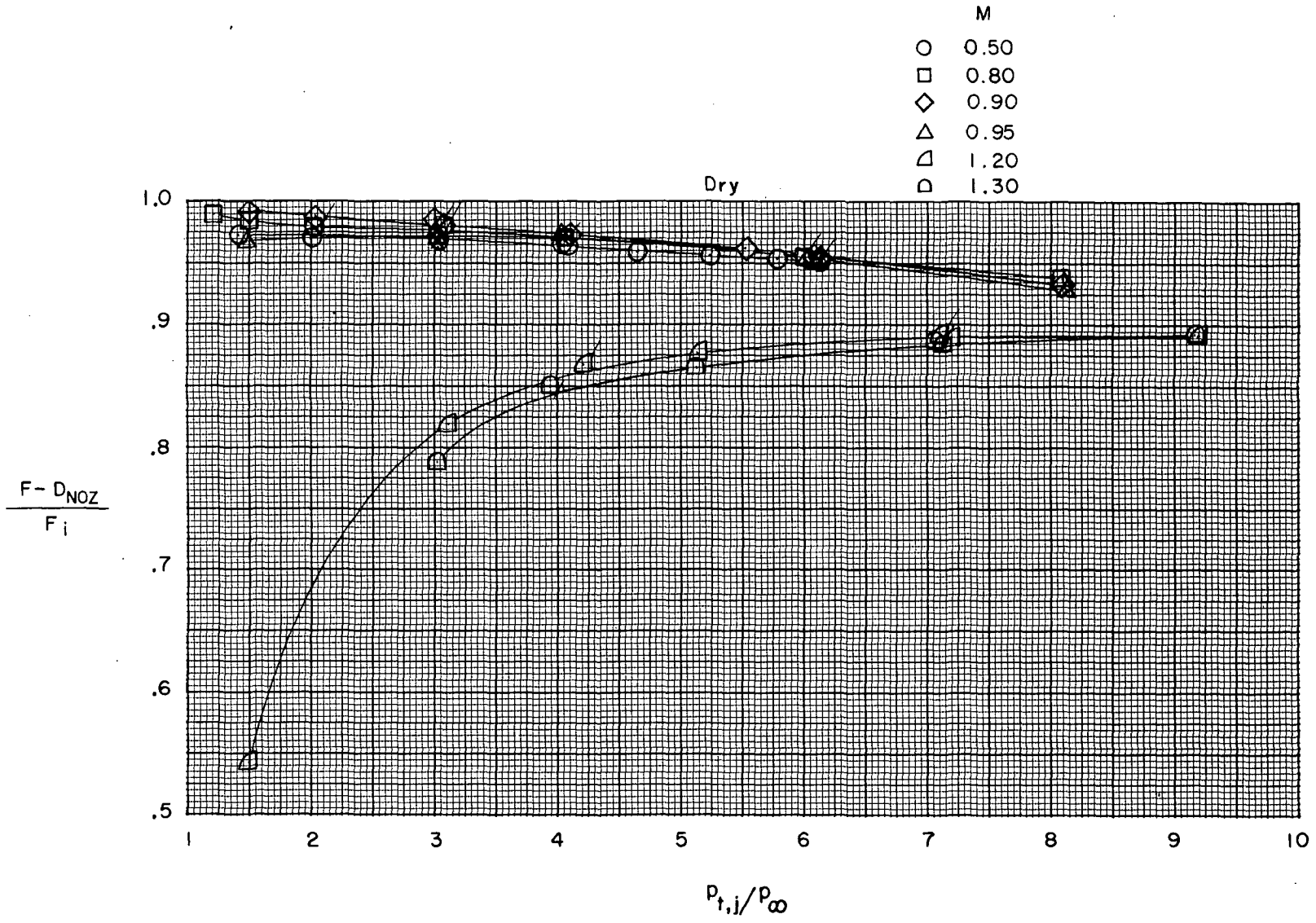

(d) Close-spaced afterbody; alternate 2 interfairing; $\beta = 5^o$.

Figure 29.- Continued.

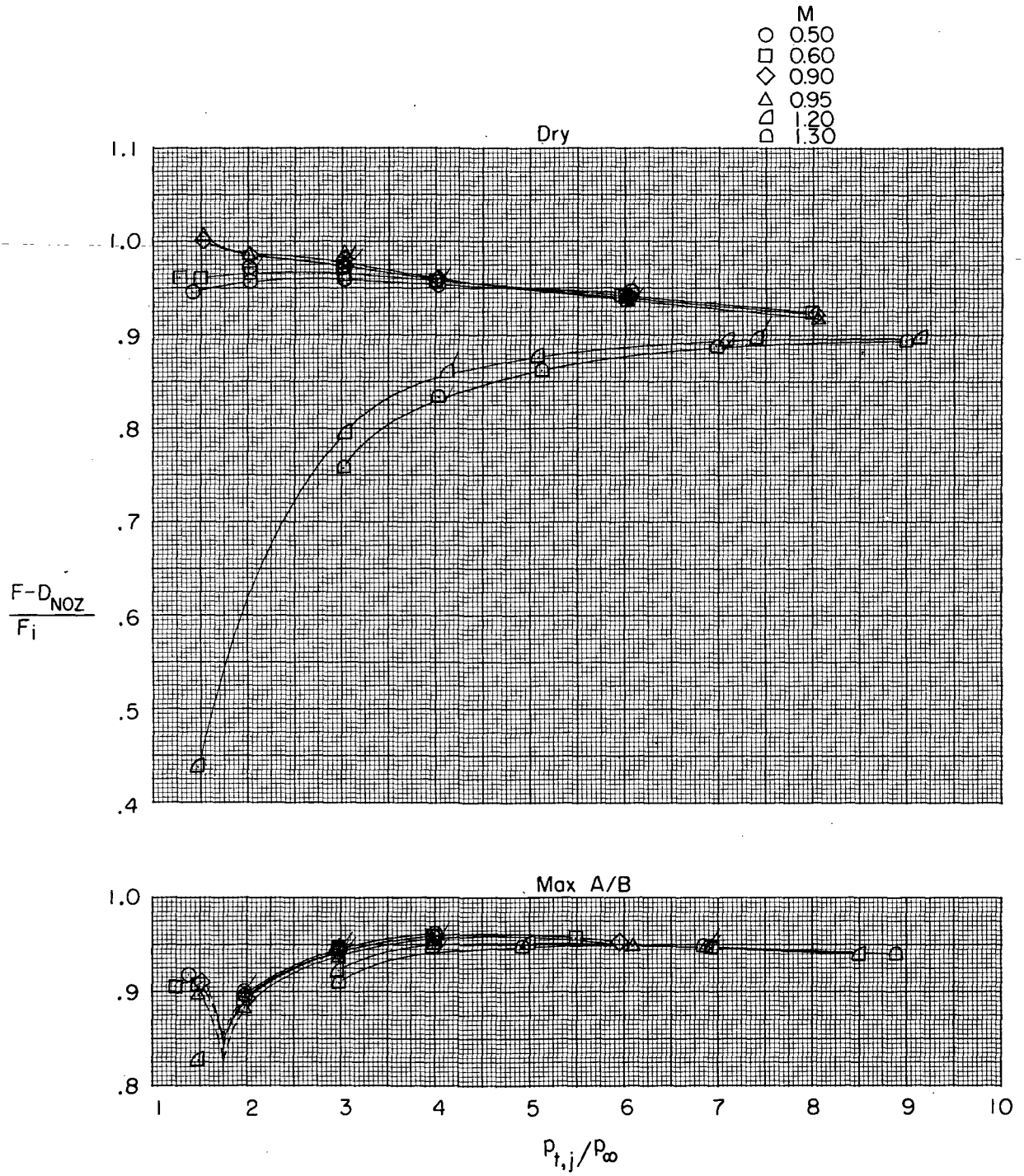

(e) Close-spaced afterbody; basic interfairing; $\beta = -5^o$.

Figure 29.- Continued.

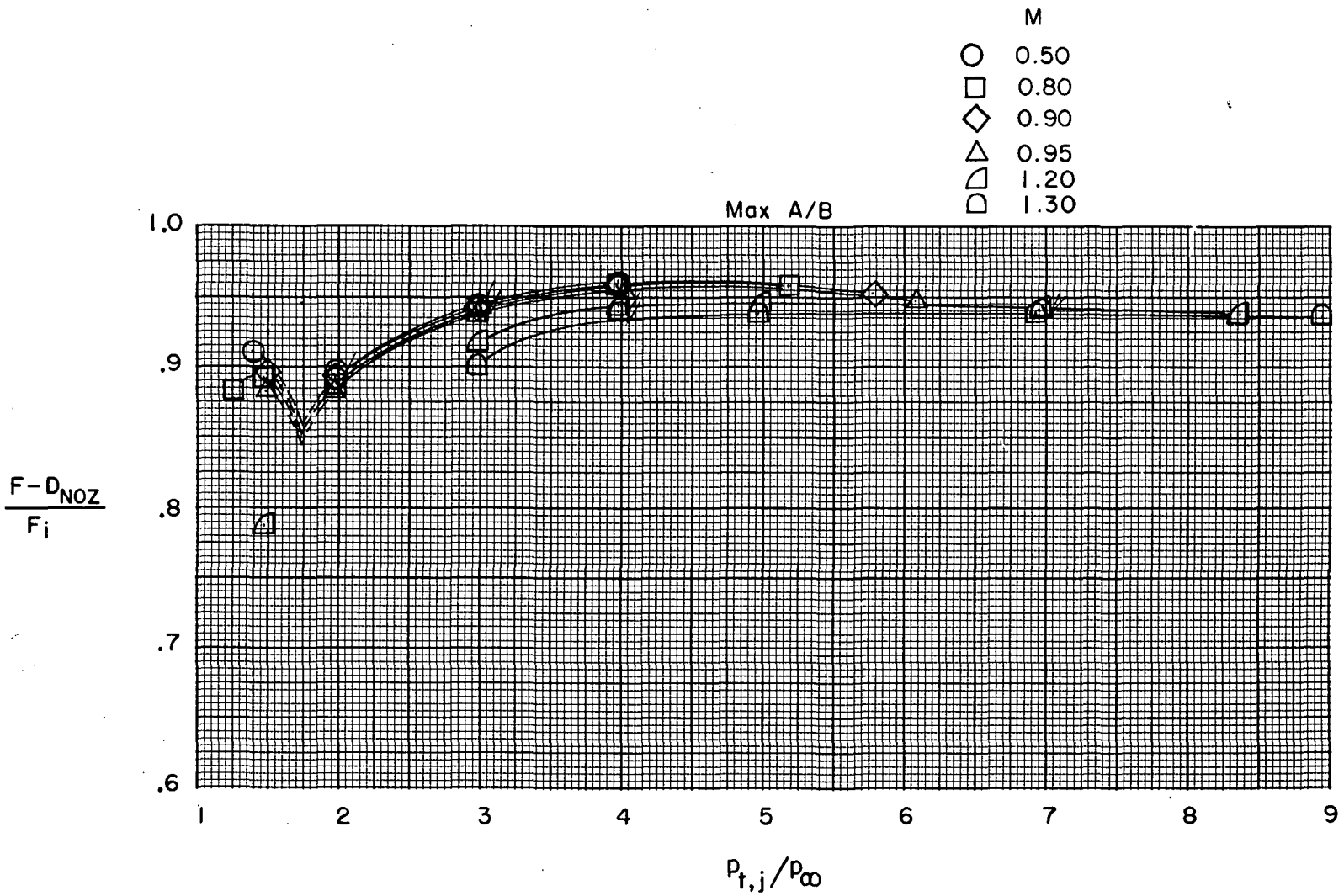

(f) Close-spaced afterbody; alternate 2 interfairing; $\beta = -5^o$.

Figure 29.- Continued.

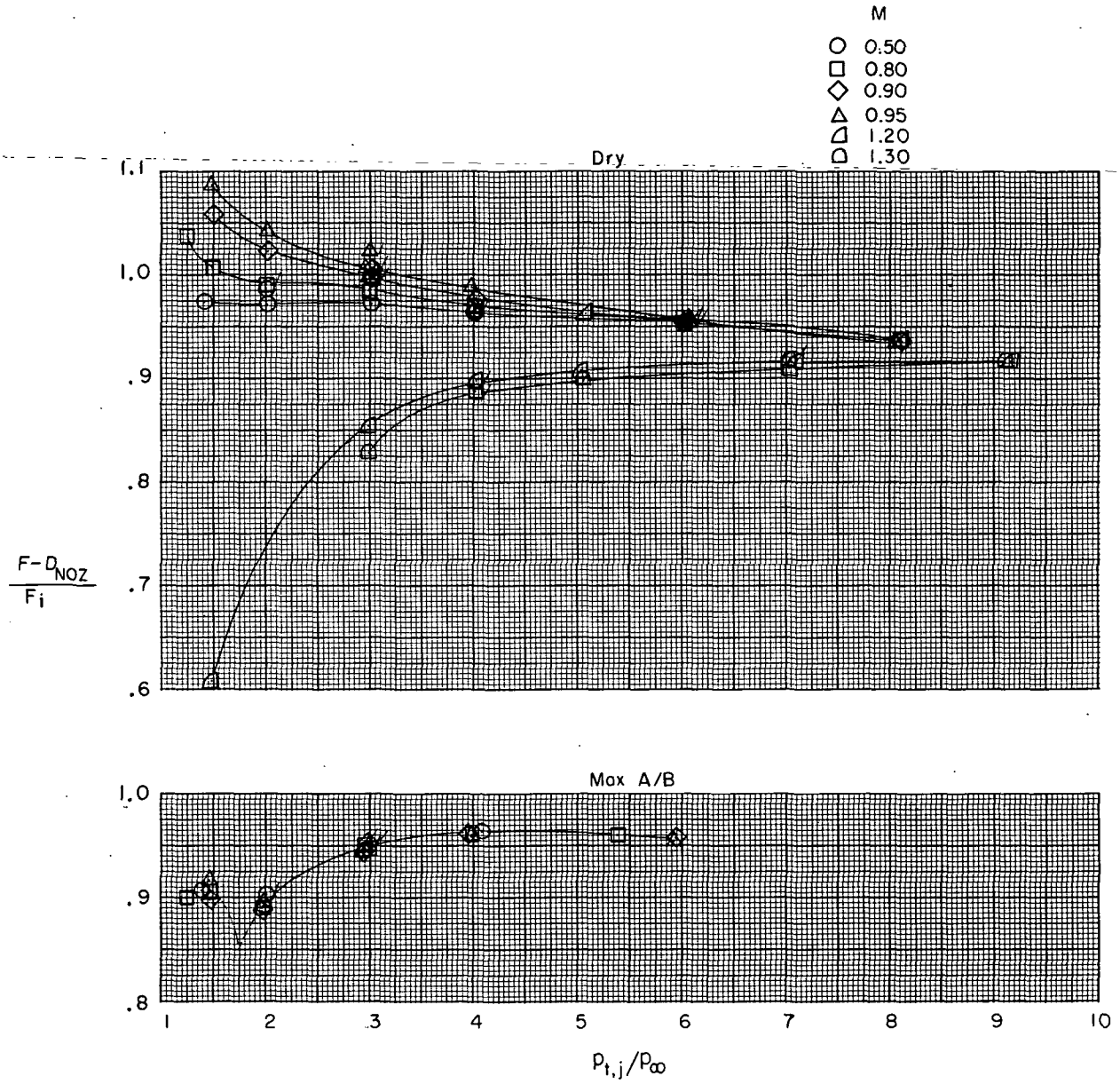

(g) Wide-spaced afterbody; basic interfairing; $\beta = 0^o$.

Figure 29.- Continued.

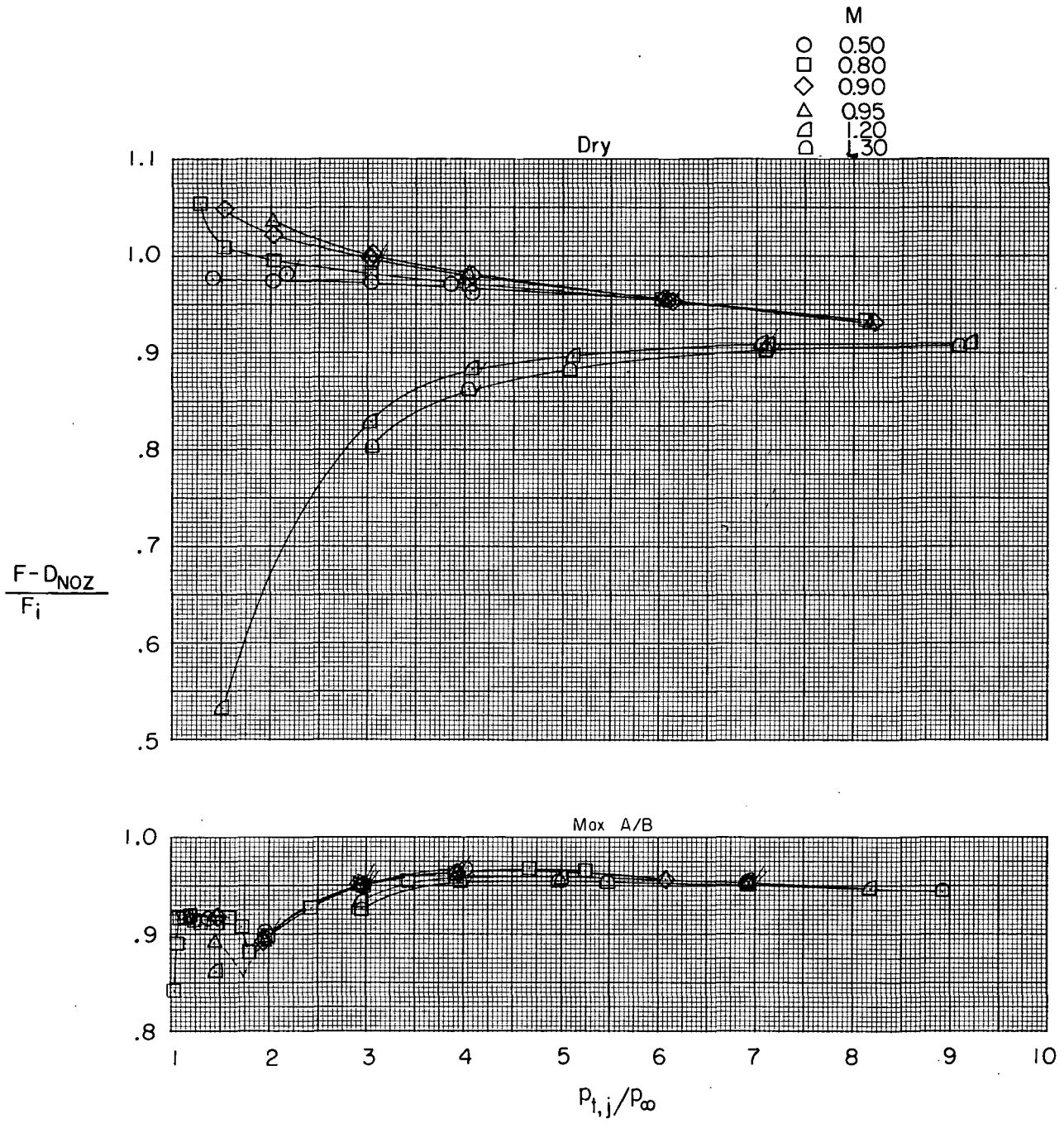

(h) Wide-spaced afterbody; alternate 1 interfairing; $\beta = 0^{o}$.

Figure 29.- Continued.

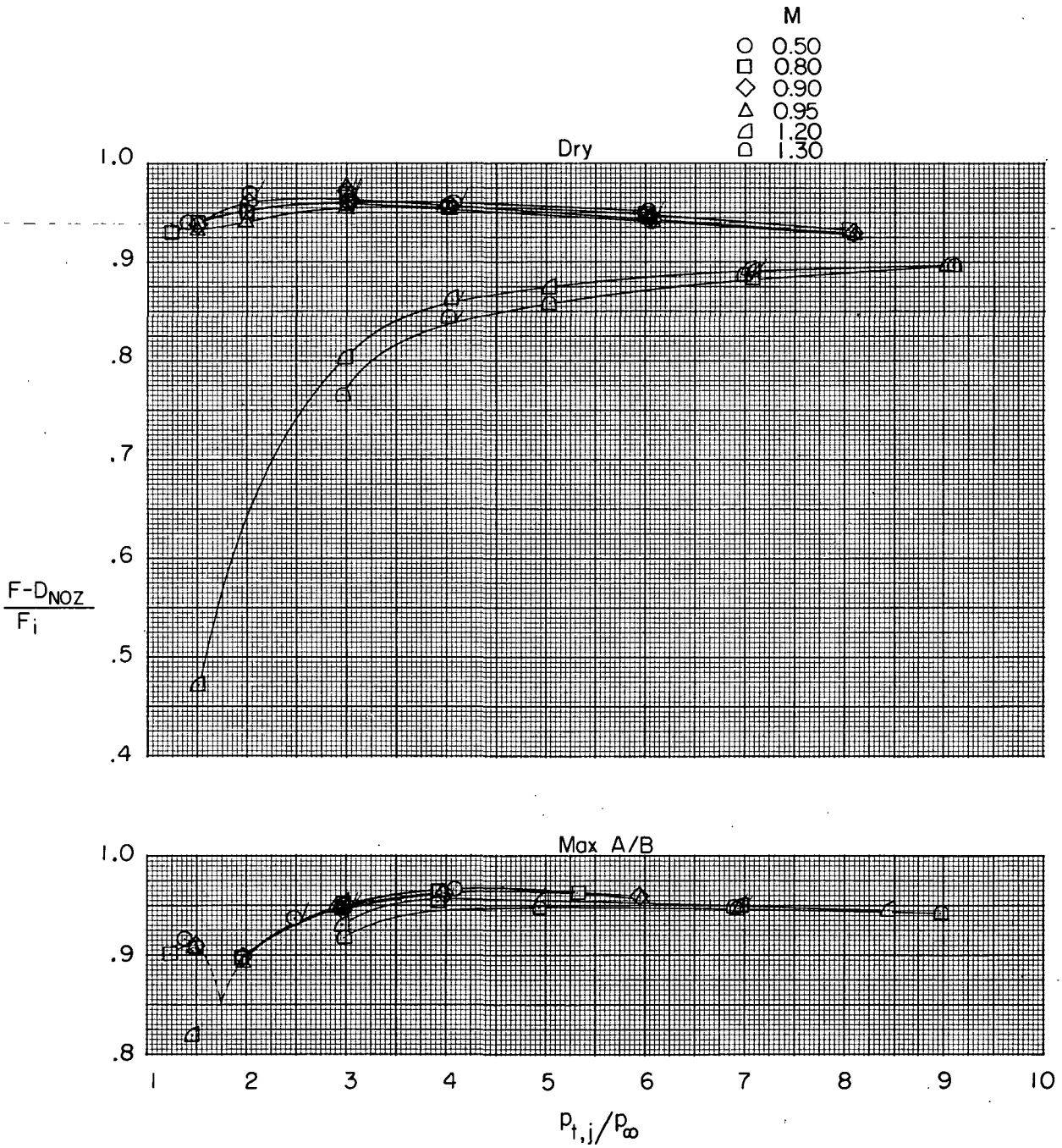

(i) Wide-spaced afterbody; alternate 2 interfairing; $\beta = 0^{o}$.

Figure 29.- Continued.

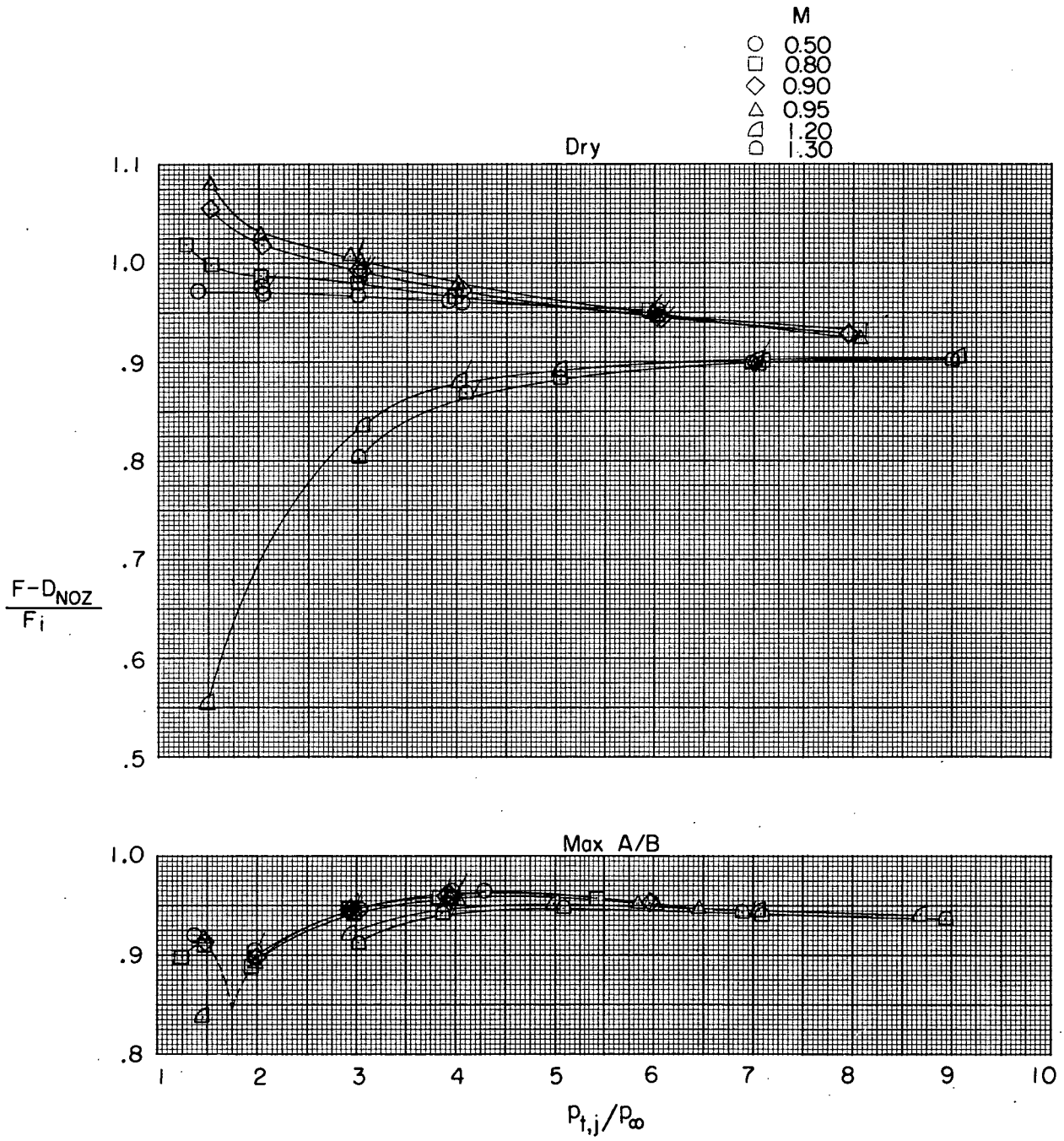

(j) Wide-spaced afterbody; basic interfairing; $\beta = 5^o$.

Figure 29.- Continued.

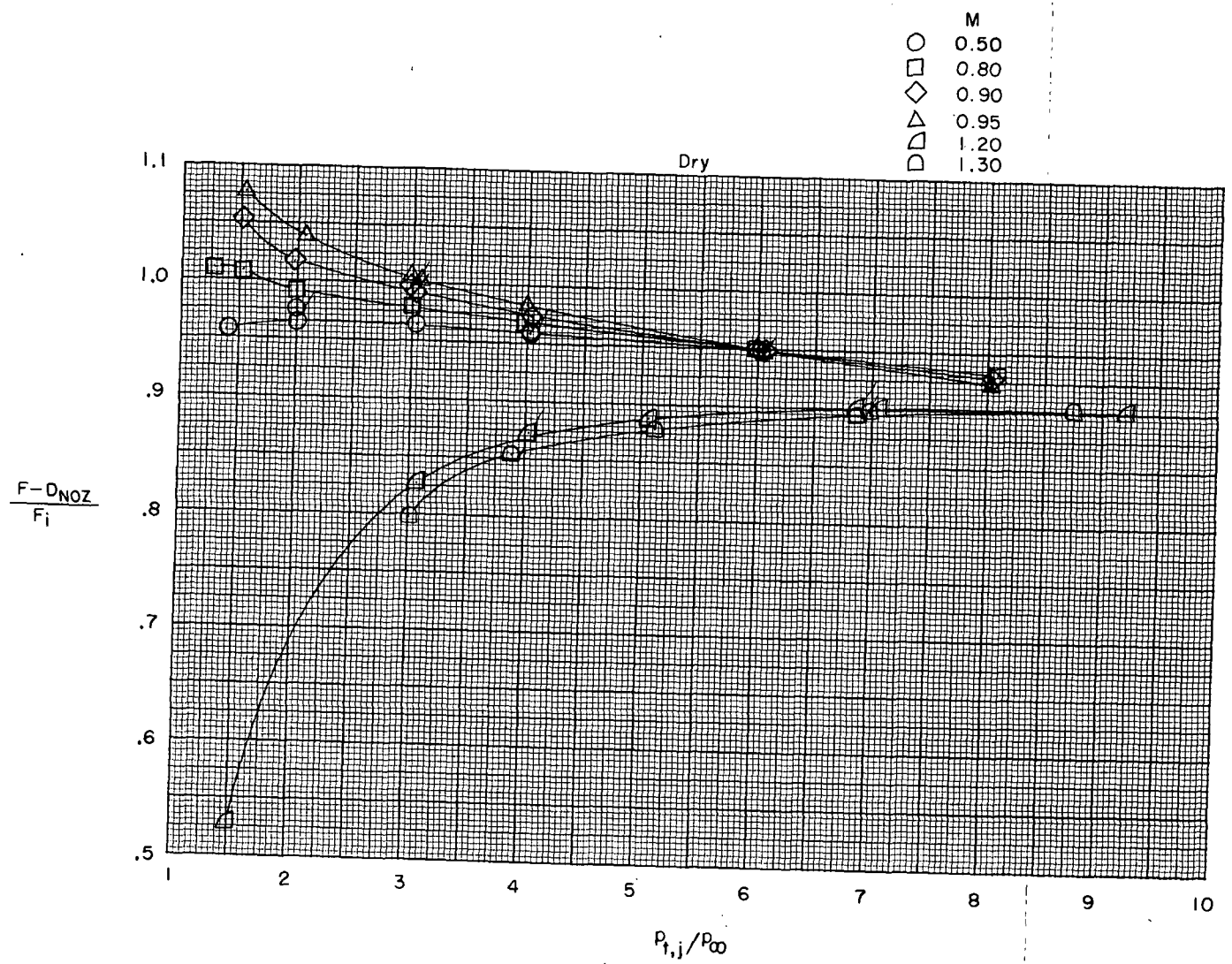

(k) Wide-spaced afterbody; alternate 1 interfairing; $\beta = 5^o$.

Figure 29.- Continued.

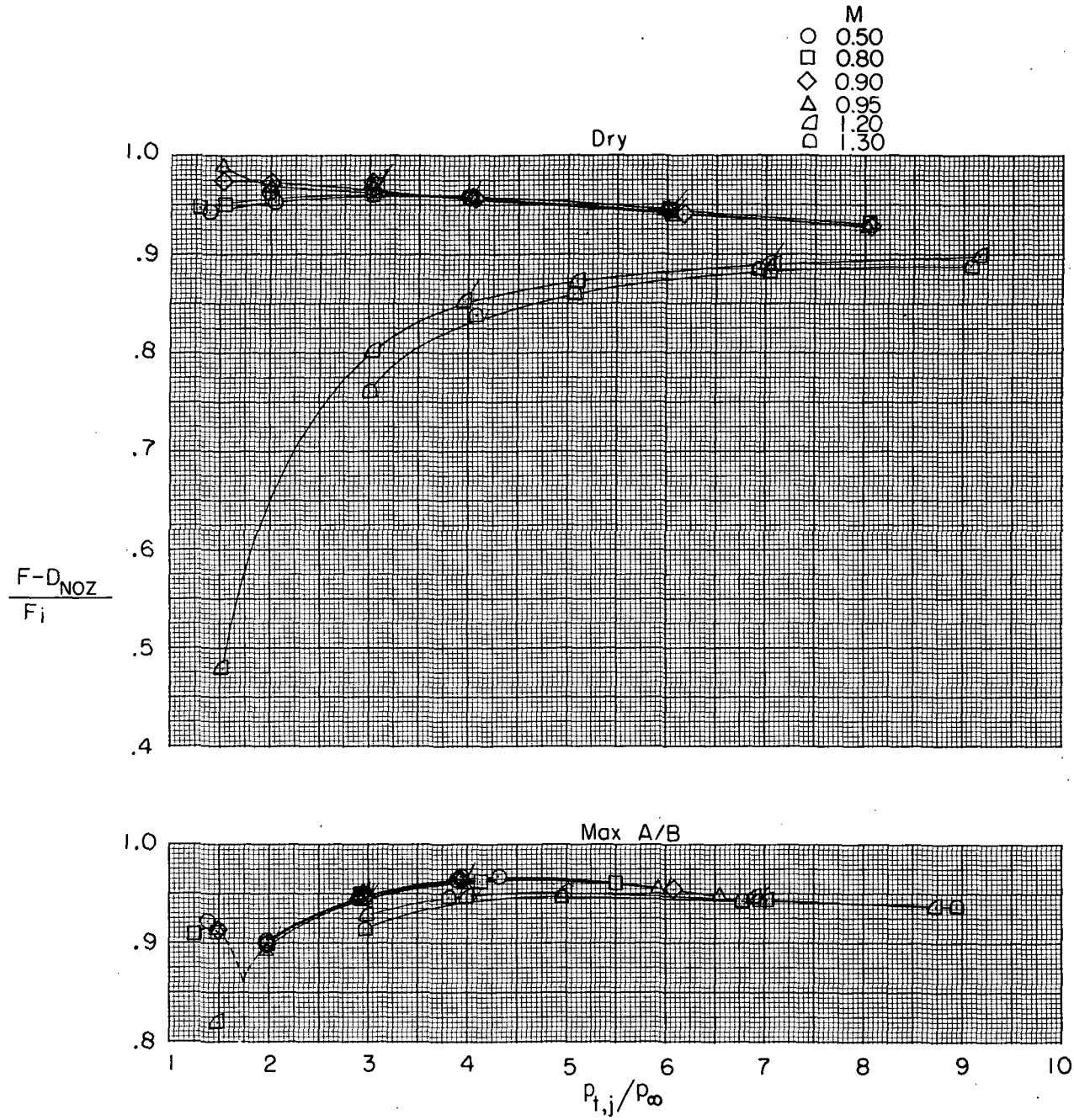

(l) Wide-spaced afterbody; alternate 2 interfairing; $\beta = 5^{o}$.

Figure 29.- Concluded.

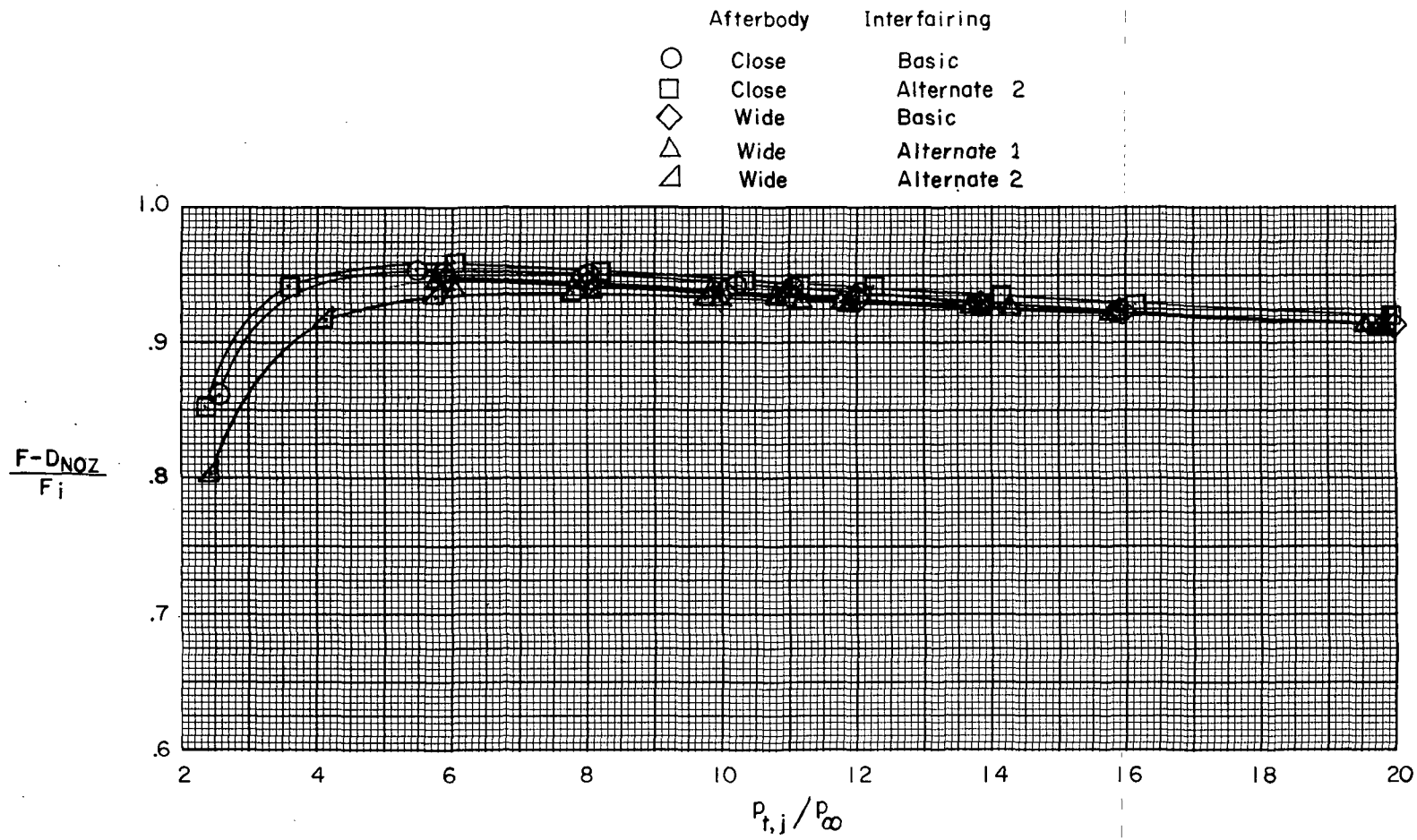

Figure 30.- Variation of thrust-minus-nozzle-drag ratio with jet total-pressure ratio for several combinations of *afterbodies and interfairings.* $M = 2.20$; *max* A/B *nozzles;* $\beta = 0^{o}$.

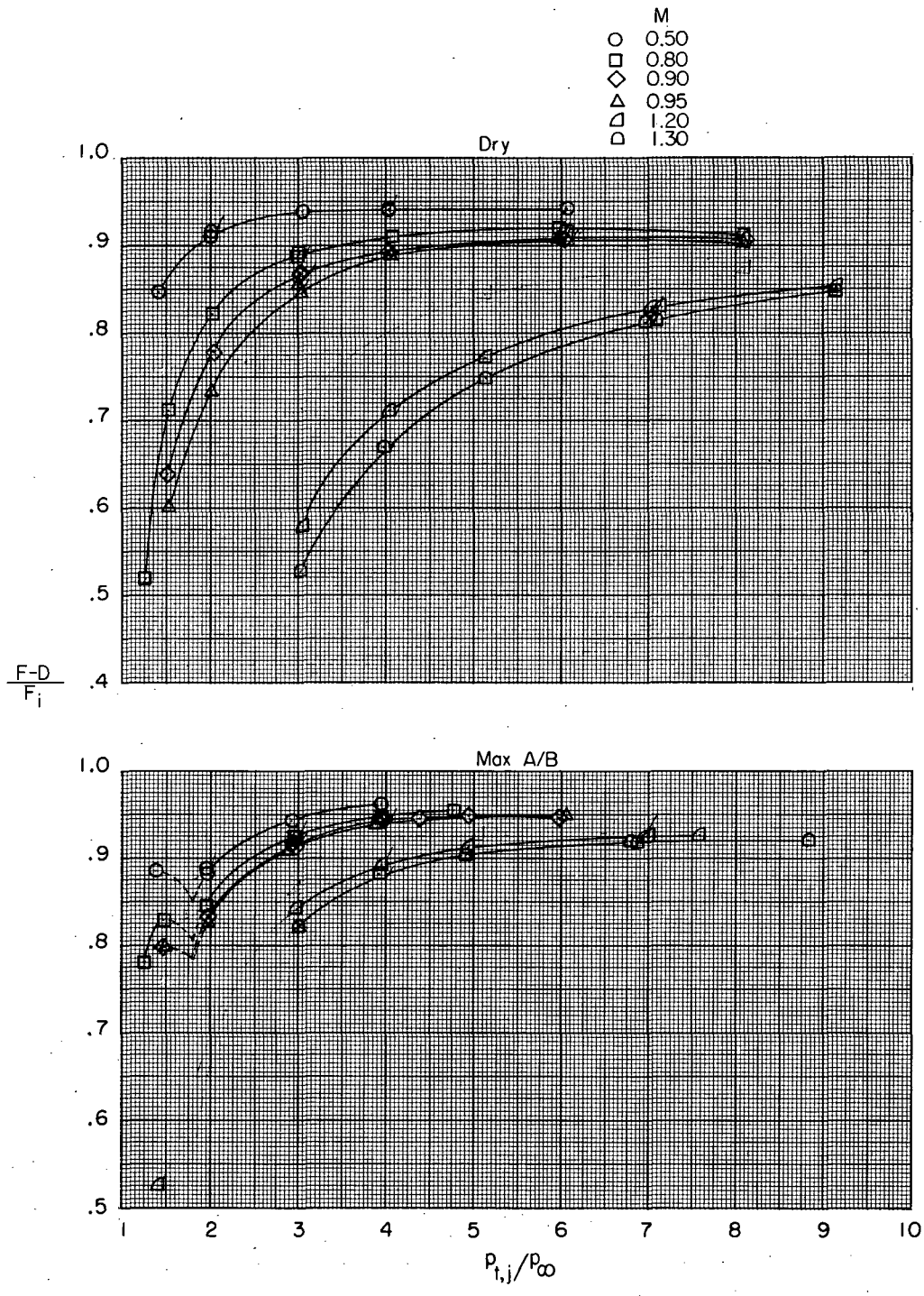

(a) Close-spaced afterbody; basic interfairing; $\beta = 0^{o}$.

Figure 31.- Variation of thrust-minus-total-drag ratio with jet total-pressure ratio for two nozzle power settings. Flagged symbols indicate decreasing jet total-pressure ratio.

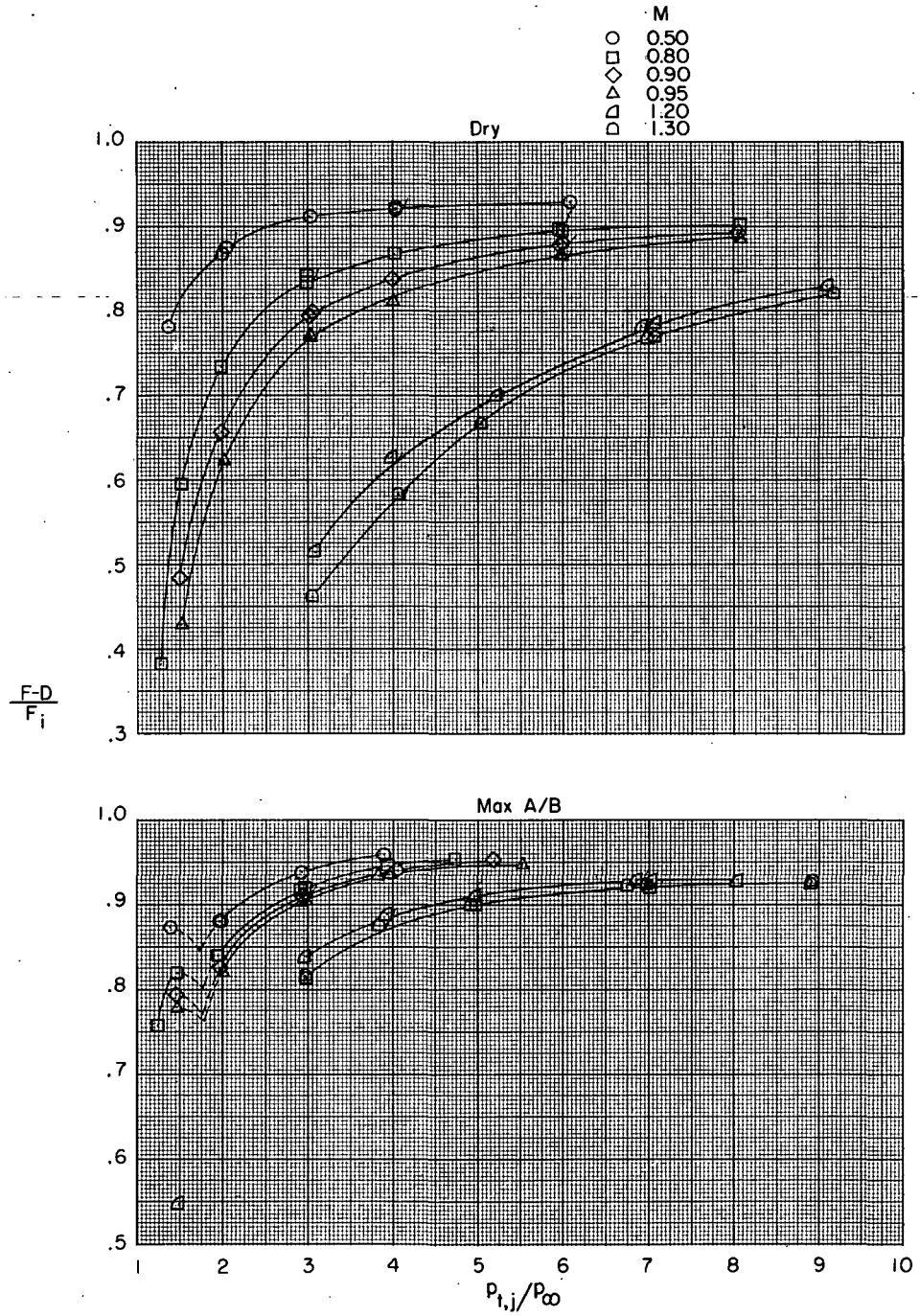

(b) Close-spaced afterbody; alternate 2 interfairing; $\beta = 0^{o}$.

Figure 31.- Continued.

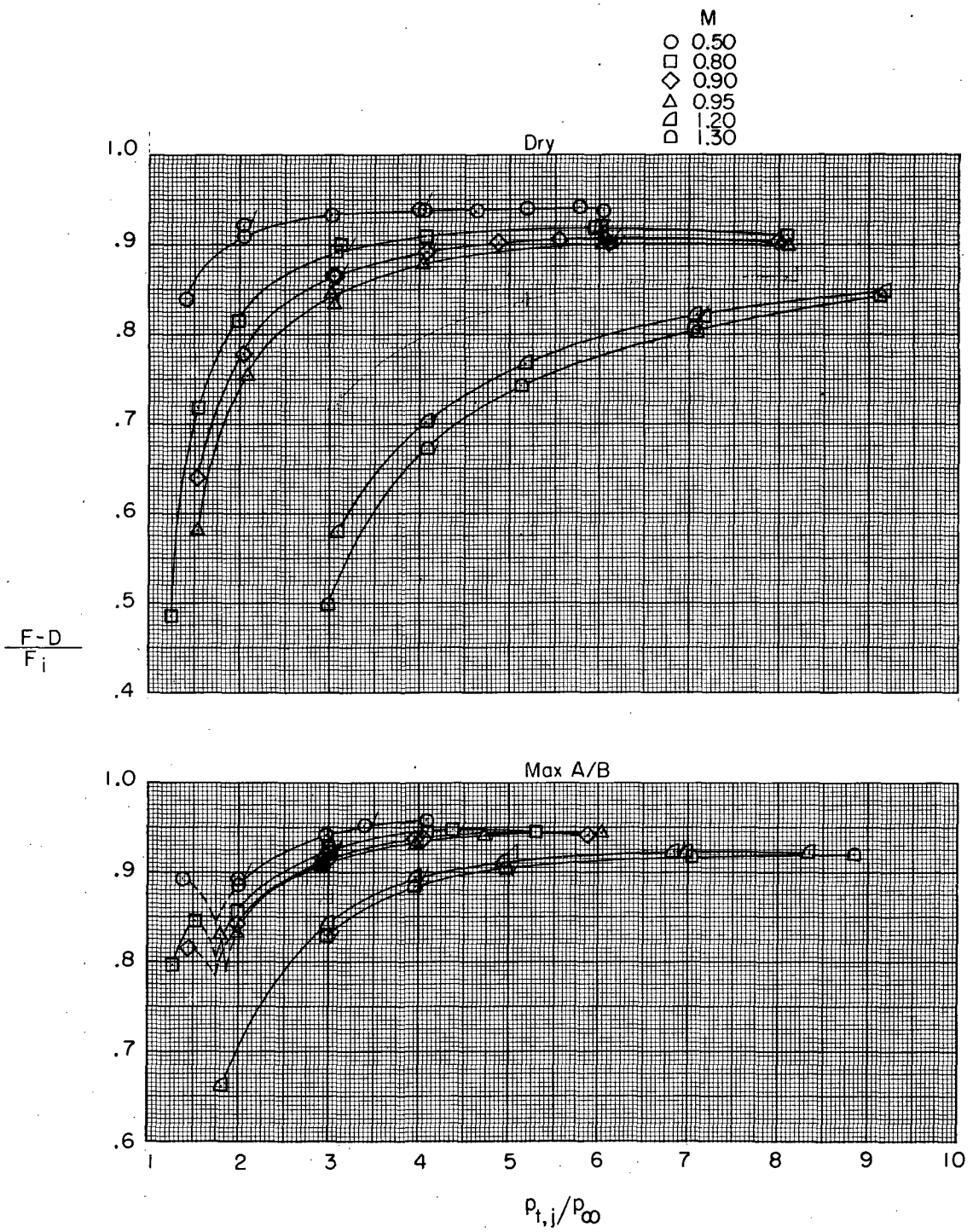

(c) Close-spaced afterbody; basic interfairing; $\beta = 5^{o}$.

Figure 31.- Continued.

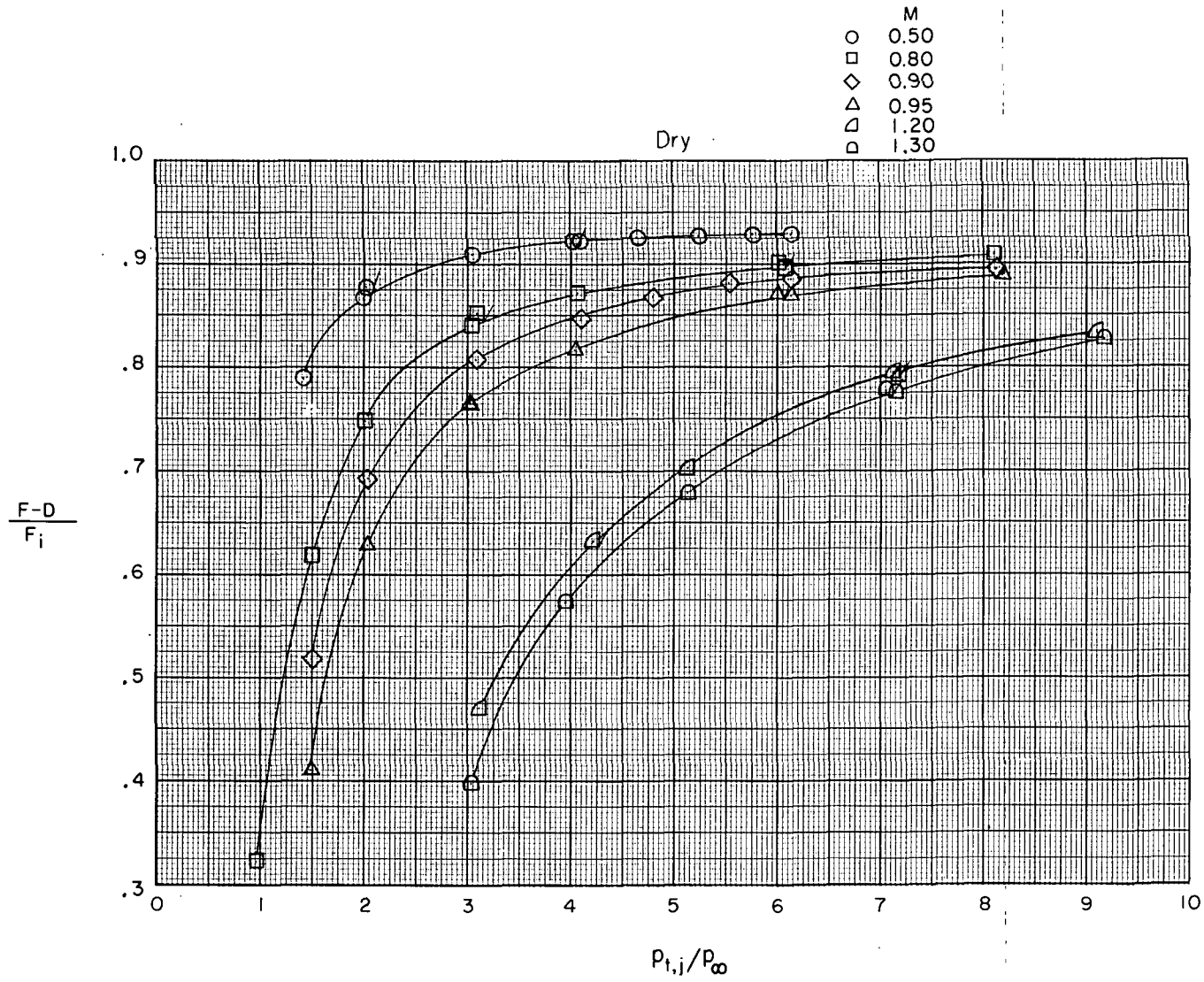

(d) Close-spaced afterbody; alternate 2 interfairing; $\beta = 5^{o}$.

Figure 31.- Continued.

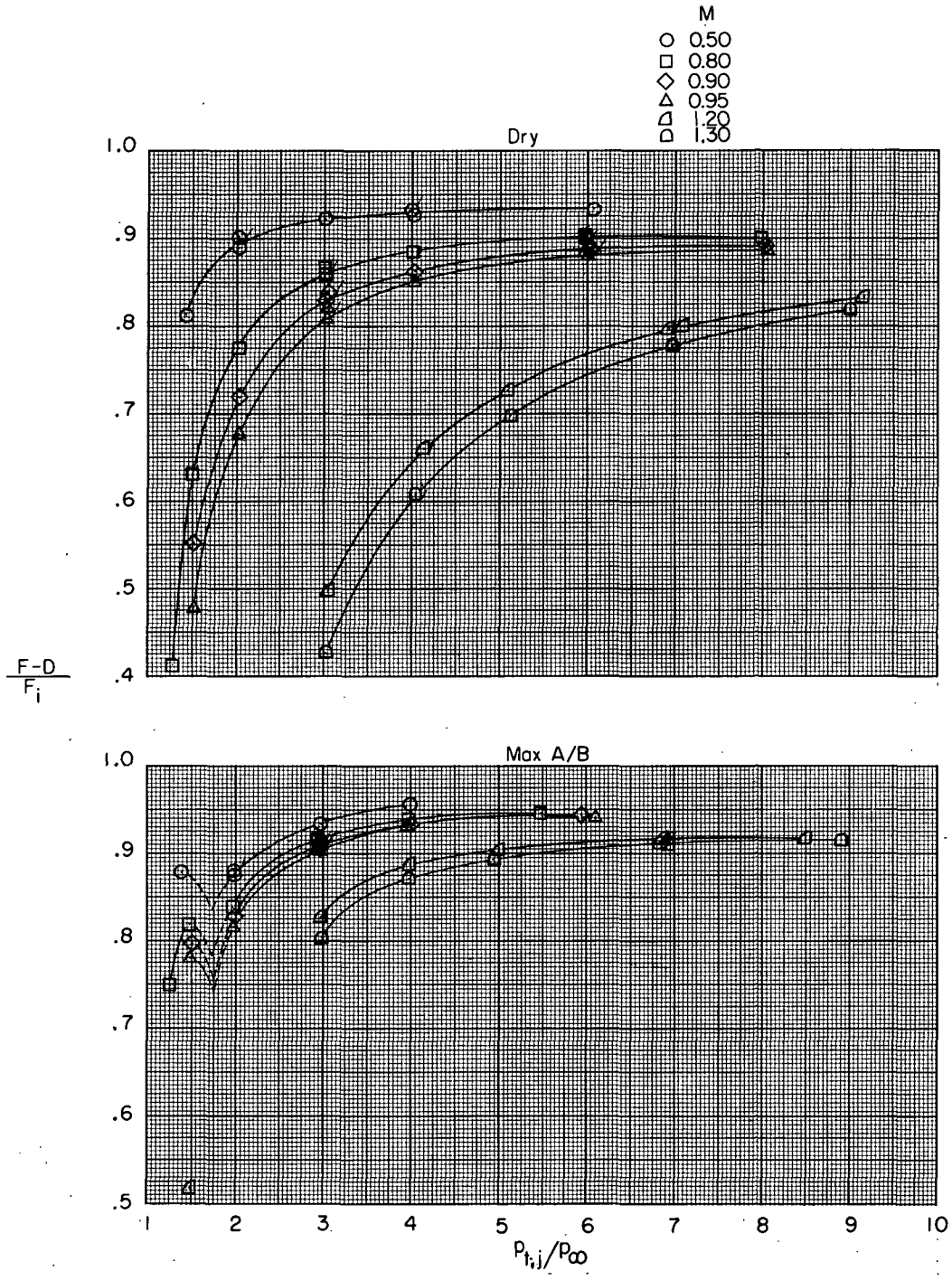

(e) Close-spaced afterbody; basic interfairing; $\beta = -5^{o}$.

Figure 31.- Continued.

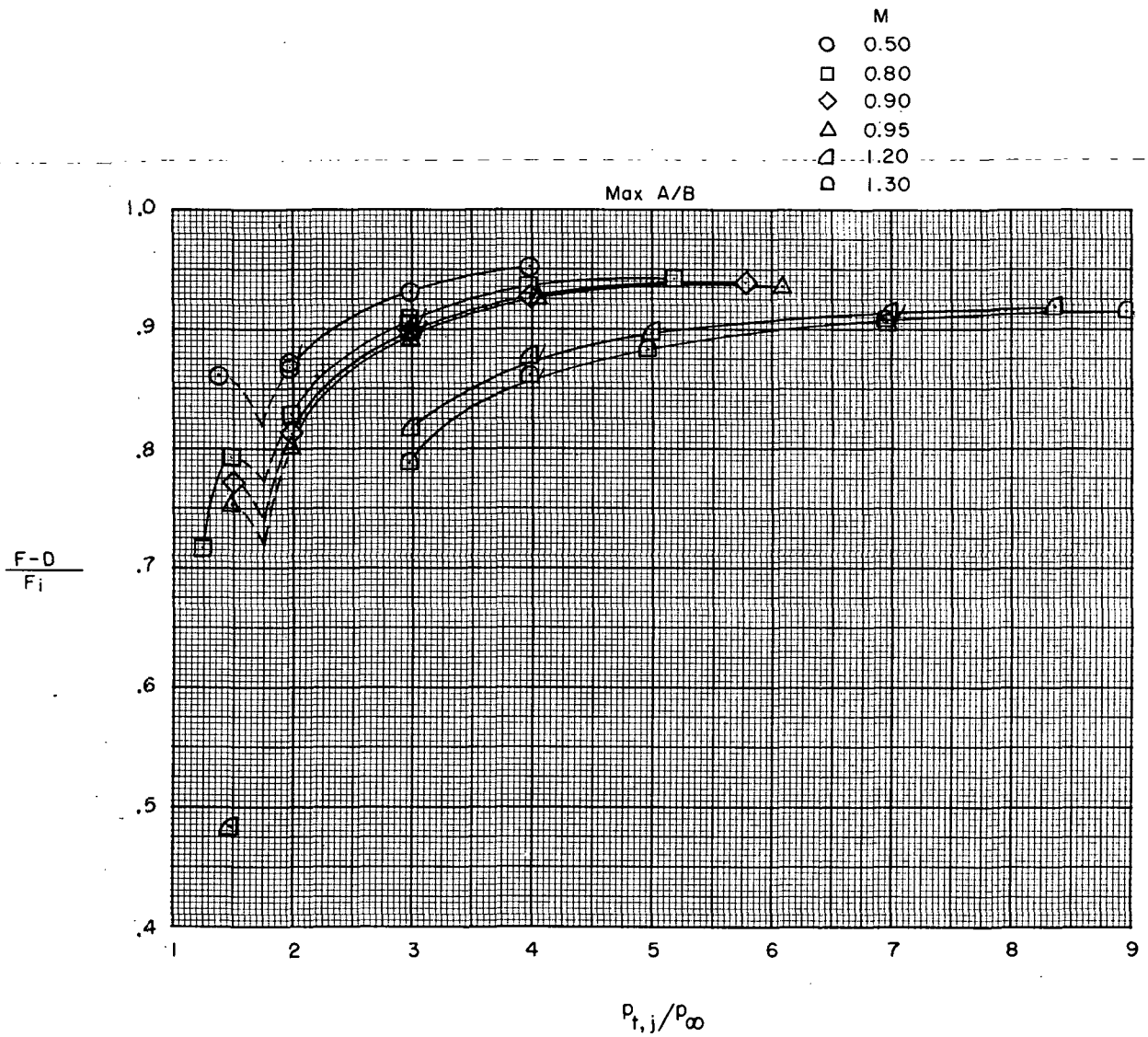

(f) Close-spaced afterbody; alternate 2 interfairing; $\beta = -5^{o}$.

Figure 31.- Continued.

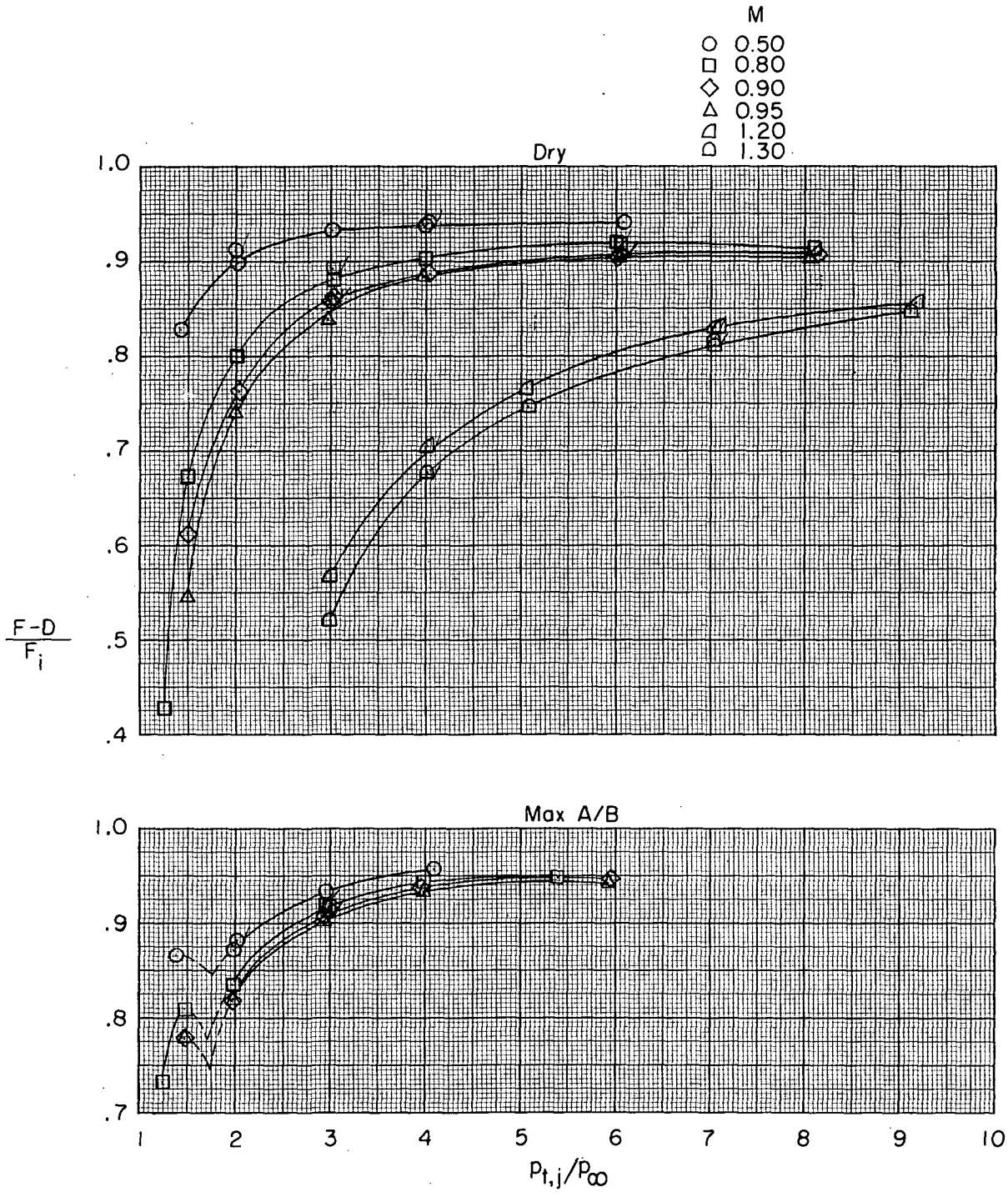

(g) Wide-spaced afterbody; basic interfairing; $\beta = 0^{o}$.

Figure 31.- Continued.

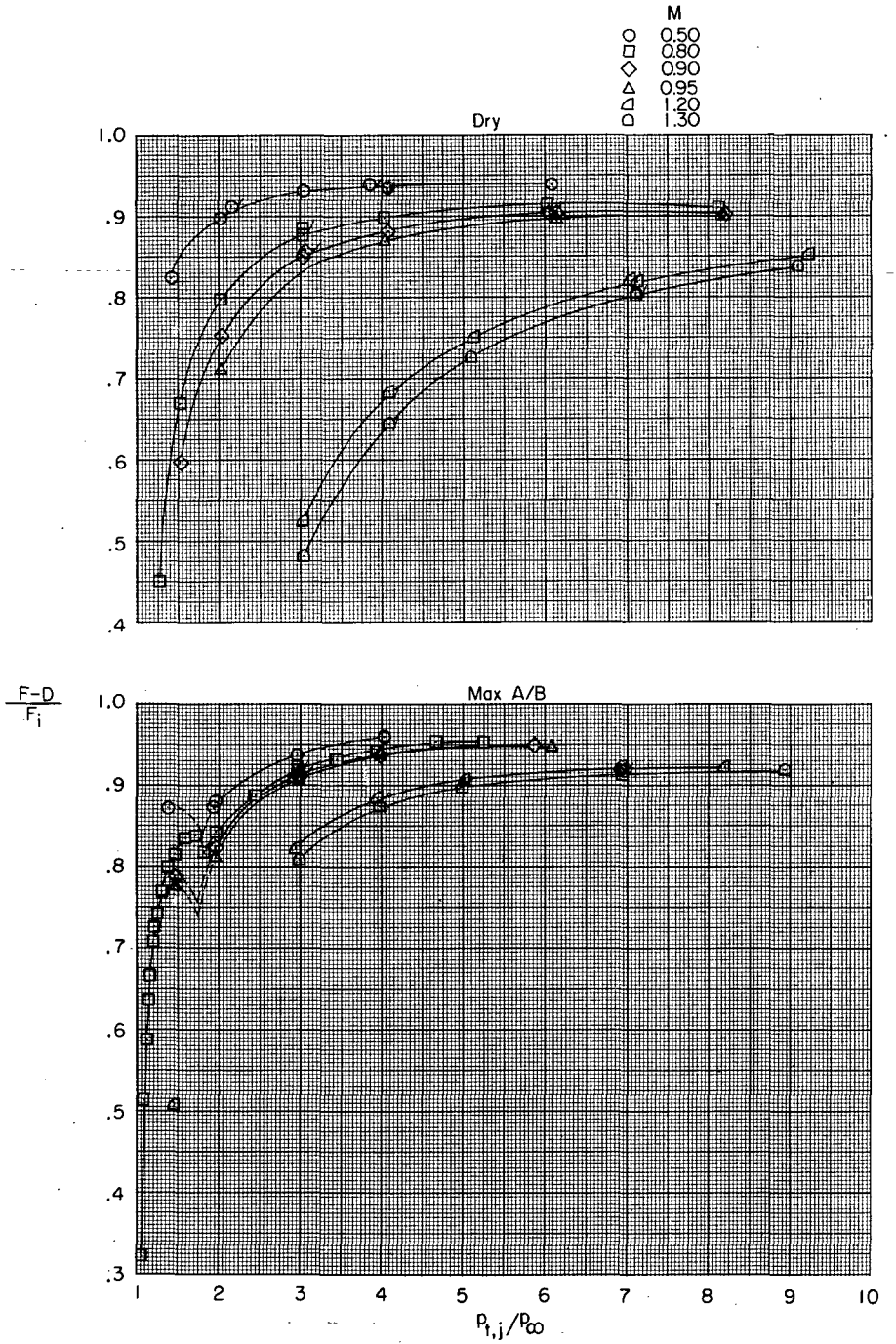

(h) Wide-spaced afterbody; alternate 1 interfairing; $\beta = 0^{o}$.

Figure 31.- Continued.

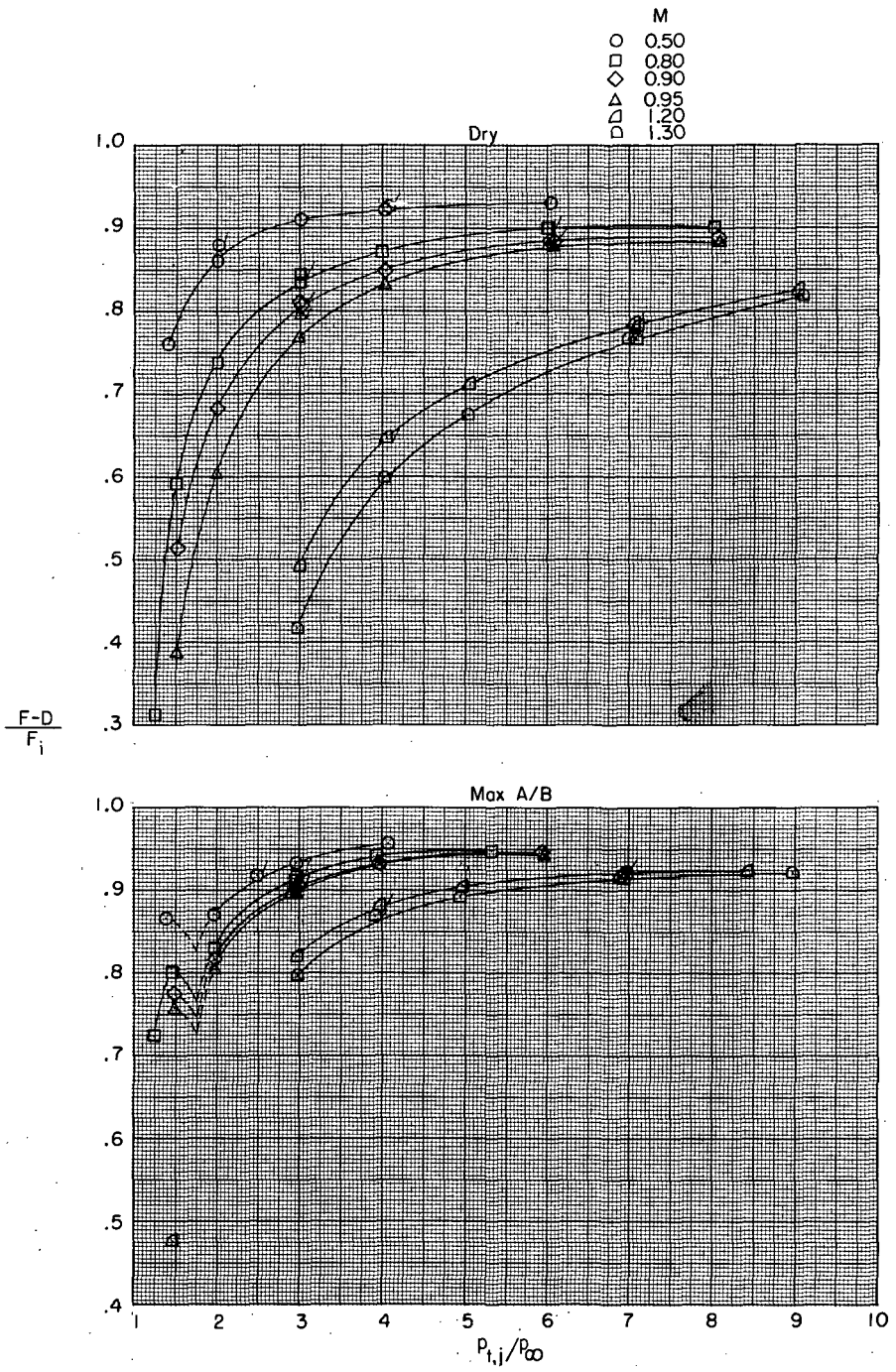

(i) Wide-spaced afterbody; alternate 2 interfairing; $\beta = 0^{o}$.

Figure 31.- Continued.

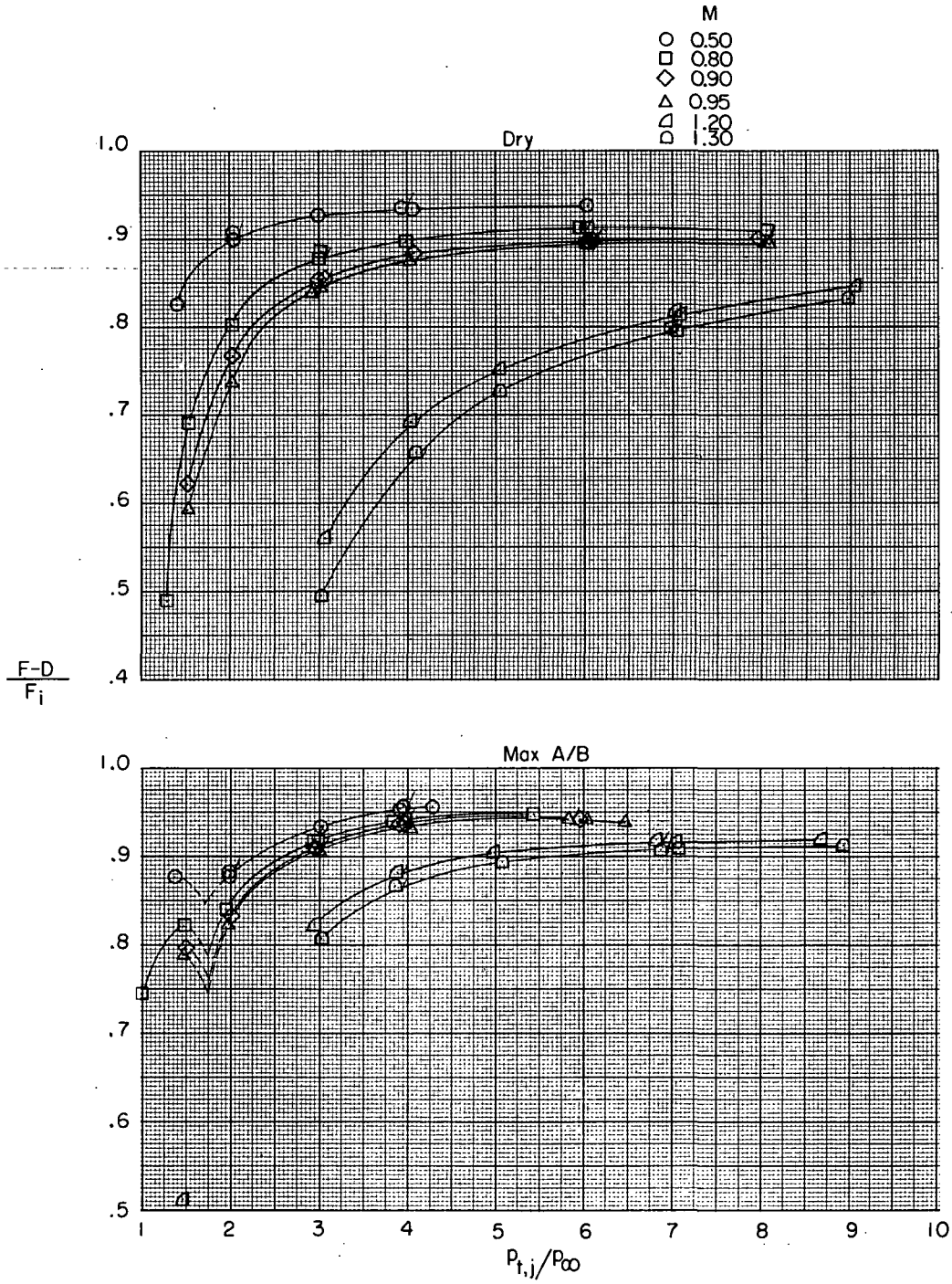

(j) Wide-spaced afterbody; basic interfairing; $\beta = 5^{o}$.

Figure 31.- Continued.

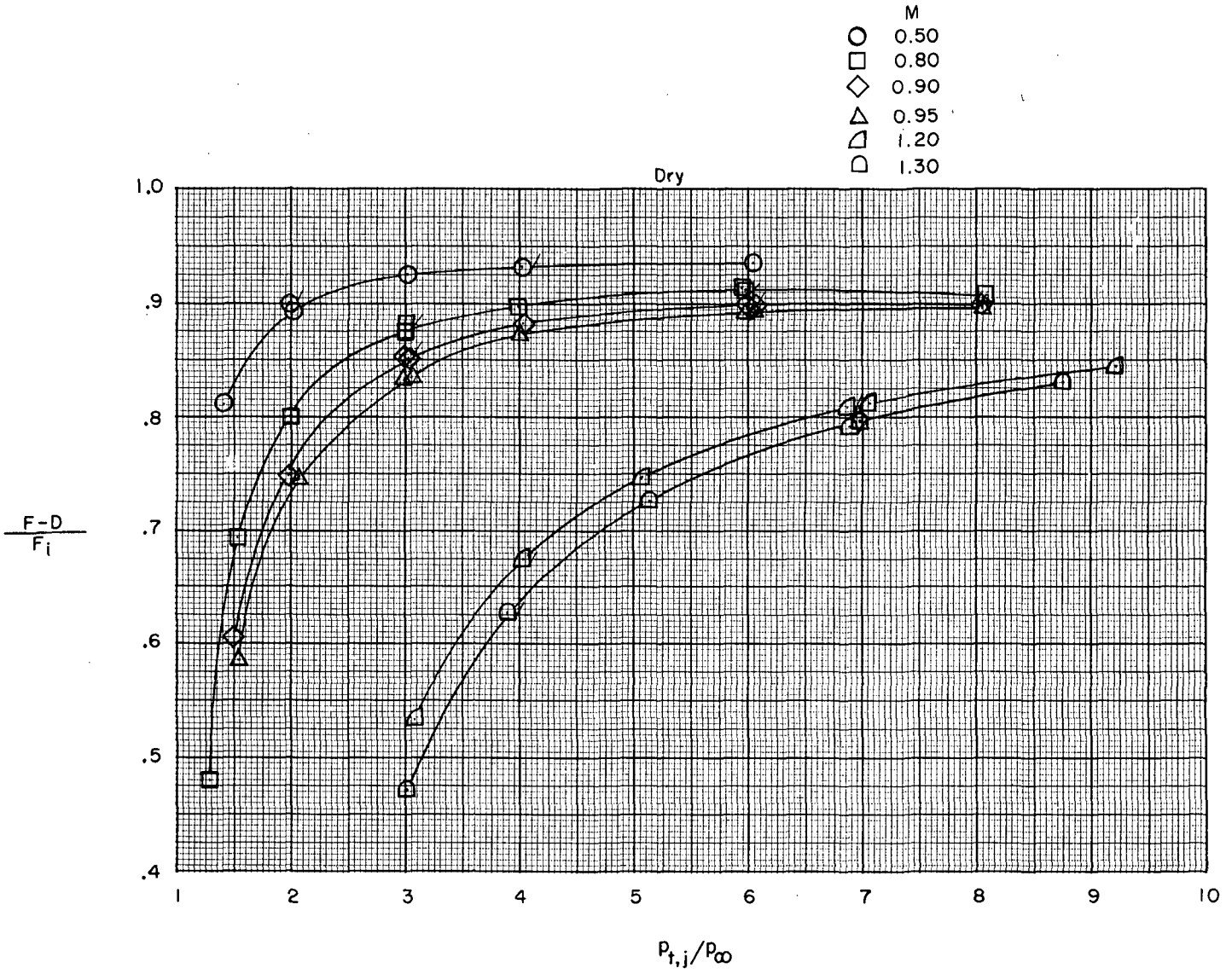

(k) Wide-spaced afterbody; alternate 1 interfairing; $\beta = 5^{o}$.

Figure 31.- Continued.

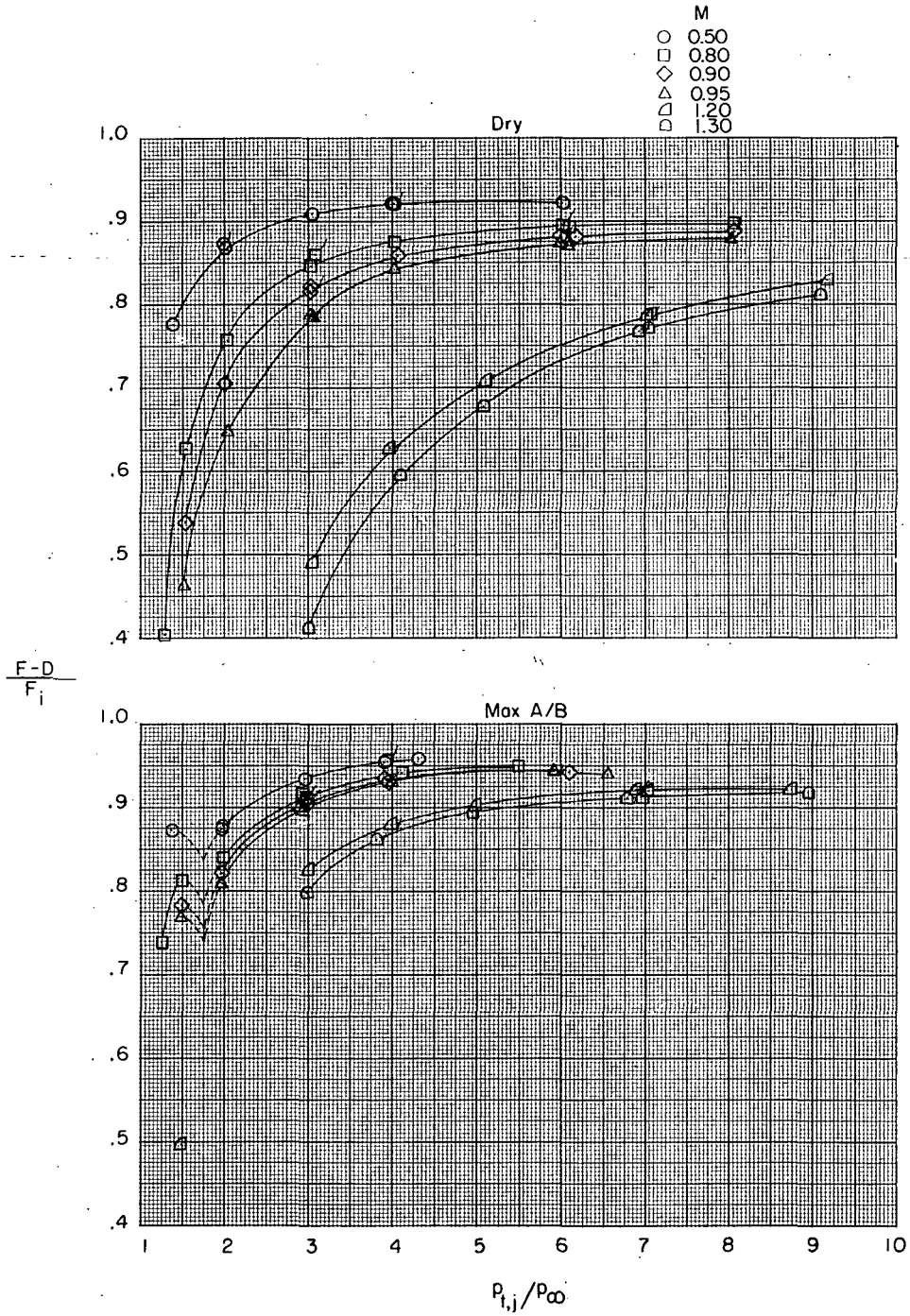

(l) Wide-spaced afterbody; alternate 2 interfairing; $\beta = 5^{o}$.

Figure 31.- Concluded.

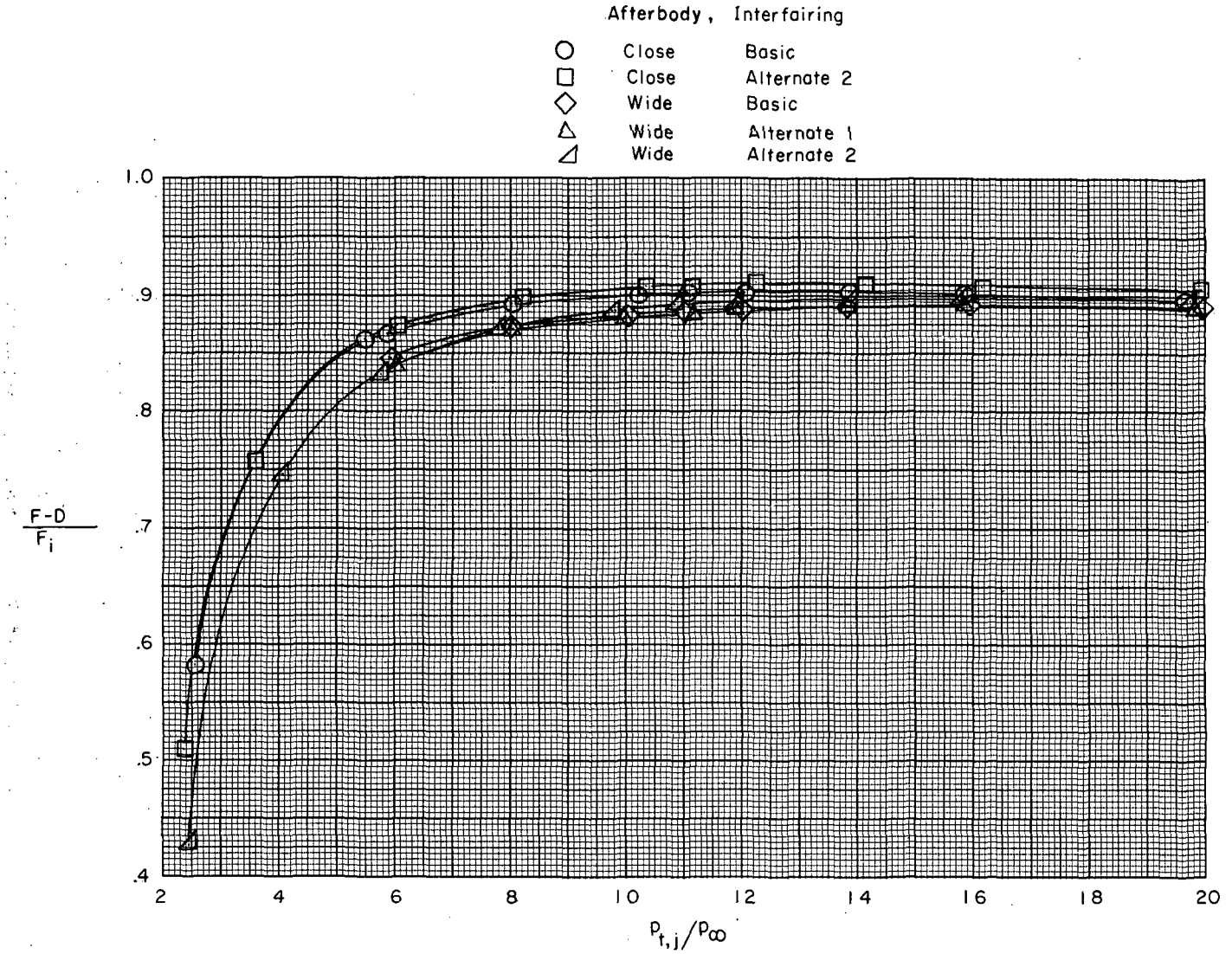

Figure 32.- Variation of thrust-minus-total-drag ratio with jet total-pressure ratio for several combinations of afterbodies and interfairings. M = 2.20; max A/B nozzles; $\beta = 0^{o}$.

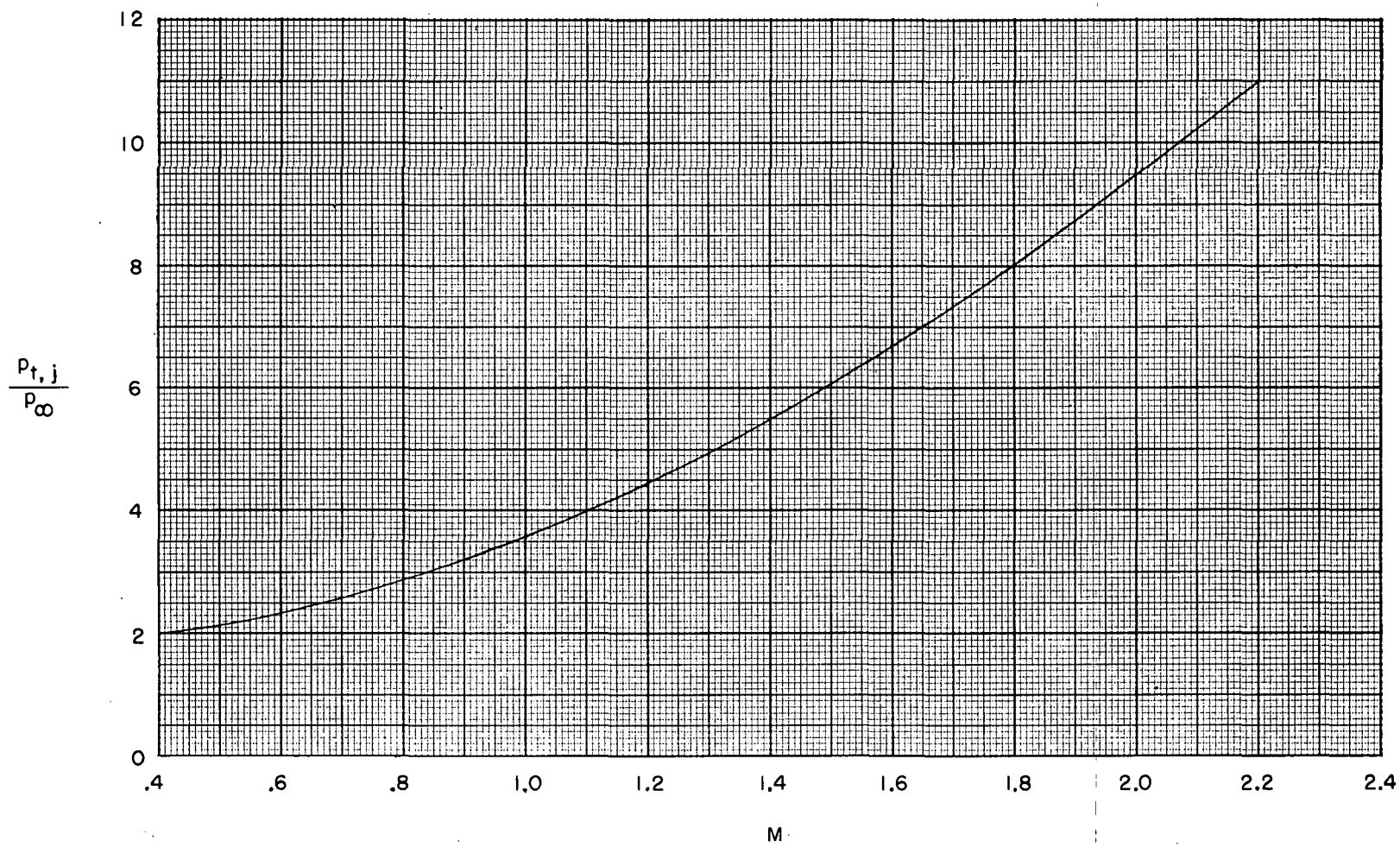

Figure 33.- Typical jet-total-pressure-ratio schedule for a turbofan engine.

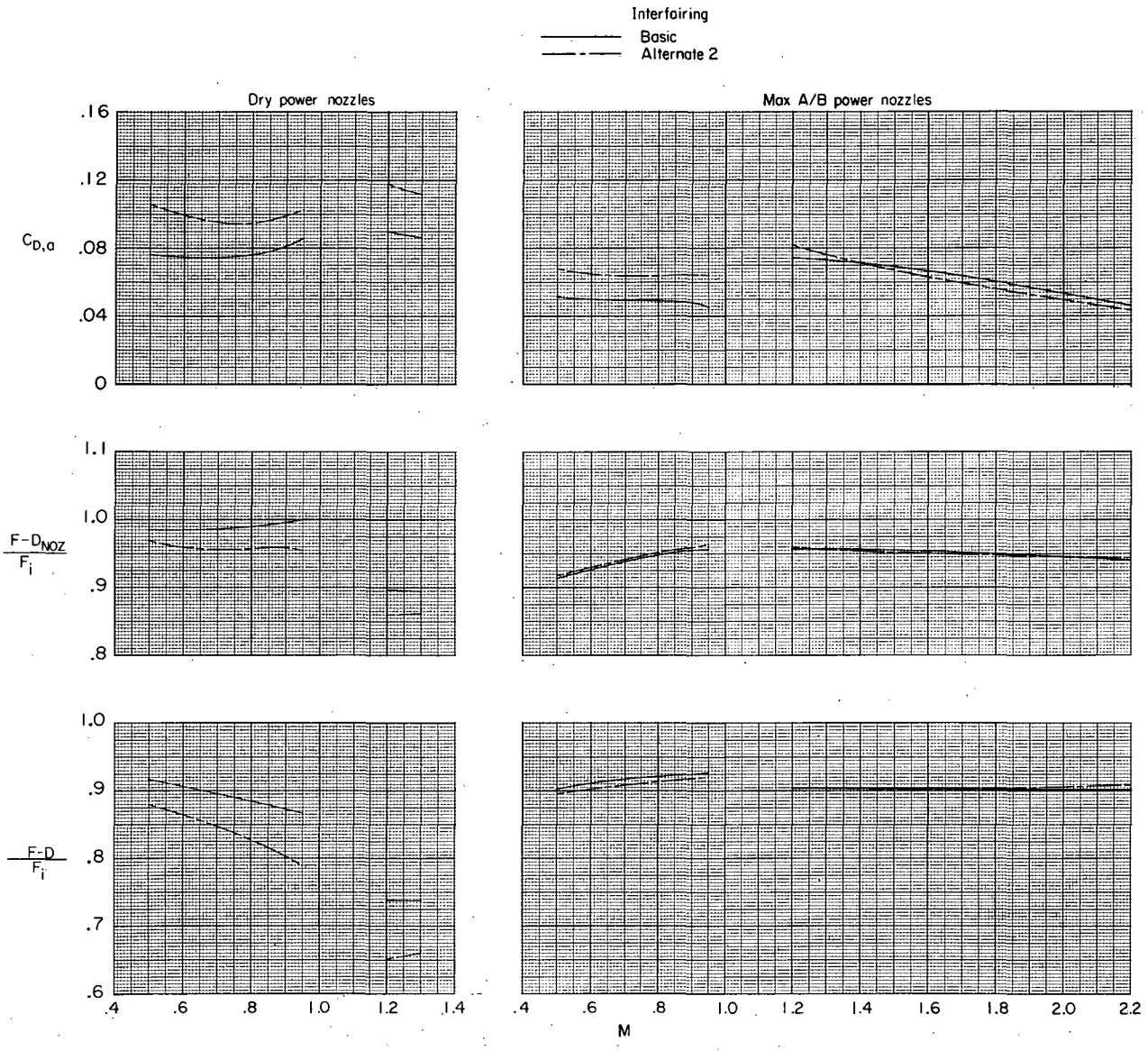

(a) Close-spaced afterbody; $\beta = 0^{o}$.

Figure 34.- Variation of afterbody drag coefficient, thrust-minus-nozzle-drag ratio, and thrust-minus-total-drag ratio with Mach number for the scheduled jet total-pressure ratio. Effect of nozzle power setting and interfairing shape.

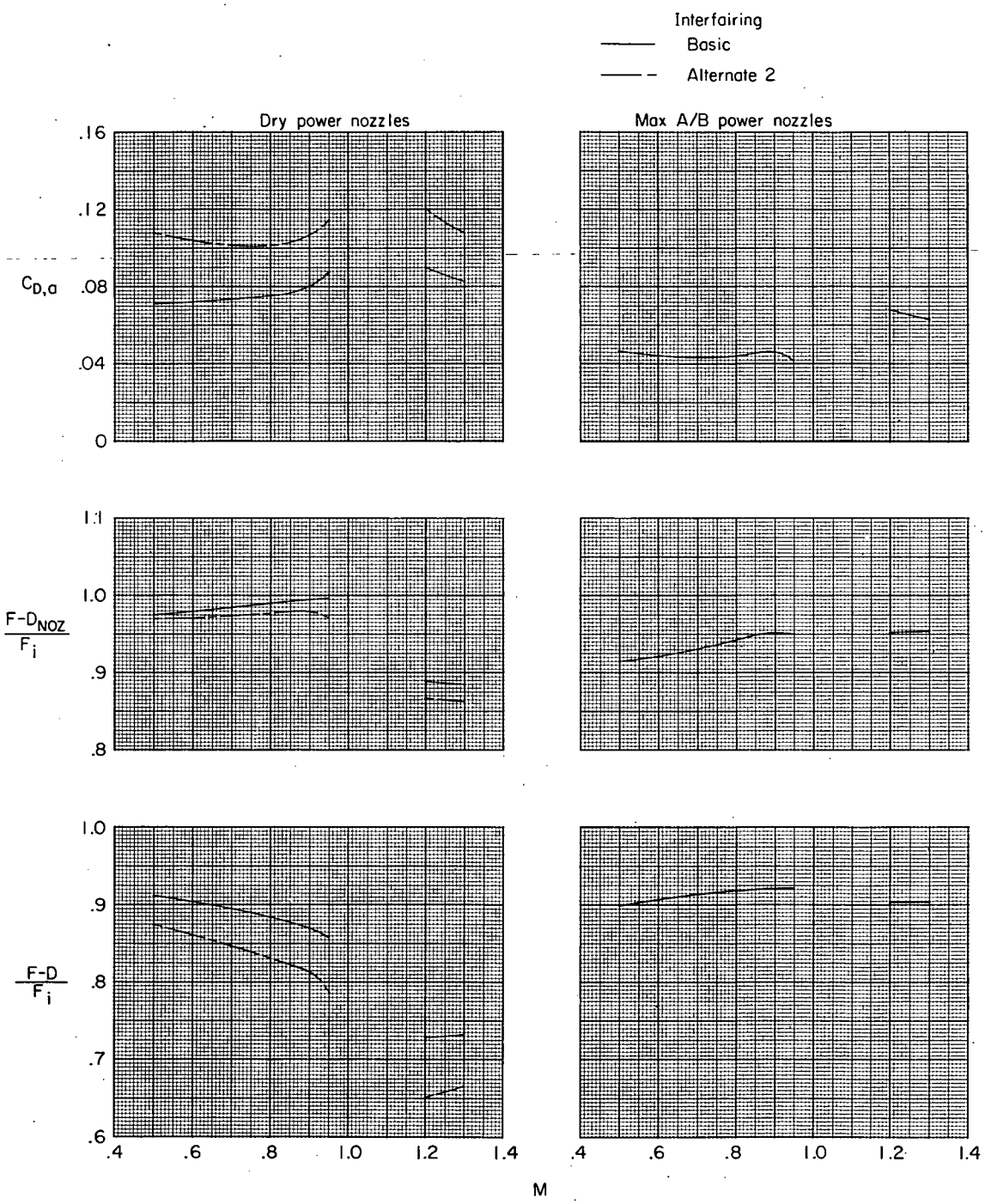

(b) Close-spaced afterbody; $\beta = 5^{o}$.

Figure 34.- Continued.

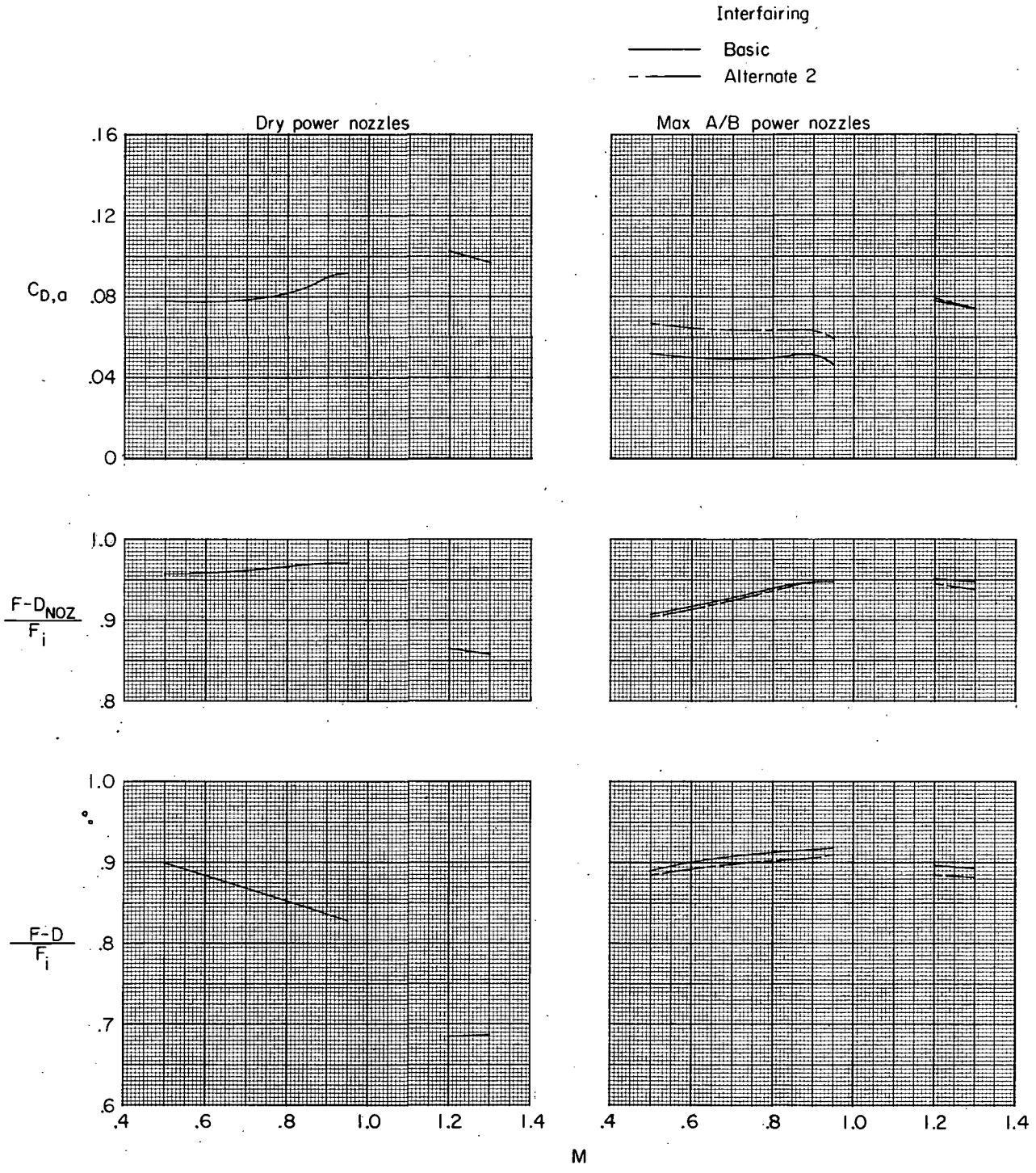

(c) Close-spaced afterbody; $\beta = -5^{o}$.

Figure 34.- Continued.

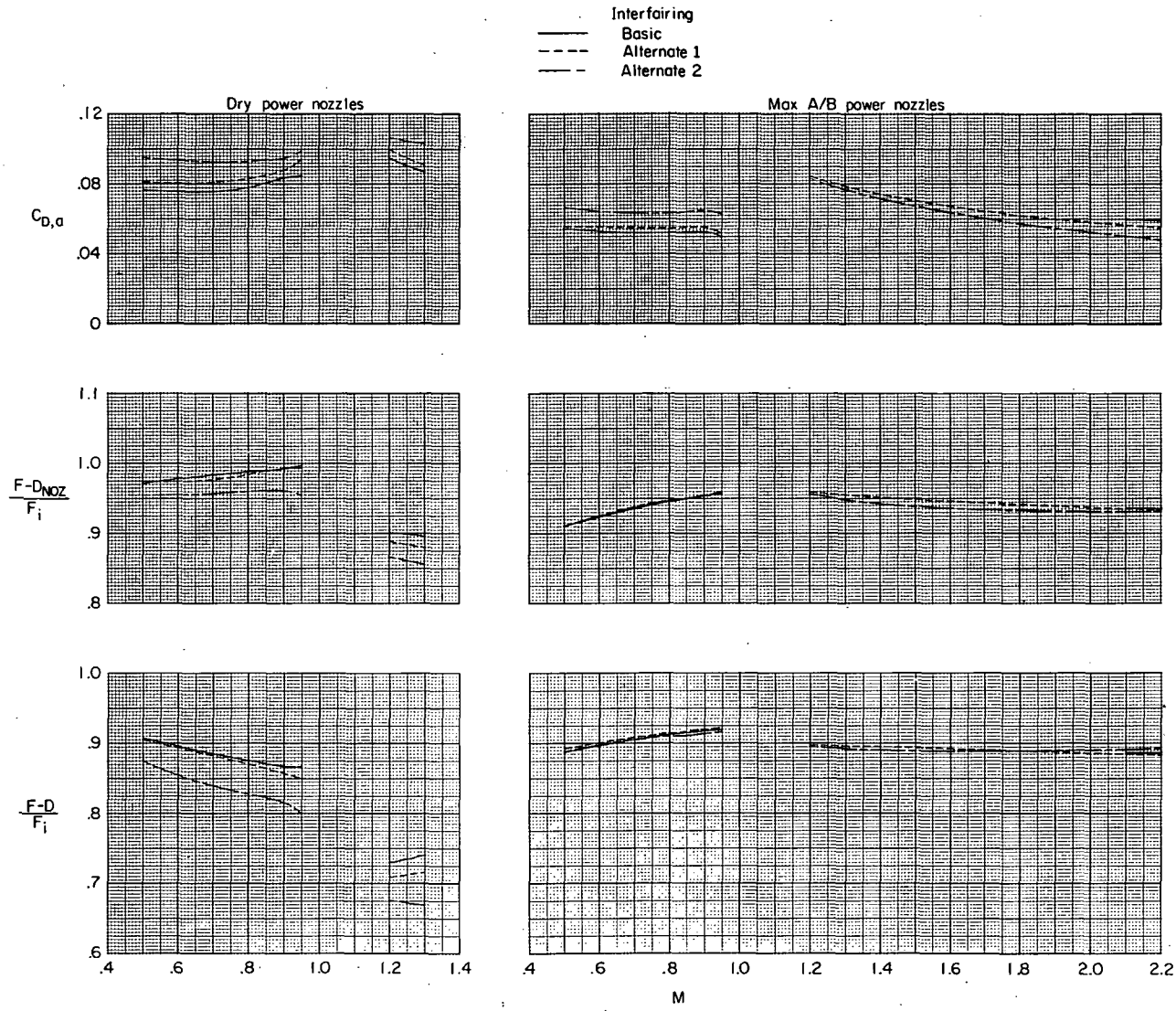

(d) Wide-spaced afterbody; $\beta = 0^{o}$.

Figure 34.- Continued.

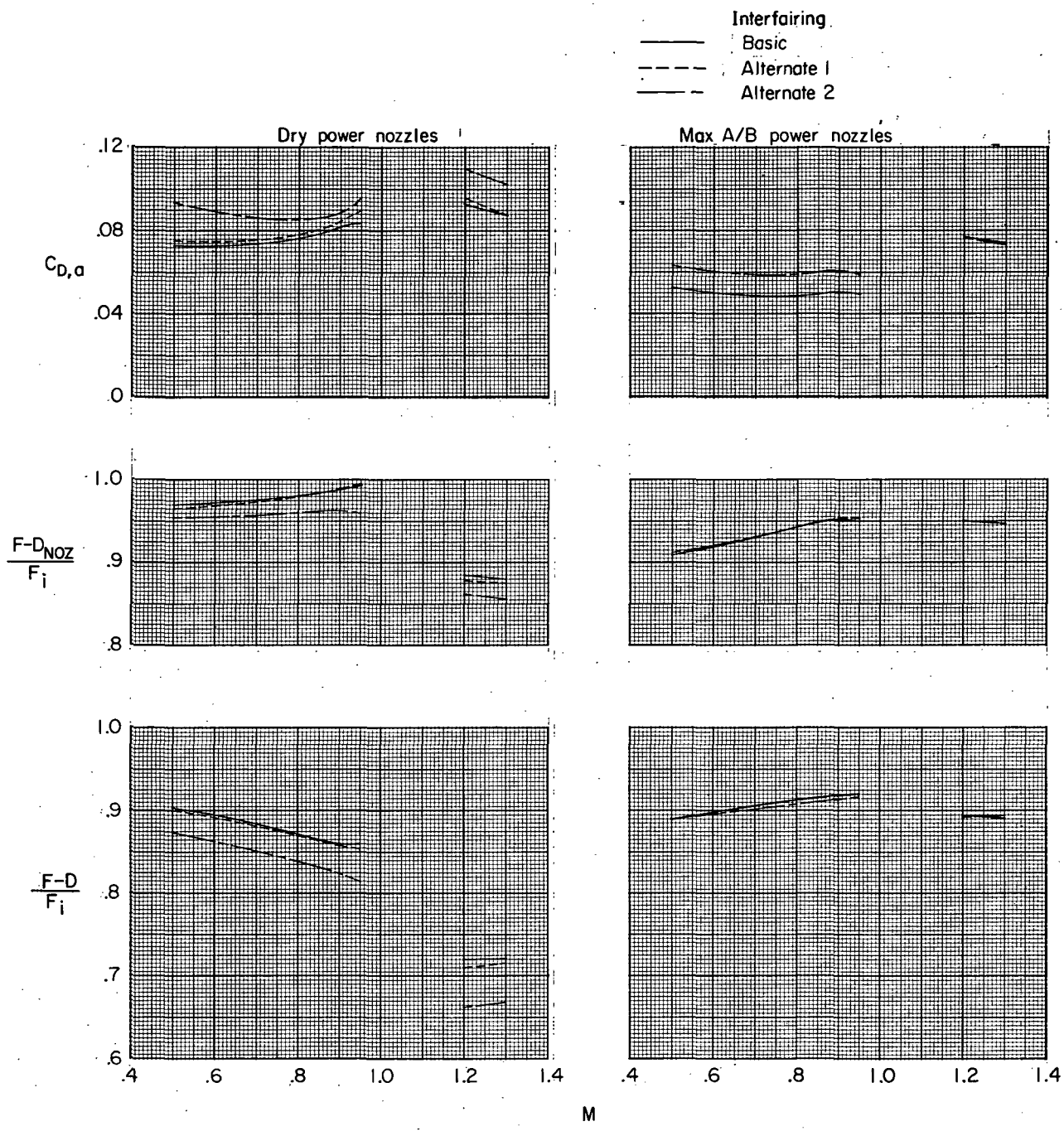

(e) Wide-spaced afterbody; $\beta = 5^{o}$.

Figure 34.- Concluded.

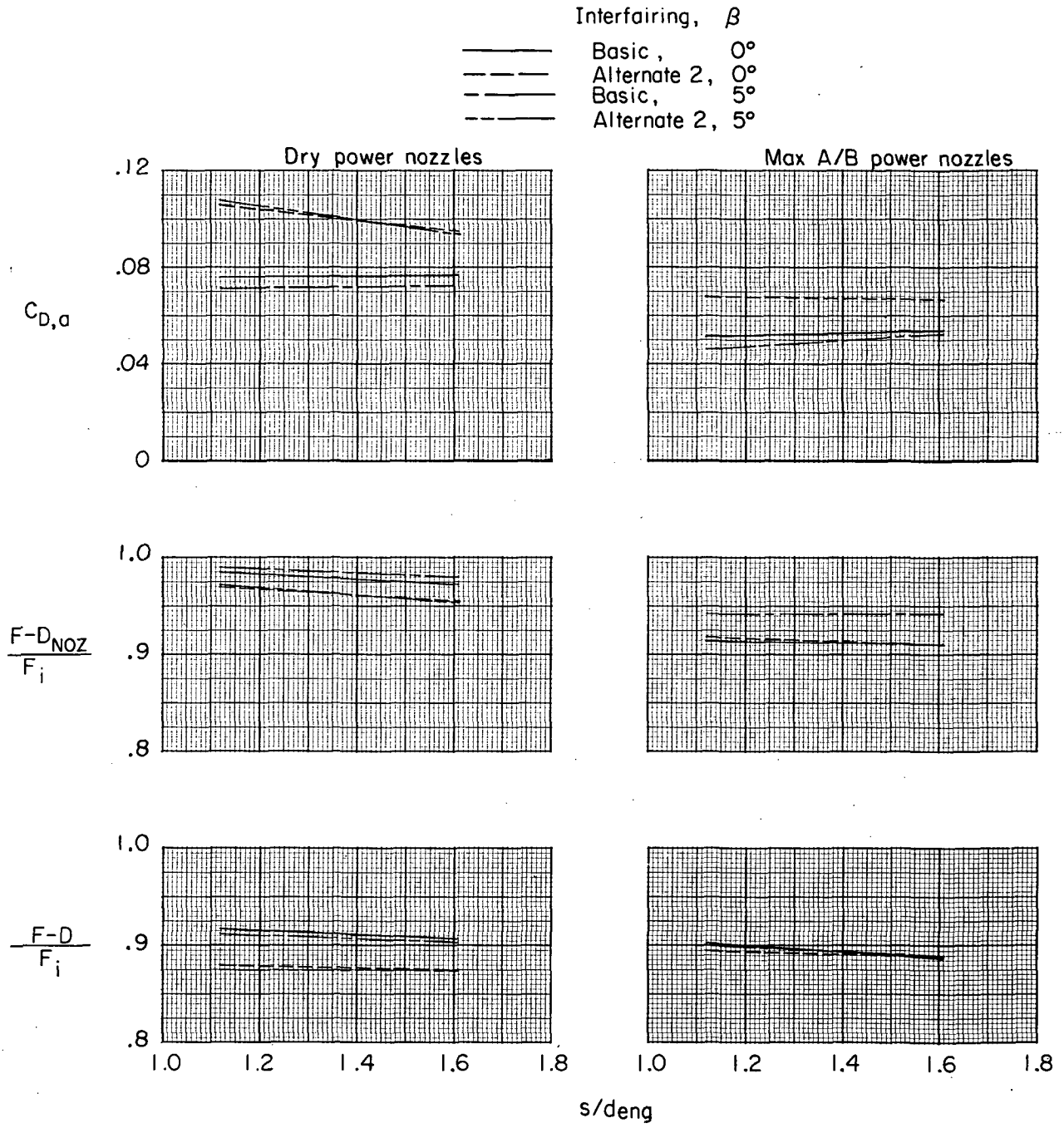

(a) M = 0.50.

Figure 35.- Effect of engine lateral spacing on drag coefficient, thrust-minus-nozzle-drag ratio, and thrust-minus-total-drag ratio.

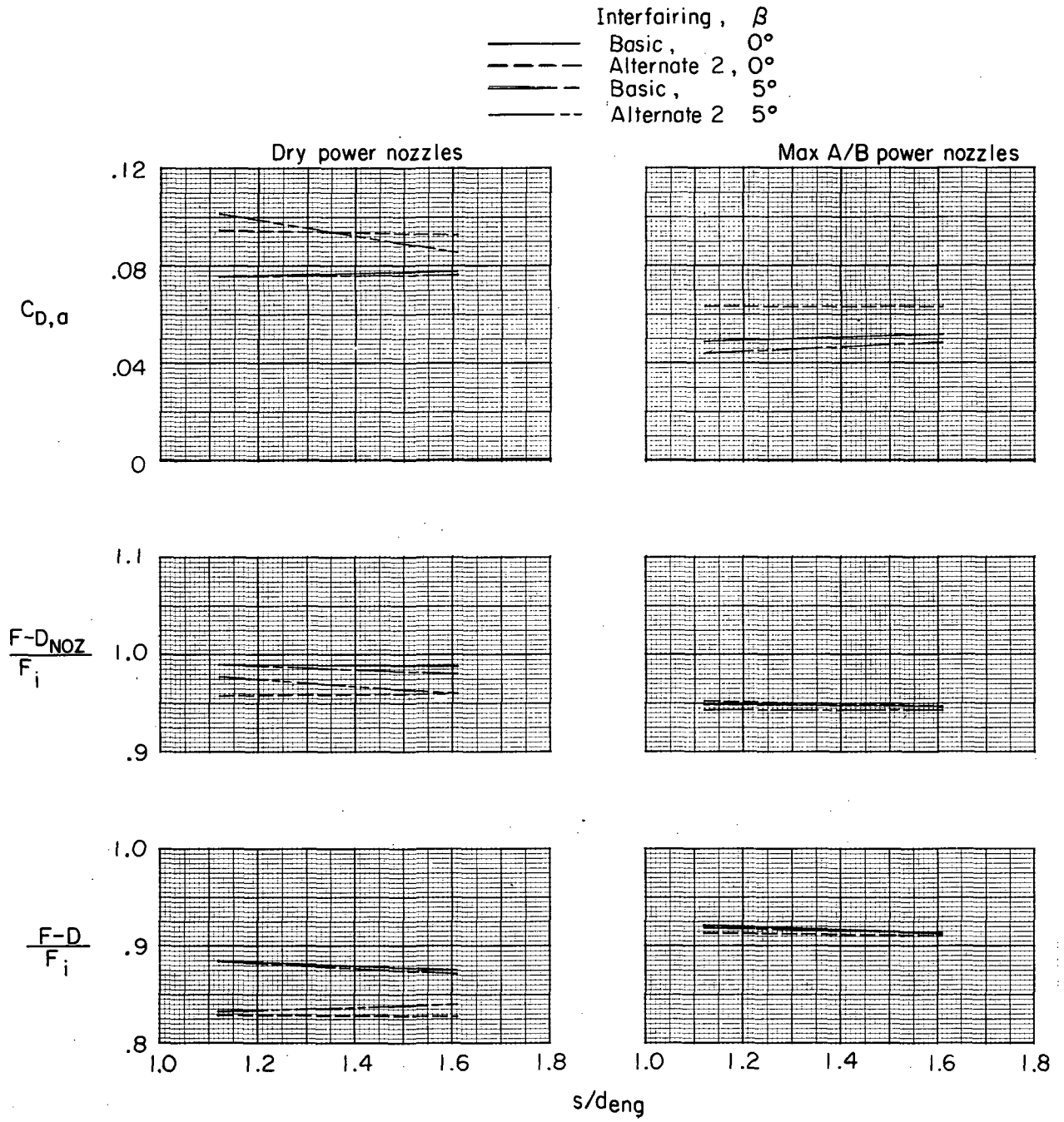

(b) M = 0.80.

Figure 35.- Continued.

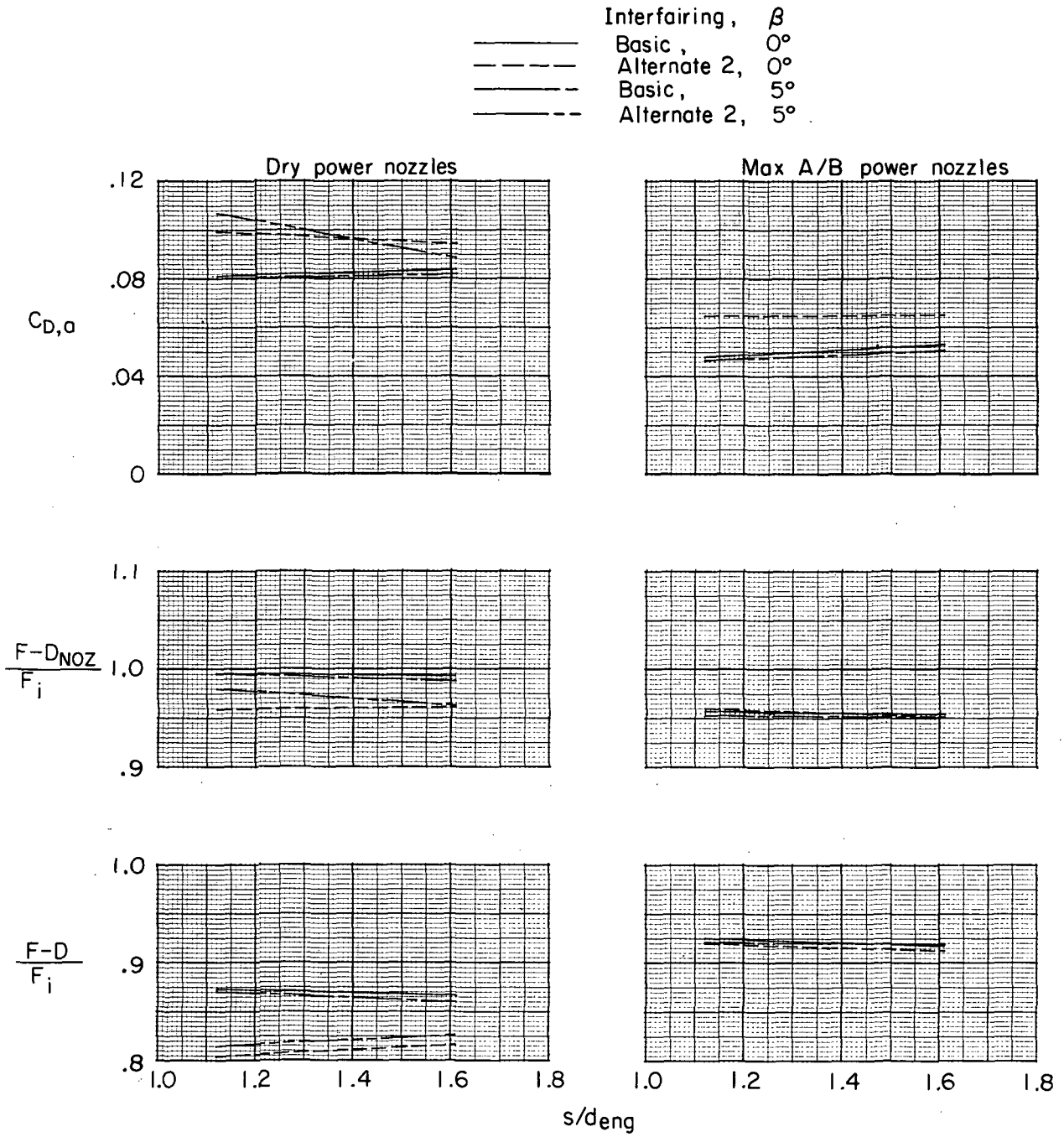

(c) M = 0.90.

Figure 35.- Continued.

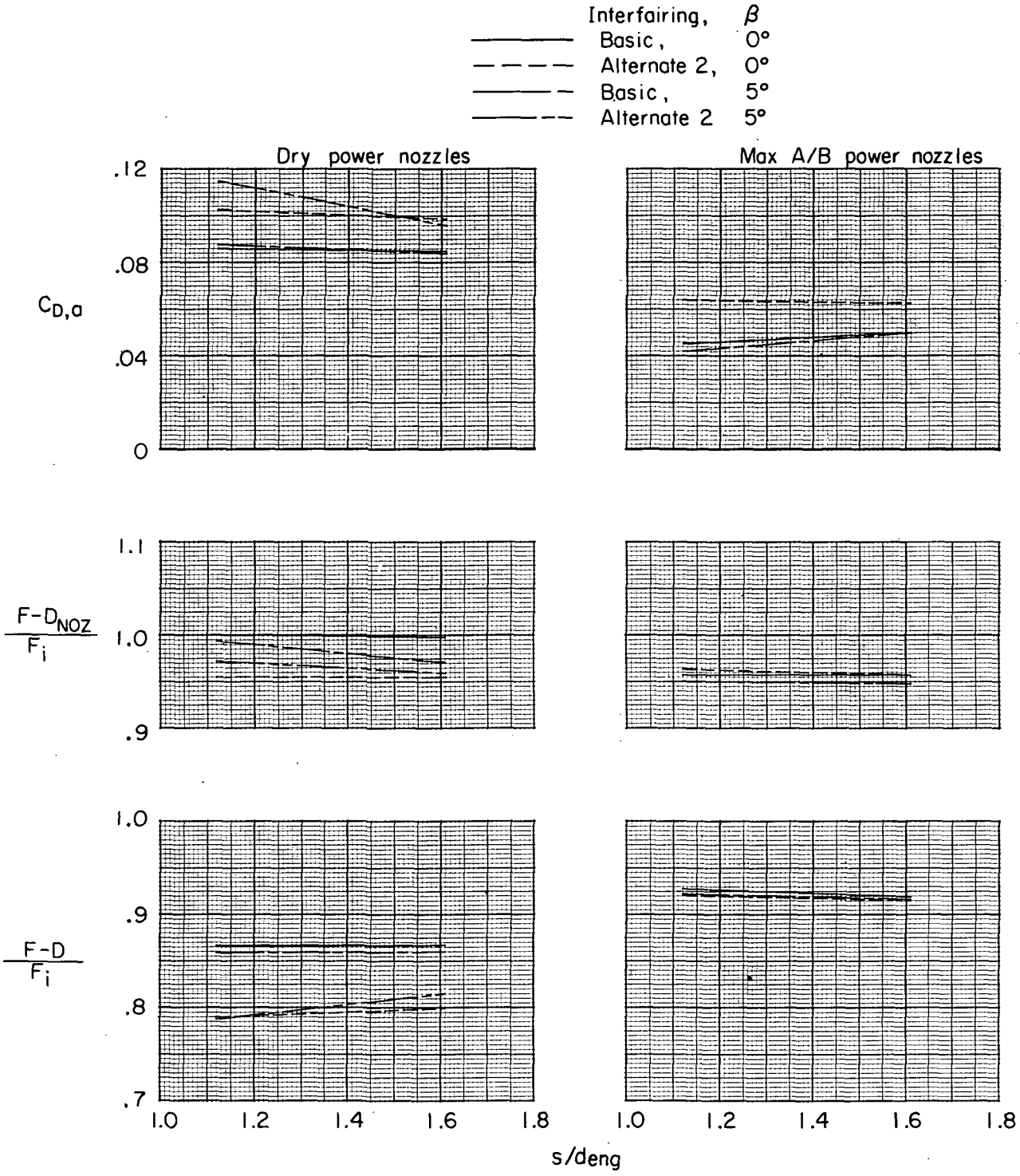

(d) M = 0.95.

Figure 35.- Continued.

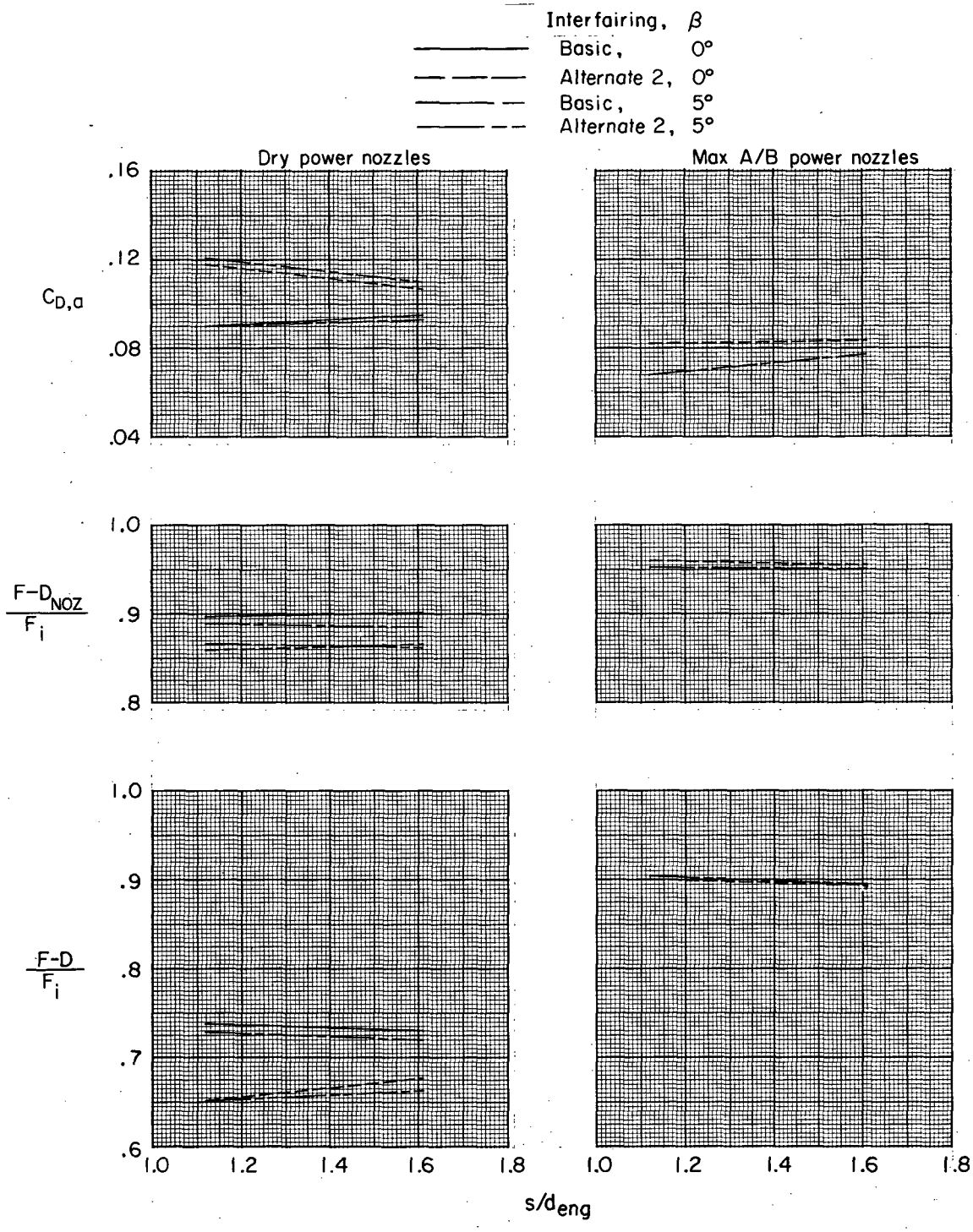

(e) M = 1.20.

Figure 35.- Continued.

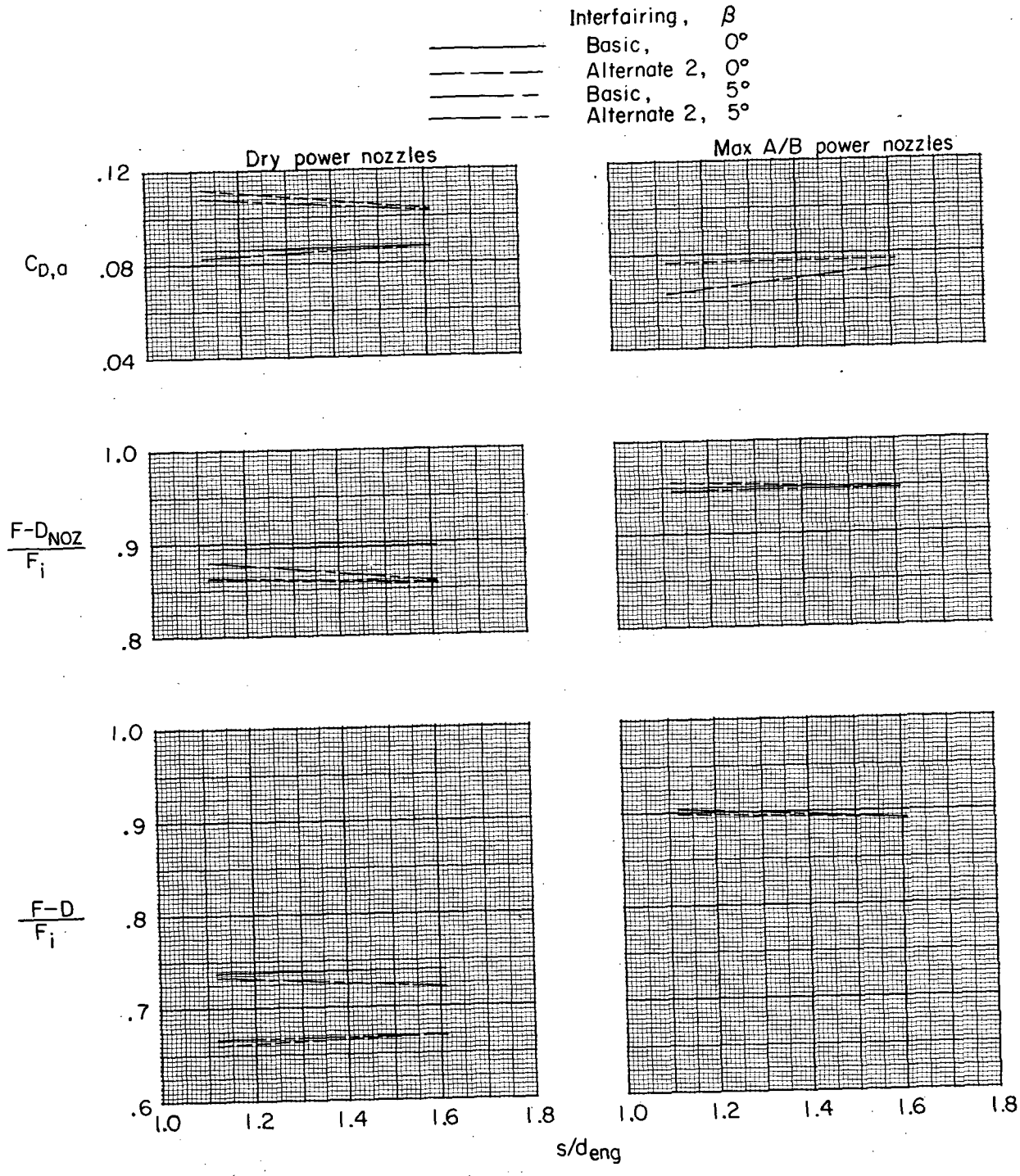

(f) M = 1.30.

Figure 35.- Continued.

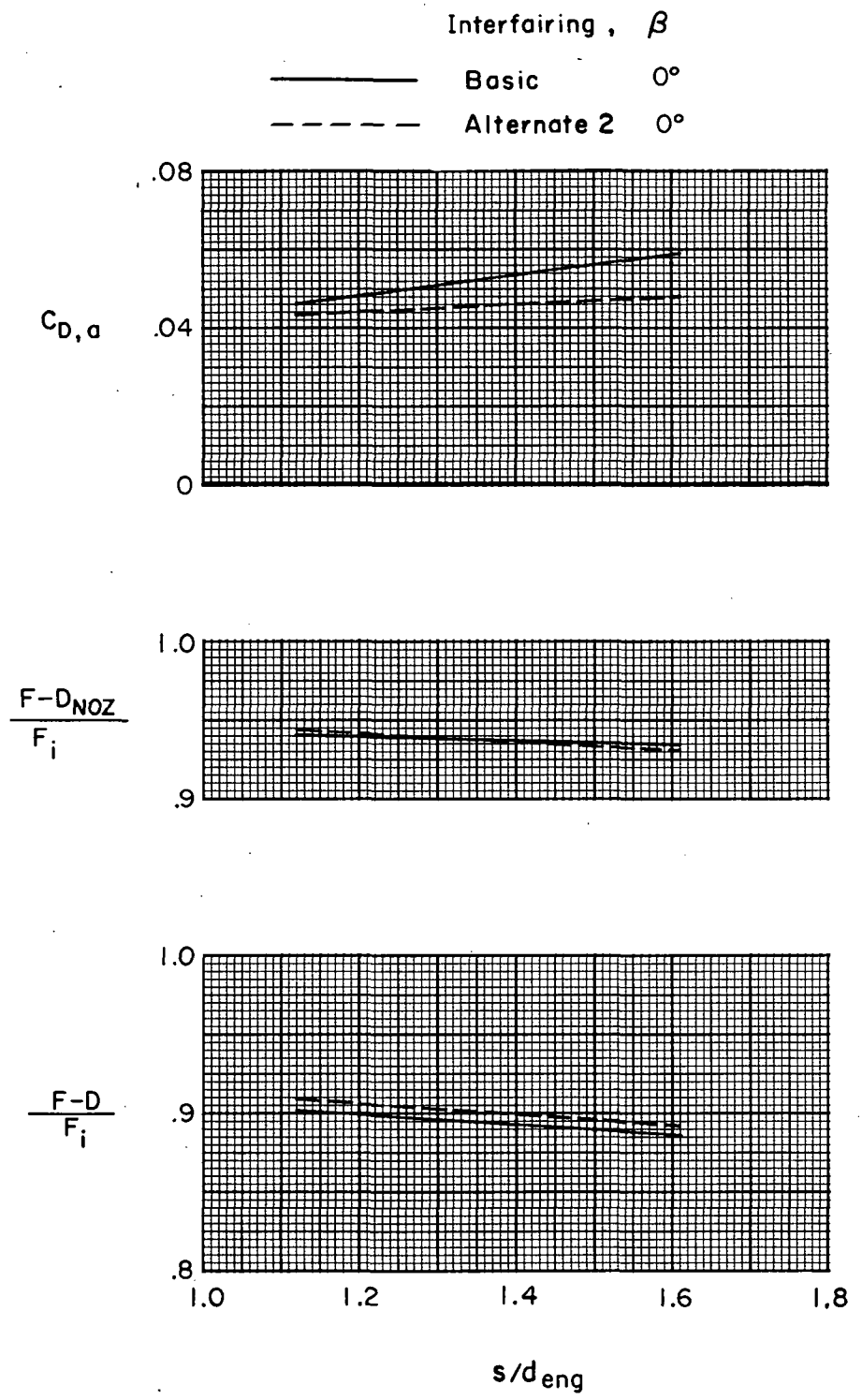

(g) M = 2.20.

Figure 35.- Concluded.

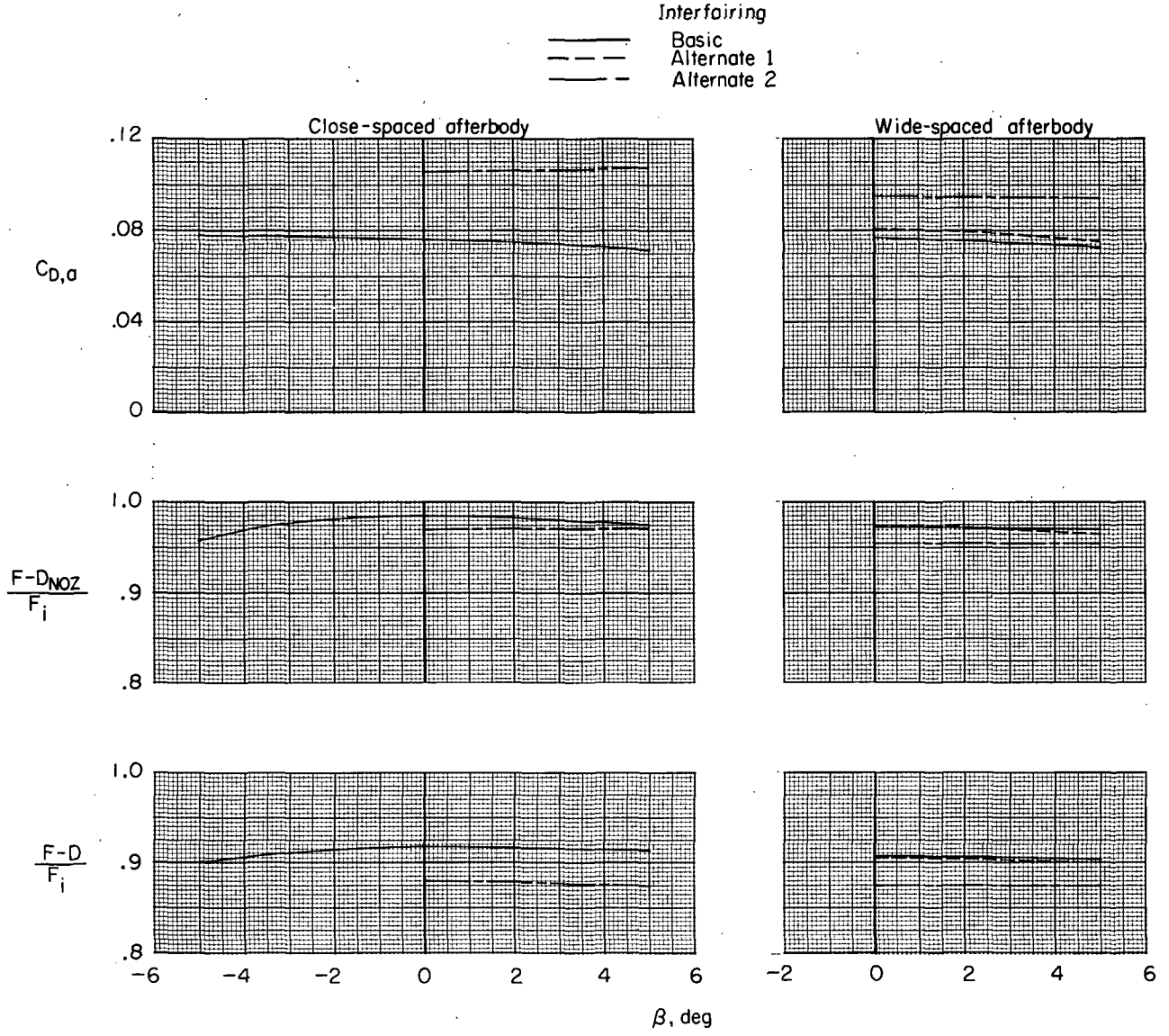

(a) Dry power nozzles; M = 0.50.

Figure 36.- Effect of nozzle cant angle on afterbody drag coefficient, thrust-minus-nozzle-drag ratio, and thrust-minus-total-drag ratio at several Mach numbers and scheduled jet total-pressure ratios.

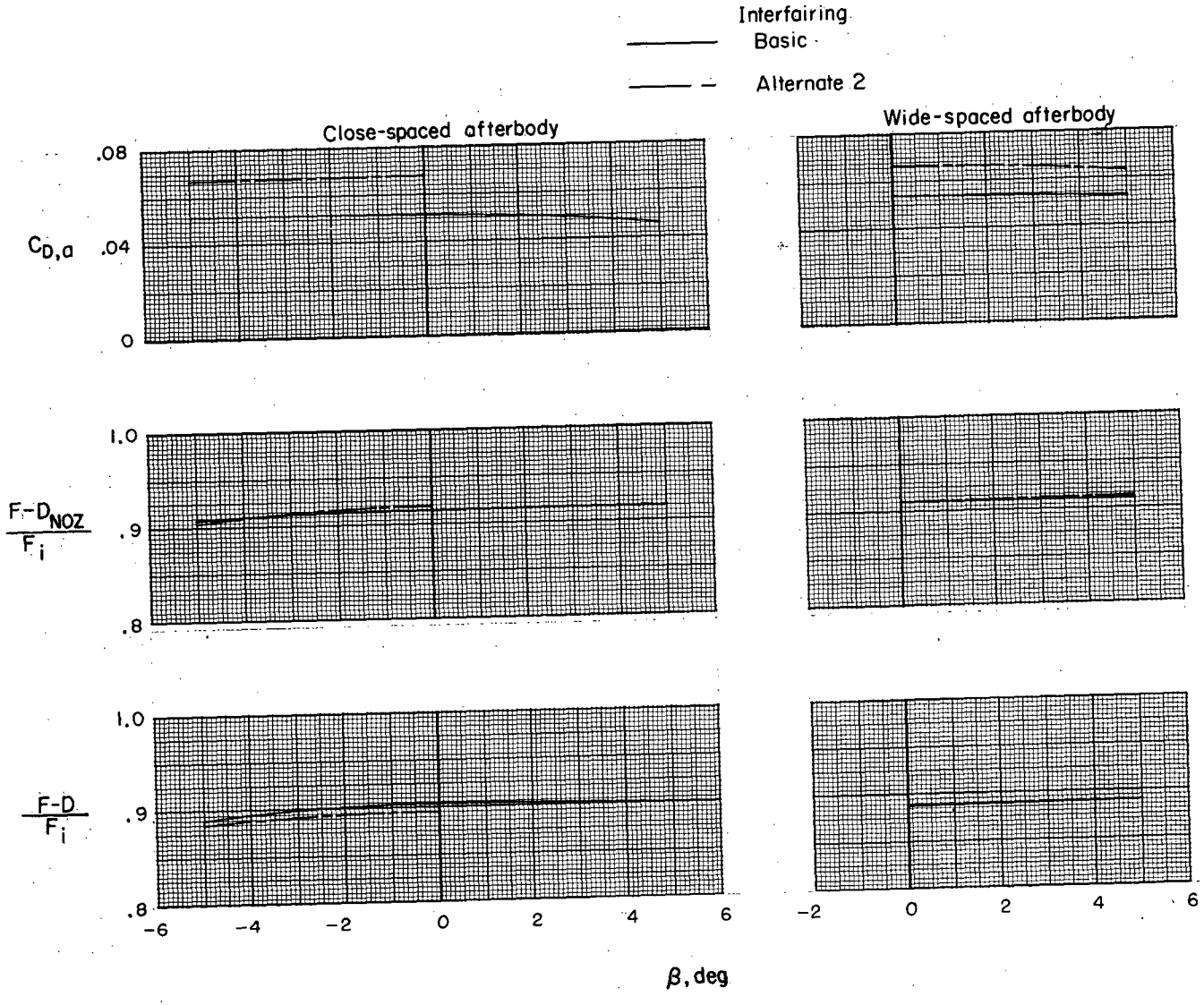

(b) Max A/B power nozzles; M = 0.50.

Figure 36.- Continued.

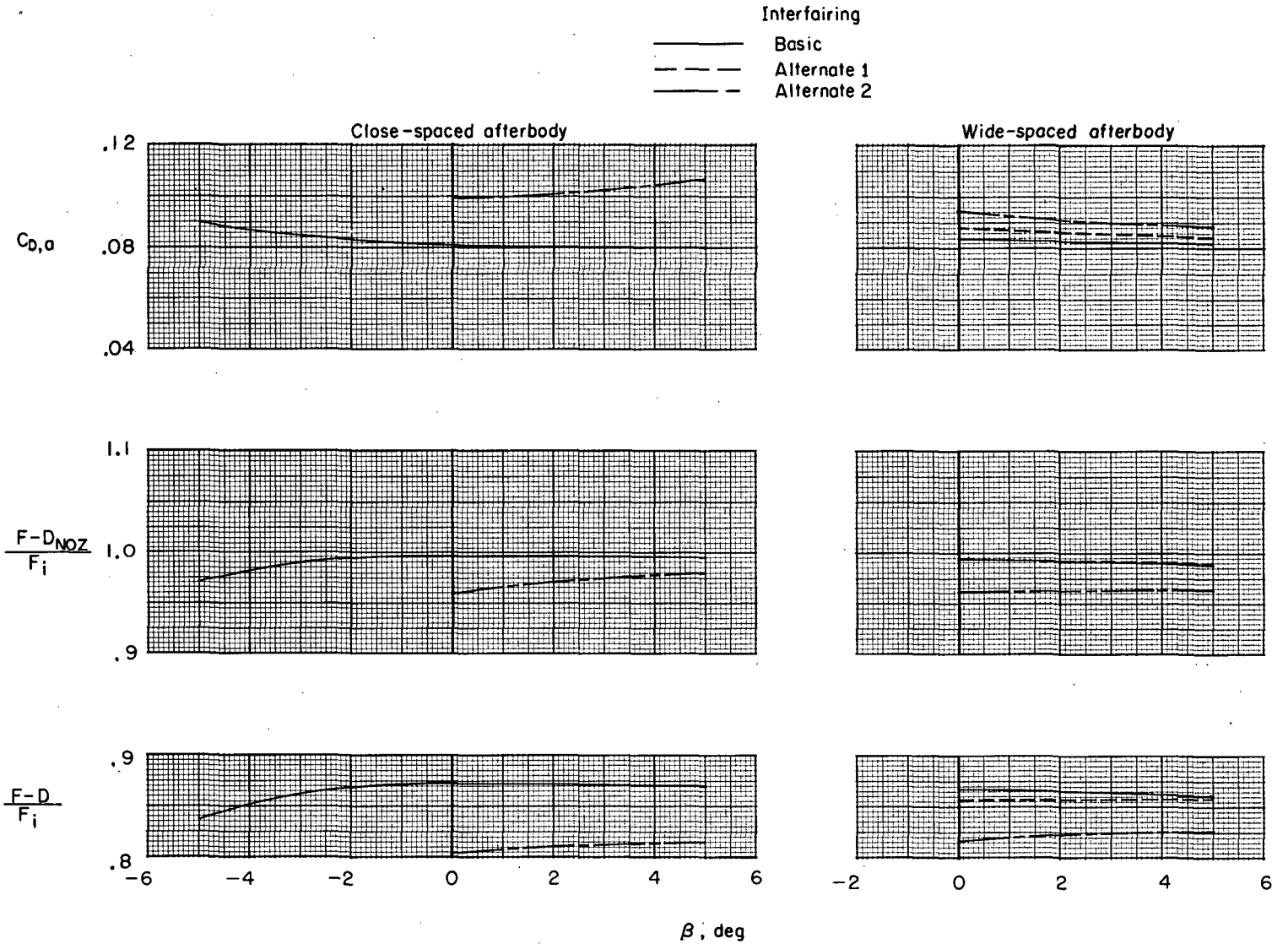

(c) Dry power nozzles; M = 0.90.

Figure 36.- Continued.

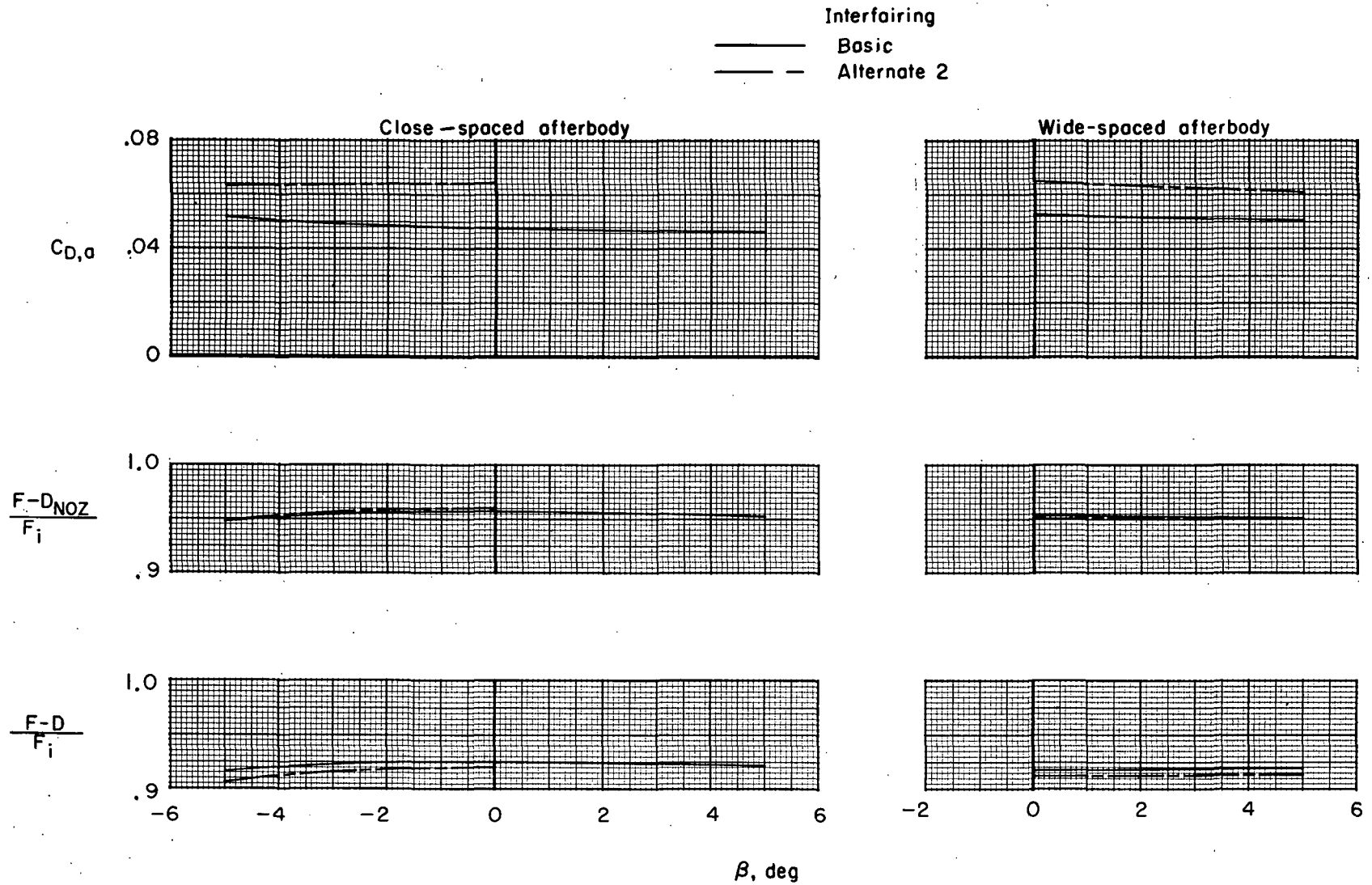

(d) Max A/B power nozzles; M = 0.90.

Figure 36.- Continued.

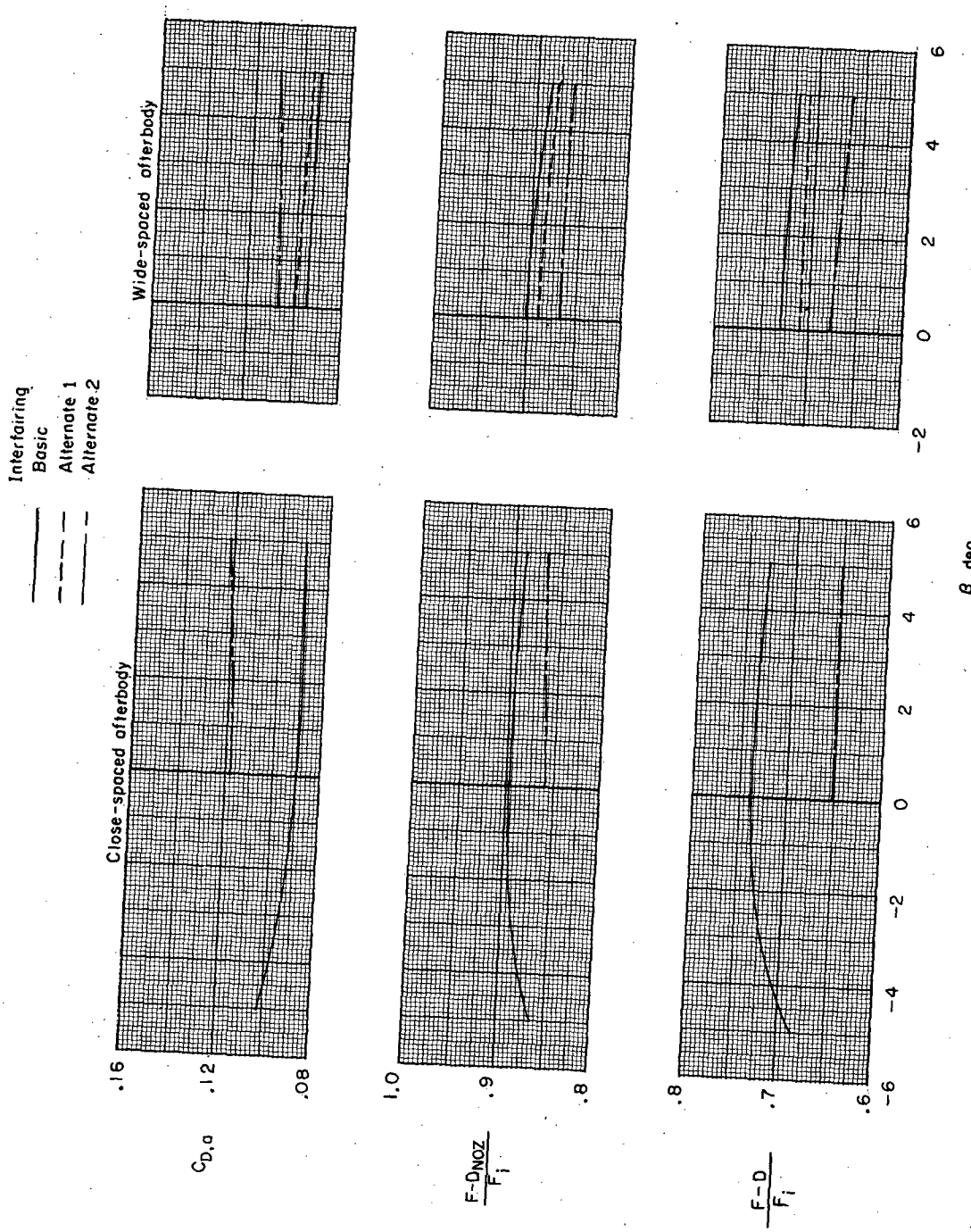

(e) Dry power nozzles; M = 1.20.

Figure 36.- Continued.

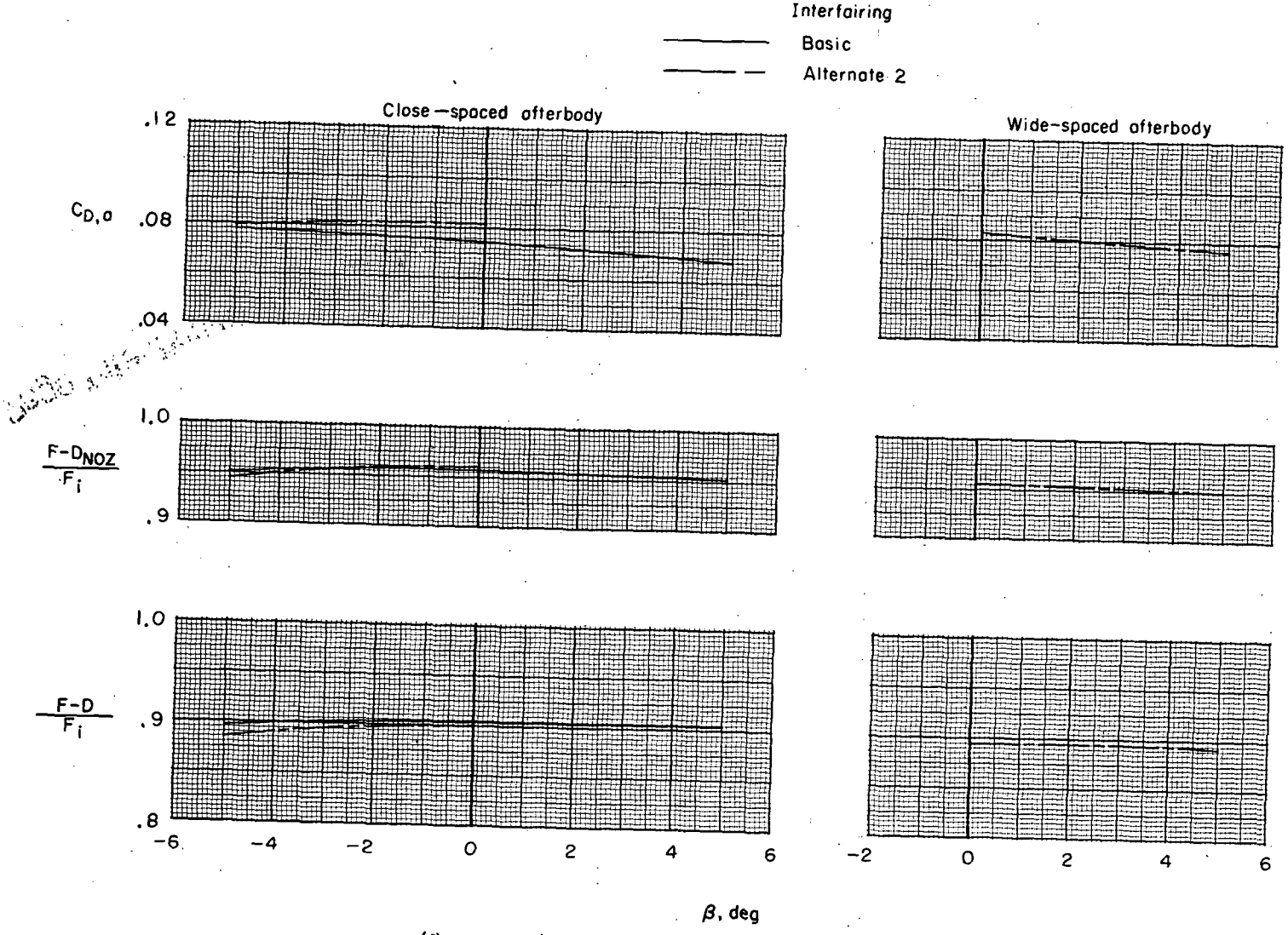

(f) Max A/B power nozzles; M = 1.20.

Figure 36.- Concluded.

NATIONAL AERONAUTICS AND SPACE ADMINISTRATION
WASHINGTON, D.C. 20546

OFFICIAL BUSINESS
PENALTY FOR PRIVATE USE $300

FIRST CLASS MAIL

POSTAGE AND FEES PAID
NATIONAL AERONAUTICS AND
SPACE ADMINISTRATION
451

U.S.MAIL

POSTMASTER : If Undeliverable (Section 158 Postal Manual) Do Not Return

"The aeronautical and space activities of the United States shall be conducted so as to contribute . . . to the expansion of human knowledge of phenomena in the atmosphere and space. The Administration shall provide for the widest practicable and appropriate dissemination of information concerning its activities and the results thereof."

—NATIONAL AERONAUTICS AND SPACE ACT OF 1958

NASA SCIENTIFIC AND TECHNICAL PUBLICATIONS

TECHNICAL REPORTS: Scientific and technical information considered important, complete, and a lasting contribution to existing knowledge.

TECHNICAL NOTES: Information less broad in scope but nevertheless of importance as a contribution to existing knowledge.

TECHNICAL MEMORANDUMS: Information receiving limited distribution because of preliminary data, security classification, or other reasons. Also includes conference proceedings with either limited or unlimited distribution.

CONTRACTOR REPORTS: Scientific and technical information generated under a NASA contract or grant and considered an important contribution to existing knowledge.

TECHNICAL TRANSLATIONS: Information published in a foreign language considered to merit NASA distribution in English.

SPECIAL PUBLICATIONS: Information derived from or of value to NASA activities. Publications include final reports of major projects, monographs, data compilations, handbooks, sourcebooks, and special bibliographies.

TECHNOLOGY UTILIZATION PUBLICATIONS: Information on technology used by NASA that may be of particular interest in commercial and other non-aerospace applications. Publications include Tech Briefs, Technology Utilization Reports and Technology Surveys.

Details on the availability of these publications may be obtained from:

SCIENTIFIC AND TECHNICAL INFORMATION OFFICE

NATIONAL AERONAUTICS AND SPACE ADMINISTRATION

Washington, D.C. 20546